

Flaw-Limited Transport in Germanium-on-Silicon Photodiodes

by

Jason S. Orcutt
B.S. Electrical Engineering
Columbia University, 2005

SUBMITTED TO THE DEPARTMENT OF ELECTRICAL ENGINEERING IN PARTIAL
FULFILLMENT OF THE REQUIREMENTS FOR THE DEGREE OF

MASTER OF SCIENCE IN ELECTRICAL ENGINEERING
AT THE
MASSACHUSETTS INSTITUTE OF TECHNOLOGY

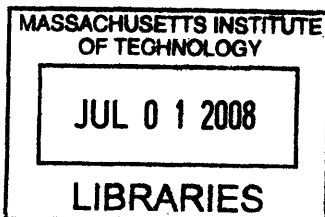
JUNE 2008

©2008 Massachusetts Institute of Technology. All rights reserved.

Signature of Author: _____
Department of Electrical Engineering
May, 2008

Certified by: _____
Rajeev J. Ram
Professor of Electrical Engineering
Thesis Supervisor

Accepted by: _____
Terry Orlando
Professor of Electrical Engineering
Chairman, Committee for Graduate Students



ARCHIVES

Flaw-Limited Transport in Germanium-on-Silicon Photodiodes

by

Jason S. Orcutt

Submitted to the Department of Electrical Engineering on
May 23, 2008 in Partial Fulfillment of the
Requirements for the Degree of Master of Science in
Electrical Engineering

ABSTRACT

Epitaxial germanium growth on silicon substrates has enabled a new class of photodiodes that can be integrated with traditional silicon electronics. Previous workers using low-throughput growth techniques have demonstrated device functionality sufficient for many applications. To enable commercial integration, however, similar performance must be achieved using high throughput epitaxy. In this work, the current performance of germanium-on-silicon photodiodes fabricated by MIT colleagues using one such technique, low pressure chemical vapor deposition (LPCVD), is analyzed.

The measured electrical characteristics of multiple diode geometries are fit to finite-element simulation to extract bulk and surface generation rates as a function of bias voltage. The extracted rates are then fit in conjunction with known states from the germanium defect literature to find the densities and field dependant cross sections of physical flaws believed to limit this promising class of devices. General interest photodiode performance is then quantified by optoelectronic measurements and analyzed in the context of the flaw limited transport. Device applicability for integration with an existing photonic sampling system is analyzed and intersymbol interference, noise and linearity metrics are measured and discussed. In conclusion, a pathway for improved devices based upon improved fabrication techniques to reduce identified flaw densities combined with changes in device design is proposed.

Thesis Supervisor: Rajeev J. Ram
Title: Professor of Electrical Engineering

Table of Contents

Table of Contents	3
Chapter 1 – Introduction	7
A Thousand Foot Overview of Silicon VLSI	9
Previous Work on Silicon Photonics	12
General Photodiode Device Design	15
Modification of Device Performance by Flaw States	20
Scope of this thesis	23
Chapter 2 – Electrical Characteristics of Ge-on-Si Photodiodes	27
Strawman Ge-on-Si Photodiode Device Structure	27
Known Electronic Issues Resulting from Epitaxial Growth and Processing	29
Threading Dislocations	29
Passivation Interface Flaws	32
Autodoping of Epitaxial Intrinsic Region	32
Strained Film Bandgap Narrowing	33
Current-Voltage Measurements	33
Thermoreflectance Imaging of Spatially Dependant Power Dissipation.....	37
Finite Element Model Construction	39
Electrostatic Device Simulation Results	44
Matching Simulated and Measured I-V Responses with Carrier Lifetime Fitting	47
Parameters for Physical Flaw Models	53
<i>A Priori</i> Bulk Threading Dislocation Model.....	55
Detailed Bulk Threading Dislocation Model Construction	56
Detailed Edge State Flaw Model.....	59
Field Dependant Cross Section Fitting	60
Poole-Frenkel Thermionic Emission Enhancement	61
Hurkx Trap Assisted Tunneling	65
Lui and Migliorato Combined Model	67
J-Model Polynomial Cross Section Enhancement	69
Comments and Possible Explanations of Fitting Results	72
Chapter 3 – Optical Characteristics of Ge-on-Si Photodiodes	75
Optical Conversion Efficiency	77
Responsivity Measurement	77
Internal Quantum Efficiency Estimates.....	82
Responsivity Simulation.....	84
Spatial Responsivity	87
Measurement.....	87
Simulation	88
Thermally Dependant Responsivity Measurements	89
Small-Signal Frequency Response	91

Measurement.....	92
Simulation	94
Spatially Resolved Frequency Response	95
Pulse Response.....	96
Measurement.....	97
Simulation	99
Changes to the DC Model for Improved Frequency Response Matching.....	101
Chapter 4 – Application Specific Performance Characterization	103
EPIC Optical Sampling Front End Analog to Digital Converter	103
Linearity Performance	104
Noise Floor	108
Spurious Free Dynamic Range	108
Sampling System Bandwidth Requirements	109
Impact of Trap States on Inter Sample Interference.....	112
Chapter 5 – Conclusion and Future Work	119
Dark Current Reduction	119
Bandwidth-Efficiency Product Analysis	120
Potential Responsivity Improvements	121
Addition of an Anti-Reflective Coating	122
Reduction of the Threading Dislocation Density	123
Improved Surface Passivation	123
Potential Bandwidth Improvements	124
Elimination of P+ Seed Layer.....	124
Reduction of the Threading Dislocation Density	126
Improved Surface Passivation	128
Summary of Future Work	128
Experiment	128
Simulation	129
Theory.....	130
Fabrication.....	131
Conclusion.....	132
Appendix A – Sentaurus Input Files.....	135
Structure Generation Scripts.....	135
Circular Diode 2-D Cylindrical Coordinates Structure	135
Rectangular Diode 2-D Transverse Structure	140
Rectangular Diode 3-D Structure.....	142
Device Simulation Command Files.....	144
Parametric Lifetime Variation for I-V Fitting	144
Center Responsivity Simulation.....	146
Overfill Responsivity Simulation.....	149
Spatial Responsivity Simulation	151
Optical AC Analysis.....	153
Optical Transient Analysis	156
Material Parameter Definition.....	160
Germanium (Key Parameters Only)	160

FlawedGermanium (Differences From Germanium Only)	163
Silicon (Key Parameters Only)	163
Syntax Required for Explicit Trap Definition.....	167
Material Parameter File Syntax	167
Command File Syntax	168
Appendix B – Matlab Scripts	171
Dark Current Fitting.....	171
fit_single_temp_version2.m	171
getSimCurrent.m	176
fit_lifetimes_vs_field.m	176
Transmission Matrix Optical Analysis.....	182
Tmatrix_geslab_oxide_sweep_lambda.m.....	182
Tmatrix_geslab_oxide_sweep.m	184
Measurement Postprocessing	185
freqresponse_nofit.m.....	185
pulse_response.m	188
Sampler Performance Specifications	192
required_pulse_bw.m	192
Appendix C – Python Scripts	195
Sentaurus Output File Postprocessing	195
extract_datafiles.py.....	195
extract_fields.py.....	197
References.....	201

Chapter 1 – Introduction

In the early days of semiconductor device research, circa 1950, the material of choice was germanium. However, barring a few temporary threats of relevancy from germanium and its alloys, silicon dominated the electronic integrated circuit (IC) and very large scale integrated (VLSI) circuit industries for the next fifty years. The reasons behind this are complex and often focus on practical manufacturing issues. From a purely technical perspective, the inability of germanium to be well passivated by an oxide interface made it a poor choice for electronic integrated circuit devices where field effect transistor technology (FET) requires a long carrier lifetime near oxide interfaces.

Now as the success of pure silicon VLSI device scaling has enabled the exponential growth of the computation capabilities of a single processing chip, standard silicon electronic technology is facing energy and density roadblocks in getting the raw and processed data on and off the chip. Another hugely successful technology of the 20th century, photonics, has offered communication solutions for length scales ranging from across oceans to across data centers; however, to efficiently handle the data I/O from a single piece of silicon in a dense, energy-efficient manner, the photonic interface must be integrated on-chip. This requirement stems from the parasitic dissipation when the nanoscale transistors are forced to drive macroscopic loads for external signaling. Taken to the logical conclusion, the photonic interface is most efficient when integrated in the front-end of the electronic process as close to the transistor blocks generating the desired data. Similar arguments for front-end photonic integration can be seen in a more general set of systems that stand to benefit by eliminating the energy, density and complexity costs associated with interfaces between electronics and photonics. One might argue that this integration could be achieved in the maturing photonics processes such as III-V semiconductor manufacturing, but the maturity of silicon VLSI, currently achieving seven orders of magnitude higher integration, guarantees the ability to massively integrate devices that can be manufactured with its techniques.

Many previous investigators have made strides in creating a set of devices that can be integrated with similar techniques to silicon VLSI as will be detailed further later in this introduction. Devices such as modulators, waveguides and wavelength selective filters can be well manufactured using standard silicon and oxide materials; however, photodiodes require a material with a smaller bandgap than silicon to absorb the light traveling in the silicon waveguides. Shorter wavelength techniques that would allow for silicon based photodetectors do not look promising due to the long absorption length and substrate diffusion problems long associated with integrated silicon detectors. Both of these problems stem from using silicon as the absorbing material where the generation cannot be limited to the active area by bandgap engineering and the indirect bandgap requires weaker phonon assisted absorption processes. Instead, the reintegration of a compatible material such as germanium that offers a smaller bandgap and a direct band minima alignment near telecommunication wavelengths offers a greater possibility to produce a useful device. The optical generation can then be limited to the active region of the diode and made smaller due to a higher absorption coefficient.

The silicon-only nature of traditional electronics VLSI is also changing. Germanium, in the form of low mole fraction silicon-germanium, is being introduced to induce strain on the silicon devices. In a larger change, the Si-SiO₂ interface, long the cornerstone of FET technology, is being replaced with hybrid passivation technology to introduce high dielectric constant materials between the transistor's silicon channel and gate. This leads to the possible introduction of non-silicon materials in the transistor channel, possibly including pure germanium. These epitaxial steps, long necessary in III-V photonic device processing, have traditionally been absent from the low cost silicon VLSI technology.

The confluence of the need and opportunity for integrable germanium detectors has caused many investigators to produce a variety of devices epitaxially grown on silicon substrates [1-23]. Many growth techniques have been studied, but only recently has work been attempted on the kind of low cost, high throughput growth technology that is required by the silicon VLSI field [24]. Initial results have fallen below design targets and performance achieved in

previous germanium on silicon epitaxial photodiodes. The purpose of this thesis is to first quantitatively examine the state of performance in these Ge-on-Si diodes and then construct a model that matches device behavior to enable future device design.

A Thousand Foot Overview of Silicon VLSI

The silicon VLSI community for high-volume products has long been dominated by metal-oxide-semiconductor field effect transistors (MOSFETs), and as such the fabrication process has been tailored around these transistors to optimize their performance in digital logic circuits. The traditional VLSI MOSFET consists of a heavily doped polysilicon gate separated from the single-crystalline silicon channel by a thin, thermally grown silicon dioxide layer. The silicon channel is connected on each end by a source and drain connection. A cross-sectional TEM of an advanced MOSFET as would be found in a current microprocessor chip is shown in (Figure 1). The dopant polarities of these two connections are opposite from the channel doping and much larger in magnitude. Two types of transistors are created: choosing a p-doped channel and n+-doped source/drains creates a NFET; choosing an n-doped channel and p+-doped source/drains creates a PFET. The dominant circuit process is able to produce both complementary types of transistors and is therefore known as complementary metal oxide silicon (CMOS).

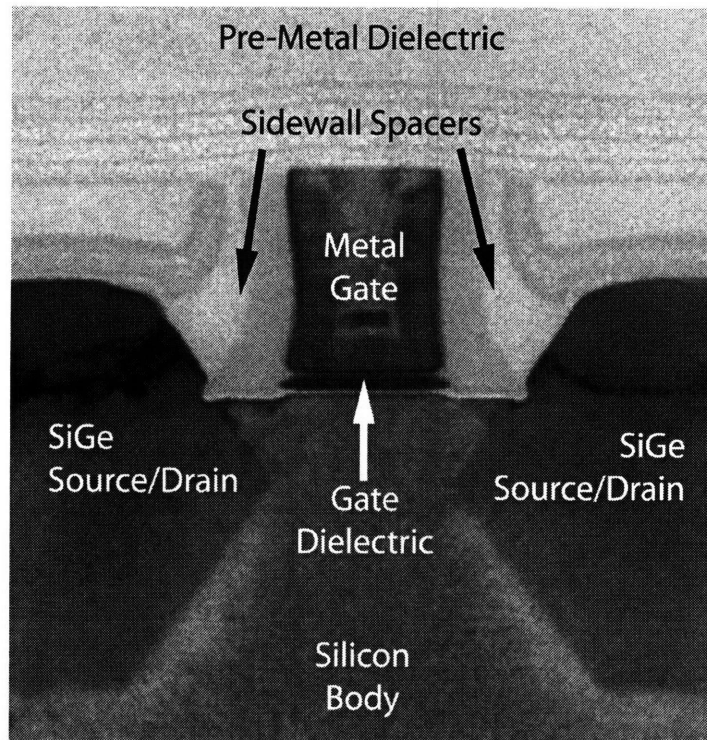


Figure 1. Scanning electron micrograph of a 45nm PFET with major features labeled. Source: Intel.

At the highest-level, the CMOS fabrication process is divided into two halves, the front and back ends. The semiconductor devices are fabricated in the front-end and metal interconnections are fabricated in the back-end. A brief overview of these flows, focusing on aspects relevant for photonic devices will be presented below. Further details can be found from any number of introductory electronics books [25, 26].

Starting wafers for fabrication, typically 300 mm in diameter, are divided into two types: silicon-on-insulator (SOI) and bulk. SOI wafers use a thin silicon device layer 50-100 nm thick on top of a thin oxide layer 50-145 nm thick supported by a 775 μm silicon handle wafer [27]. This breaks the electrical connection from the device body to the silicon substrate that is commonly found in standard bulk wafers where an epitaxial silicon device layer is grown directly on the thick, heavily doped silicon handle wafer.

The front-end processing to define the transistors involves primarily a sequence of precise lithography steps to mask a large number of dopant implant steps. Additionally, the

polysilicon gate must be deposited over a thermally grown thin oxide. This gate serves to mask further implant steps to self-align the source and drain regions. A relatively new addition to CMOS front-end processing has already been mentioned. In addition to defining the source and drains as implanted regions, strain-engineering has led to etching away the silicon from these regions and epitaxially growing low mole fraction silicon germanium source/drains. This step introduces the possibility of integrating other epitaxial growth steps into the device layer which previously consisted solely of material deposition and doping.

Once the transistors are defined, the process progresses to the back-end processing by depositing a thick layer of dielectric, typically phospho-silicon glass (PSG). This planarizes the wafer for further processing and isolates the sensitive device layer from contamination by materials used in the back-end. At this point, narrow square vias are etched to make electrical contact to the devices and filled with a refractory metal, typically tungsten. These initial contact points then need to be wired together to create the final circuit by the near universal technique of copper damascene layers. To define each interconnection layer, a dielectric is deposited and then etched to pattern the desired planar wires. Then a thin barrier metal, typically TaN, is deposited to shield the subsequent uniform copper deposition from diffusing into the insulating dielectric. This layer is then chemically-mechanically polished to remove the uniform copper shorting the desired wires. This step also planarizes the chip to allow this process to begin on the next layer. An additional intermediate step also defines vias to connect between these planar wire layers. A cross-section of such a finished stack-up is shown in (Figure 2). This final result is far more fragile to temperature than the initial device layer. Whereas processing temperatures in the front end range up to 1000 C, the backend thermal budget is limited to approximately 400 C.

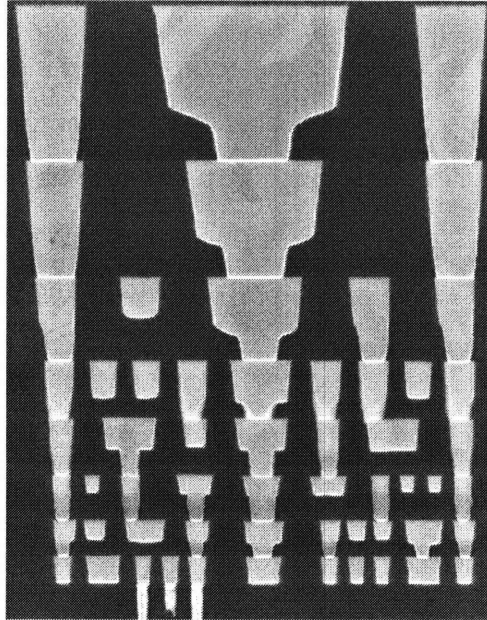


Figure 2. Cross sectional scanning electron micrograph showing the interconnecting metal layers in the backend stackup of a finished microprocessor. Source: Intel.

To provide the necessary data and power connections to the increasingly dense device layer, a large quantity of these back-end wiring layers are currently required. The total thickness in modern processes is $> 5 \mu\text{m}$. This macroscopic network of copper contributes a large quantity of parasitics and requires significant power dissipation to charge and discharge the associated capacitance. The bandwidth-density provided by these wires has been scaling slower than the transistor and therefore computational density of the front-end. This problem becomes more severe when you look at the off-chip communication problem associated with these back-end wires connecting through the package onto the circuit board to drive the large copper traces of a circuit board to communicate with another chip.

Previous Work on Silicon Photonics

In addition to the general trends of photonic and electronic integration, the specific goal of finding a more efficient communication channel that can directly interface with the transistors in the front end of a CMOS process has driven silicon photonic work. One alternative approach that should be mentioned is the flip chip mounting of transmitters and receivers made with III-V materials onto the finished silicon electronics wafer. This eliminates

the process compatibility problem of photonic devices, but has other associated problems. In addition to not being as economical a pathway to introduce thousands of links into a single chip, it still has all of the associated parasitics of not only the back-end stackup but also the mounting bond wires. Instead, it is desirable to produce an arbitrary number of integrated devices integrated into the front-end process without the parasitic and scalability problems of flip-chip mounted devices. The majority of the early work in this field has focused on introducing silicon photonics into SOI based CMOS and the discussion here will be limited to that area.

Since nearly all uses of silicon photonics requires a large number of usable links instead of just a few transmitters or receivers, a proposed platform must be able to directly integrate not only both of these devices but also waveguides to direct the travel of light on chip. In a SOI platform, waveguides can be created by increasing the thickness of the oxide between the device layer and the handle wafer. By patterning the device layer, it is possible to create an isolated pathway of high-index silicon surrounded by a low-index dielectric. This waveguide tightly confines the light due to the high index contrast (HIC) and has been shown to have low loss [28].

To integrate transmitters, waveguides can be formed into interferometric and resonant photonic structures such as Mach-Zehnder interferometers (MZIs) and ring resonators. The resonant condition of these structures can then be modified by changing the refractive index of the waveguides. In silicon, this can be achieved very quickly by carrier injection by placing the waveguide into the intrinsic region of the p-i-n diode [29]. Promising work in ring resonator modulators has demonstrated transmitters suitable for ten gigabit on-chip interconnect applications [30, 31].

The integration of receivers within a silicon chip poses a slightly larger problem. With the exception of defect-mode detectors, a smaller bandgap material than silicon must be used for optical absorption in the detector [32]. Early work in this field has relied on flip-chip bonding technology that allows III-V photodiodes to be mounted on the silicon wafer after processing

[33]. This approach with limited scalability suffers not only from the comparatively large electrical parasitics of the macroscopic bond pads required, but also from the large required device area for alignment tolerance and large mode size [34]. Instead, it is desirable to have a photodetector integrated in the waveguiding layer of the process front-end that has low capacitance and connection parasitics.

Since the current CMOS process already includes silicon germanium epitaxy for strain engineering, there is recent interest in making photodiodes in a similar process. The change in going from a low mole fraction SiGe to pure germanium requires that lattice relaxation must occur as the 4% lattice mismatch prohibits coherently strained films. Early workers were able to create good quality germanium films by first growing silicon germanium and increasing the mole fraction through graded layer buffers to reduce dislocation densities [35]. Although good material quality was achieved with this technique, the multistage growth results in thick films and requires long growth times with demanding control. This approach is ill-suited to the rapid, high-throughput world of CMOS processing.

Recent workers have instead attempted to perform a single step, direct germanium on silicon growth by carefully optimizing seed layer doping, thermal ramping and post process annealing [2]. This work in ultra high vacuum chemical vapor deposition (UHVCVD) reactors has yielded 10 Gb/s datacom grade vertically illuminated detectors [3, 4, 9, 10, 14, 15, 18]. Recent work has demonstrated similar growth techniques to achieve high quality waveguide integrated photodiodes directly integrated with silicon compatible waveguides [36, 37].

However, a remaining limitation to VLSI integration is that current commercial epitaxial systems on CMOS fabrication lines use the higher throughput low pressure chemical vapor deposition (LPCVD) reactors. The work in this thesis will focus on examining photodiode performance that is limited by the material quality of these systems to evaluate the potential of future photodiodes manufactured in this way.

General Photodiode Device Design

It is first necessary to understand a few basic aspects of photodiode design to understand how material quality impacts device performance. Fundamentally, photodiodes are simple p-n junctions. The only difference between the introductory device class junction and commercial products is extensive optimization. First of all, the device is always operated in reverse bias with the junction electric field acting to separate the electron-hole pairs generated by incident light.

Ideally, all incident light should be absorbed only in the high field depletion region. This goal is often aided by introducing a smaller bandgap material without doping between the p and n regions. This type of heterostructure p-i-n diode allows for high device performance, but requires a complicated fabrication. The photodiodes that will be examined in this thesis are instead p-i-n diodes all made of the same germanium material on a silicon substrate that is transparent to the wavelengths of interest. The consequence of this design is that in addition to current generated by electron hole pair drift in the depletion region, photons generated in the p and n regions can diffuse into the depletion region and contribute to current as well. This "diffusive-tail" can slow the transient response of the photodiode. A cartoon of such a prototypical p-i-n diode is shown in (Figure 3).

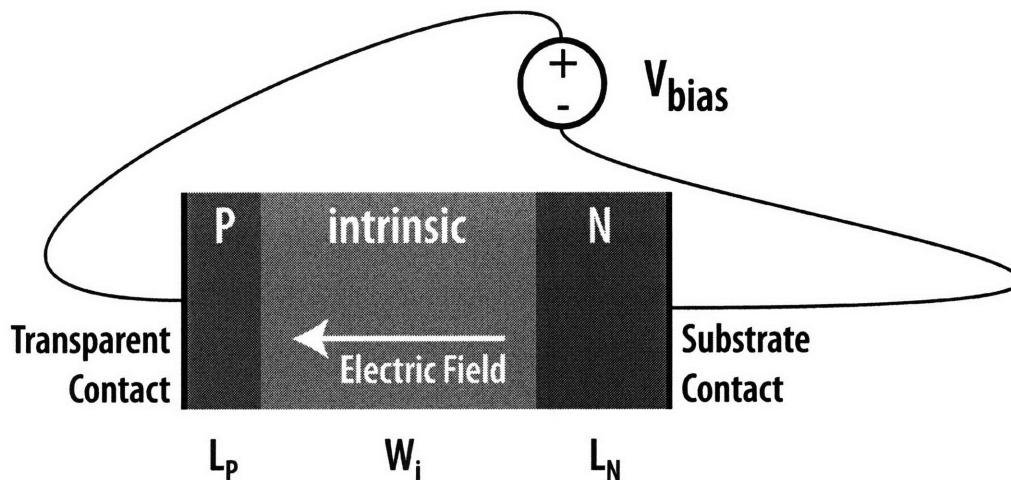


Figure 3. Cartoon of prototype p-i-n diode.

Current generated by incident photons is the desired signal, but other sources of current are present as well. In addition to photon excitation, shown in (Figure 4), thermal generation independent of incident light can cause electron-hole pairs that contribute to current as shown in (Figure 5). These other current sources are often called dark current as they are present without optical illumination and are a parasitic noise source that interferes with device function.

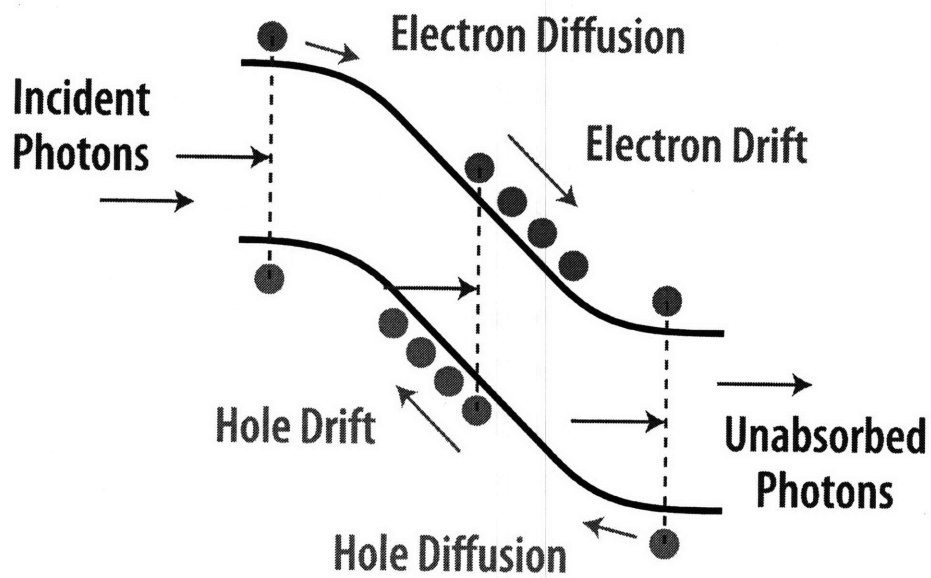


Figure 4. Cartoon illustrating the transport mechanisms of optically generated electron-hole pairs in various regions of a reverse biased p-i-n diode.

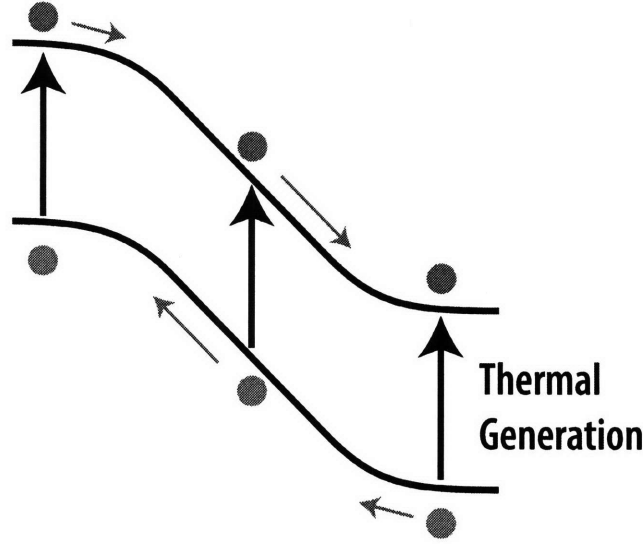


Figure 5. Cartoon depicting the contribution of thermally generated carriers in reverse bias current.

The magnitude for these two current sources can be easily approximated. For the optical generation, the incident optical power is reduced by device reflection and incomplete absorption. Additionally, the incident photons need to be calculated by dividing the power by the photon energy. The current is then determined by multiplying by the charge of the electron modified by the internal quantum efficiency, η , that is the fraction of generated electron-hole pairs that contribute to current. The resulting product can be expressed in terms of the reflectivity, r , incident power, P_0 , Ge film thickness, t_{film} , absorption coefficient, α_{Ge} , and photon energy, E_{photon} , as:

$$I_{opt} = q\eta \frac{(1-|r|^2)P_0}{E_{photon}} [1 - \exp(-\alpha_{Ge}t_{film})] \quad (1.1)$$

All of these quantities except for the internal quantum efficiency can be easily estimated by simple calculations and literature review. The internal quantum efficiency depends on several transport parameters but can be roughly estimated as follows. In order for the absorbed photons to contribute to current, they must be absorbed within approximately one diffusion length of the depletion region with a total length of $L_p + L_n + W_i$. Recombination within this region further reduces the current by the fraction of generated carriers that recombine. The

approximate internal quantum efficiency can therefore be written for a photodiode illuminated from the p-side in terms of the excess carrier recombination rate, U_{excess} , optical generation rate, G_{opt} , p-side width, x_p , and n-side width, x_n , as:

$$\eta \approx \frac{G_{opt} - U_{excess}}{G_{opt}} \left[e^{-\alpha_{Ge}(x_p + W_i + x_n)} - e^{-\alpha_{Ge}(x_p + W_i + L_n)} - \left(e^{-\alpha_{Ge}(x_p - L_p)} - e^{-\alpha_{Ge}x_p} \right) \right] \quad (1.2)$$

The relation between incident optical power is very often consolidated into the experimental parameter of responsivity and expressed as such as shown in Equation (1.3). This parameter having units of A/W contains all of the dc photoresponse information for a given wavelength and will be determined by measurements for the Ge on Si photodiodes in Chapter 3.

$$I_{opt} = RP_0 \quad (1.3)$$

A similar expression can be obtained for thermal generation by the use of minority carrier lifetimes. Thermal current can be estimated by calculating the generation in each region that contributes to current. For the quasineutral regions, the generation is equal to the recombination by the principles of detailed balance and can therefore be expressed by dividing the minority carrier density with the minority lifetime. The thermal current can therefore be expressed in terms of the area, A , minority carrier densities, n_{p_0} and p_{n_0} , minority lifetimes, τ_n and τ_p , and the depletion region generation, G_0 , as:

$$I_{therm} = qA \left(\frac{n_{p_0}}{\tau_p} L_p + G_0 W_i + \frac{p_{n_0}}{\tau_n} L_n \right) \quad (1.4)$$

The depletion region generation can be estimated by first assuming that midgap flaw recombination observing Shockley-Read-Hall statistics dominates as is often the case for indirect gap semiconductors. The recombination rate can therefore be written in terms of the electron density, n , hole density, p , and intrinsic carrier density, n_i , as [38]:

$$U^{SRH} = \frac{np - n_i^2}{\tau_p(n - n_i) + \tau_n(p + n_i)} \quad (1.5)$$

When electron and hole densities are much less than intrinsic carrier density as is the case in the depletion region of a diode, the recombination rate becomes negative and the expression for the intrinsic region generation in this limit can be obtained:

$$G_0 = \frac{n_i}{\tau_p + \tau_n} \quad (1.6)$$

This generation rate can be inserted back into equation (1.4) and the minority carrier densities can be expressed in terms of the majority carrier densities, n_n and p_p , and the intrinsic carrier density:

$$I_{therm} = qA \left(\frac{n_i^2 L_p}{p_p \tau_p} + \frac{n_i W_i}{\tau_n + \tau_p} + \frac{n_i^2 L_n}{n_n \tau_n} \right) \quad (1.7)$$

For wide bandgap semiconductors where n_i is small, thermal generation is dominated by the contribution from the depletion region. The difference between silicon, bandgap 1.12 eV, and germanium, bandgap 0.661 eV, results in a depletion region to diffusive region current ratio of approximately 3000 for silicon and 0.1 for germanium [39]. This means that for germanium the diffusion needs to be included in dark current analysis which requires a full accurate model of the device for realistic theory. It is therefore troubling that current papers published on germanium photodiode dark current only include the generation contribution from the depletion region [40].

The transient or frequency responses of a p-i-n diode are less tractable by analytical theory. To gain some insight into the factors that effect device performance, the simplification of only considering depletion region electron-pair generation yields analytical formulas. This analysis can be setup by considering sinusoidally modulated light being absorbed at the two edges of the depletion region. The electron hole pairs must then drift across the depletion region, a process that takes a finite time determined by the drift velocity. The electrons or holes coming from the other side of the depletion region are then out of phase with the electrons and holes being generated at that location as shown in (Figure 6). The result is a dephasing of the absorbed light, limiting the frequency response of the photodiode:

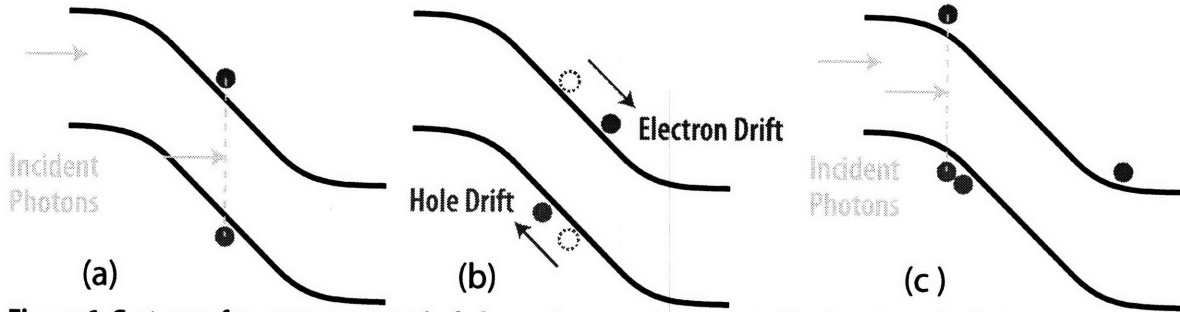


Figure 6. Cartoon of two separate optical absorption events separated by less than the hole transit time.

$$I_{opt}(t) = RP_0 \int_0^{W_i} \exp\left(j\omega\left(t - \frac{x}{v_{drift}}\right)\right) dx \quad (1.8)$$

$$I_{opt}(t) = RP_0 \frac{v_{drift}}{W_i} \frac{1 - \exp\left(-j\omega \frac{W_i}{v_{drift}}\right)}{j\omega} \exp(j\omega t) \quad (1.9)$$

$$\left| \frac{v_{drift} \exp(j\omega_{3dB}t)}{j\omega_{3dB}W_i} \left[1 - \exp\left(-j\omega_{3dB} \frac{W_i}{v_{drift}}\right) \right] \right|^2 = \frac{1}{2} \rightarrow \omega_{3dB} = \frac{2.4}{W_i / v_{drift}} \quad (1.10)$$

This analysis should be a rough guide to understand the fundamental limit to the frequency response of a p-i-n photodiode. Photodiode frequency response goes down with increasing intrinsic region width for a given drift velocity. It should also be noted that the relevant drift velocity is the hole drift velocity which is slower than the electron drift velocity. It is interesting to note that the shortening of intrinsic region width directly reduces the responsivity as shown above in Equation (1.1). This tradeoff results in a traditional bandwidth-efficiency product for vertically illuminated photodiodes as will be discussed further in Chapter 4.

Modification of Device Performance by Flaw States

The epitaxial material quality of the germanium film determines the device performance largely by the addition of flaw states which interfere with ideal p-i-n device behavior. A flaw in the material, potential sources of which will be discussed in Chapter 2, breaks crystal symmetry causing a localized state to form in the traditionally forbidden region of the

semiconductor bandgap. These flaws can contribute to reduced carrier lifetime and increased generation that contributes to dark current or can exhibit trapping behavior in which carriers are temporarily localized in their path across the depletion region, resulting in decreased frequency performance.

To determine which states will act as traps and which will act as recombination-generation (R-G) centers, the capture and emission probabilities for these flaws must first be considered. The model used to consider such a flaw is shown in (Figure 7) and consists of a flaw with a specified energy and capture cross section for carriers in the conduction and valence bands. If the flaw is to act as a trap, it will re-emit captured carriers to its original band after a time delay; if it is to act as a R-G center, it will instead emit captured carriers to the other band thereby destroying an electron-hole pair. The levels where these probabilities are equal, labeled E_{Dn} and E_{Dp} for electrons and holes respectively, are considered the demarcation levels between trap and R-G behavior [41]. For example, the electron demarcation level can be determined by first specifying the probabilities of emission to the conduction and valence bands:

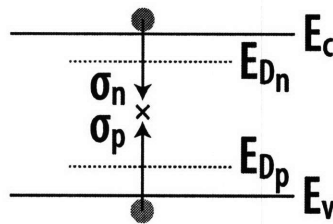


Figure 7. Schematic of flaw parameters.

$$P_c^n = N_c \sigma_n v_{therm} \exp\left(-\frac{E_c - E_{Dn}}{kT}\right) \quad (1.11)$$

$$P_v^n = p \sigma_p v_{therm} \quad (1.12)$$

As shown, the probability of the electron emission to the conduction band is determined by the thermal energy required, capture cross section and the conduction band density of states. The valence band emission probability is simply determined by the capture cross section for

holes and the hole density. Setting these two probabilities equal to each other, the electron demarcation level can be solved for:

$$E_{D_n} = E_c - kT \ln \left(\frac{N_c \sigma_n}{p \sigma_p} \right) \quad (1.13)$$

In general, these demarcation levels show that it is the deep states that act as R-G centers and the shallow levels that act as traps. The next biggest question for the photodiodes is what happens if either traps, R-G centers or both are present. The possibilities for flaws interacting with optically generated carriers are shown in (Figure 8). The traps can increase the transit time and therefore reduce frequency response. The R-G centers can annihilate carriers that are contributing to current, thereby reducing the internal quantum efficiency. In the dark, R-G centers simply become the physical cause of the carrier lifetimes discussed for the derivation of the thermal generation current. The statistics that determine the rate for a localized flaw is called Shockley-Read-Hall (SRH) and will be discussed during the specific flaw model construction in Chapter 2.

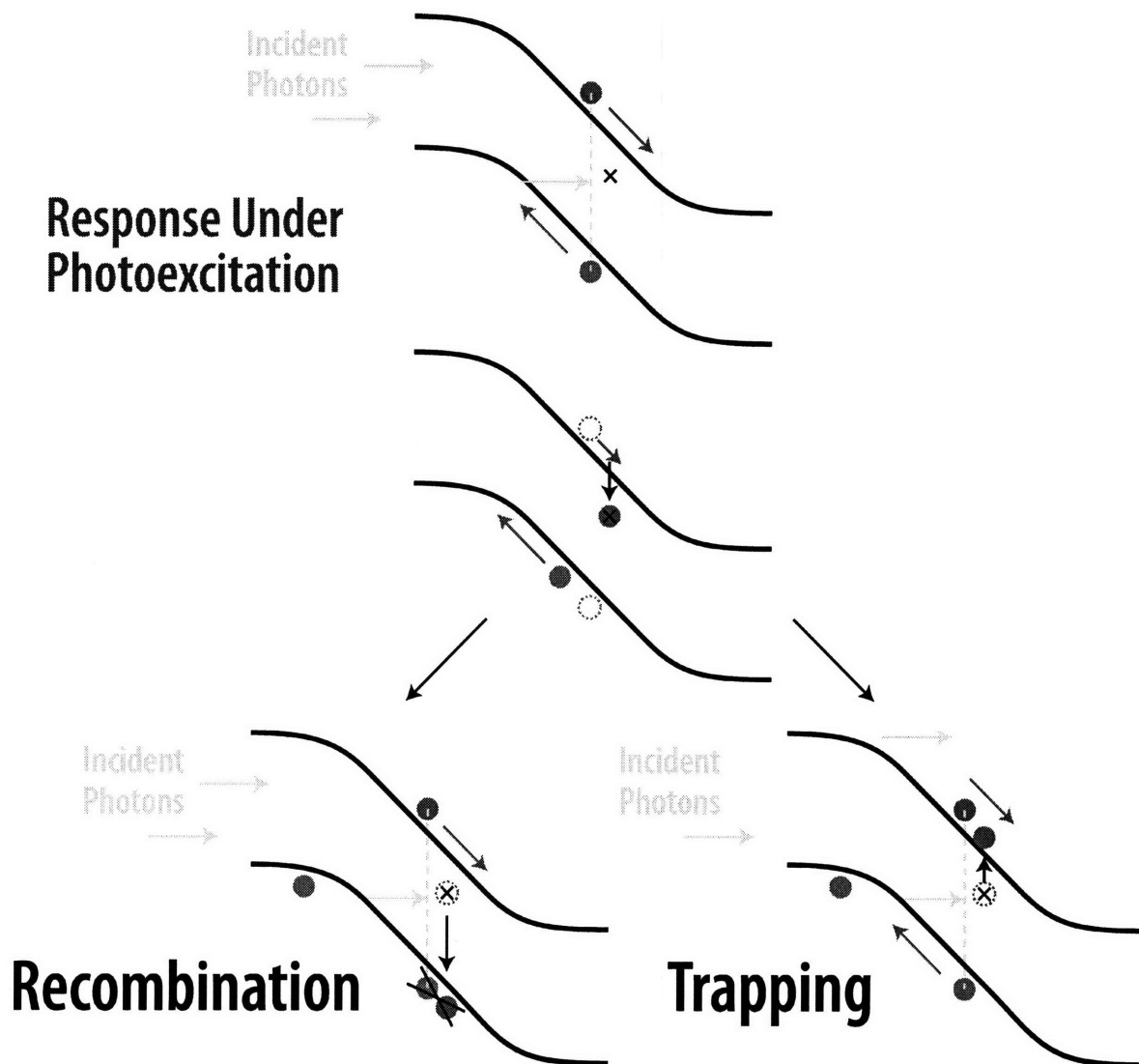


Figure 8. Cartoon of possible flaw related processes involving optically generated carriers.

Scope of this thesis

The current performance of the germanium-on-silicon photodiodes can be understood in terms of contributions from intrinsic device design and flaw states. To understand first the current performance and then to attempt to quantify the physical phenomena involved, several experiments will attempt to be understood with a priori theory and finite element simulation over the next three chapters. The theoretical models will be based largely upon the ideas presented in this introduction. The finite element simulations will be performed with Synopsys's Sentaurus TCAD tool suite. A model representing best guess device

parameters will be developed in Chapter 2 and further refined by comparing this model with the DC electrical diode characteristics. General purpose optical performance characteristics for these diodes will be experimentally characterized in Chapter 3. These measurements will be compared to simulations using the finite element model constructed and refined in Chapter 2. Characterization of special interest to analog applications will be examined in Chapter 4 in the context of a photonic front-end sampling system.

Chapter 2 – Electrical Characteristics of Ge-on-Si Photodiodes

The characterization of Ge-on-Si photodiodes in this thesis will be limited to a single wafer of devices. These devices that will be introduced in detail in the following sections are very similar as a result of this batch fabrication and allow for accurate comparative analysis between diodes. To provide a simulation framework to understand the current state of Ge-on-Si photodiode technology and predict future improvements, a finite-element model is constructed in Synopsys's Sentaurus TCAD tool suite to match the test diodes. The finite-element model will be constructed parametrically such that experimental comparative analysis can be matched in simulation. This procedure will allow for the extraction of device transport parameters for future simulations in coming chapters. The functional form of the extracted device parameters will then be analyzed to compare results with known physical models. This will allow for a hypothesis for physical flaws currently impacting device performance to be constructed.

Strawman Ge-on-Si Photodiode Device Structure

The device structure that will be used as a technology analysis platform to investigate flaw-limited transport for the rest of this thesis is shown in (Figure 9). It is my intent that the analysis and conclusions drawn will be applicable to the class of similarly grown germanium epitaxial photodiodes with a high degree of commercial relevancy, but only various transverse geometries of this structure will be used for all measurements and simulations presented. The details of device fabrication have been presented in detail elsewhere [24], and a brief overview will be presented here.

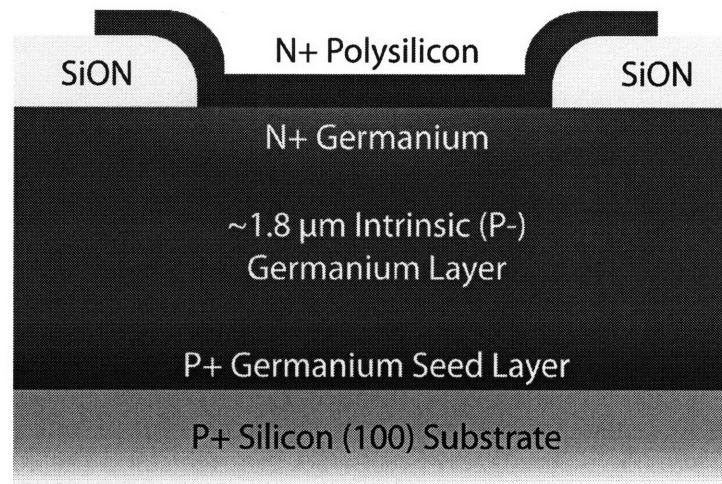


Figure 9. Uniform epitaxy device under study cross section cartoon.

The germanium layer is uniformly grown in an Applied Material Epi Centura low-pressure chemical vapor deposition (LPCVD) system on a standard 6 inch p+ (100) silicon wafer. This method of growth is high-throughput due to the relatively high pressures and growth temperatures used. Similar reactors are currently used in CMOS fabrication lines where throughput is a top priority. Although such a system is necessary for practical high-volume integrability, the material quality produced is traditionally of poorer quality than the methods previously used for germanium on silicon photodiode growth such as MOCVD, UHVCVD and MBE [24]. Additionally, the pure germanium is directly grown on the silicon surface without using silicon germanium graded buffers with gradually increasing Ge mole fraction that have been shown to reduce material defects caused by the mismatched epitaxy [35]. This reduces total growth time, thickness and complexity, again at the expense of material quality. To alleviate some of these issues, the growth begins at low temperature (350 C) and high p-type (boron) doping concentration to quickly relax the film and improve thickness uniformity [42]. The growth temperature is then increased to 800 C and the doping gas flow is turned off. This step is intended to create a thick intrinsic region for the pin diode, but the doping gas remains in the chamber due to the high pressure and “autodopes” the growth to a low p-concentration. The final germanium layer is approximately 2 μm thick.

This uniform film is then lithographically processed into many diodes sharing the same layers along the growth direction, but different transverse geometries. A 300 nm thick SiON layer is

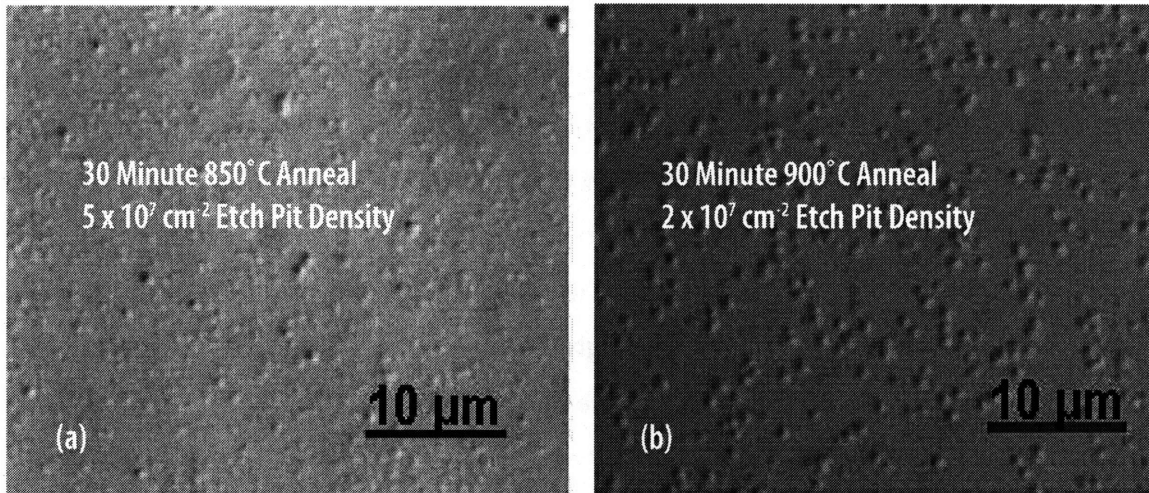
deposited with PECVD to passivate the germanium surface and to insulate later contact steps. Next, a window opening is etched in the nitride to define the transverse geometry of the diode to create squares, rectangles, octagons and circles of various sizes. Polysilicon is deposited with a 5 μm overlap of each window opening and ion implanted to form the n side of the diodes. Etch vias are then made down to the silicon substrate near each photodiode to expose the backside contact to the p-side of the diode. A second oxide passivation layer is deposited to avoid shorting the diode through these etch holes and a Ti/Al contact layer is deposited to form pads suitable for probing the photodiodes.

Known Electronic Issues Resulting from Epitaxial Growth and Processing

Unlike traditional epitaxial growth where the material lattice constants are carefully chosen to allow a single crystal lattice to form with little or no interfacial defect formation, the thickness of the germanium layer and the 4% lattice mismatch to the silicon require two separate lattices with two separate lattice constants to form. The interface between the two lattices is expected to be defect rich as the germanium relaxes to its preferred interatomic spacing. This defected seed layer's impact on device performance can be minimized by heavy doping to ensure that thermal generation does not contribute to dark current.

Threading Dislocations

The relaxation of the lattice spacing has a more important impact on the overall film quality and device performance by producing threading dislocations that propagate along the growth direction, producing electrically active defect complexes at each crystal layer. The quantity of these threading dislocations can be reduced by a number of growth techniques including the ramped growth thermal profile and post-growth anneals [2, 3, 9-12, 23, 24]. The quantity of threading dislocations in the final film can be evaluated most easily by using a defect selective etch to produce pits where the threading dislocations intersect the film surface. These measurements were performed on the LPCVD Ge-on-Si films under two different anneal conditions as shown in (Figure 10).



Measurements are courtesy of David Danielson

Figure 10. Nomarski micrographs of LPCVD Ge-on-Si films etched with defect-selective iodine solution

The measured etch pit density of the germanium films used for the devices in this thesis has been previously reported as $5 \times 10^7 \text{ cm}^{-2}$ [43]. This value is consistent with other direct Ge-on-Si epitaxial results [3, 24]. Existing threading dislocations are shown by the TEM in (Figure 11).

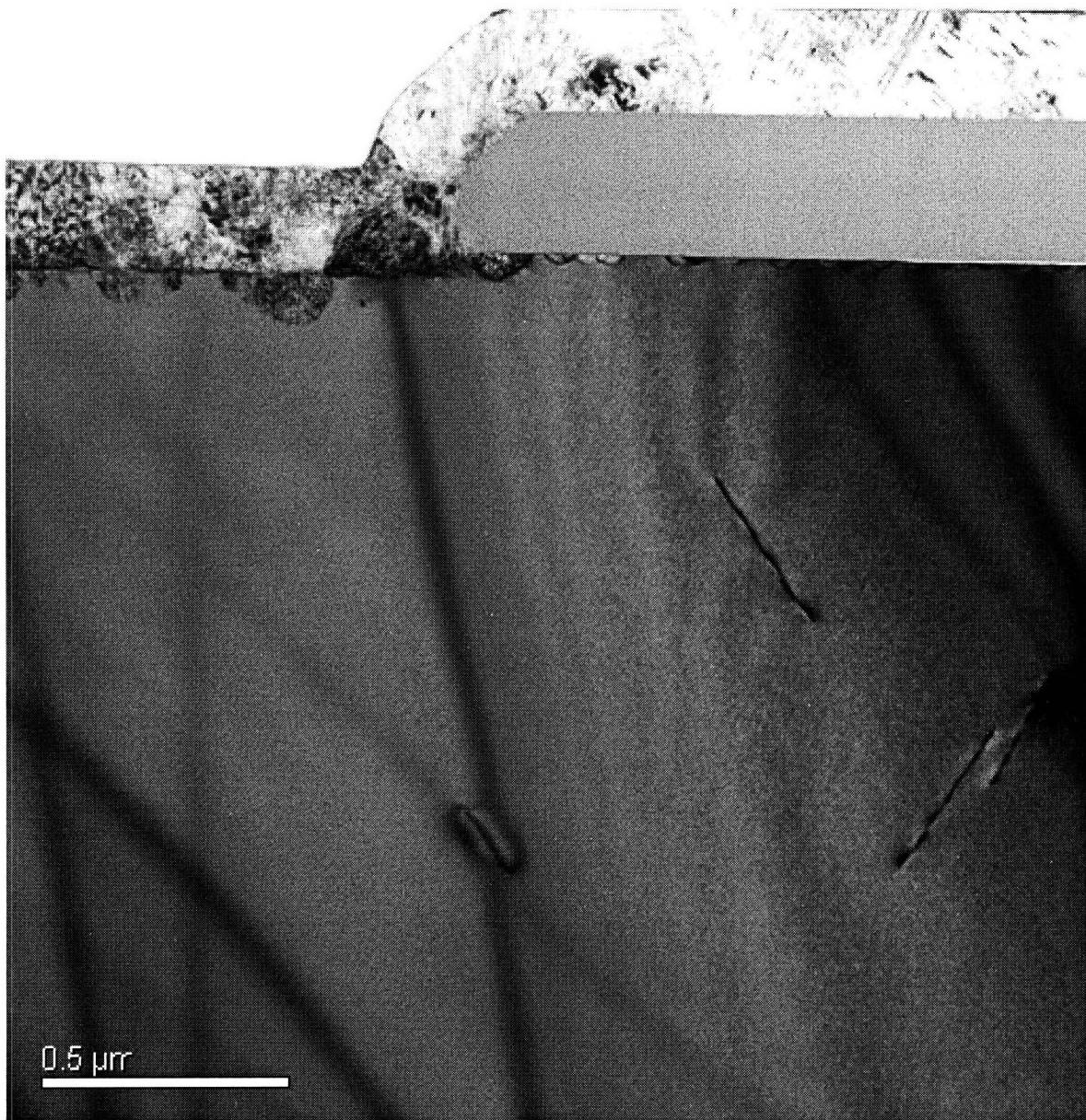


Figure 11. Film TEM showing threading dislocations at diode window edge. TEM analysis courtesy Analog Devices.

To estimate the true number of electronically active defects in the film, a few other scaling factors are required. First, since threading dislocations often propagate in close proximity to each other, etch pits may overlap, causing an underestimation of the total number. Previous work has shown that a simple scaling factor of approximately 0.555 etch pits per threading dislocation is observed by comparing etch pit studies with threading dislocation densities observed by transmitted electron microscopy (TEM) [43]. Additionally, the number of

electrically active states per unit length of the dislocation is required to obtain a density estimate. This has been obtained rigorously by many investigators in the silicon case to be approximately 10^6 cm^{-1} [44]. The one study performed in germanium obtained a similar result of $1.6 \times 10^6 \text{ cm}^{-1}$ [45]. The combination of these factors yields an estimated film defect density of approximately $2 \times 10^{15} \text{ cm}^{-3}$. The exact nature of the film defects will be left for later sections that test defect assumptions against measured data, but it is sufficient for the following discussion to say that they will act both as recombination-generation centers and carrier traps.

Passivation Interface Flaws

Another source of recombination-generation centers and carrier traps is almost certainly to be found near the germanium/SiON interface. As mentioned in the introduction to this thesis, passivation techniques for germanium lag significantly behind those of silicon. This is typically modeled in terms of a carrier recombination velocity at the interface. However, this picture may not be sufficient to account for traps and recombination-generation centers that are created close to the interface by diffusion of defects or impurities into the bulk germanium. As a result, let us assume that there is an additional degradation of electronic film quality near the passivation interfaces. To keep the discussion as general as possible, I will switch to the term “flaw,” as used by Schottky, to describe these near interface defects and impurities as well as the bulk threading dislocation defects.

Autodoping of Epitaxial Intrinsic Region

The final known degradation worth reiterating regarding the processed material quality is the p- autodoping of the intended intrinsic region. Although an intentional impurity atom in the epitaxial seed layer, boron’s presence in the rest of the germanium film must be regarded as a flaw and deviation from ideal device design. The magnitude of this effect has been well quantified by spreading resistance profilometry (SRP) by Solecon Laboratories. The result of this doping is that at low reverse bias voltages, the majority of the germanium film is not depleted. As will be further explained in Chapter 3, this results in carriers generated from

absorbed light undergoing diffusive transport in the quasi-neutral regions instead of rapidly being separated by drift in the depletion region.

Strained Film Bandgap Narrowing

The one key benefit from this type of epitaxial growth is a strain on the germanium layer. Instead of a lattice mismatch strain that is found in epitaxy of similar lattice constant material, relaxed crystal growth still exhibits a thermal strain caused by the thermal expansion coefficient difference between silicon and germanium. The two materials are unstrained at the peak growth temperature, but when the wafer is cooled back to room temperature the materials attempt to expand a different amount and a strain is induced on the thinner germanium layer. This effect can be increased by performing post-growth cyclic anneals between room temperature and the maximum growth temperature to reduce the quantity of strain relaxing dislocations. The resulting strain has been previously reported for these specific growth conditions to cause a 30 meV reduction in the direct bandgap of the germanium [2]. This has a favorable effect on both the optical absorption at 1550 nm and the carrier mobility [11].

Current-Voltage Measurements

Current-voltage (I-V) measurements and scaling trends of these diodes have been presented previously [24], and show interesting characteristics. To gather a complete set of data for analysis under known conditions, I reproduced these measurements as a function of temperature on the six different circular diodes shown in the optical micrographs of Figure BB. Diode current was measured as a function of forced voltage using an Agilent 4156C semiconductor parameter analyzer. Due to the low device currents encountered at low temperatures, care was taken to minimize dielectric leakage by using guard shields forced at the same voltage as the measurement line down as close to the probe tips as possible. The leakage current floor was measured to be in the 10's of fA. Temperature control was accomplished by probing the devices in a Desert Cryogenics Table Top Prober (TT-Prober) system cooled to 4 K by liquid helium and temperature swept by a heater controlled with a

Lakeshore Cryogenics temperature controller. Actual device temperature is measured by a calibrated silicon diode in the copper mounting stage and believed to be accurate due to the low power dissipation of the I-V measurements and the reduced black body radiation from the liquid helium cooled radiation shield in the TT-Prober. Lakeshore Cryogenics Cry-Con thermal compound is used to mount the photodiode sample to the copper mounting stage.

The complete set of measured data is shown in (Figure 12). Several aspects of these measurements deserve further note. The scaling of the diode current at reverse bias without optical illumination (dark current) is surprisingly linear with radius instead of quadratic as detailed in (Figure 13). As described in the pin diode overview of Chapter 1, the dark current is a bulk effect and should scale with the volume of the depletion region. Since the axial stackup is identical for the different diodes, the volume scales with device area and the dark current is supposed to follow this trend as well. When the dark current for the diodes is plotted as a function of radius as shown in (Figure 13), however, the current scaling is linear instead of quadratic. One possible explanation is an additional parasitic dark current source is present at the edge of the devices causing a perimeter dominated scaling. This will be investigated further with simulations and measurements later in this chapter.

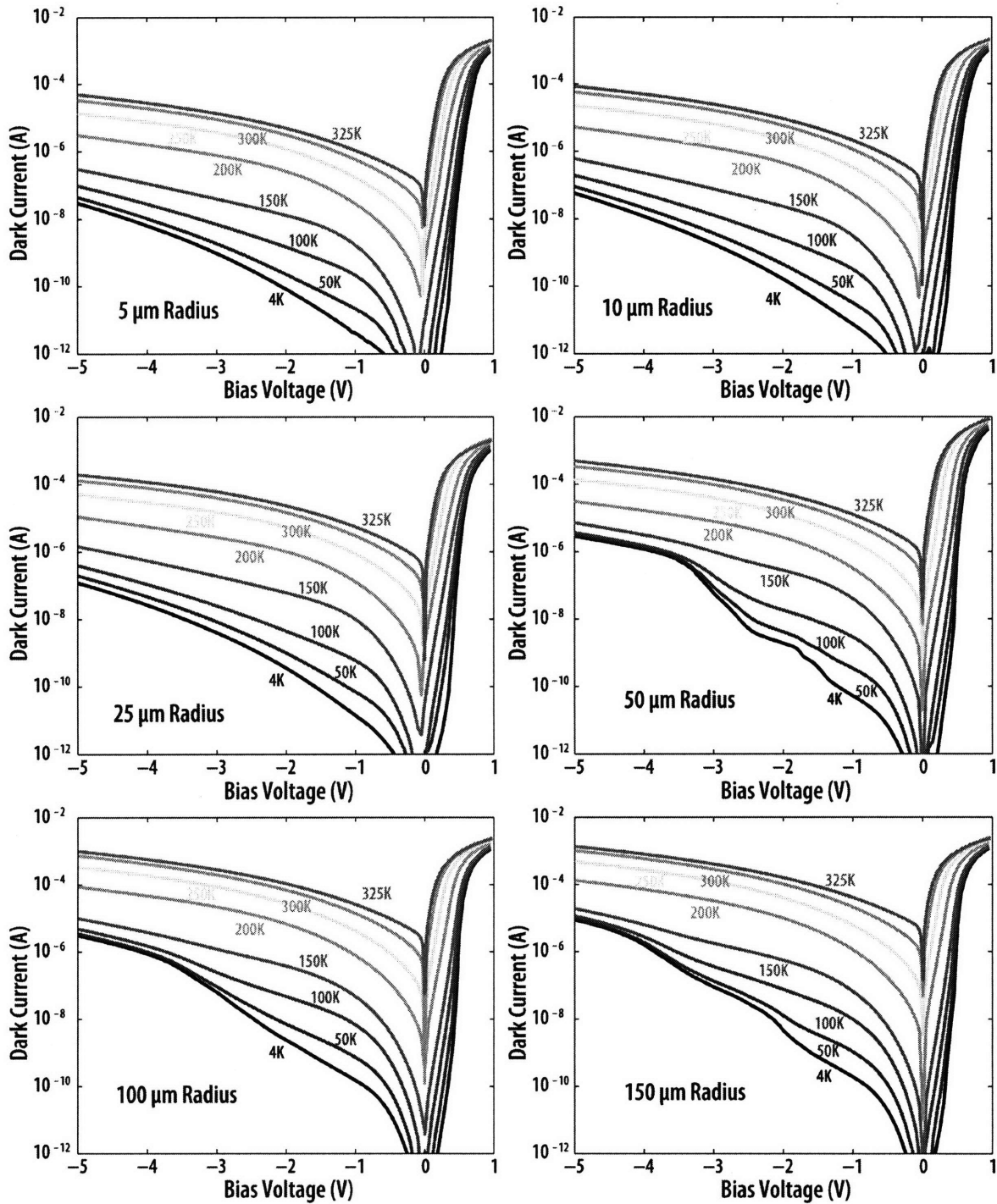


Figure 12. The I-V characteristics of six diodes are measured at temperatures ranging from 4 K to 325 K. Additional data lines for 225 K and 275 K are not displayed.

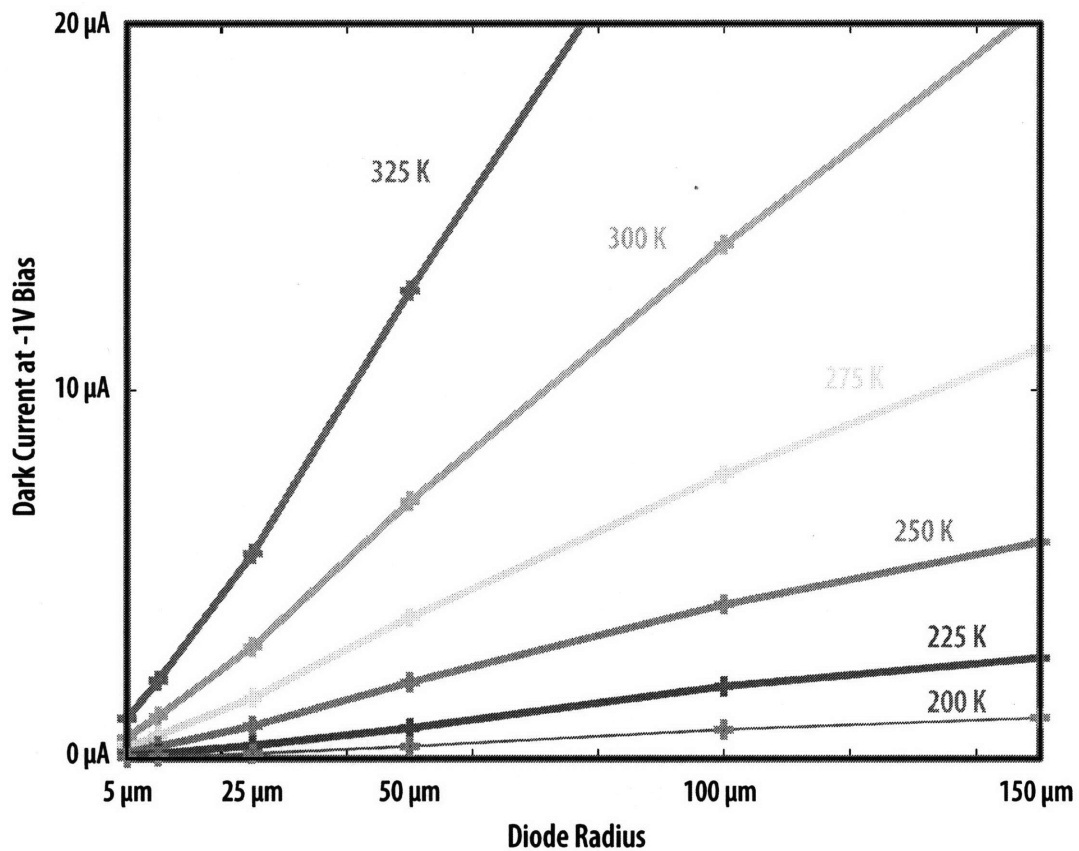


Figure 13. Diode dark current scaling with radius for various temperatures.

One other interesting feature of the I-V-T curves is apparent only in the low temperature regime. In most of the smaller diodes, the dark current freezes out to smaller and smaller values at low temperatures at all bias. In the larger area diodes, however, there is a region at high bias and low temperature where the dark current does not freeze out and shows very little temperature dependence. This appears to be a function of the film area, unlike the high temperature results, and is only present in larger diodes. This effect can be seen in (Figure 12) and (Figure 14).

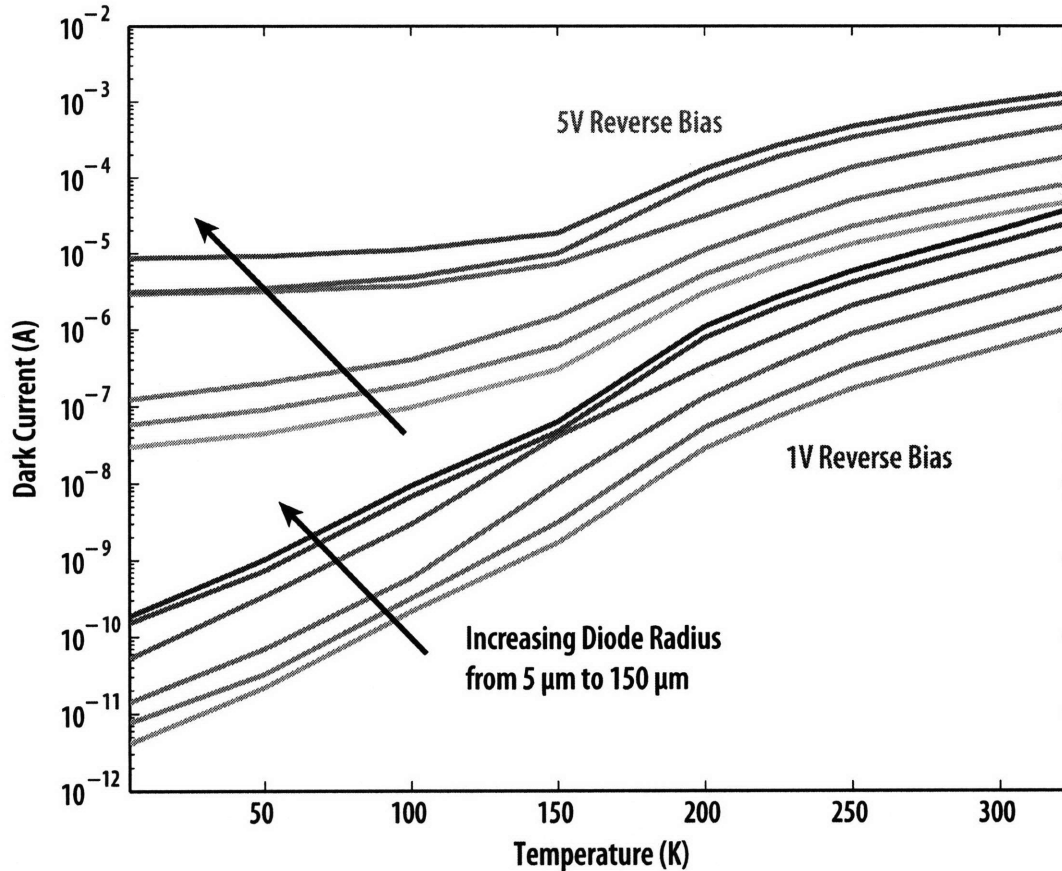


Figure 14. Diode dark current scaling with temperature for various diode sizes.

Thermoreflectance Imaging of Spatially Dependent Power Dissipation

Since the leakage current scales with device perimeter, it is assumed that the current is also physically located at the device perimeter. Therefore, by imaging the heating produced by this current, it should be possible to test this hypothesis and confirm the perimeter passivation interface's dominant role in leakage current. This analysis was performed on a $20 \mu\text{m} \times 100 \mu\text{m}$ diode by thermoreflectance imaging.

Thermoreflectance imaging uses the change in reflectance of a material with changing temperature to examine spatial thermal profiles [46-50]. Measurement accuracy is obtained by modulating the heat source, in this case device current, and performing lock-in imaging to extract the fractional change in reflectance as a function of area [51, 52]. This change in reflectance can then be translated into a change in temperature by calibration coefficients for

the illumination wavelength used. However, thermal expansion can cause reflection changes, especially at edges, and can result in spurious reflection signals.

To image the current heating in the diodes, the reverse bias was increased to -10 V to achieve measureable reflectance signal as shown in (Figure 15). To ensure that this signal is not merely a spurious edge signal, the diode was imaged in forward bias at equal power dissipation as shown in (Figure 16). Comparing these two images, it is clear that there is increased power dissipation at the perimeter in reverse bias where the forward bias image only shows spatial variation due to current crowding to the top device current. This confirms a generation current spatially located to the perimeter of the diode at the passivation interface.

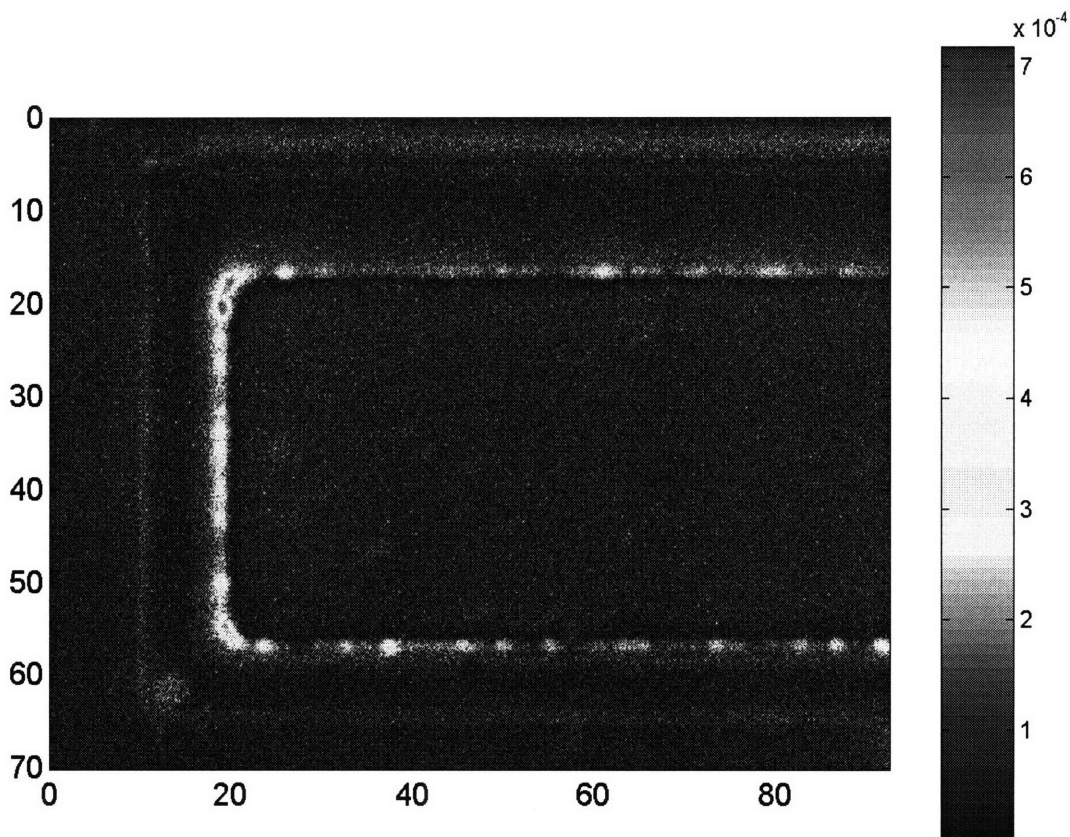


Figure 15. Thermoreflectance imaging of the spatial power dissipation for a reverse biased 20x100 micron diode. X and Y position axis units are microns. Colorbar is shown in uncalibrated units of fractional change in reflection.

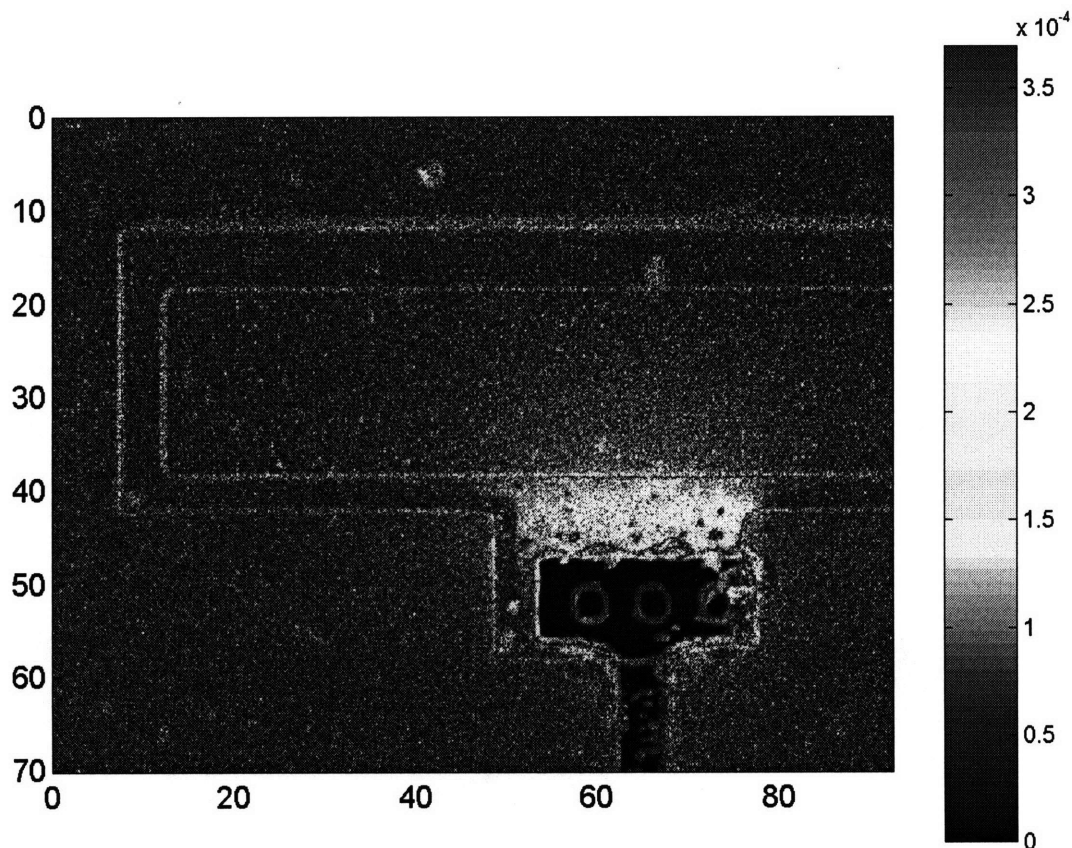


Figure 16. Thermoreflectance imaging of the spatial power dissipation for a forward biased 20x100 micron diode. X and Y position axis units are microns. Colorbar is shown in uncalibrated units of fractional change in reflection.

Finite Element Model Construction

In order to understand current device performance, a finite-element model is constructed to match these DC measurements using the Sentaurus TCAD suite described in the introduction. Previous efforts to match I-V measurements on these Ge-on-Si diodes were performed in Synopsys's previous generation device simulator, Medici [24]. Since Medici is fundamentally based on 2-D code, it was impossible to reproduce the correct scaling trends for different sized diodes based upon physical effects at the perimeter interfaces and bulk film. Additional comparisons between previous work and the current effort will be addressed as the considerations for the current model are explained.

Instead of using full 3D coordinates to allow the finite element model to describe arbitrary window geometries, 2D cylindrical coordinates were employed to accurately model circular window diodes with greatly increased computational efficiency. A geometry script was written to parametrically generate diode structures as included in Appendix A. One instance of this script for a 10 micron window size is shown in (Figure 17). Layer thicknesses are taken from processing parameters and the window openings and polysilicon lid overlaps are taken from the optical micrographs shown in (Figure 18). Additionally, to simulate degraded material quality at the perimeter passivation interface, a dummy material labeled "FlawedGermanium" was created and replaced the germanium within 100 nm of the SiON. Contacts were placed at the polysilicon edge and the silicon top and bottom surfaces.

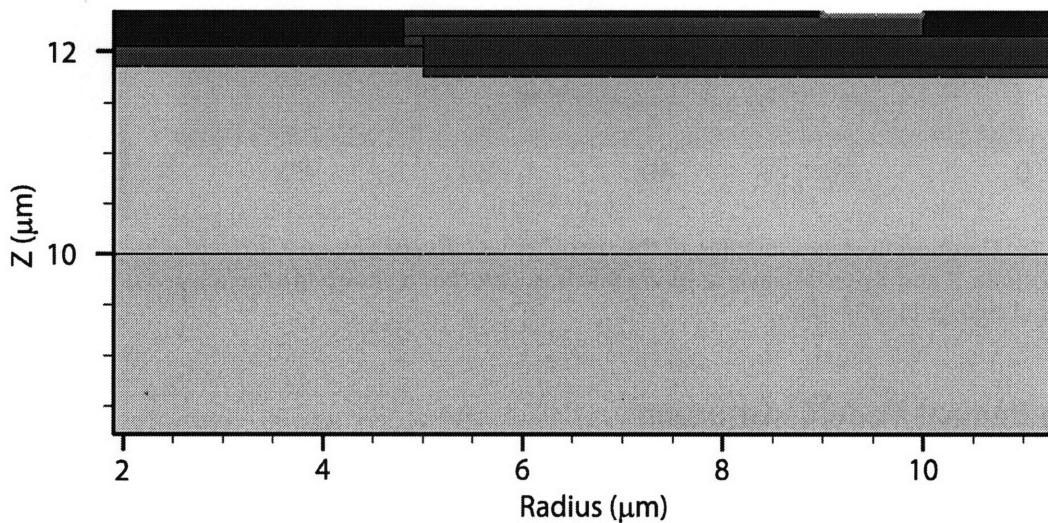


Figure 17. Detailed view of diode simulation model boundary file. Deep purple corresponds to polysilicon, light purple to silicon, yellow to germanium, maroon to oxide, light maroon to SiON. Contacts are bright purple lines.

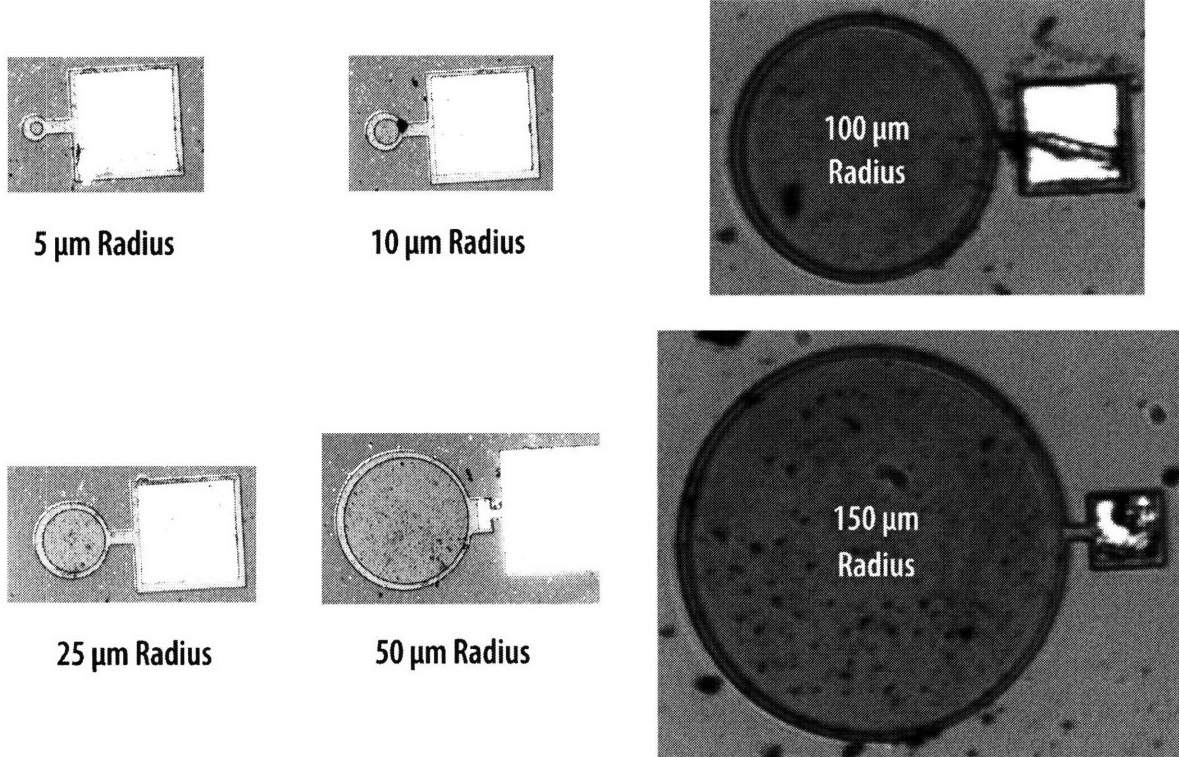


Figure 18. Optical micrographs of diodes under study. Exact window radii and overlap lengths were extracted from these images.

The script generated boundary geometry is then meshed into a Delaunay mesh suitable for finite element simulation as shown in (Figure 19). Doping densities are added to this mesh based upon spreading resistance profilometry measurements, shown in (Figure 20), performed by Solecon Laboratories. Since this measurement only accounts for electrically active carrier concentration caused by the net effect of n-type and p-type dopants, no information can be directly obtained for the lower concentration compensating dopants in each region. Therefore to find, for example, the phosphorus doping in the p-type region, an exponential is fitted to the doping profile of the n-type side immediately before the carrier concentration drops precipitously due to interaction with the p-side. This exponential is then assumed to be constant for the rest of the film. A similar strategy is employed to extend the boron doping profile. This approach is in direct contrast to the previous simulation attempt in Medici where constant doping profiles assuming ideal, distinct n-type, intrinsic and p-type regions were used [24].

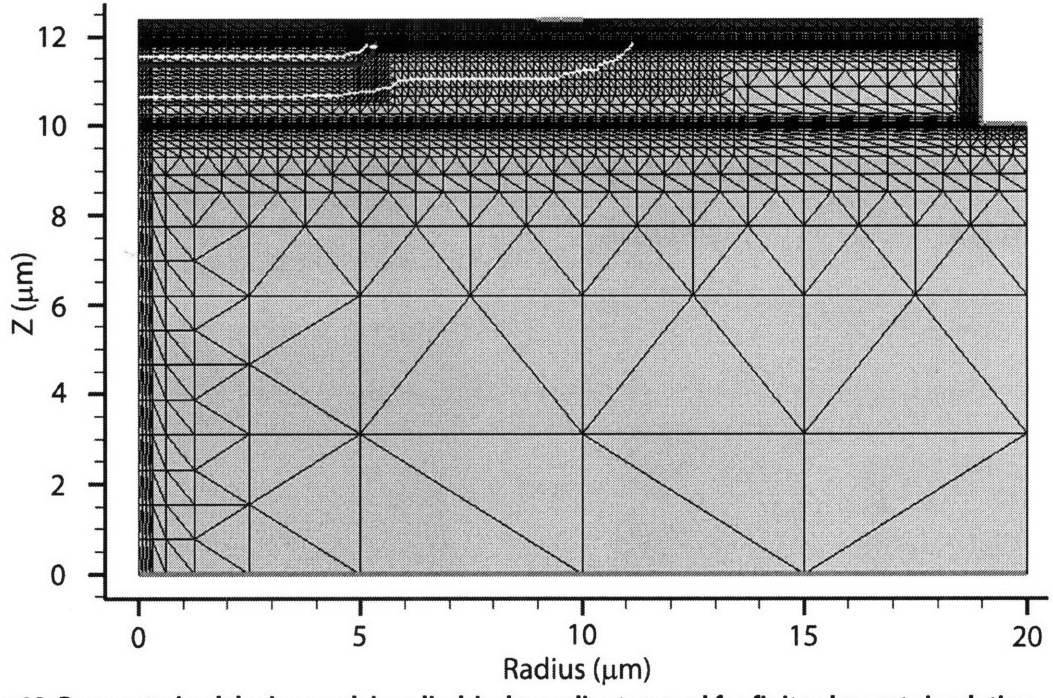


Figure 19. Parameterized device mesh in cylindrical coordinates used for finite element simulation

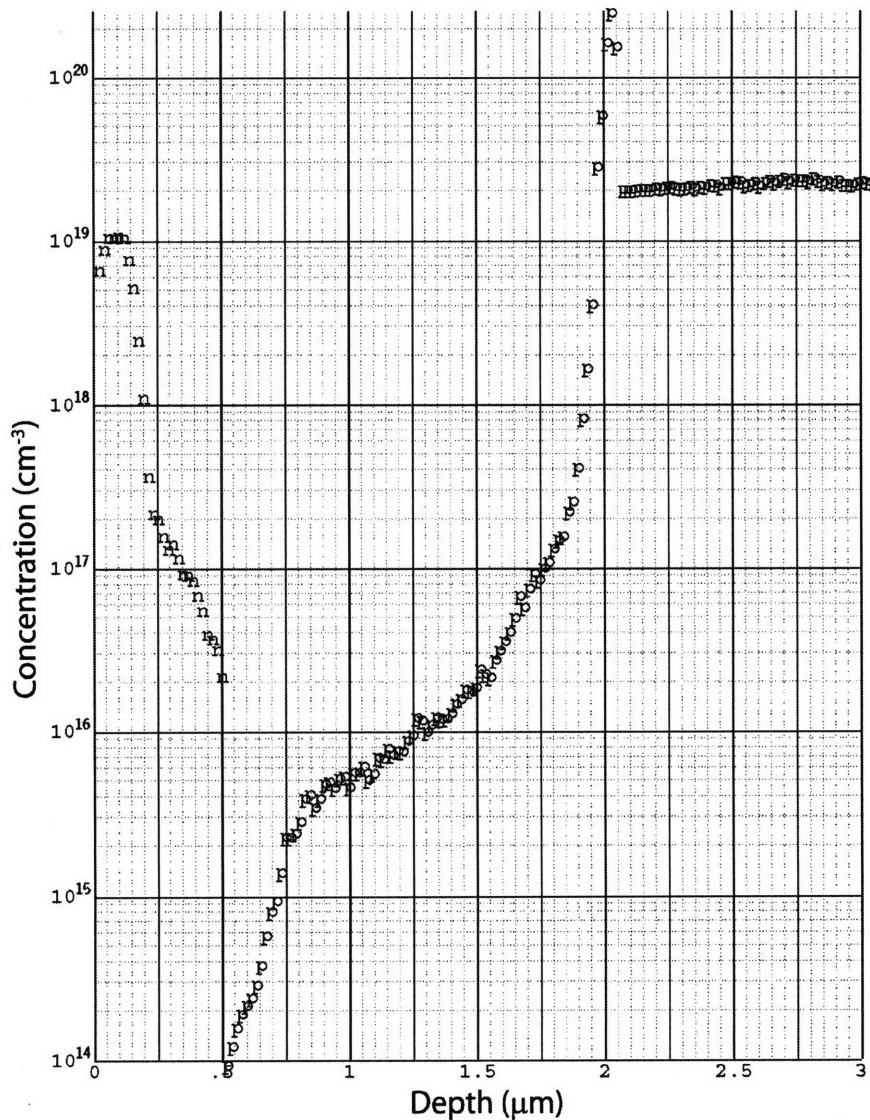


Figure 20. Spreading resistance profilometry measurement performed by Solecon Laboratories.

With the finite-element simulation mesh determined by these steps, simulation material parameters are next determined. For the initial electrostatic simulations carrier lifetimes in the germanium and FlawedGermanium are left as simulation parameters input to a standard SRH recombination model. Lifetimes in the silicon and polysilicon are left to simulator defaults of 1 microsecond as their use as contact materials render the specific value unimportant. Since band alignment is important to heterojunction transport and intrinsic density is critical for generation rate models, bandgap narrowing for germanium was used in the Jain-Roulston

model using literature values [53]. Full details of simulation parameters can be found in Appendix A.

Finally, required physical models must be switched on if not on by default. Due to the high doping densities, Fermi statistics, turned on by the Sentaurus keyword "Fermi", must be used instead of the Boltzmann approximation that is the default for computational efficiency. Additionally, double mesh points at the heterointerfaces, turned on by the Sentaurus keyword "Heterointerfaces", must be used to correct for the bandgap change and correctly model transport.

Electrostatic Device Simulation Results

Using this model, device behavior was simulated using the finite element simulator, Sentaurus Device produced by Synopsys. Initial simulations attempt to reproduce the measured I-V curves by sweeping the voltage bias of one contact. The Poisson equation is then solved coupled to electron and hole continuity equations to simulate the carrier densities and resulting current based on the aforementioned physical models and material parameters. Since the lifetimes in the bulk and "flawed" germanium regions are left as simulation parameters, an initial choice of 1 ns in the bulk and 1 ps in the flawed region is chosen for initial analysis.

One important result of this simulation is an analysis of the depletion of the bulk germanium film. As previously explained, a parasitic boron doping extends throughout the film that is supposed to be intrinsic for ideal p-i-n diode function. However, increasing reverse bias can sweep out existing carriers to widen the depletion region, so a key question is how much of the germanium film is depleted at a given bias point. This result determines how much of the absorbed light is quickly swept to the device contacts in the depletion region for a fast response and how much is absorbed in the quasineutral regions allowing the possibility for a slow diffusive tail to the diode response. At a low reverse bias of -1V, the depletion region is a small fraction of the germanium thickness as shown in (Figure 21). The width of the depletion region can be increased by a stronger reverse bias such as -5V as shown in (Figure 22). This

width increase comes at the cost of the increased dark current measured in the experimental I-V-T measurements of (Figure 12).

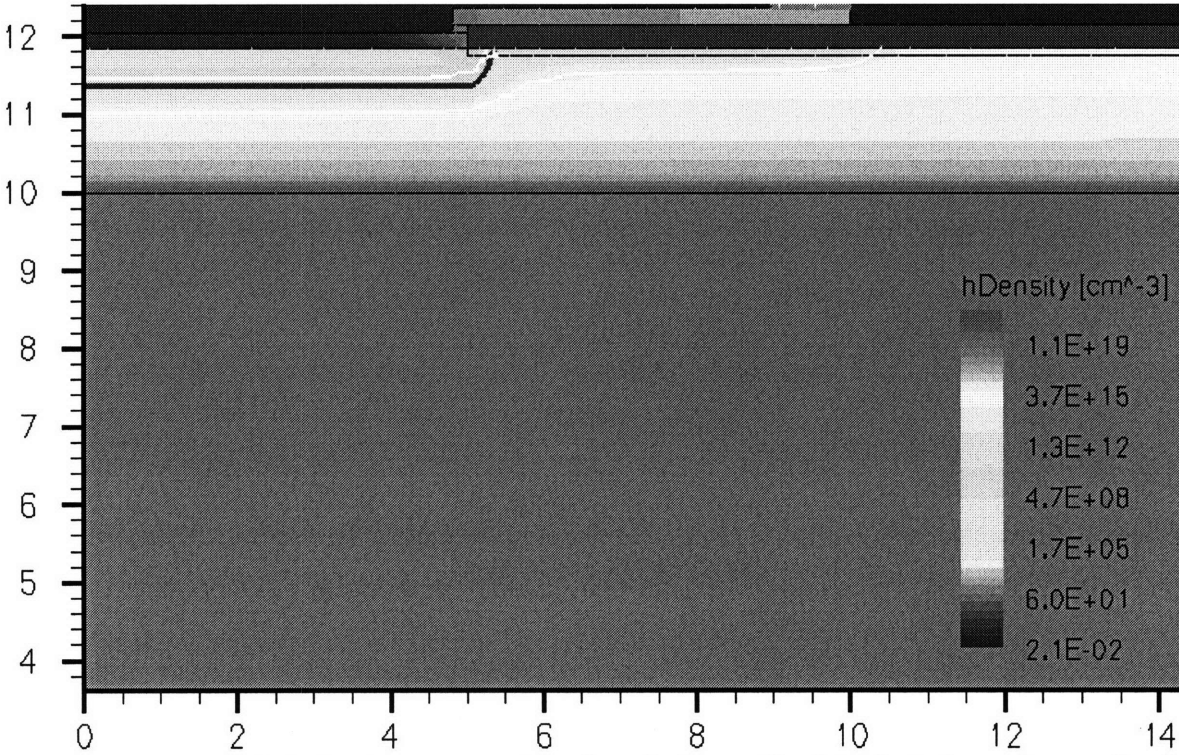


Figure 21. Germanium hole density concentrations show the lower side of the depletion region –outlined in white – at 1V (a) and 5V (b). Brown line represents pn junction.

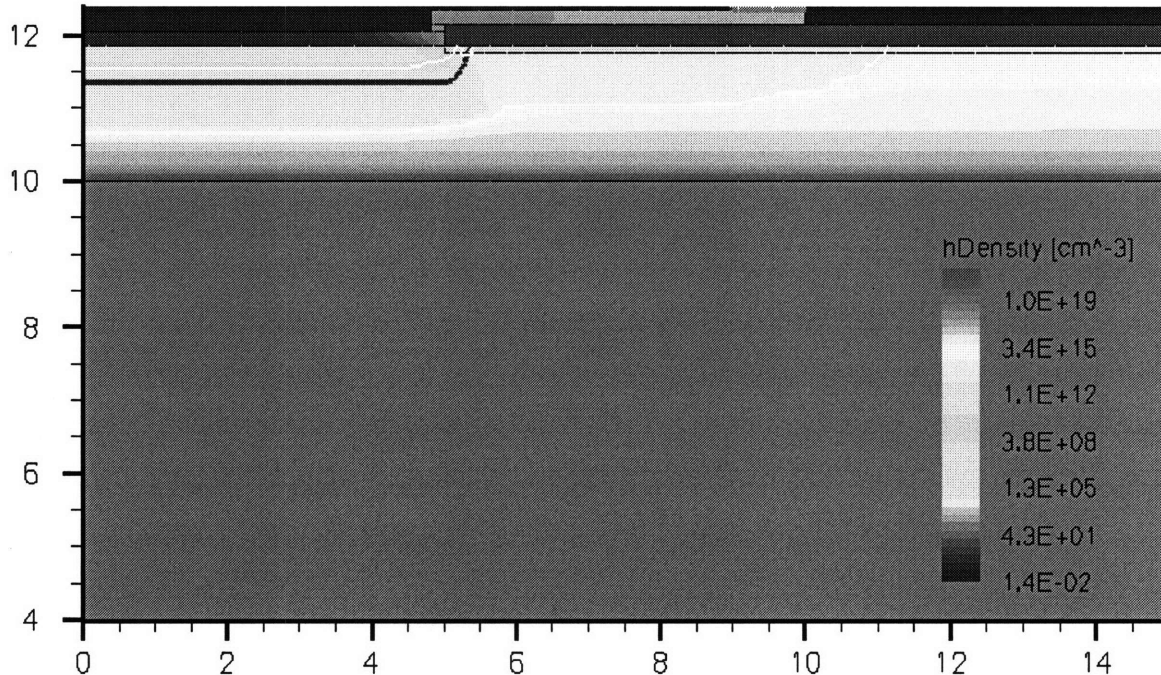


Figure 22. Germanium hole density concentrations show the lower side of the depletion region –outlined in white – at 1V (a) and 5V (b). Brown line represents pn junction.

As previously noted, this increased reverse bias current is observed to scale with diode perimeter instead of diode area. Some insight into this problem can be seen in the depletion regions observed in the simulations of (Figure 21) and (Figure 22). At the diode edge, the polysilicon top contact overlaps the diode window by 5 μm . The separating oxide is < 300 nm thick and contains a nitrided layer that increases the dielectric constant. The result is that the structure closely resembles a MOS capacitor and observes the same depletion effects commonly found in such devices. The result is that a large germanium area is depleted surrounding desired depletion region where defects due to the poor germanium passivation are expected to be present in large numbers. This depletion causes the electron hole pairs generated by the defects to be separated by the electric field and contribute to current.

Additional understanding of device behavior can be extracted from the energy band diagrams. This plot, shown at -1V bias in (Figure 23), is generated by slicing the finite element datasets using the visualization tool Tecplot SV along the cylindrical coordinate z-axis. The result of bandgap narrowing and heavy doping concentrations can be seen at the heterobarriers in these plots. Particularly disturbing is the large hole barrier formed at the p-

type substrate interface, implications of which will be discussed later in terms of possible avenues of device behavior.

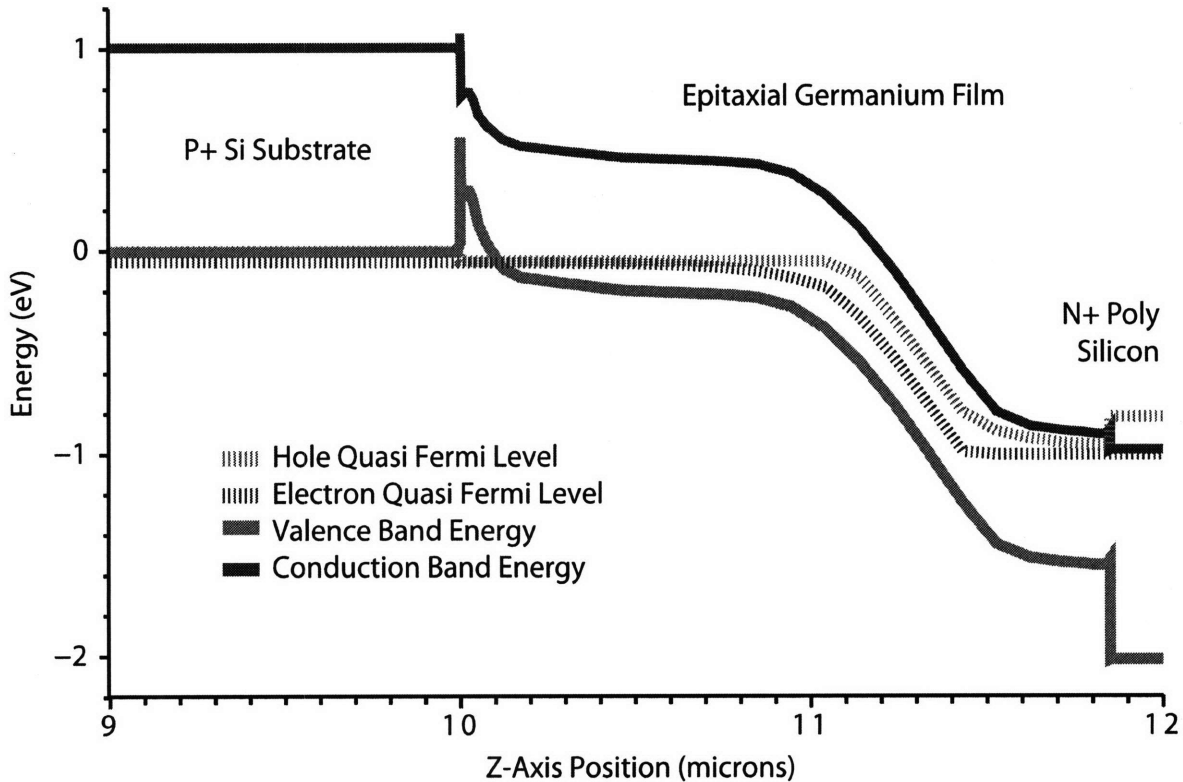


Figure 23. Energy band diagram of Ge-on-Si diode at -1V bias. Slice taken along the Z axis 1 micron from the diode center.

Matching Simulated and Measured I-V Responses with Carrier Lifetime Fitting

Since the simulated carrier lifetimes are fixed semi-randomly in these initial simulations, poor fitting with experimental I-V results are expected. This is indeed the case as shown for a 10 μm diode in (Figure 24), but moreover, the reverse bias dependence of the experimental curves differs from simulation. Since depletion width widening and all other traditional reverse bias dependences are included in this simulation, it is clear that the actual carrier lifetimes in these regions must be changing as well. Therefore, it is not only necessary to find the correct combination of surface lifetime and bulk lifetime to match experimental results, but this must be done independently at every bias point.

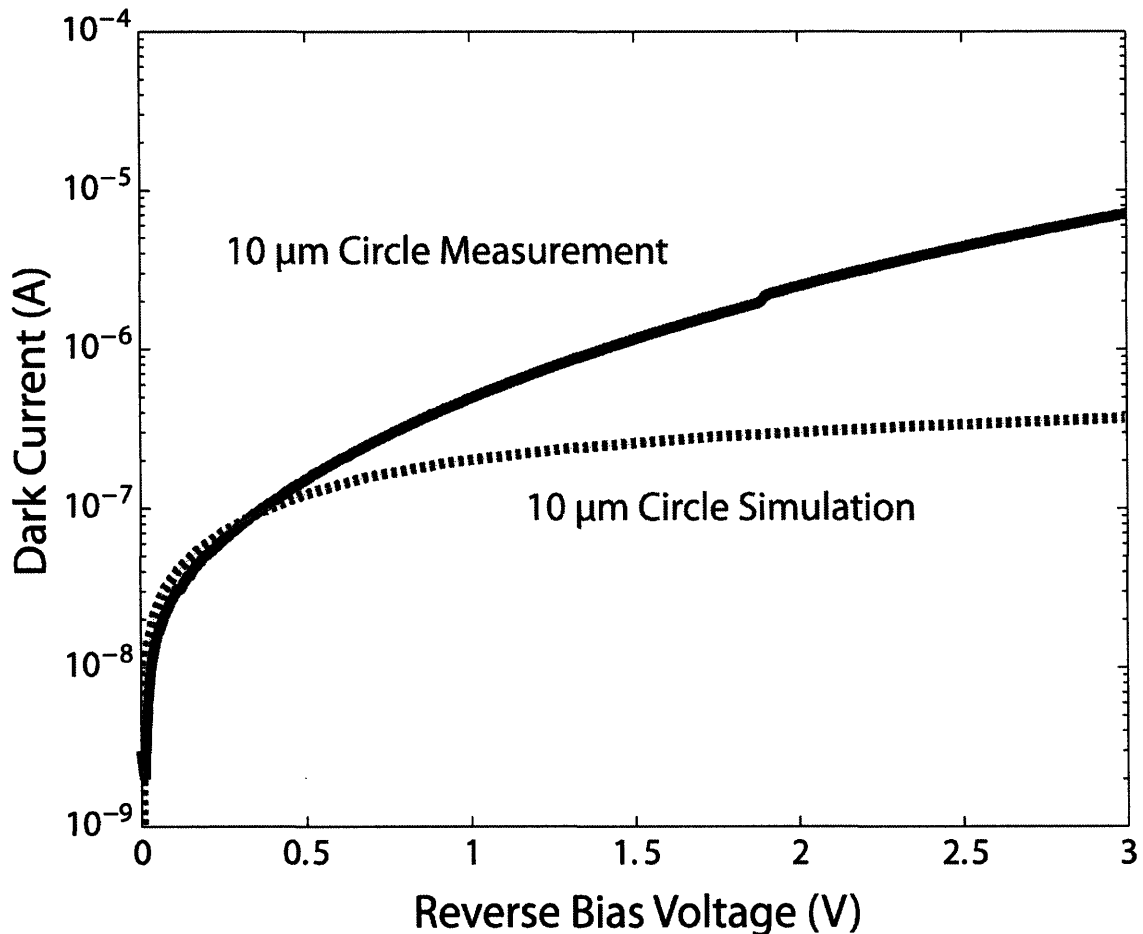


Figure 24. Dark current experiment vs. simulation for 10 micron radius diode prior to detailed analysis.

In order to separate bulk and surface lifetimes, three different diode radii are considered to isolate perimeter and area contributions. A similar approach was taken by simply analyzing current scaling for different window geometries to remove the surface recombination contribution to dark current at a single bias point for SiGe diodes [40]. Instead of this simple approach, parametric device simulation using the described finite-element framework is chosen to accurately extract the correct bulk and surface lifetimes for each bias point. This enables other device currents such as minority carrier generation within a diffusion length of the space charge region and the effect of an increasing depletion region volume to be eliminated from the fitting. As such, 4016 of the above quasistationary I-V simulations were performed at each temperature varying the bulk and surface lifetimes for three diode sizes.

This simulation data is then consolidated using the Python scripts included in the appendix into Matlab data files for I-V data as a function of diode radius, bulk lifetime and surface lifetime. A Matlab script, also included in the appendix, is then used to load this data and the experimental I-V files and fit interpolating functions to each to resolve sample point discrepancies. A uniform sampling of 50 bias points between 0.1 V and 5 V is then examined to find what combinations of bulk lifetime and surface lifetime simulation data points match the measured device current for each diode window size. This procedure generates 3 lines on the bulk lifetime and surface lifetime plane as shown for 0.5 V bias in (Figure 25). Since the diodes are fabricated on a uniform film on the same wafer, these fundamental physical parameters should be the same for all three diodes as determined by the intersection point of these lines. For examples that due not intersect as cleanly as the 0.5 V bias point shown, the intersection points of each line with the others is calculated and the coordinate lifetimes are averaged for the bulk and surface lifetime axis.

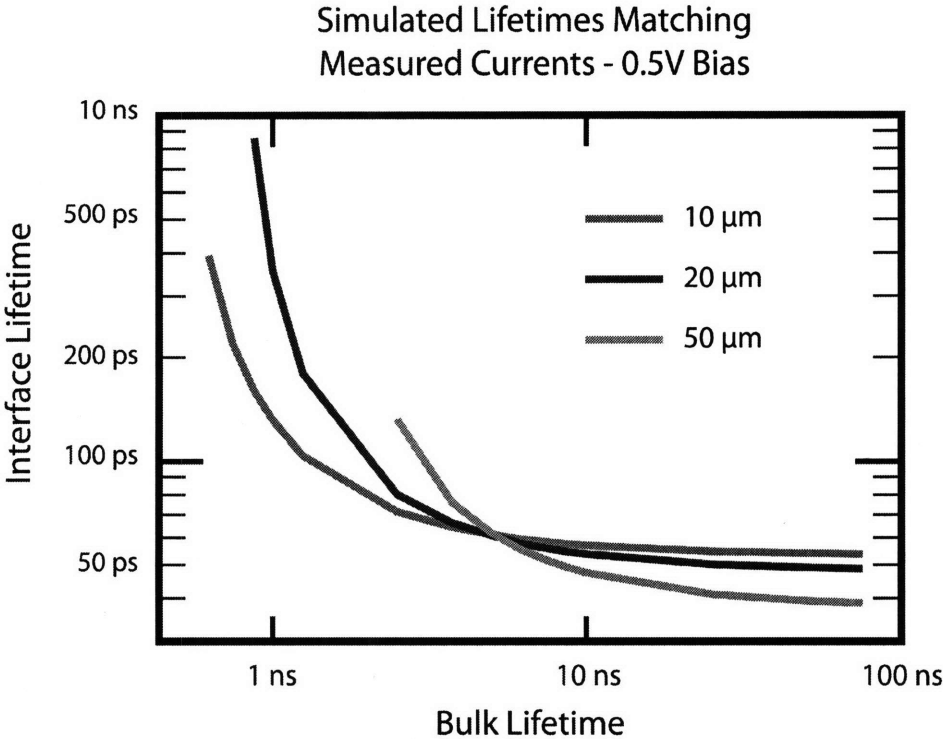


Figure 25. Intersecting lifetime fit lines for three different diode window diameters at 0.5 V reverse bias.

Since this procedure is repeated for every bias point, the fit bulk and surface lifetimes for each bias point are found as shown in (Figure 26).

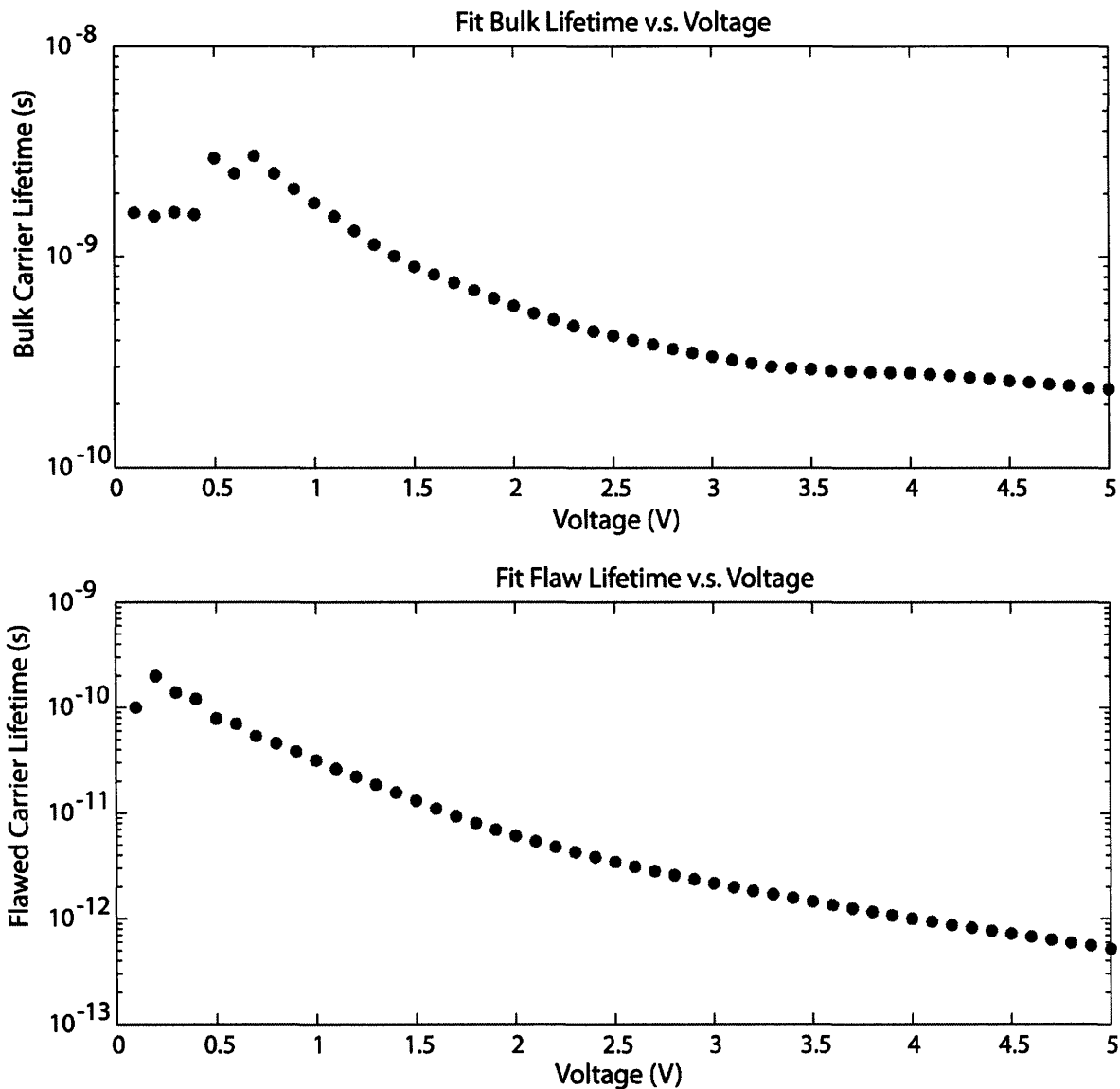


Figure 26. Fit carrier lifetime for surface and bulk germanium regions extracted by matching parametric simulations to measured I-V data.

It is next important to understand what is fundamentally being varied in the simulations with the carrier lifetimes that corresponds to a physical effect in which we are interested. The carrier lifetimes being varied are held equal to each other and are inputs to Sentaurus's

Shockley-Read-Hall (SRH) statistical recombination-generation model discussed generally in the introduction and shown in Equation (2.1).

$$U^{SRH} = \frac{np - n_i^2}{\tau_n \left[p - n_i \exp\left(\frac{E_t - E_i}{kT}\right) \right] + \tau_p \left[n - n_i \exp\left(\frac{E_t - E_i}{kT}\right) \right]} \quad (2.1)$$

This expression is then simplified to Equation (2.2) when we apply the simplifying assumptions that the electron and hole concentrations in the depletion region are much less than the intrinsic density, the carrier lifetimes are equal and the trap energy is equal to the intrinsic energy.

$$U^{SRH} = \frac{n_i}{2\tau_0} \quad (2.2)$$

The assumptions of midgap traps and equal carrier lifetimes are explicit in the simulation framework and therefore do not introduce error. The carrier density assumption requires some justification. By examining the simulated carrier densities at various points in the depletion region of the finite element mesh using Tecplot SV, electron and hole densities are estimated to be between $1 \times 10^{10} \text{ cm}^{-3}$ and $2 \times 10^{12} \text{ cm}^{-3}$ for various spatial and bias points. Since the effective intrinsic carrier density calculated in the depletion region is $8.5 \times 10^{13} \text{ cm}^{-3}$, the observed carrier densities are at least 40x smaller than the effective carrier density. This is not exact, but errors of a few percent are acceptable to greatly simplify the analysis.

The simplicity of this equation allows for an easy translation of the simulation parameter of carrier lifetime to the simulator's defect contribution to the generation rate using only the germanium intrinsic density that is well defined in the low-doped regions in question. For the bulk film, the resulting generation rate per unit volume is the quantity of interest, but for the flawed surface region, it is desirable to integrate over the region thickness to produce a generation rate per unit area.

The previously calculated lifetimes are observed to vary over an order of magnitude as a function of bias. In order to begin to understand the physics behind the lifetimes and their variations, the bias point must be translated into the physical variable of electric field. This is easily obtained from the finite element simulations by using the CurrentPlot function of Sentaurus to enable the electric field value of specified points to be recorded in the simulation data files. This is recorded for the bulk depletion region at the pn junction $2\ \mu\text{m}$ from the center of the diode and for the surface in the middle of the polysilicon lid overhang at half the thickness of the FlawedGermanium material region. This data is then loaded into the Matlab script and fit with an interpolating function to translate the bias voltages into center and edge field values as shown in (Figure 27). This allows for the final result of the fitting analysis shown in (Figure 28) for 300 K.

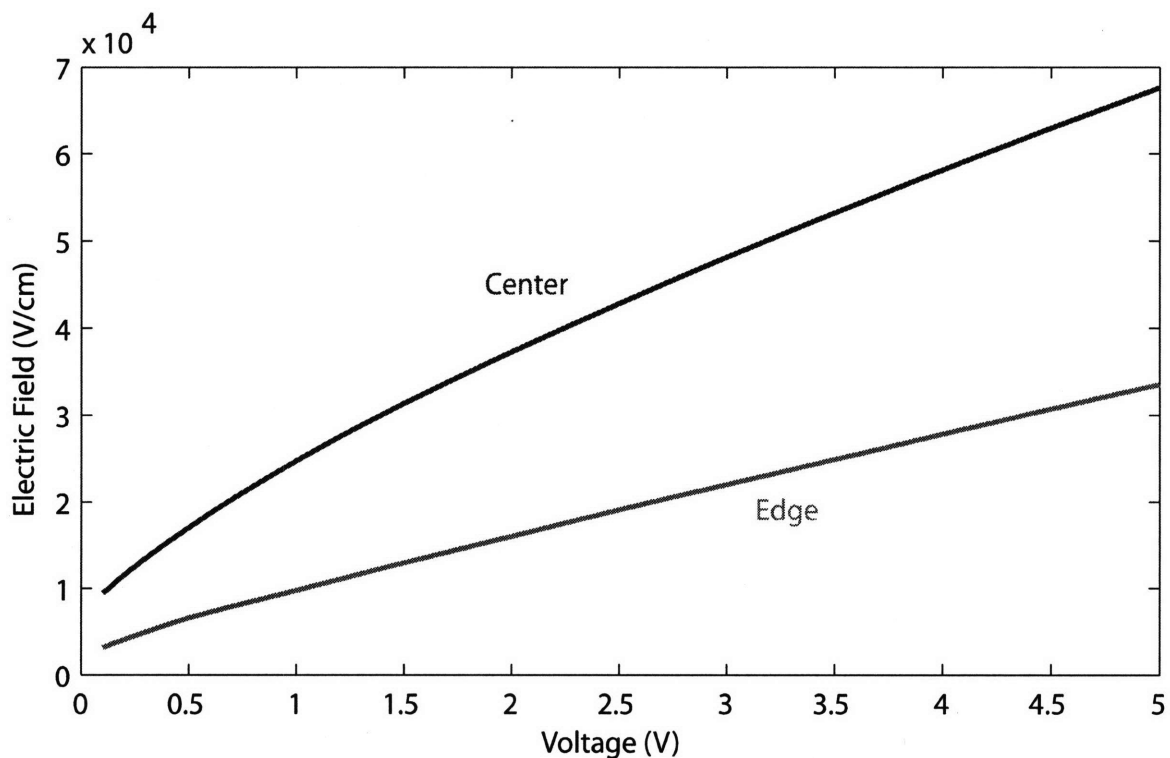


Figure 27. Simulated electric fields as a function of bias for the center and the edge of the diodes.

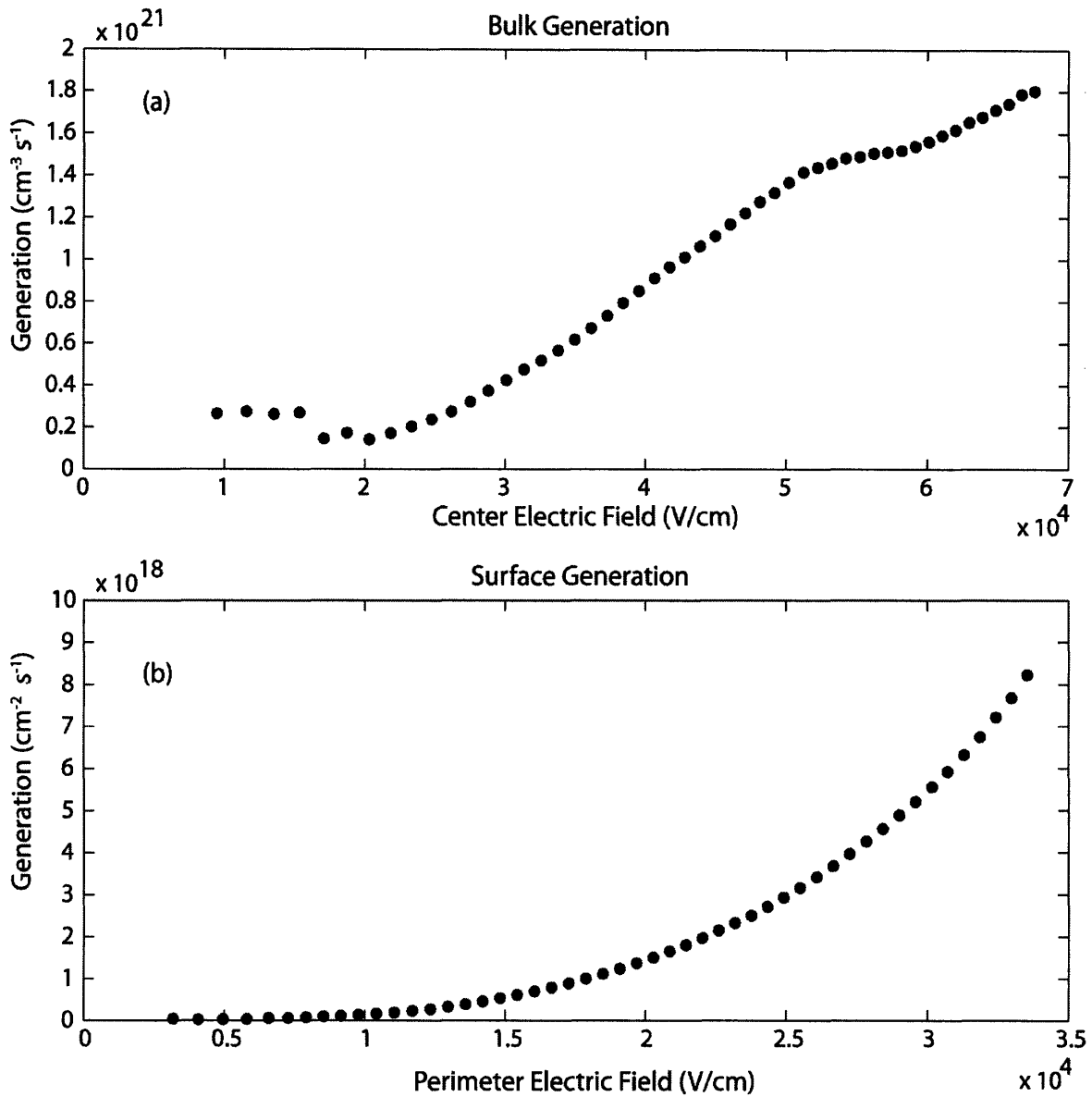


Figure 28. Surface and bulk generation rates as a function of electric field extracted by matching parametric simulations to measured I-V data.

Parameters for Physical Flaw Models

Due to the fundamentals of lattice mismatched epitaxial growth, threading dislocations to relieve the strain in the germanium film are inevitable. This symmetry breaking requires the creation of localized states that have energies in the traditionally forbidden zone of the semiconductor bandgap. As described in the introduction, SRH recombination models can predict resulting reductions in the semiconductor lifetimes. Experimentally, the correlation

between threading dislocation density and carrier lifetime for germanium has long been accepted as shown in (Figure 29) from Wertheim and Pearson 1957 [45]. In general, threading dislocation density has directly correlated to material quality and device performance for many material systems. This trend was analyzed by Lester et al. 1995 as shown in (Figure 30) for visible light LEDs [54]. However, it is important to note that there are important counter examples to this trend such as blue LEDs produced by the Nichia Chemical Company in the mid 1990s in the GaN on sapphire material system [55]. Although the threading dislocation density was 10^{10} cm^{-2} , four to six orders of magnitude higher than the previous GaP and GaAs on SiC LEDs, they were ~ 100 times brighter than those diodes [56].

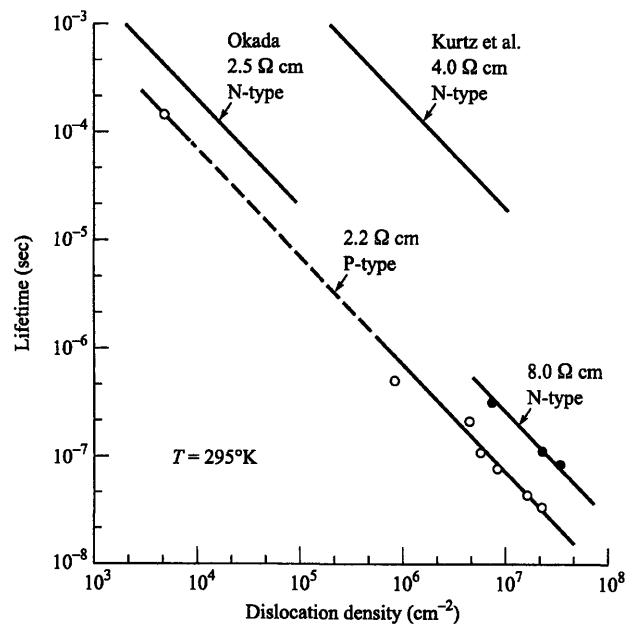


Figure 29. Germanium carrier lifetime as a function of dislocation density for various doping densities from Pearson, 1957.

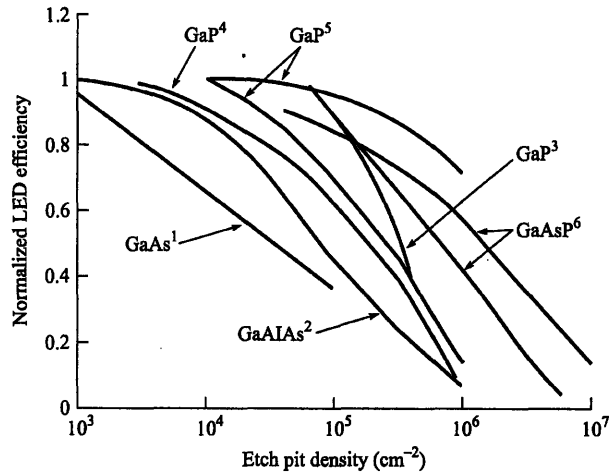


Figure 30. Correlation between threading dislocation density (measured by etch pit density) and visible wavelength LED efficiency for various material systems from Lester et al., 1995.

***A Priori* Bulk Threading Dislocation Model**

A rudimentary model for flaw recombination at dislocations based on the SRH theory can be obtained by following the work of Kittler and Seifert 1981 [57]. In this work, the trap energy level is assumed to be roughly midgap as is generally the case for threading dislocation flaws. The rate of recombination per unit length of a dislocation can be written in terms of an electrically active defect density per unit length, n_t , a capture cross section, σ , and the thermal velocity, v_{th} , as shown in Equation (2.3).

$$\gamma = n_t n_i \sigma v_{th} \quad (2.3)$$

The capture cross section is assumed to be roughly atom sized, or $\sim 10^{-14}$ cm². Additionally, the electrically active defect density per threading dislocation length has been thoroughly analyzed in silicon and determined experimentally by one investigator in germanium. The typical silicon value is quoted to be 10^6 cm⁻¹ and the one germanium datapoint for a dislocation core state is 1.6×10^6 cm⁻¹. Since the thermal velocity is quite well known, these simple parameters offer a rough pass theoretical prediction that turns out to compare quite poorly to experiment when multiplied by the previously calculated threading dislocation density of 2.4×10^7 cm⁻² as shown in (Figure 31).

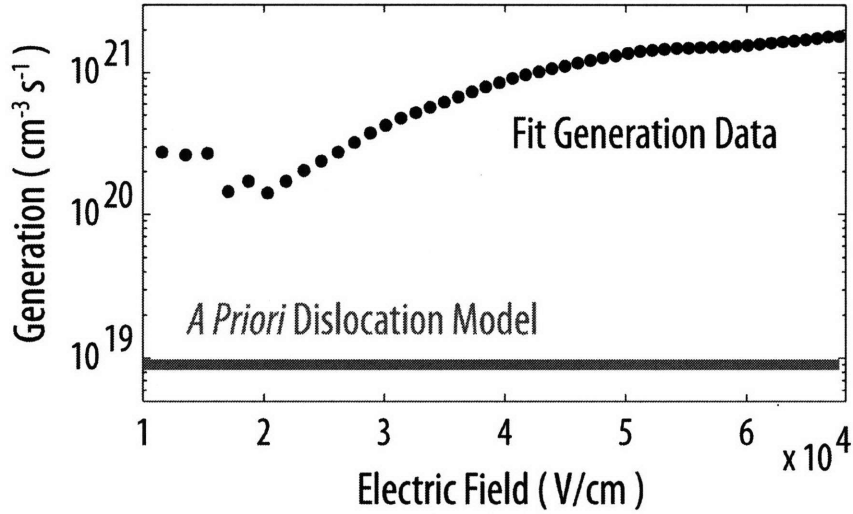


Figure 31. *A priori* generation rate resulting from estimated dislocation behavior.

Detailed Bulk Threading Dislocation Model Construction

Since a first order analysis is insufficient, Equation (2.3) can be expanded to split the cross section into an electron and hole cross section weighted by the trap energy level. The resulting equation resembles the more general SRH formula and is shown in Equation (2.4).

$$\gamma = n_i^d v_{th} n_i \frac{\sigma_n^d \sigma_p^d}{\sigma_n^d \exp\left(\frac{E_i^d - E_i}{kT}\right) + \sigma_p^d \exp\left(\frac{E_i - E_i^d}{kT}\right)} \quad (2.4)$$

Additionally, since the fit recombination rates are strongly field dependant, this can be further generalized to explicitly include field dependant cross sections as the number of defects, thermal velocity and trap energy are not changing with applied field as shown in Equation (2.5). The bulk recombination rate described in this equation is obtained by multiplying by the areal threading dislocation area.

$$U_{bulk}(F) = N_d n_i^d v_{th} n_i \frac{\sigma_n^d(F) \sigma_p^d(F)}{\sigma_n^d(F) \exp\left(\frac{E_i^d - E_i}{kT}\right) + \sigma_p^d(F) \exp\left(\frac{E_i - E_i^d}{kT}\right)} \quad (2.5)$$

Within this formalism, the trap density has already been set by experimental studies of threading dislocation density in the device in question and literature values for electrically active flaws per unit length. The next piece of information to gather is an estimate of the trap energy. In silicon, threading dislocation flaws form a single trap energy at precisely midgap [58]. This continues to be true in silicon germanium alloys until a germanium mole fraction of 0.73, which corresponds to the traditional point where the conduction band switches from a silicon-like to a germanium-like structure [35]. In germanium, the majority of investigators have reported deep electron trapping at $E_c - 0.42$ eV and $E_c - 0.29$ eV and deep hole trapping at $E_v + 0.18$ eV in DLTS studies [35, 59-62]. Additionally, shallow traps have been reported at $E_c - 0.09$ eV, $E_v + 0.09$ eV and $E_v + 0.025$ eV [63].

Since the germanium bandgap is 0.66 eV, the electron trap at $E_c - 0.29$ eV is 40 meV away from the midgap and the electron trap at $E_c - 0.42$ eV is 90 meV away from the midgap. As seen in Equation (2.5) and discussed in the introduction, flaws with energies closest to midgap are the most efficient recombination-generation centers. Therefore, one would initially assume that the $E_c - 0.29$ eV flaw would be the dominant R-G center. However, since the two levels are still relatively close to midgap, the cross-sections could cause one or the other to dominate.

Additional information can be found in the literature for both traps. DLTS studies have extracted the electron capture rate to be $1.8 \times 10^{-12} \text{ cm}^3 \text{ s}^{-1}$ for the $E_c - 0.29$ eV flaw [59]. Using the electron thermal velocity of $3.1 \times 10^7 \text{ cm s}^{-1}$, a zero field capture cross section of $5.8 \times 10^{-20} \text{ cm}^2$ for electrons can be obtained. For the $E_c - 0.42$ eV flaw, the zero field electron capture cross-section is explicitly calculated to be $5 \times 10^{-12} \text{ cm}^2$ [62]. Although DLTS studies have yielded no information for the hole cross sections, they illustrate that the $E_c - 0.29$ eV flaw may not dominate.

To clear up this confusion, another key experiment must be explained as it is important in deciding the final flaw state for further modeling. In Grillot et al. 1996, germanium is grown on thick buffer layers to reduce threading dislocation density and p-i-n diodes are formed [35].

At low bias, only the good material quality sections farthest from the heterointerface are depleted, yielding a more pure germanium layer. Higher biases push the depletion region into material regions where the flaws from the threading dislocations should be more numerous. The temperature dependence of the dark current of this device is then plotted for various bias voltages and the effective activation energy is extracted as shown in (Figure 32). At low biases, the high quality germanium film yields activation energies similar to the germanium bandgap. This means that the generation is dominated by intrinsic processes. At high biases, the contribution of flaw generation dominates and one observes an energy that becomes closer and closer to the $E_c - 0.42$ eV flaw energy. This identifies the dominant defect from the threading dislocations in agreement with the DLTS identified flaw.

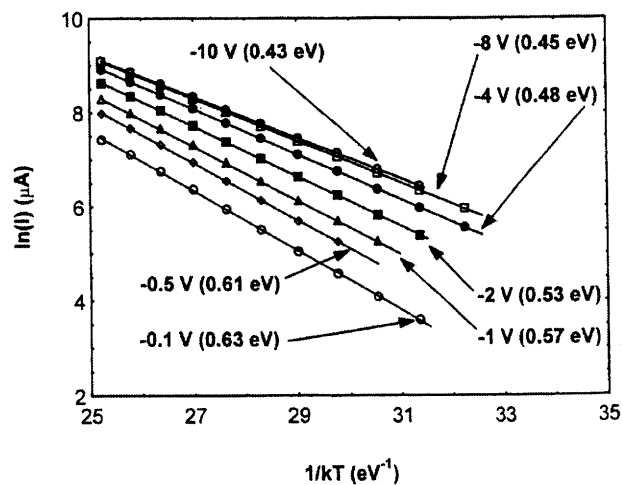


Figure 32. Arrhenius plot for germanium on silicon diodes showing the observed leakage current activation energy under different bias conditions. Increasing reverse bias depletes a larger fraction of the film and allows generation in the poor material quality initial layers of the film to contribute to current. From Grillot et al., 1995.

Henceforward the $E_c - 0.42$ eV flaw will be considered as the sole generation source related to the bulk threading dislocations. Further detailed studies of the temperature dependence of the generation rate in these diodes could verify this assumption as will be discussed in the future work section. Since a known flaw, the divacancy, is associated with this approximate energy level and cross section, this dislocation level will be referred to by the divacancy name and the 'd' superscript [64-67]. The zero-field capture cross section for the holes and the field

dependencies of both cross sections will next need to be obtained by fitting various models to the extracted experimental results as will be detailed in a further section.

Detailed Edge State Flaw Model

The surface interface flaws could result from a greater number of physical sources. Carrier lifetime reduction at germanium passivation interfaces have long been an issue in devices. One specific type of flaw called an A-center is understood to result from a complex in which a germanium atom vacancy is replaced by an oxygen atom as shown in (Figure 33) [68].

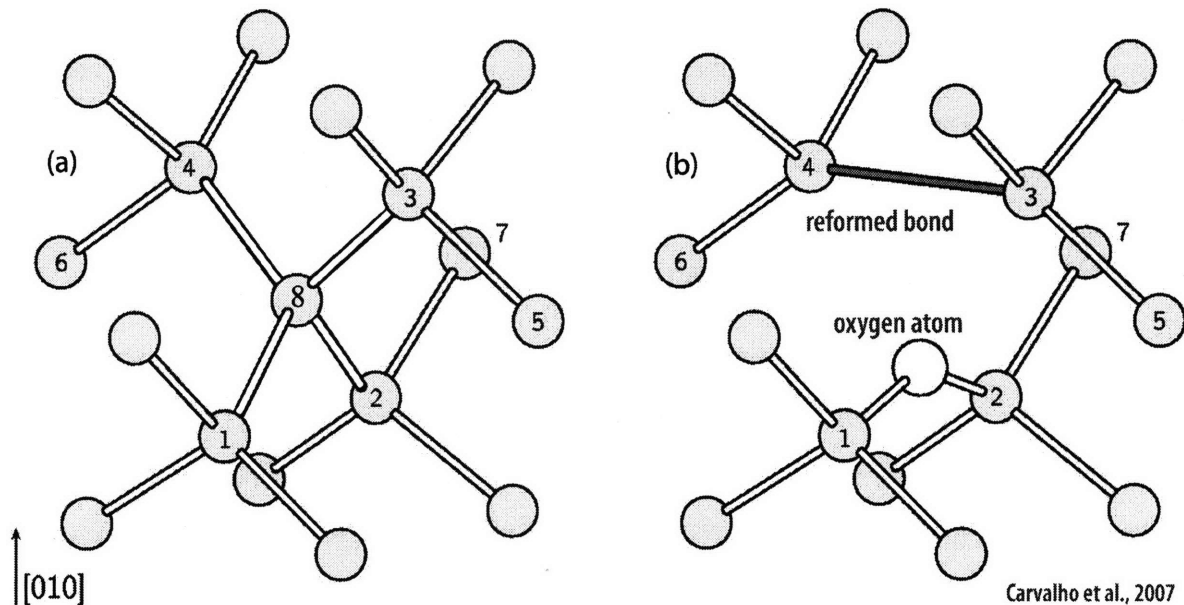


Figure 33. Original germanium lattice, (a), modified by the replacement of Ge atom 8 with an oxygen atom to form an A-center, (b).

This state is known as a common passivation related defect. Additionally, A-centers have been shown to form in threading dislocations near oxide interfaces in a correlated density to the threading dislocation density [69]. This defect is relatively unique for germanium in the mass of experimental data that is corroborated by theoretical predictions [68, 70]. Although multiple charge states of vacancy-oxygen complexes exist, the one observed in annealed dislocations has an electron trap energy of $E_c - 0.21$ eV and a zero-field electron cross section of 2.6×10^{-15} cm² [67, 69, 71, 72]. These values can be used for a starting point of a generation

model similar to the one developed for standard dislocation traps. Adapted to include a different cross section and a fixed dislocation length that contains the oxygen modification of the threading dislocation states to yield a surface generation rate per unit area, the generation fitting model for the dislocation A-center is shown in Equation (2.6).

$$U_{surf}(F) = N_d n_i^a l_{oxygen} \nu_{th} n_i \frac{\sigma_n^a(F) \sigma_p^a(F)}{\sigma_n^a(F) \exp\left(\frac{E_i^a - E_i}{kT}\right) + \sigma_p^a(F) \exp\left(\frac{E_i - E_i^a}{kT}\right)} \quad (2.6)$$

Again, careful temperature dependant generation analysis is necessary to confirm that the trap energy level is indeed consistent with the literature A-center values. However, the same approach taken for the bulk generation will be used for the surface generation rates in which the hypothesized trap model will be used at 300K to extract the resulting field dependence and zero-field cross-sections.

Field Dependant Cross Section Fitting

Ideally, a diode's reverse bias current scaling should scale linearly with the increased volume of the depletion region. However, since all volume scalings were accurately extracted in the finite element simulations by the loading of measured doping profiles, the fact that the fit generation rates increase with field indicates a real field dependant cross section that serves to further increase the reverse bias current. This scaling is important as the increasing dark current interferes with device performance as the bias is increased to deplete more of the germanium layer for better high-frequency performance.

Many existing field dependant models have been proposed and validated to be effective in various devices. The better established models will be attempted to be used to fit the experimental data first, especially Poole-Frenkel as this has been proposed by other investigators previously [24]. The electrically active trap densities per unit length for the below model fitting sections are kept constant: $5.5 \times 10^7 \text{ cm}^{-1}$ for the divacancy and $8 \times 10^{10} \text{ cm}^{-1}$ for the A-center. The oxygen diffusion length used is 100 nm in correspondence with the finite element model. These numbers are the result of the final model fit and will be derived in

that section. The cross sections will be fit to the combined cross section terms in Equations (2.5) and (2.6) for the bulk and surface respectively that produces the experimentally observed generation rate. These combined cross section terms are shown prior to fitting on both semilog and linear axes for both the bulk and the surface flaws in (Figure 34). One initial comment prior to detailed fitting is that these cross sections are approximately the same magnitude as initially assumed in the a priori threading dislocation model, roughly the atomic area or 10^{-14} cm².

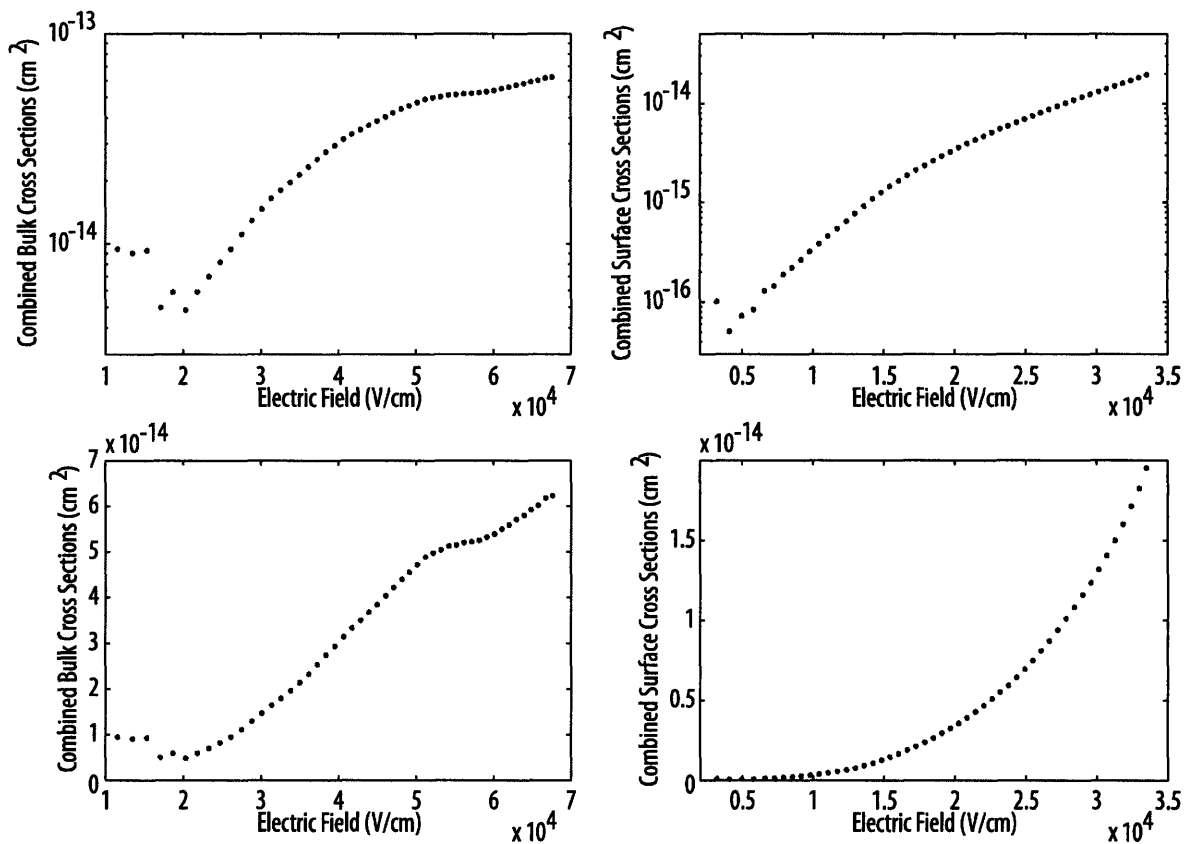


Figure 34. Extracted flaw cross sections as a function of electric field plotted on linear and semilogarithmic axes.

Poole-Frenkel Thermionic Emission Enhancement

Before describing the specific forms of the Poole-Frenkel related models, it is first necessary to introduce a few points regarding the potential wells for flaws. If the state is charged due to either a fixed charge or the charge resulting from a captured carrier, the well is determined by

a Coulomb potential and is therefore called a Coulomb well (cylindrical coordinates, flaw at origin):

$$E(r) = -\frac{q^2}{4\pi\epsilon r} \quad (2.7)$$

The uncharged state is assumed to be of negligible spatial extent such as to resemble a Dirac delta function and is therefore called a Dirac well (cylindrical coordinates, flaw at origin):

$$E(r) = -\delta(r) \quad (2.8)$$

For any given recombination process, a flaw will have to capture both an electron and a hole. To temporarily do away with the hole abstraction, an electron will have to be captured from the conduction band and then be emitted to the valence band. These two events will occur when the flaw state has a different charge and therefore potential well shape: one charged and therefore Coulomb; one neutral and therefore Dirac. Acceptor states therefore present Coulomb wells while emitting a hole to the valence band and Dirac wells while emitting an electron to the conduction band. Donor states act in the predictably opposite manner [73].

When external electric fields are applied to these potentials, the resulting potential profiles are a superposition of the well and this field. For the Coulomb well, the new field is given by Equation (2.9) for electric field, F , along the z-axis.

$$E(r, \theta) = -\frac{q^2}{4\pi\epsilon r} - qFr \cos \theta \quad (2.9)$$

The barrier height is now lowered for $0 \leq \theta \leq \frac{\pi}{2}$ as shown schematically in (Figure 35).

Location and magnitude of the barrier lowering can then be calculated:

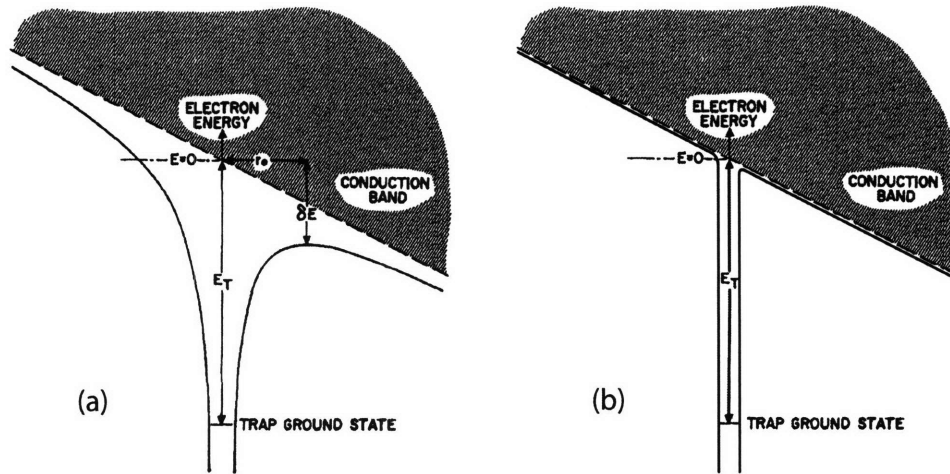


Figure 35. Potential wells formed by a flaw in an electric field. Barrier lowering occurs for the Coulomb well, (a), but not for the Dirac well, (b).

$$r_0(\theta) = \sqrt{\frac{q}{4\pi\epsilon F \cos\theta}} \quad (2.10)$$

$$\Delta E(\theta) = \sqrt{\frac{q^3 F \cos\theta}{\pi\epsilon}} \quad (2.11)$$

For the Dirac well, the barrier height does not change as its spatial extent is the limit approaching zero. Therefore for the acceptor flaw states under consideration, the hole cross section will be increased and the electron cross section will remain unchanged. The traditional Poole-Frenkel cross section enhancement for the hole capture is derived by calculating the increased thermionic emission over the barrier at the minimum point at $\theta = \frac{\pi}{4}$

[74]:

$$\sigma_p(F) = \sigma_{p_0} \left[1 + \exp\left(\frac{1}{kT} \sqrt{\frac{q^3 F}{\pi\epsilon}}\right) \right] \quad (2.12)$$

This cross section enhancement can be plotted relative to the experimental data as shown in (Figure 36). Since the scaling does not match the experimental data well, no further optimization was performed and the following zero field cross section values produced the closest fitting cross sections and were used in the plot:

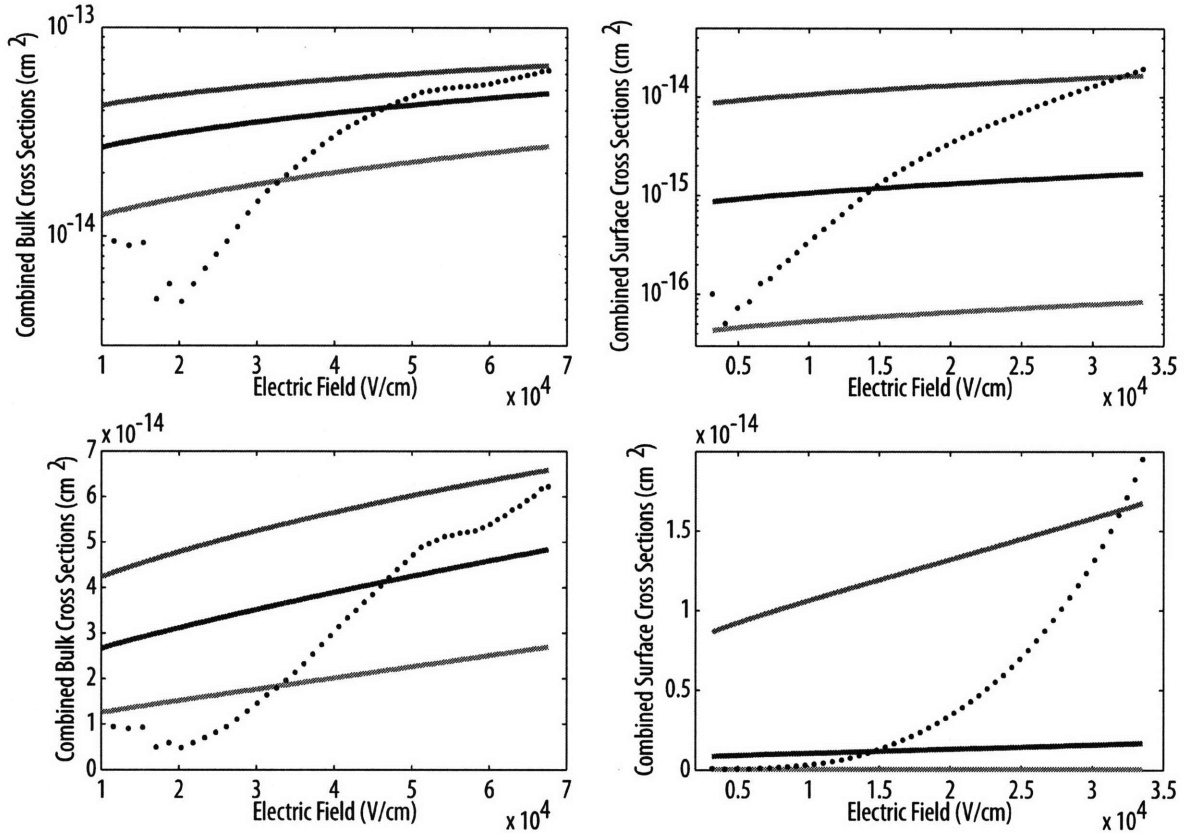


Figure 36. Extracted cross sections and 1D Poole-Frenkel model fit lines are displayed on linear and semilogarithmic scales for the bulk and interface states.

A-center zero field hole cross sections (cm ⁻²)	$2 \times 10^{-13}, 2 \times 10^{-14}, 1 \times 10^{-15}$
A-center zero field electron cross sections (cm ⁻²)	1×10^{-8}
Divacancy zero field hole cross sections (cm ⁻²)	$4 \times 10^{-16}, 2 \times 10^{-16}, 8 \times 10^{-17}$
Divacancy zero field electron cross sections (cm ⁻²)	6×10^{-12}

A more rigorous treatment was developed by J.L. Hartke in the 1967 paper in which the full 3-D potential was used to derive the increased emission rate shown in Equation (2.13) [75]. This modified form is still commonly called the Poole-Frenkel effect and is the form used in the Sentaurus PooleFrenkel model [73].

$$\sigma_p(F) = \sigma_{p_0} \left[1 + \frac{1}{\alpha^2} (1 + (\alpha - 1) \exp(\alpha)) - \frac{1}{2} \right], \quad \frac{1}{kT} \sqrt{\frac{q^3 F}{\pi \epsilon}} \quad (2.13)$$

This cross section enhancement is again plotted relative to the experimental data as shown in (Figure 37). Since the scaling is does not match the experimental data well, no further optimization was performed and the following zero field cross section values produced the closest fitting cross sections and were used in the plot:

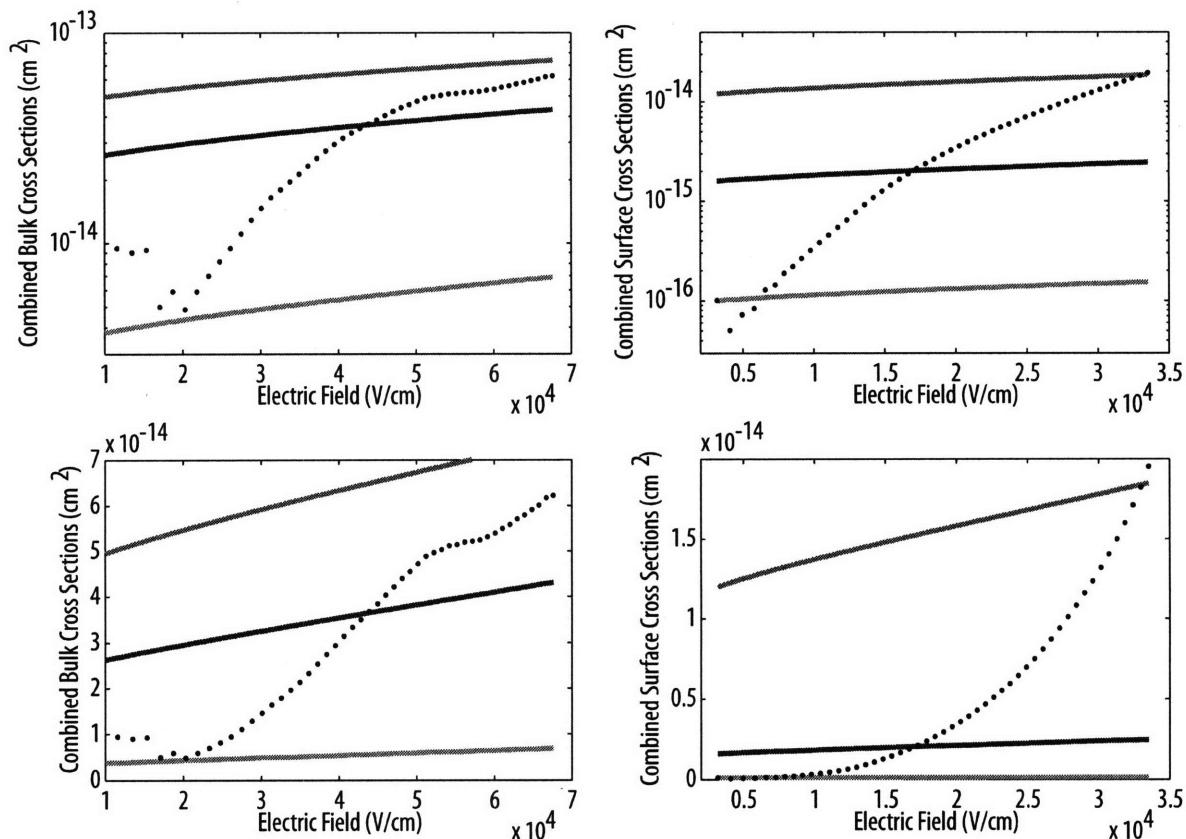


Figure 37. Extracted cross sections and 3D Poole-Frenkel Model fit lines are displayed on linear and semilogarithmic scales for the bulk and interface states.

A-center zero field hole cross sections (cm^{-2})	$6 \times 10^{-13}, 8 \times 10^{-14}, 5 \times 10^{-15}$
A-center zero field electron cross sections (cm^{-2})	1×10^{-8}
Divacancy zero field hole cross sections (cm^{-2})	$9 \times 10^{-16}, 4 \times 10^{-16}, 5 \times 10^{-17}$
Divacancy zero field electron cross sections (cm^{-2})	1×10^{-11}

Hurkx Trap Assisted Tunneling

An alternative model for field enhancement, first detailed by Hurkx et al. 1992, focuses on emission and capture aided by tunneling instead of thermionic emission [76]. This physical

model, shown in (Figure 38), considers the probability of tunneling into the potential well of a flaw through the triangular barrier formed by the external electric field and the flaw. The Coulomb well barrier lowering is ignored and therefore the enhancement is identical for Coulomb and Dirac wells. This therefore means that both the hole and electron cross sections will observe a field enhancement. The functional forms of the resulting field dependent cross sections are:

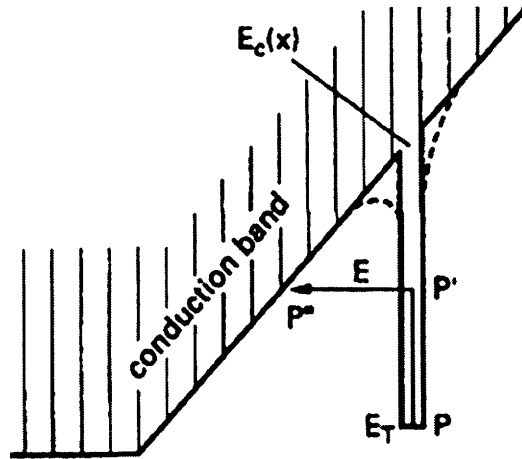


Figure 38. Quantum tunneling allows for the trapped carrier to be emitted without acquiring the energy needed to overcome the classical barrier.

$$\sigma_n(F) = \sigma_{n_0} \left[1 + \int_0^1 \exp \left(\frac{E_c - E_t}{kT} u - \frac{4}{3} \frac{\sqrt{2m_n^*} (E_c - E_t)^3}{q\hbar F} u^{3/2} \right) du \right] \quad (2.14)$$

$$\sigma_p(F) = \sigma_{p_0} \left[1 + \int_0^1 \exp \left(\frac{E_t - E_v}{kT} u - \frac{4}{3} \frac{\sqrt{2m_p^*} (E_t - E_v)^3}{q\hbar F} u^{3/2} \right) du \right] \quad (2.15)$$

This cross section enhancement model is available in Sentaurus as the Hurkx model using the numerical approximations to these integrals [76]. The best fitting cross section enhancement is again plotted relative to the experimental data as shown in (Figure 39). Since the scaling is does not match the experimental data well, no further optimization was performed and the following zero field cross section values produced the closest fitting cross sections and were used in the plot:

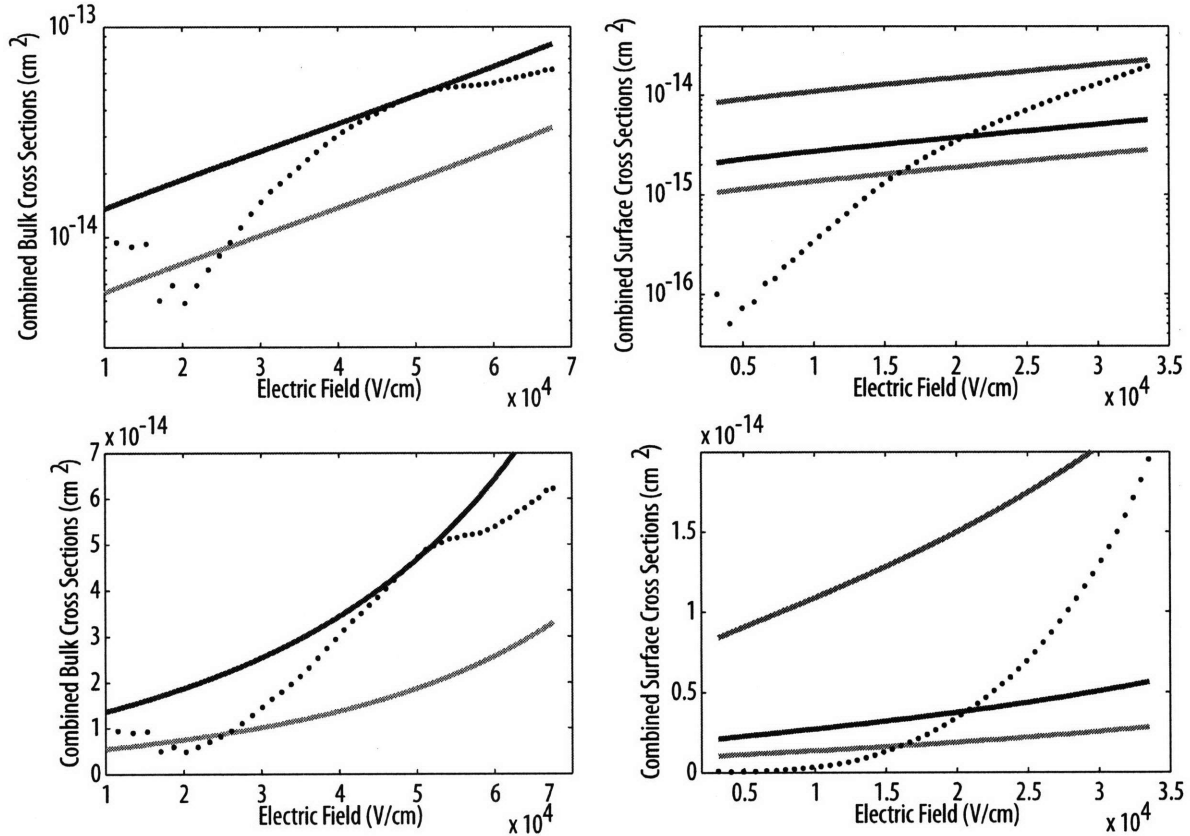


Figure 39. Extracted cross sections and Hurkx Model fit lines are displayed on linear and semilogarithmic scales for the bulk and interface states.

A-center zero field hole cross sections (cm^{-2})	$4 \times 10^{-13}, 1 \times 10^{-13}, 5 \times 10^{-14}$
A-center zero field electron cross sections (cm^{-2})	$4 \times 10^{-13}, 1 \times 10^{-13}, 5 \times 10^{-14}$
Divacancy zero field hole cross sections (cm^{-2})	$5 \times 10^{-12}, 2 \times 10^{-13}$
Divacancy zero field electron cross sections (cm^{-2})	$5 \times 10^{-12}, 2 \times 10^{-13}$

Lui and Migliorato Combined Model

A model that combines both the barrier lowering thermionic emission enhancement, tunneling contribution and the tunneling enhancement due to barrier lowering was proposed by Lui and Migliorato in 1997 [77]. In this model, the field enhanced cross section is identical to the Hurkx model for Dirac wells and therefore an acceptor electron cross section would obey Equation (2.14). The acceptor hole cross section however, includes sum the thermionic emission enhancement and tunneling contribution. Additionally, the increased tunneling rate due to the lowered barrier is included to modify the Hurkx model:

$$\sigma_p(F) = \sigma_{p0} \left[1 + e^{\frac{\sqrt{q^3 F}}{\pi \epsilon}} + \int_0^1 \exp \left(\frac{E_t - E_v}{kT} u - \frac{u^{3/2} \sqrt{2m_p^* (E_t - E_v)^3}}{3/4 q \hbar F} \left(1 - \left(\frac{\sqrt{q^3 F}}{u(E_t - E_v)} \right) \right) \right) du \right] \quad (2.16)$$

This model is the most complete available in the literature that is based upon a specific physical causality for the cross section enhancement. One noticeable improvement is that this and the Hurkx model are built around a 1-D treatment of the potential well and could be modified as Hartke demonstrated for the Poole-Frenkel model. Neither a 1-D or 3-D version of this model is currently available in Sentaurus. Despite the model sophistication, the best fitting cross section enhancement plotted in (Figure 40) does not match the experimental data well. Therefore, no further optimization was performed. The following zero field cross section values produced the closest fitting cross sections and were used in the plot:

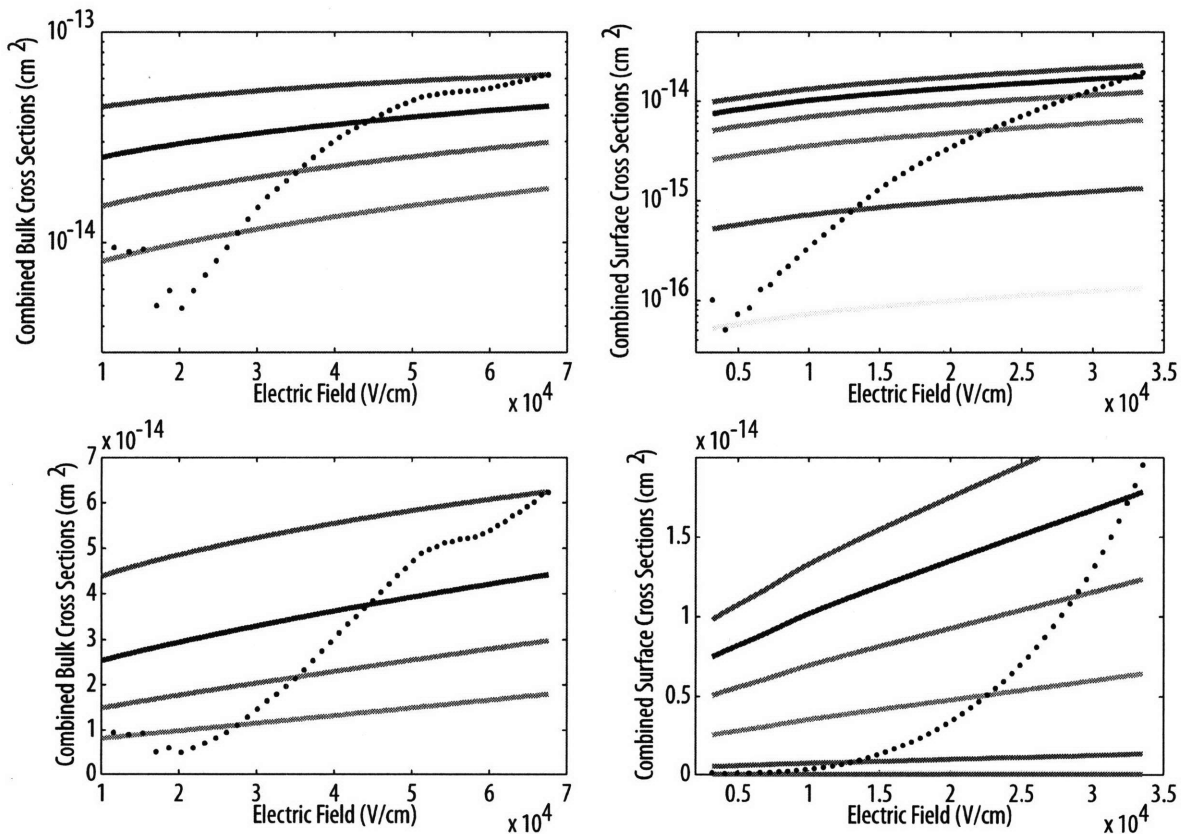


Figure 40. Extracted cross sections and Lui Migliorato Model fit lines are displayed on linear and semilogarithmic scales for the bulk and interface states.

A-center zero field hole cross sections (cm ⁻²)	2 x 10 ⁻¹³ , 1.5 x 10 ⁻¹³ , 1 x 10 ⁻¹³ , 5 x 10 ⁻¹⁴ 1 x 10 ⁻¹⁴ , 1 x 10 ⁻¹⁵ , 1 x 10 ⁻¹⁶
A-center zero field electron cross sections (cm ⁻²)	2.6 x 10 ⁻¹⁵
Divacancy zero field hole cross sections (cm ⁻²)	5 x 10 ⁻¹⁶ , 2 x 10 ⁻¹⁶ , 1 x 10 ⁻¹⁶ , 5 x 10 ⁻¹⁷
Divacancy zero field electron cross sections (cm ⁻²)	5 x 10 ⁻¹²

J-Model Polynomial Cross Section Enhancement

The final cross section enhancement model is not rigorously derived from physical theory. The J-model has instead been developed as a fitting formalism for high order equations describing the field dependence of cascade capture cross sections [78, 79]. The field dependence model is taken from a trapping rate framework based on incident alpha particle flux where the 'J' refers to particle "current" instead thermal velocity based models referred to as V-models [80]. In general, the polynomial cross sections for electrons and holes are modeled in the form of [81]:

$$\sigma_{n,p}(F) = \sigma_{n_0,p_0} \left[1 + a_1 \left| \frac{F}{V/cm} \right|^{p_1} + a_2 \left| \frac{F}{V/cm} \right|^{p_2} \right]^{p_0} \quad (2.17)$$

This model has provided close agreement with experimental results for oxide charge trapping silicon MOS capacitors under irradiation as observable in a shift of midgap voltage under applied field and dose [78]. As a result of the empirical agreement, this model has become the common parameterization for soft-error simulations in MOSFET TCAD even in the absence of rigorous physical explanations [81].

Attempting to apply this fitting formalism to the extracted germanium cross-sections, several combinations of exponents were explored for data fitting. In the closest functional form to the extracted data, a single cubic field term is used, i.e. $p_1 = 3, p_2 = 0, p_0 = 1$ with a_1 left as the fitting variable. The field enhancement is again applied only to the electron cross sections with the zero field cross sections equal to the DLTS literature values. The hole cross sections are again assumed unmodified by field and left as fitting variables. Good fitting results were

obtained using the same $\alpha_1 = 5 \times 10^{-8}$ field enhancement value for the A-center and divacancy flaws as shown in (Figure 41).

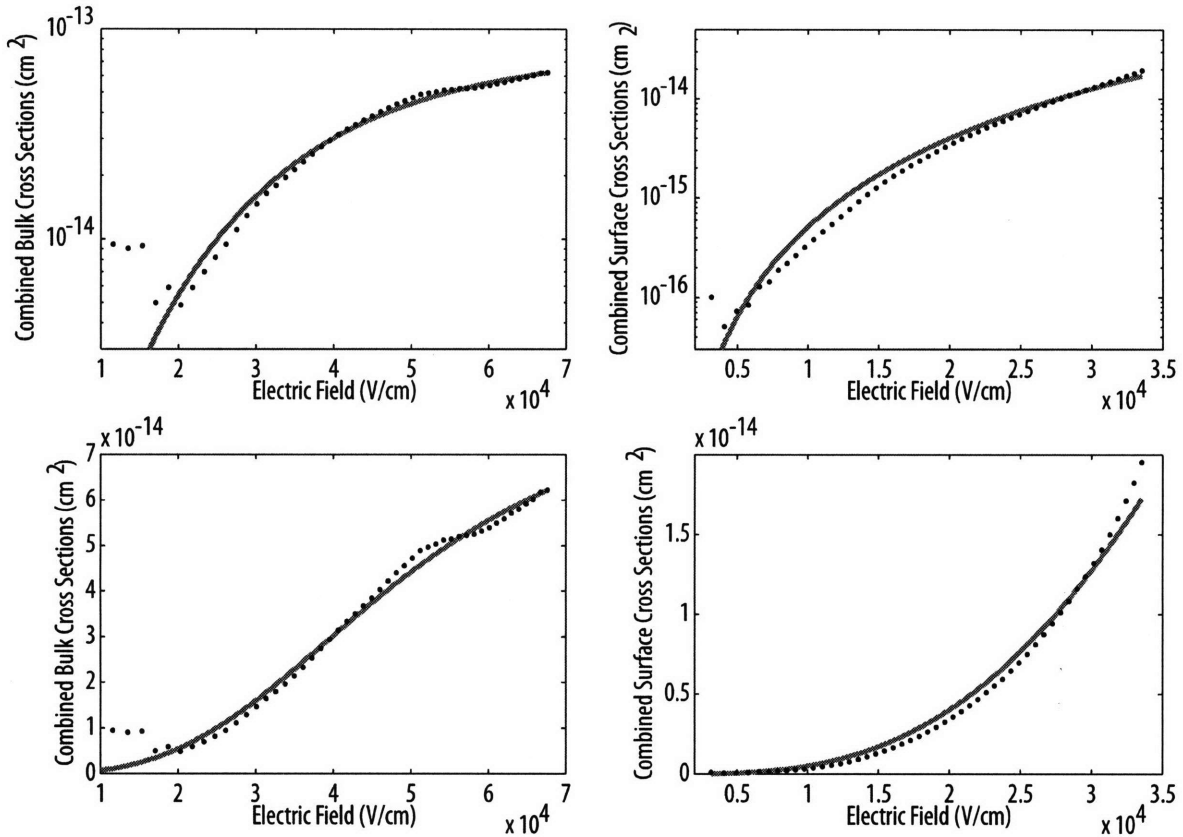


Figure 41. Extracted cross sections and J-Model fit lines are displayed on linear and semilogarithmic scales for the bulk and interface states.

Simultaneous fitting of both the edge and bulk behavior with the same enhancement function is seen as confirmation that they both stem from the same physical phenomena such as the local electrostatic environment of the threading dislocation. The fit enhancement factors are shown on linear and semilog axes in (Figure 42). The zero-field cross sections used are again the DLTS values for the electron, $\sigma_{n_0}^a = 2.6 \times 10^{-15} \text{ cm}^2$ and $\sigma_{n_0}^d = 5 \times 10^{-12} \text{ cm}^2$, and the fit hole values of $\sigma_{p_0}^a = 6 \times 10^{-19} \text{ cm}^2$ and $\sigma_{p_0}^d = 2.5 \times 10^{-22} \text{ cm}^2$.

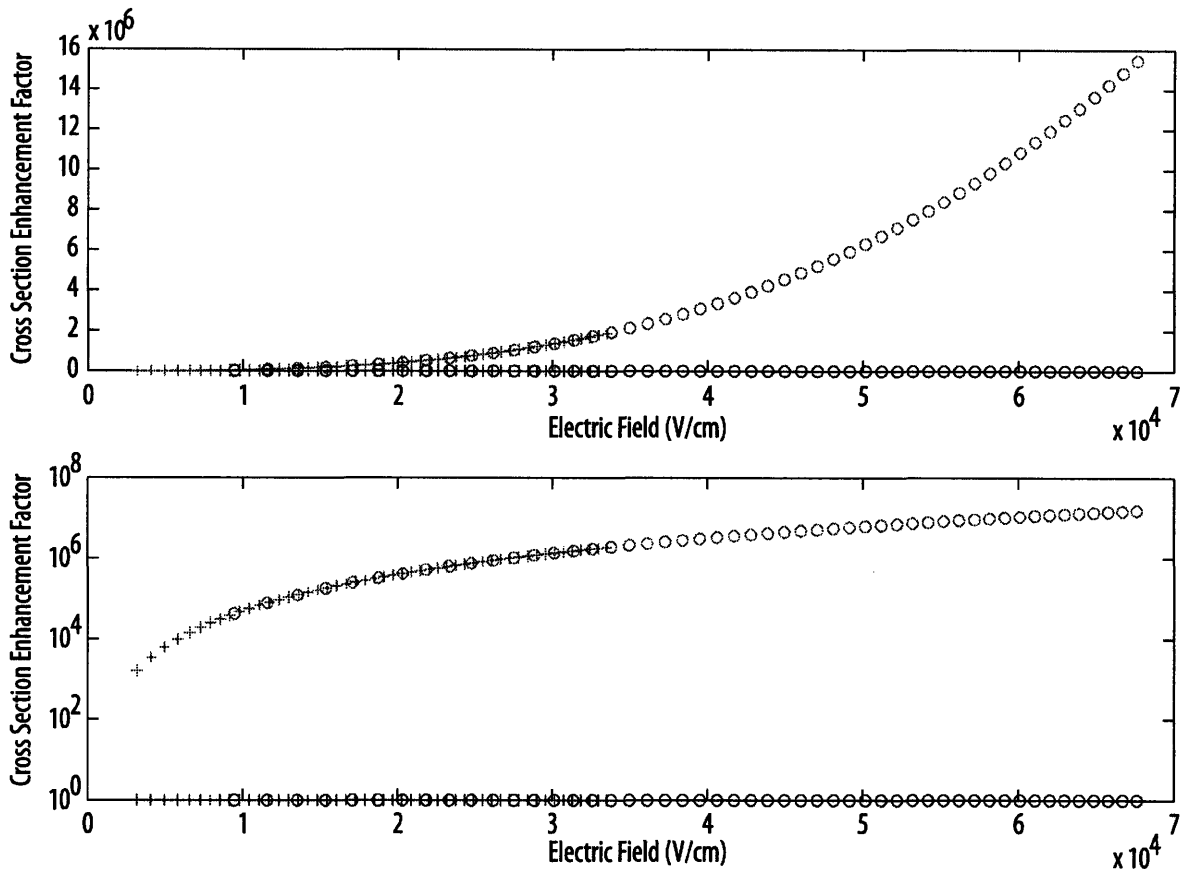


Figure 42. Cross section enhancement as a function of electric field for the J-Model fit parameters. Circles correspond to bulk flaws and crosses correspond to surface flaws. The electron cross sections (red) are modified in the J-Model while the holes (blue) remain constant.

These fitting parameters were achieved after significant optimization varying the aforementioned flaw densities and zero field hole capture cross sections. For the bulk traps, the cross section field dependence shows the cubic enhancement in the low field regions, but becomes limited by the fixed electron cross section near the high field region. Since the electron cross section is fixed by literature values, the high field region allows the density of flaw states per unit dislocation length to be fixed to $5.5 \times 10^7 \text{ cm}^{-1}$ for the divacancy.

The problem is slightly more complicated since it obeys a cubic field scaling for all field values of interest. Since the electron cross section value is fixed from the literature, the zero field hole cross section must be small enough that it dominates the cross section and therefore its field dependence. This therefore fixes the maximum hole zero field cross section to be

$\sigma_{p_0}^a = 6 \times 10^{-19} \text{ cm}^2$ as shown in the plots. The corresponding A-center line density along the dislocation is then bounded to be at least $8 \times 10^{10} \text{ cm}^{-1}$. Since the approximate intersite spacing of threading dislocation states is approximately 10^{13} cm^{-1} , a reasonable maximum line A-center line density could be derived from a 10 site spacing to be on the order of 10^{12} cm^{-1} [55]. That would allow the minimum zero field hole cross section to be approximately $4.8 \times 10^{-21} \text{ cm}^2$ for the A-center. However since the areal density of threading dislocations is estimated to be $2.4 \times 10^7 \text{ cm}^{-2}$ for these diodes, the minimum A-center line density of $8 \times 10^{10} \text{ cm}^{-1}$ would result in a flaw volume density of $1.9 \times 10^{18} \text{ cm}^{-3}$. Since the field scaling of the edge states is identical to that of the bulk states, it is unlikely that these states are interacting and forming an impurity band. Additionally, since the literature density threshold for trap interaction is roughly 10^{18} cm^{-3} , it follows that the actual A-center density and therefore line density cannot be far above the minimum [41].

Comments and Possible Explanations of Fitting Results

The most obvious remaining question from this fitting analysis is why the cross sectional field dependence is cubic as fit by the J-model formalism. One important distinction between the physical models attempted and the theorized flaw states is that the localized state models assume a neutral, isotropic surrounding environment and the theorized flaw states are in a charged dislocation line. The shallow traps in dislocations are dominated by thermally ionizable acceptors [55]. The resulting ionized flaws create a line charge density. The bands are therefore locally deformed by the charge. Since the electrostatic environment surrounding the flaw is known to modify the effective trap cross section as in the Poole-Frenkel effect, this physically different electrostatic surrounding could lead to a different functional form of the field enhancement. This question is a fundamentally important aspect of future work to investigate after this thesis.

One additional point is the relative magnitudes of zero-field cross sections required for approximate fitting of the experimental results. For the 1D and 3D variations of the Poole-Frenkel effect, the zero field hole cross section for the A-center had to be seven orders of magnitude higher than the literature predicted values. The Hurkx and Lui-Migliorato models

provided at least order of magnitude agreement with the DLTS literature electron cross section values. This suggests that tunneling may be an important contribution to the cross section enhancement. The Lui-Migliorato model especially show good approximate fitting of the experimental results using the exact electron cross section values from the DLTS literature.

Chapter 3 – Optical Characteristics of Ge-on-Si Photodiodes

The next area of characterization of the Ge-on-Si diodes focuses on their optical responses. Although the epitaxial growth's negative aspects, threading dislocations, were the focus of the last chapter, the strain resulting from the epitaxial growth has a positive impact on the optical characteristics. As described in the introduction to Chapter 2, the strain caused by the thermal expansion differences between germanium and silicon results in a bandgap narrowing of the germanium layer. Since optical absorption is directly dependant on the bandgap, this results in increased optical absorption at most wavelengths and absorption at longer wavelengths where the photon energy is less than the unstrained bandgap. Since the photon absorption in direct bandgap transistions is far stronger than indirect bandgap transitions, the 0.8 eV unstrained direct bandgap dominates the optical response. The corresponding photon wavelength of 1550 nm is highly technologically relevant as it is the center of the telcommunications C-band. As the film strain causes the direct bandgap to decrease 30 meV to 0.77 eV, the germanium film absorption extends through the C-band to cover most of the L-band as well [3, 24]. Transmission measurements on similarly grown films have demonstrated $1 \times 10^4 \text{ cm}^{-1}$ absorption at 1300 nm and $4.5 \times 10^3 \text{ cm}^{-1}$ absorption at 1550 nm as shown in (Figure 43) [82].

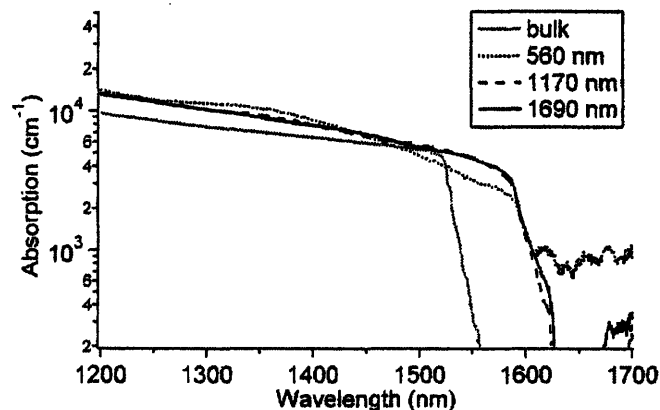


Figure 43. Germanium absorption coefficient extracted from transmission measurements by Hartmann et al., 2004. The caption lengths correspond to different germanium-on-silicon film thicknesses and are

compared to a bulk germanium sample. The thinnest germanium layer shows some strain relaxation as compared to the thicker layers.

This data does not give any detailed data on the absorption at the bandedge. Better information is shown in (Figure 44).

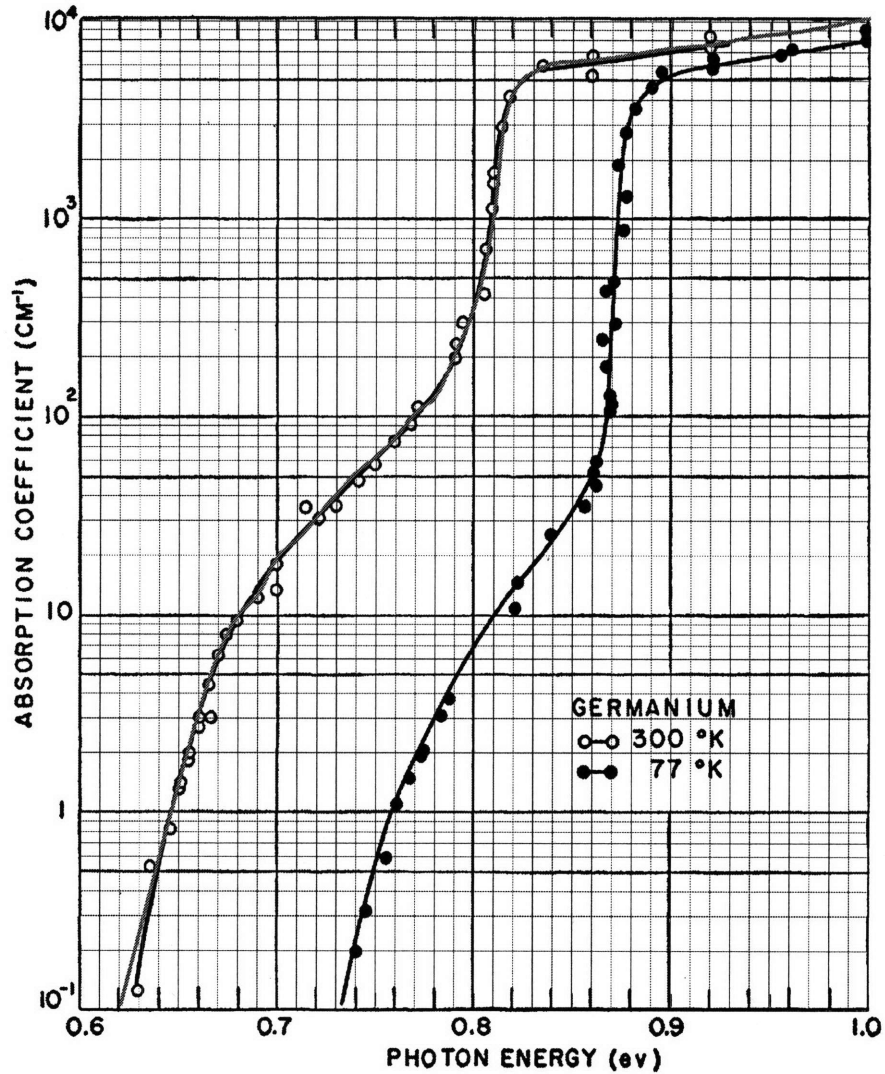


Figure 44. Germanium bandedge absorption from Dash and Newman 1955. Semi-logarithmic grid superimposed over original figure was used to generate the fit line shown in red.

Optical Conversion Efficiency

A key requirement for photodiodes, regardless of end application, is to have high conversion efficiency from incident photons to usable electron current at the electrodes. This is conceptually determined by the fraction of absorbed photons and the gain or loss suffered as the resulting electron-hole pairs travel towards the device contacts. Direct experiment can only examine the product of these two effects by shining a known incident optical power at the photodiode and measuring the current. The resulting quantity, known as responsivity, is straightforward to measure, but great care must be taken in correct calibration of the experimental setup.

Responsivity Measurement

Previous responsivity measurements had been performed on the photodiode and reported in the literature [24]. Again, in the interest of obtaining a complete, known dataset, this measurement was reproduced; however, the measured results differed by over 50%. As a result of this discrepancy, the experimental setup will be described in greater detail than would be in normal circumstances. The setup uses a widely tunable laser source that is passed through the 1-port of a circulator, out the 2-port, split in a fixed-ratio fiber coupler and focused on the photodiode by either a pigtailed GRIN lens focuser or lensed fiber. Optical power is monitored for the incident light on the tap port of the fiber coupler and the backreflected light on the 3-port of the circulator with fiber coupled power monitors. Optical power calibration (figure required) is performed for all measurement wavelengths by simultaneously triggering a free space power head and a fiber coupled power monitor to measure the power out of the focuser and the tap fiber respectively. The focal point of the focuser is determined by maximizing the back reflected power over the photodiode window. The spot size of the incident light can then be controlled by translating the focuser a known distance on the z-axis. Knife-edge measurements, shown in (Figure 45), were used to characterize spot size as a function of displacement.

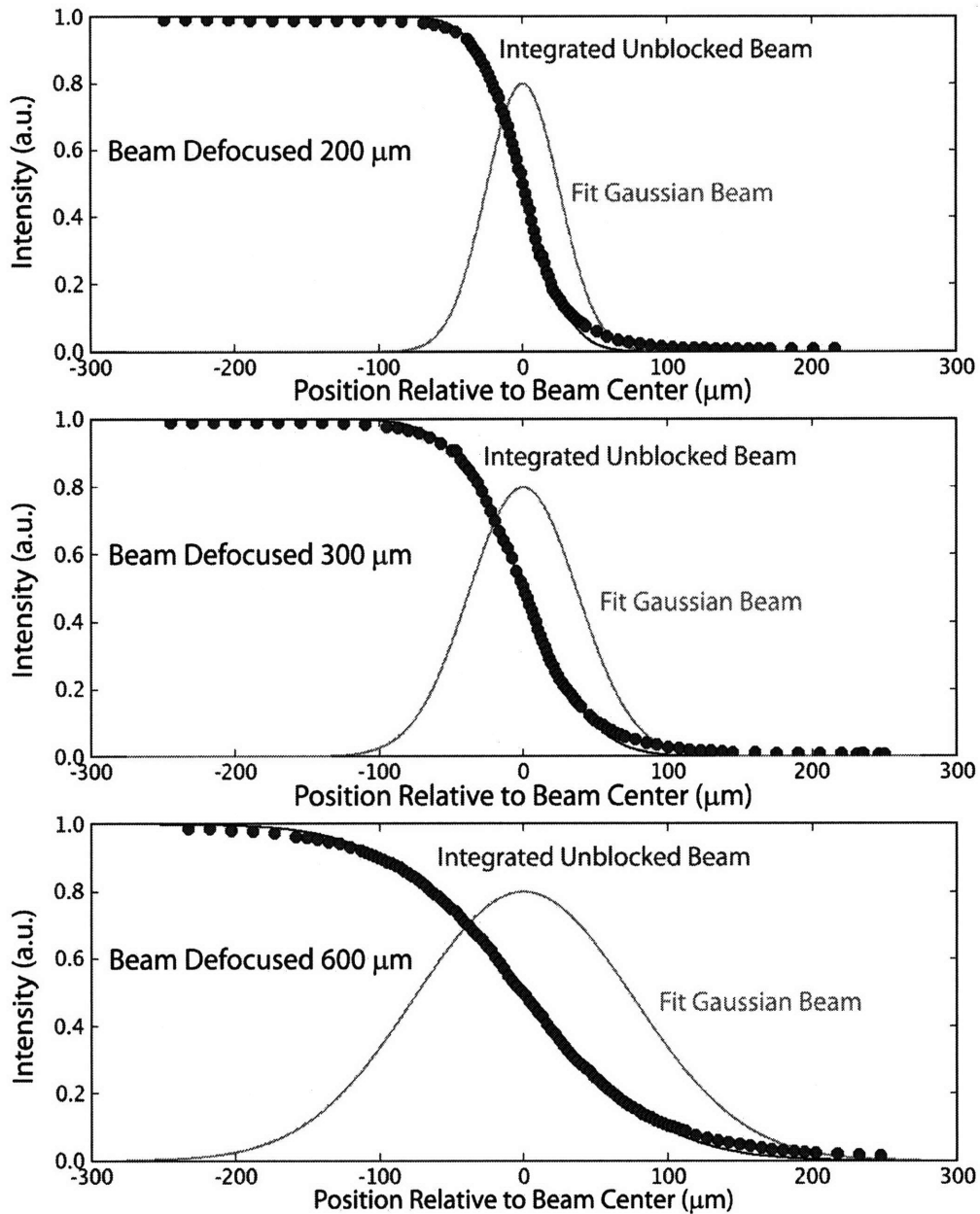


Figure 45. Knife edge measurements at 1310 nm at three defocus distances compared to a Gaussian beam model with a fit Raleigh range of 15.30 microns.

The photodiode current is measured using the same Agilent 4156 C semiconductor parameter analyzer used in the I-V measurements of Chapter 2.

Several different techniques can be used separate the current resulting from incident light from the background dark current of the photodiodes. In diodes with low responsivity and

high dark currents, it is often necessary to modulate the incident light and use lock-in techniques to measure the component of the current that is changing only at the frequency of the modulated light. In this case, since currents many times the dark current were easily obtained for all bias points of interest, a simpler technique was used. Since the dark current and the photocurrent can be modeled as independent current sources to a good approximation, photocurrent was measured at several optical power levels and fit to a line on the I-P plane with the I-intersect equal to the dark current. The slope of this fit line is the diode responsivity. Additional technical notes worth mentioning include the need to change the calibration wavelength of the power monitors synchronously with the swept power wavelength, and the need to trigger the current and power measurements simultaneously with equal integration times to reduce noise. The accuracy of these measurements was verified by measuring bare die InGaAs photodiodes from the Emcore Corporation that had been characterized in factory at 1310 nm. The resulting curve shown in (Figure 46), closely matches the 0.91 A/W calibration.

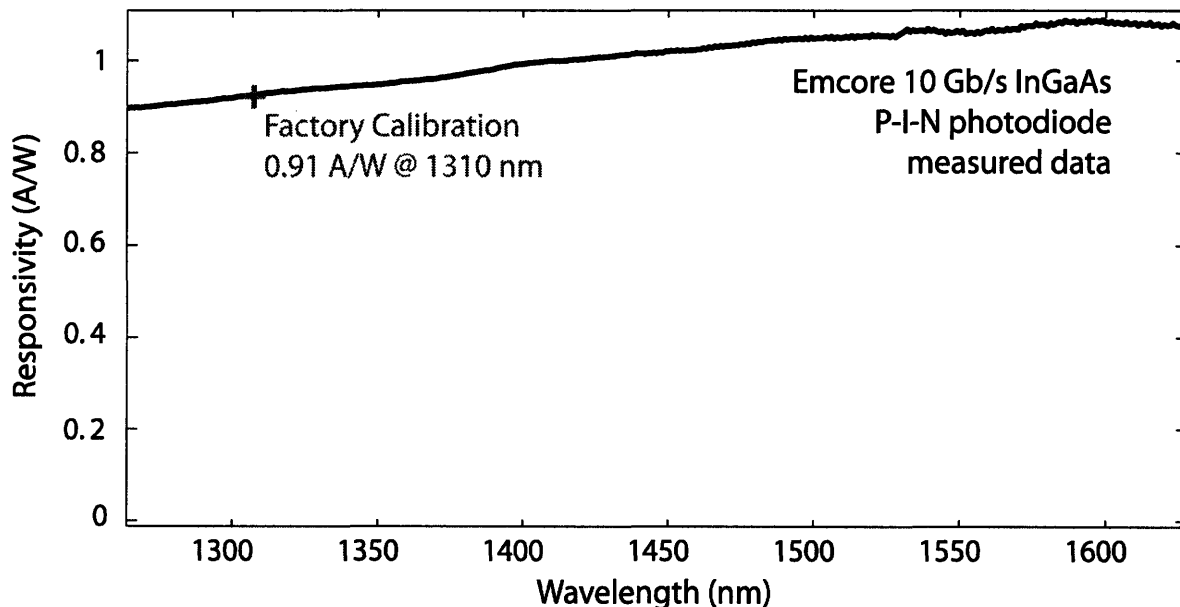


Figure 46. Measured Emcore InGaAs photodiode responsivity curve matching factory calibration at 1310 nm.

Since the photodiodes are fabricated on a blanket germanium film that does not provide any isolation against photogenerated carriers diffusing into diode depletion region, initial

responsivity measurements were performed with the spot size of the incident light much smaller than the diode window size. These underfill illumination responsivity measurements are shown as a function of optical wavelength and reverse bias in (Figure 47). Several interesting features of this measurement will be discussed in greater detail later, but the most important result is the magnitude of the 1550 nm measurement of 0.4 A/W is far below the 0.6 A/W previously measured [24].

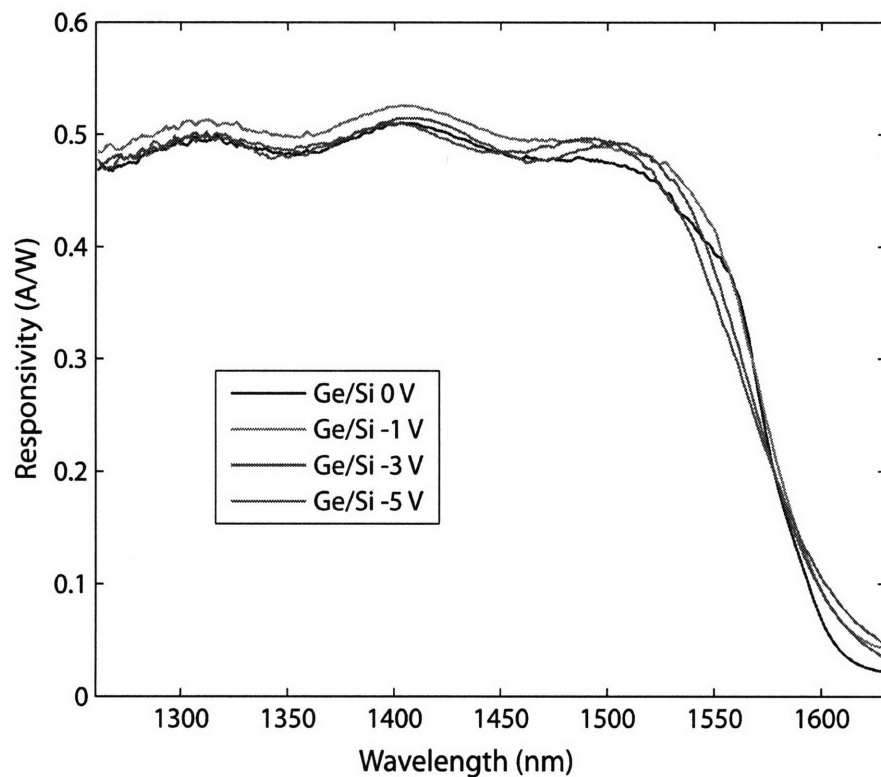


Figure 47. Ge-on-Si responsivity measured from 1260 nm to 1630 nm at four bias points.

The difference between this measurement and the previously reported value is that underfill illumination was used instead of overfill illumination. In traditional blanket film diodes, the lack of isolation allows photogenerated carriers outside the diode window to diffuse back into the depletion region and contribute to current. Since the optical power is calculated from integrating the incident power over the diode window only, this would presumably generate an increased responsivity as current would be measured from light not being considered in the incident power estimate. To replicate this measurement, the focuser was translated to

produce a 1 mm diameter spot of a similar size to the previous result. The surprising result is shown in (Figure 48) as a function of optical spot size under similar conditions. Calculating the incident power as the power density integral over the entire diode window, the responsivity goes down.

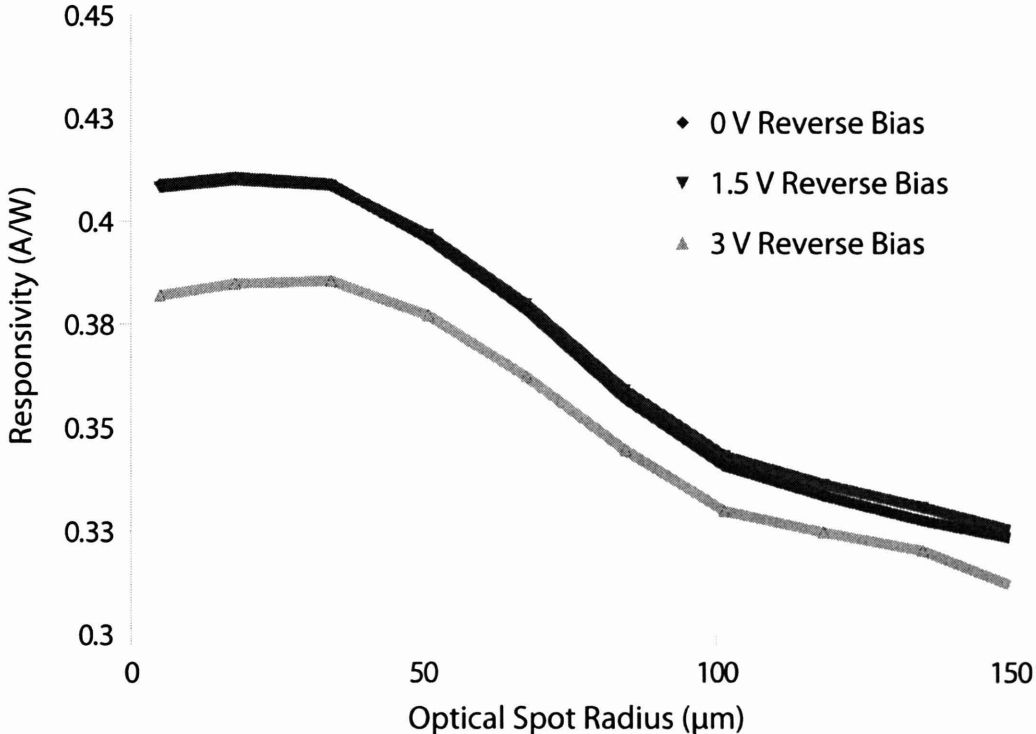


Figure 48. Overfill responsivity measurements for a 100x100 micron photodiode at three bias points.

The implications are two-fold. First, compared under similar conditions, the previous responsivity is approximately a factor of two off from the overfill responsivity measurements. Since the underfill results accurately reproduce commercial diodes and factory characterization, the overfill results must be regarded as false and serve as a warning that great care must be taken in performing responsivity measurements. Secondly, the reduction in responsivity for the overfill measurement suggests that there is a section of the diode window, presumably at the diode edge that is not contributing to photoresponse. This result suggests that the perimeter interfaces is not only an issue for dark current, but also for the more important photoresponse characteristics of the photodiode. Further studies of the

spatial dependence of photodiode characteristics will be presented in later sections after discussion of the magnitude and implications of the responsivity.

Internal Quantum Efficiency Estimates

Although responsivity is a product of generation and collection, the fundamental internal quantum efficiency (IQE), the fraction of generated electron-hole pairs that contribute to current at the contacts, can be extracted using other device information. This is a more relevant number than the responsivity for the purpose of this discussion since IQE is more immediately related to material quality, whereas responsivity is a combination of device design decisions. The devices under examination do not include simple additions such as antireflective (AR) coatings that can eliminate reflective losses over the moderate optical bandwidths required for C-Band photodiodes.

In order to extract the internal quantum efficiency (IQE) from the responsivity measurements, an estimate of the absorbed light must first be obtained. This requires both knowledge of the reflected light and the transmitted light that is not absorbed in the germanium. Film transmission measurements for similarly strained films, which have been presented previously in the literature, estimate the germanium absorption coefficient to be 4300 cm^{-1} . The refractive indices and thickness of the films that comprise the device are well known from growth conditions and ellipsometry, so the calculation of absorbed light is relatively straightforward using a transmission matrix formalism. This results in an estimate of 73% of the incident light absorbed in the film. The internal quantum efficiency, η , is then calculated from the measured responsivity, R , as shown in Equation (3.1) to correct for the photon energy, E_{photon} , and incomplete absorption in terms of the structure's transmittance, $|t|^2$, and reflectance, $|r|^2$.

$$\eta = R \frac{E_{\text{photon}}}{q(1 - |r|^2 - |t|^2)} \quad (3.1)$$

The absorption and transmission through the film can be calculated by using a transmission matrix formalism. The results of this analysis is shown in (Figure 49).

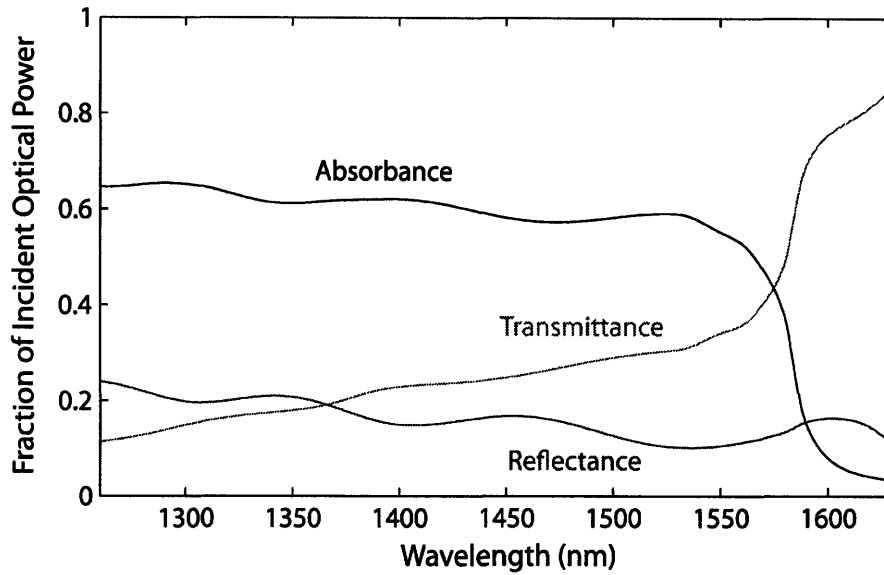


Figure 49. Transmittance, reflectance and absorbance as a function of wavelength calculated using the T-Matrix method.

The quantum efficiency is calculated over a wide bandwidth and shown in (Figure 50).

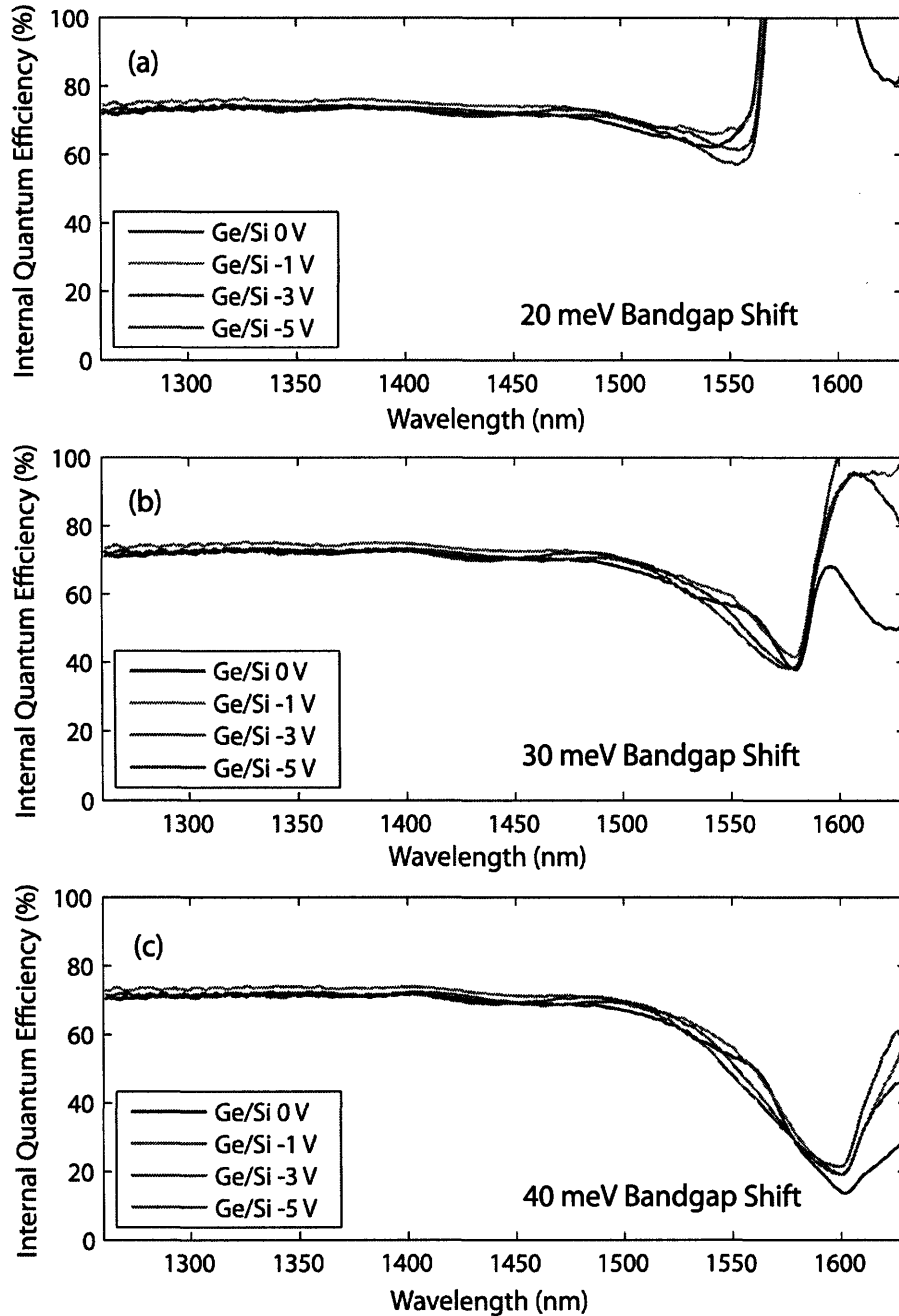


Figure 50. Extracted quantum efficiency from structural optical T-Matrix calculations for various assumptions of bandedge shift.

Responsivity Simulation

Since the internal quantum efficiency is not 100%, internal recombination processes are limiting the optical efficiency of the photodiodes. The two key sources of recombination

losses are recombination in the depletion region to limit carrier current contribution and recombination in the quasineutral regions before the carriers can diffuse to the depletion region and contribute to current. For finite element modeling of these effects, the measurement extracted bulk carrier lifetime accurately represents the flow limited recombination processes and the SRP doping profile determines the sizes of the depletion and quasineutral regions.

The cylindrical coordinate finite element model for a 20 μm circular diode developed in Chapter 2 is used for responsivity simulation. The responsivity is simulated at -1 V for 1550 nm light using the bulk and surface lifetimes fit in Chapter 2. To simulate the optical input, the OptBeam physics model was used with a 5 μm radius step profile at the center of the diode. The finite element mesh is refined for optical absorption calculations by the command RecBoxInteg to ensure an accurate optical generation profile. The resulting optical generation profile and total recombination rates are shown in (Figure 51) and (Figure 52) respectively.

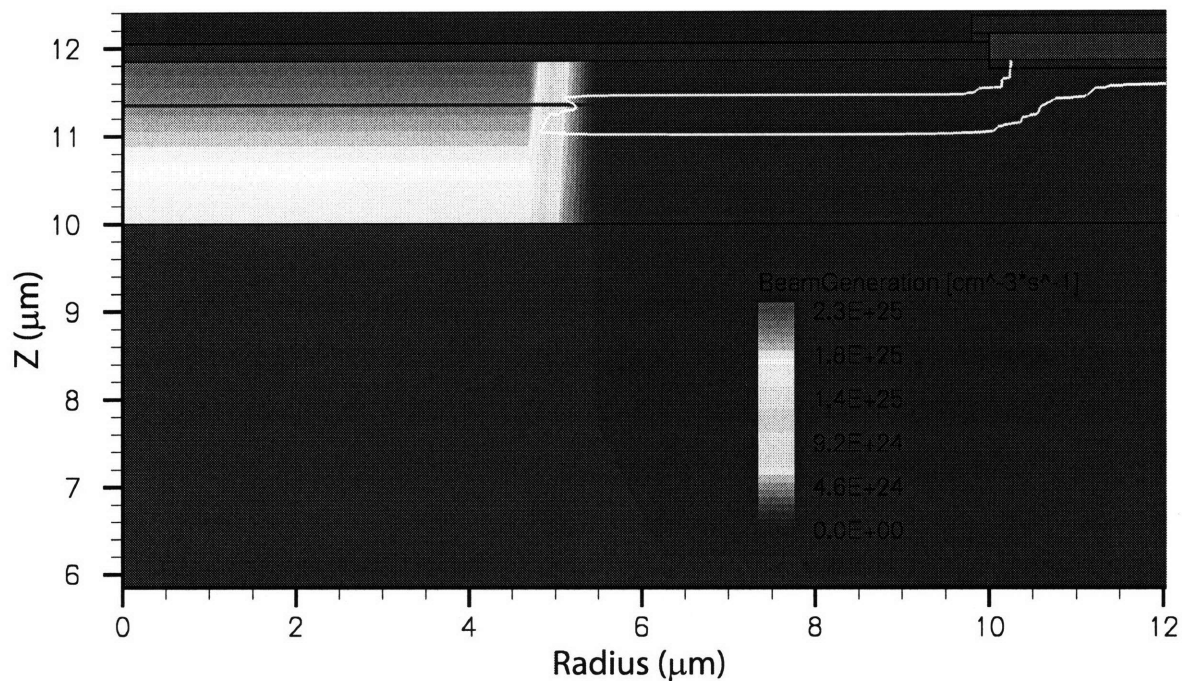


Figure 51. Optical generation in cylindrical coordinates.

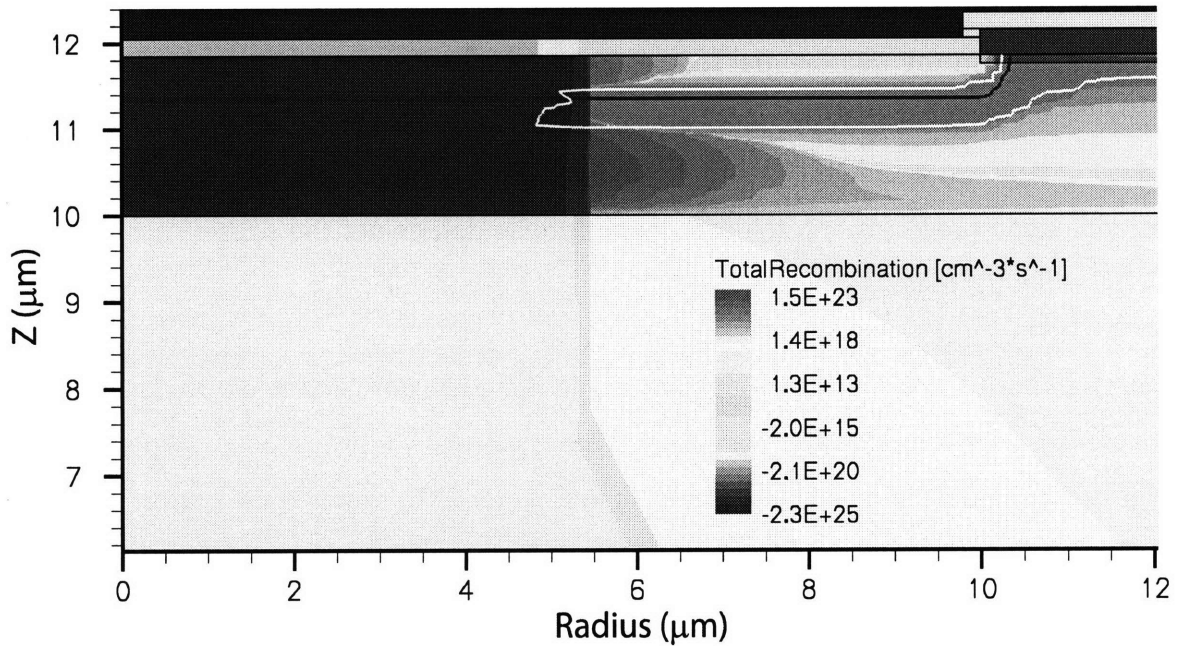


Figure 52. Recombination rate under optical generation in cylindrical coordinates.

The simulated currents resulting from the various optical powers are shown in Table 1.

Optical Power (μW)	Current (μA)
1000	427.1
800	342.8
600	256.4
400	171.3
200	86.1

Table 1. Responsivity simulation data points.

Since the dark current is simulated to be $1.092 \mu\text{A}$, the excess photocurrent can be calculated by subtracting the dark current from the simulated current. The responsivity can then be calculated by dividing the photocurrent by the optical power and averaging over all of the simulation points to be 0.43 A/W . This agrees very well with the measured 0.42 A/W responsivity. The recombination rates extracted by the I-V curve fitting therefore show consistency with the optical measurements.

Spatial Responsivity

In Chapter 2, the leakage current was demonstrated to be largely localized to the diode perimeter both by thermal spatial imaging and the scaling trends of dark current. Since this leakage was due to flaw generation observing SRH statistics, the SRH recombination due to these same states is expected to reduce the responsivity by causing the optically generated carriers to recombine. The responsivity is therefore expected to be spatially dependant.

Measurement

To test this hypothesis, the responsivity was measured as described above on a 1.5 micron spacing in a line across the diodes. To achieve better spatial resolution, the pigtailed focuser was replaced by a lensed fiber that was manufacturer specified to have a 1.2 micron $\frac{1}{e^2}$ spot size at 1550 nm. The working distance was specified to be 25 microns and the exact placement of the fiber was found by maximizing the backreflection from the diode. The translation was performed manually using a flexure stage with differential micrometers. Each translation measurement was performed by turning the micrometers in only one direction to eliminate backlash error. The flexure stage action translated the fiber 1.5 times the micrometer travel as specified by the manufacturer and verified within the accuracy of standard machinist's calipers. The measured data for a 20 micron and 100 micron wide rectangular diodes is shown in (Figure 53) and (Figure 54) respectively.

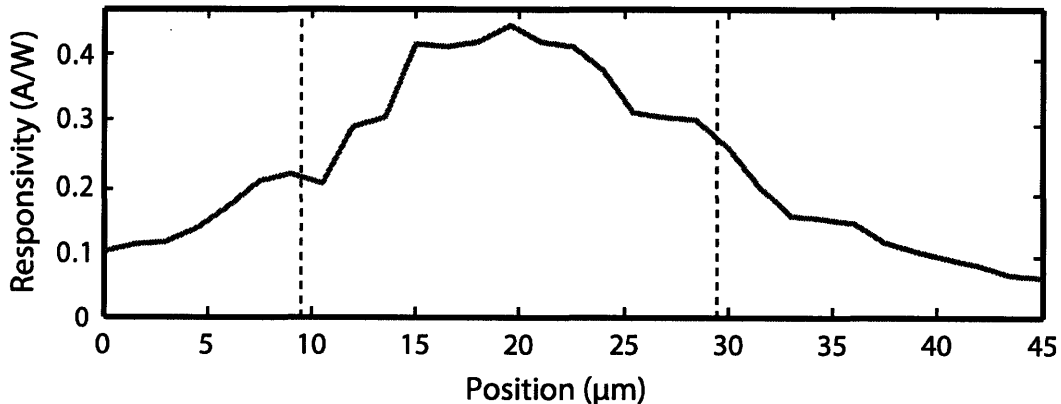


Figure 53. Spatial responsivity measurement for a 20 micron wide rectangular diode at -1V reverse bias.

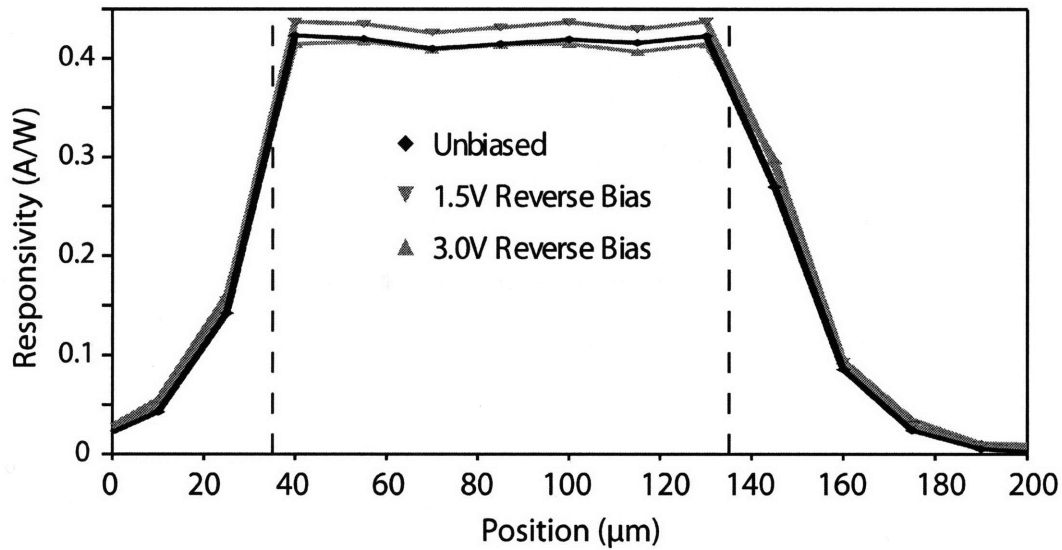


Figure 54. Spatial responsivity measurement for a 100 micron square diode.

The diode response is observed to reduce within 5 microns of the passivation interface. Since the absorption, reflectivity and film thickness remain constant, this reduction must be attributed to an increase in recombination that serves to reduce the internal quantum efficiency.

Simulation

Since the simulated perimeter flaw densities are too high to yield quasistationary Poisson equation convergence, this effect cannot easily be simulated at this point. Future work can solve this problem for direct simulation of the spatial responsivity. An easier simulation can be performed on the finite element diode model without increased perimeter recombination to show that the idealized diode model conflicts with experiment as shown in (Figure 55).

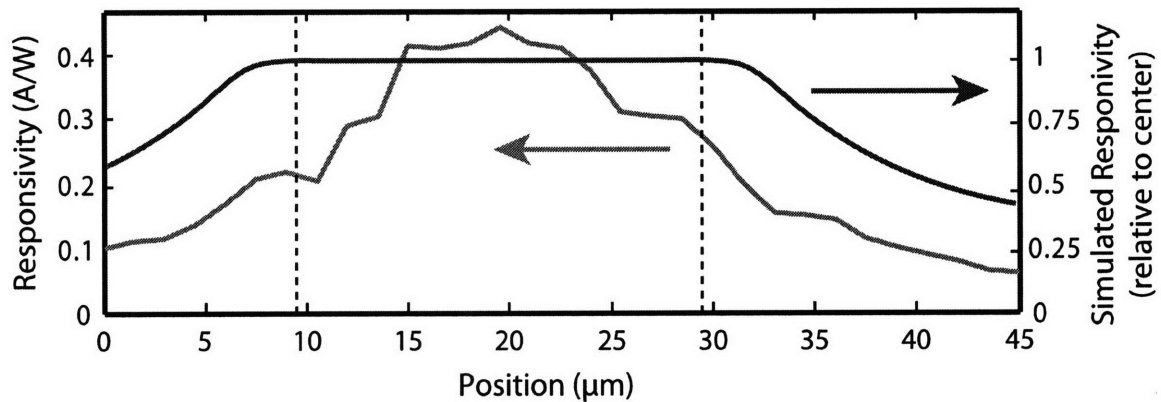


Figure 55. Simulated response (blue line) is compared to measured results (red line).

Thermally Dependant Responsivity Measurements

Since the responsivity is theorized to be degraded by flaw dominated recombination, it is possible that responsivity could increase at lower temperatures as deep levels become further from the bands compared to kT and therefore less effective R-G centers. These measurements were performed in the same Desert Cryogenics TT-Prober System used for the I-V-T measurements of Chapter 2. The thermal expansion inherent in temperature swept measurement required realigning the optical input at every temperature point. The optical input for these measurements was a manufacturer specified 5 micron GRIN lens pigtailed to a fiber. The resulting data plotted for five wavelengths is shown in (Figure 56).

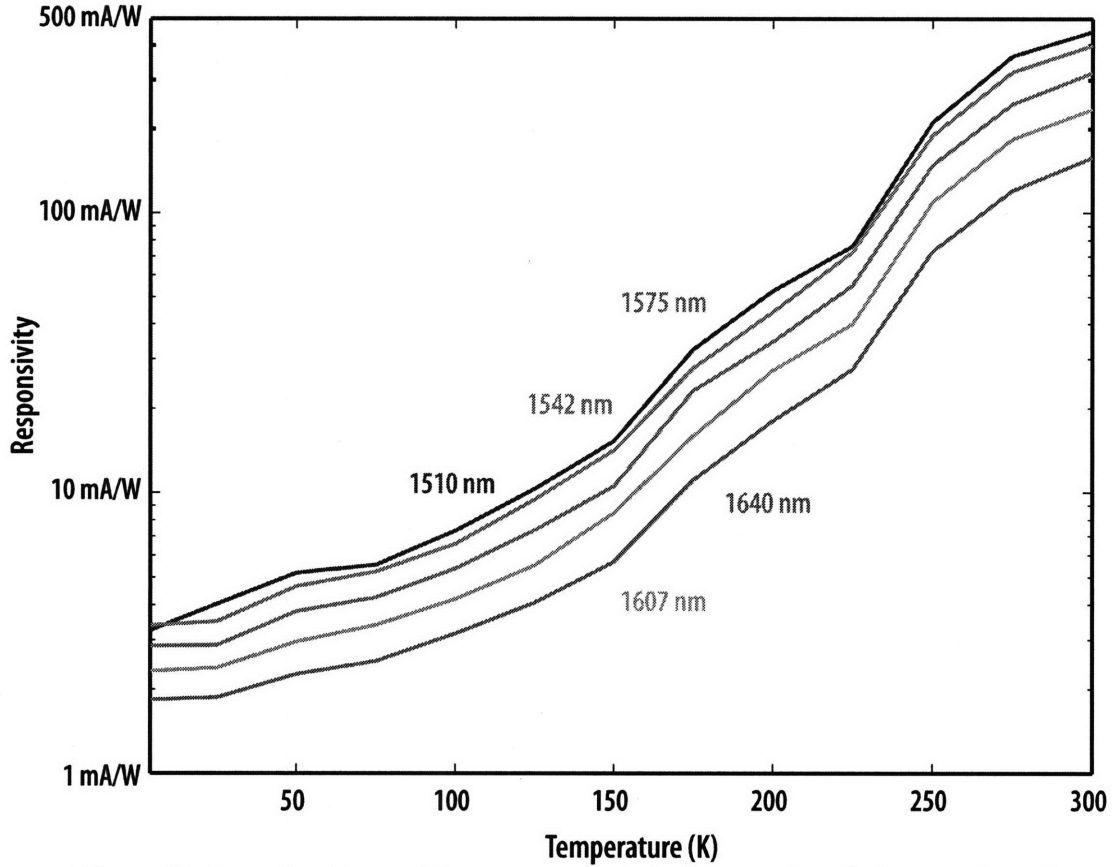


Figure 56. Thermally dependant responsivity measurements for five wavelengths for an unbiased 50 micron radius circular diode.

Contrary to expectations, there is no increase in responsivity at decreasing temperature. Since the absorption as a function of temperature is not known, it is possible that the internal quantum efficiency is going up. The exact behavior of the bandedge absorption as the temperature decreases is a competition between the increasing bulk bandgap and an increasing thermal strain, which would decrease this bandgap. Comparing the 300 K absorption to the 77 K absorption in (Figure 44), a bandgap increase of 70 meV is estimated from a 233 K temperature change. Alternatively, the strain caused by the thermal expansion coefficient difference between silicon and germanium from the peak processing temperature of 850 °C to room temperature results in a 30 meV bandgap decrease for a 825 K temperature change. Crudely comparing the bandgap change as a function of temperature for these two effects, the bulk bandgap change is seen to be almost an order of magnitude stronger.

This would result in the bandgap shrinking significantly over the temperature range studied here. It is therefore unclear whether or not the internal quantum efficiency is increasing as the temperature is decreased as would be expected by the influence of deep flaw dominated recombination on the responsivity. However, the application level implication of these measurements is that no responsivity improvements can be had by cooling the photodiodes for the wavelengths considered.

Small-Signal Frequency Response

The next important performance characteristic to quantify for the Ge-on-Si photodiodes is the frequency response. Several factors can limit the frequency response of a diode in a real world measurement. In addition to the intrinsic carrier transit time limit discussed in the introduction, the common RC limit of the electrical parasitics can also limit the frequency response. This limit can be easily calculated by extracting the series resistance from the forward bias region of the I-V curves as shown in (Figure 57).

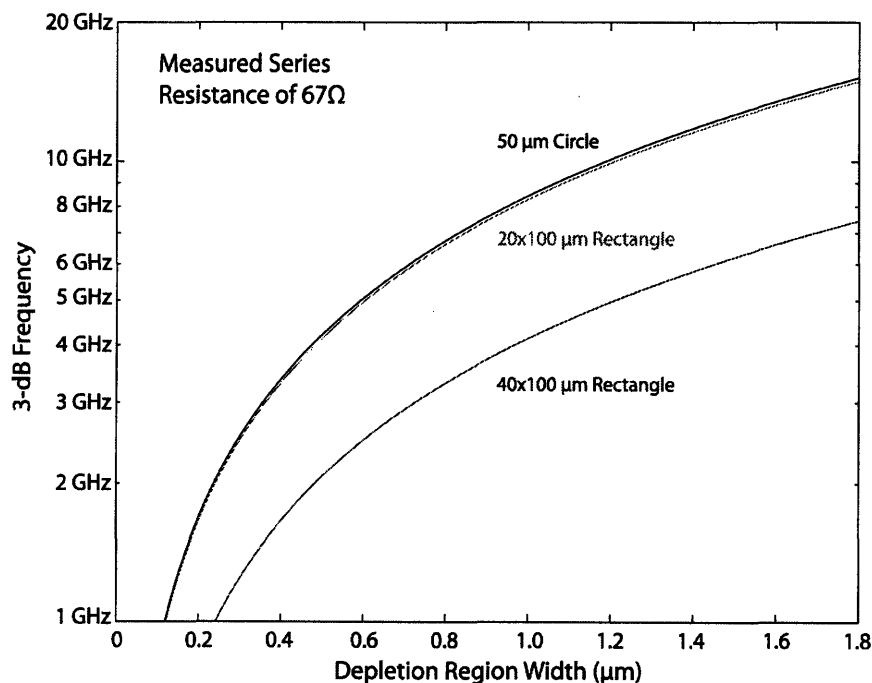


Figure 57. Calculated RC limit to frequency response for various diode sizes as a function of depletion region width.

Since the depletion region width is limited by autodoping of the intrinsic region in the photodiodes under study, the depletion width and therefore the RC frequency response limit is expected to change strongly with reverse bias. It is unclear, however, whether the RC limit will in fact dominate the diode frequency response. The first step to understanding the frequency performance of the diodes is therefore to measure its bias dependence. Although there are a few ways of measuring the frequency response, and an alternative will be discussed later, the small-signal modulation technique is the most straightforward and closely resembles a large number of analog applications.

Measurement

To measure the frequency response, light from an Agilent 1470-1580 nm tunable laser was modulated by a Avanex F-10 lithium niobate Mach-Zehnder modulator. Since the lithium niobate modulator is polarization sensitive, polarization maintaining fiber was used between the output of the laser and the input of the modulator. The measured output polarization extinction ratio of >15 dB over the wavelengths of interest is sufficient to ensure a high maximum modulation depth.

The modulator input was provided by an Anritsu MG3692B 20 GHz signal generator. The modulator's optical input was then sent to the photodiode under test and tapped with a 5/95 splitter to the lightwave front end to an HP 22 GHz microwave spectrum analyzer. The electrical output from the photodiode, directly probed by a Cascade Microtech air-coplanar 40 GHz probe, was passed through a Picosecond Pulse Labs bias tee to the electrical input of the microwave spectrum analyzer. Since the desired measurement bandwidth of 20 GHz is larger than the 8 GHz 3-dB bandwidth of the modulator, the electrical input power had to be modified to maintain a constant modulation depth of 5%. This was achieved by measuring the DC and modulated optical power at the lightwave input of the microwave spectrum analyzer for each frequency point and adjusting the signal generator power until the modulation depth fell in the range of 4.9% to 5.1%. The final optical input power to the device under test is calculated from this optical tap power using the calibration from the responsivity measurements. The electrical output power from the photodiode at the stimulus frequency is

then measured at the electrical input channel of the microwave spectrum analyzer. The electrical output power divided by the optical input is the desired optical-to-electrical S_{21} response. The bias of the photodiode is swept by applying a voltage to the DC port of the bias tee using a semiconductor parameter analyzer to produce the frequency response curves shown in (Figure 58) for a 20x100 micron diode.

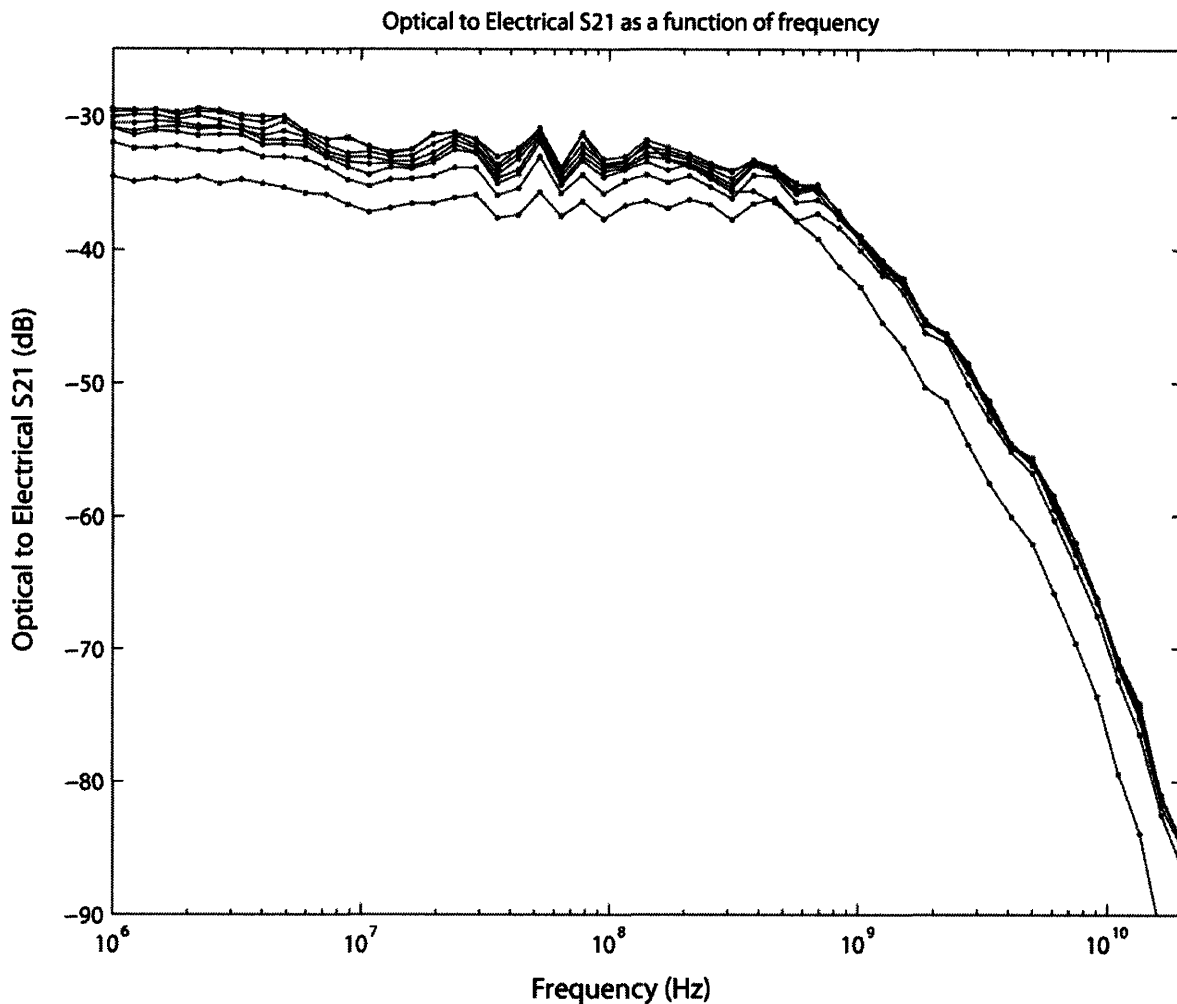


Figure 58. Measured small-signal modulation frequency response in underfill illumination. Bias voltages range from 0 V to 10 V.

These curves show that the frequency response pins with increasing bias beyond 1V. This phenomena is not expected from the RC limit due to the increased depletion region width with reverse bias. The 0V curve shows a 3-dB frequency of approximately 1.5 GHz. This is

approximately the RC-limit for a narrow depletion region, but the pinning at approximately 1.8 GHz is far below the larger depletion region RC-limit of 8-10 GHz. Although the diode behavior is therefore not showing RC-limited behavior in this region, it is not clear what is setting the frequency performance limit. As discussed in Chapter 1, the photodiode performance could be limited by the fundamental p-i-n diode transit time limit or trap degraded performance.

Simulation

As a first attempt to answer this question, the finite element model developed from Chapter 2 is used without explicit trap states to examine the fundamental transit time response of the photodiodes. Again, using a cylindrical coordinate system, a Gaussian optical generation profile corresponding to the 1.2 micron fiber spot size is added to the center of the diode. Although the measured diode was a 20x100 micron rectangle, a 50 micron circular diode was used in simulation to enable the use of cylindrical coordinates. These two diode windows should have approximately the same area and have the same RC-limit as shown in (Figure 57). To provide an accurate RC-limit calculation, the measured 67 Ohm series resistance was added to the contacts of the finite element model. The frequency response simulations were then performed in Sentaurus by adding the keyword Optical to the standard AC analysis feature. This allows a sinusoidal modulation to be applied to the optical generation profile and calculates the corresponding current modulation at the diode contacts. The resulting simulation data shown for the same bias points as measured in (Figure 58) is shown in (Figure 59).

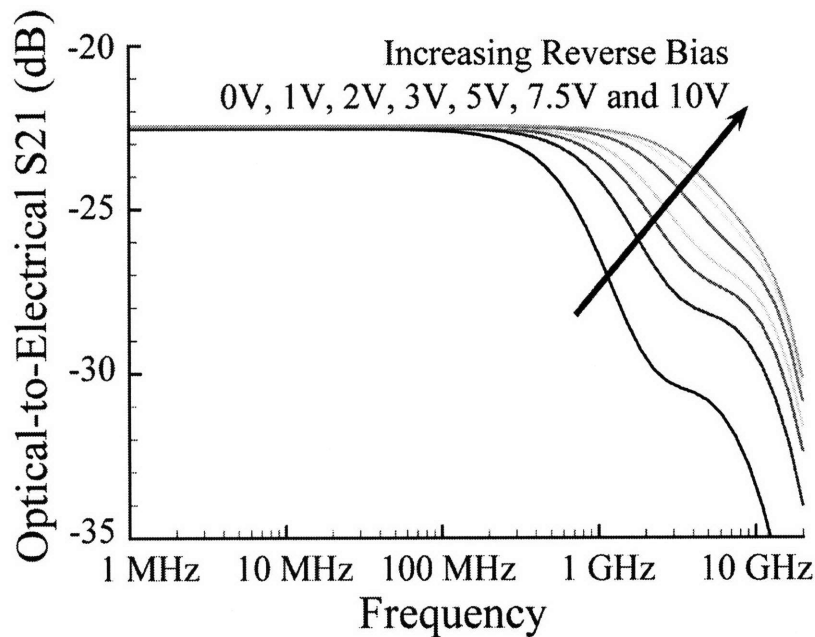


Figure 59. Simulated bias free frequency response at diode center

The frequency response in this simulation shows no pinning behavior and shows a bias dependence similar to the RC-limit. However, the roll off of the frequency response is greater than the 20dB/decade expected from a single pole RC response. This fact suggests that it is both the RC and transit time limit that would contribute to limiting the trap-free photoresponse of these diodes.

Although the measured frequency response matches the initial roll-off of the 0V simulation curve, the high bias measurements do not achieve the bandwidths predicted in simulation. This suggests that a third physical effect, presumably carrier trapping, is limiting the diode frequency response for all but the zero bias point.

Spatially Resolved Frequency Response

Since the dark current and responsivity have shown a spatial dependence due to interface localized flaw states and the frequency response appears to be flaw dominated at high bias, it seems likely that the frequency response will also be spatially dependent. To test this hypothesis, the frequency response was measured as a function of position along a linear translation of the 20x100 micron diode studied in both the spatial responsivity and center

frequency response measurements. Again, the micrometer was stepped in 1.5 micron increments, but instead of measuring the responsivity at each point, the above described small signal frequency response sweep was performed as shown in (Figure 60).

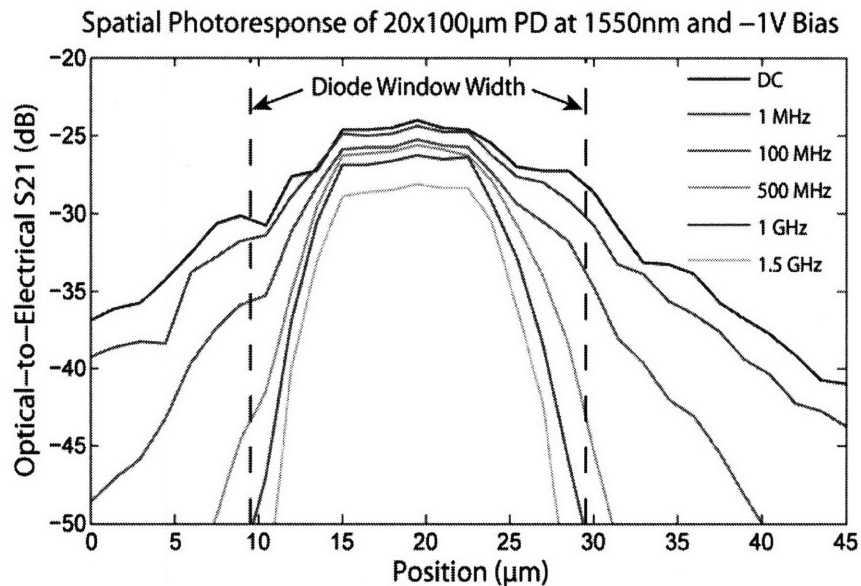


Figure 60. Measured small-signal modulation frequency response as a function of position

The spatial dependence of the frequency response is far more dramatic than the DC photoresponse. At the window edge, the 1.5 GHz photoresponse is down greater than 20 dB from the diode center. This is the first piece of direct experimental evidence that the flaw states limit the frequency response of the Ge-on-Si photodiodes.

Pulse Response

To get greater physical understanding of the high speed behavior of the photodiodes, it is desirable to understand the time domain behavior of the diodes responding to an impulse excitation. If the response is symmetric, i.e. the rising edge is equal to the falling edge, the diode response is presumably limited by the low-pass filtering effect of the RC parasitic. If the response is a single peak but the rising edge is faster than the falling edge, the diode is probably limited by diffusive transport in the quasi-neutral regions. This behavior is caused by

the depletion region drift providing a rapid current rise and the slower diffusive transport adding a current tail to the response that lasts long after the generation impulse. The final option is the presence of secondary pulses characteristic of long time constant traps, filled in the generation event, discharging after the pulse.

Measurement

To perform this measurement, a 150 fs modelocked 1550 nm erbium-doped fiber laser (courtesy Jeff Chen, MIT) was used as the optical impulse source. Due to dispersion in the fiber setup leading to the photodiode, the estimated pulse width of the incident pulse is estimated to be 4 ps. The time domain electrical response of the photodiode is measured on a HP digital sampling oscilloscope with a 12.5 GHz bandwidth. Since the optical pulse train is not synchronized to any reference frequency source, the measurement was triggered by tapping the optical signal with a 5/95 splitter and sending it to a 12.5 Gb/s Ortel digital receiver hooked up to the oscilloscope sample trigger port. The measurement setup was first verified by disconnecting the laser output from the device under test and putting it directly into the optical port of the oscilloscope. The measured 3-dB bandwidth of 12 GHz corresponds well with the stated front end bandwidth of 12.5 GHz. The laser output was then directed to the photodiode and the impulse response was measured at various bias points as shown in (Figure 61).

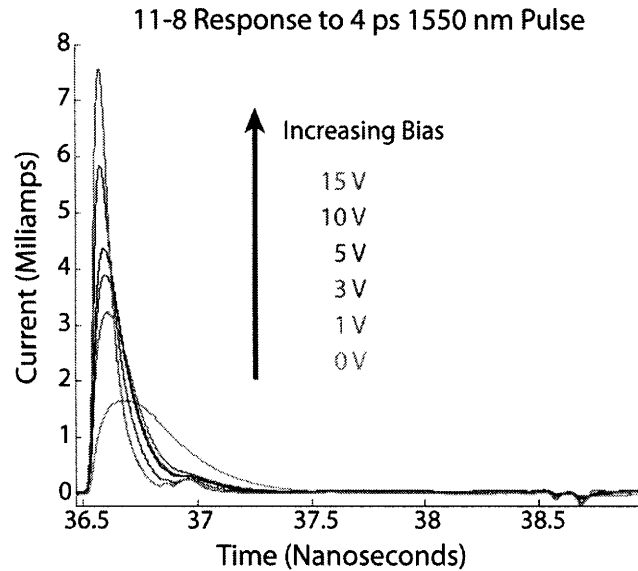


Figure 61. Time domain pulse response measurements.

At low bias, the response is asymmetric as predicted for the case where diffusive transport limits the tail of the photoresponse. At high bias, the increased depletion of the germanium film allows more of the photoresponse to be dominated by the faster drift transport and the main pulse response looks narrow and increasingly symmetric. However, even at high bias, there is an afterpulse 500 ps behind the primary response that corresponds to the theorized trap states. Since the relative magnitude of the primary response is substantially larger than the trap response, the frequency response is expected to increase as is evident when the FFT of the time domain response is taken as shown in (Figure 62).

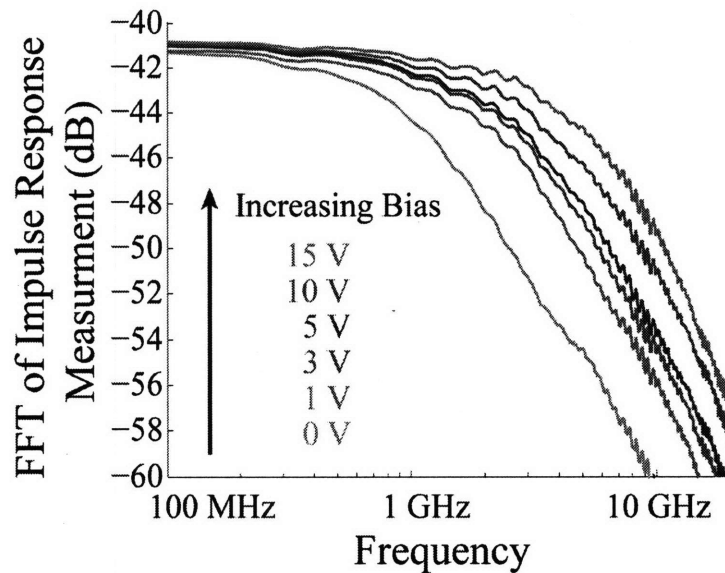


Figure 62. Fast Fourier Transform of pulse response data plotted in the frequency domain.

As opposed to the small signal modulation measurement, this frequency response is seen to increase with increasing bias. This can be explained by the high magnitude of the pulsed excitation greatly exceeding the number of active traps. The small signal response, on the other hand, is of a much smaller magnitude and is dominated by the trap response. Additionally, the observed 500 ps delay of secondary peak, corresponds closely with the observed small signal limit of 1.8 GHz. Further experiments to saturate the traps with another high intensity DC optical signal in the small signal measurements could possibly show the transition from a trap limited to transit time limited transport regime.

Although there are still traps present in these pulse response measurements, the saturation of these states allows the frequency response to closely resemble the simulated trap free device response. The similarity between these two results demonstrates that the various transport parameters used in the device simulation are close enough to approximately match device function.

Simulation

The intrinsic diode pulse response can be simulated using the finite element model previously developed. Each bias point was simulated separately to reflect the bulk and

surface lifetimes fit in Chapter 2. The desired bias point was reached using a quasistationary analysis. Next, 1 μ s setup transient analysis is performed to ensure steady state conditions. The optical pulse response is then simulated using a Gaussian pulse of approximately 4 ps with a peak power of 100 mW to match the experimental conditions. The resulting transient responses are then plotted in (Figure 63).

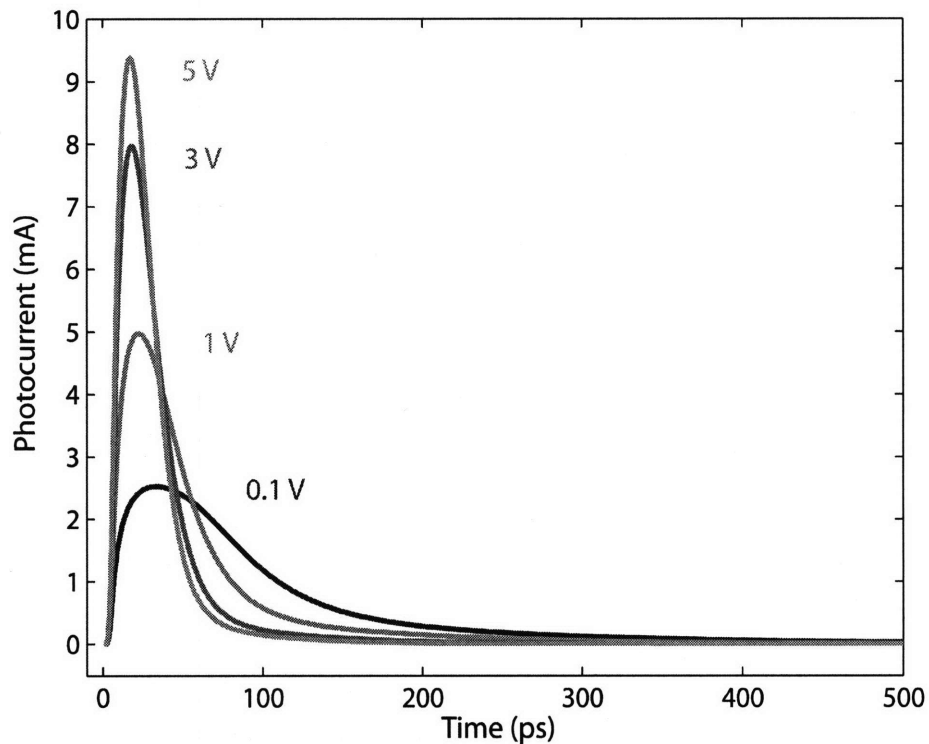


Figure 63. Simulated optical pulse response at four bias points.

To enable frequency domain analysis, the time domain data was then fit to a spline interpolating function and resampled at a timestep of 1 ps. The Fourier transform of the resulting dataset is shown in (Figure 64).

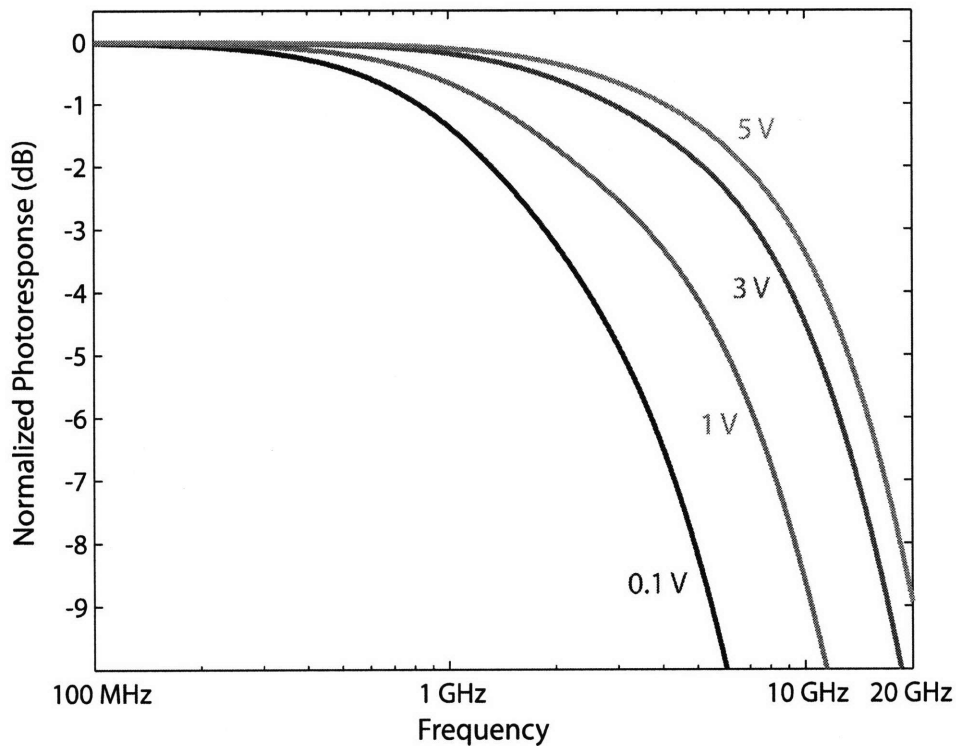


Figure 64. Fast Fourier Transform of simulated pulse responses. Simulation data was interpolated to provide uniform sample time spacing prior to transform.

Changes to the DC Model for Improved Frequency Response Matching

The trap states that affect the unsaturated frequency response of the photodiode must result from different flaw states than were found to match the DC I-V curves. This can be understood in terms of the demarcation levels introduced in the introduction. If a flaw energy level is too deep in the energy gap, captured carriers are likely to be emitted to the other energy band resulting in a recombination event as opposed to being reemitted to its original band to act as a trap.

The dislocation states also contain shallow traps that can act as efficient trap states as discussed in the flaw model section of Chapter 2. Due to the dark current dominance on deep traps, the trap densities cannot be fit from the I-V curves like the deep traps. The actual fitting of these trap states and discussion of their physical causes will be beyond the scope of this thesis, but could be matched by developing simulations to reproduce the pulse response measurements and fitting the secondary pulses to discrete trap models.

Chapter 4 – Application Specific Performance Characterization

Although there are a myriad of applications for a device as fundamental as a photodiode in a platform as universal as silicon processing, the optimizations of the devices under study are focused for an optical sampling system in advanced analog-to-digital converters. The requirements of a sampling system include non-traditional metrics such as a linearity and noise as well as traditional metrics such as bandwidth and linearity. One easier aspect of the sampling system is that the individual channel sampling rates are generally much less than traditional data rates for optical communications. This could relax the bandwidth specification, for which the measurements of Chapter 3 show poor current performance.

EPIC Optical Sampling Front End Analog to Digital Converter

The basic premise of the giga-Hertz optical sampling technology (GHOST) assisted analog-to-digital converter is to reduce the sampling jitter by using an optical front end based upon a low jitter modelocked laser [83-85]. The basic system is shown in (Figure 65) and requires the on chip integration of a modulator, waveguides, filters and detectors. The net sampling rate of this system is projected to be up to 40 gigasamples per second with an effective number of bits (ENOB) of 10. This is accomplished by interleaving 20 sampling channels by use of the filter bank to ensure that the conventional electronic analog to digital converters run at an achievable 2 Gs/s line rate. The photodiode requirements are then reduced to the accurate reproduction of a 2 GHz repetition rate pulse train.

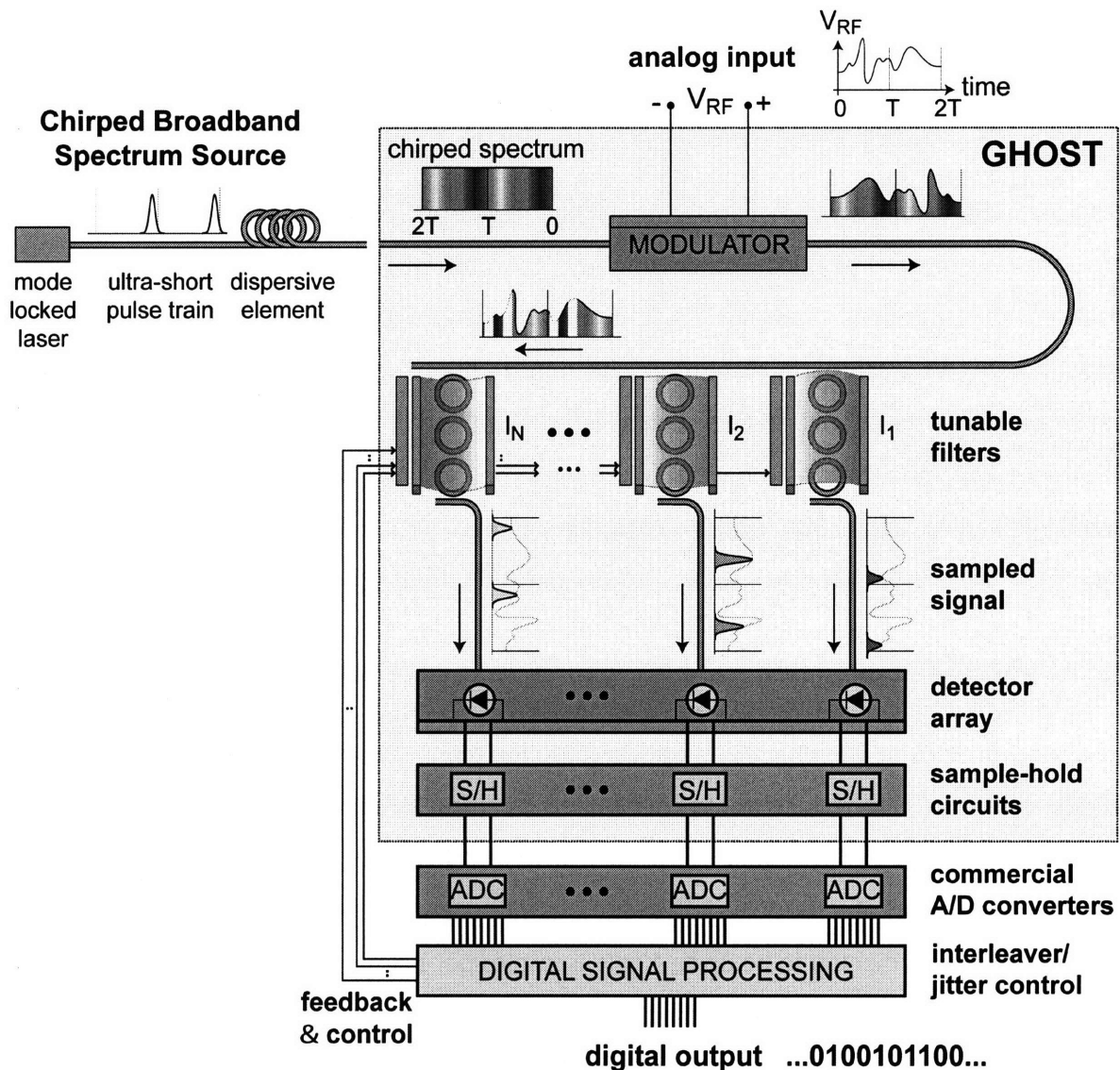


Figure 65. GHOST system cartoon. Germanium-on-silicon photodiodes would be used as the on-chip detector array. Figure courtesy Milos Popovic.

Without full justification, the system specifications imply the following required detector characteristics: linear dynamic range sufficient for 10 ENOB, 2 GHz bandwidth, 0.3 A/W responsivity.

Linearity Performance

A linear dynamic range specification of a photodiode needs to be measured in a combination of tests to quantify the magnitude of spurious harmonic tones and the noise spectral power.

The combination of these two measurements can be expressed in terms of a spurious free dynamic range (SFDR). This quantity can be defined by finding the point where the harmonic powers equal the noise power of the bandwidth of interest. The ratio between this power and the corresponding linear tone power is defined as the SFDR.

Additionally, since all systems of interest have a finite bandwidth and are not single tone modulated, the harmonic terms of greatest importance are not those that are strict harmonics of input tones that will usually fall outside of the system bandwidth, but instead are the mixing terms that are a combination of the addition and subtraction of input tones to fall very close to the input tone frequency and therefore within the system bandwidth. The lowest order of these terms is the third order intermodulation term (IMD3) that consists of one input tone being subtracted from the second harmonic tone of another input tone. The simplest method of measuring this quantity is a two tone test where two input tones, f_1 and f_2 , are used as inputs of the system. The IMD3 terms are then formed at $f_2 + \Delta f$ and $f_1 - \Delta f$ where $\Delta f = f_2 - f_1$.

The SFDR of the Ge-on-Si photodiodes was characterized using this type of two tone test. The fundamental challenge of the linearity measurements is that the input source must be more linear than the device under test. For the testing of a photodiode, this fact causes difficulty since lasers are in most cases far less linear than photodiodes. The most linear source available at the time of measurement was a Fujitsu 1310 nm DFB laser designed for the distribution of CATV signals. The CATV application requires linear performance to prevent the distortion of the analog signals and the intermixing of the numerous channels transmitted simultaneously. By biasing the laser far above the threshold current and using a modest 50% modulation depth, the linearity of the laser was believed to be sufficient to produce a photodiode limited measurement.

The electrical input to the laser was produced using two HP 83620A microwave synthesizers, one operating at 499 MHz and one operating at 501 MHz. This operating frequency was chosen based upon the CATV bands that the laser was designed to operate over. The

synthesizers were then passed through high dynamic range isolation amplifiers from Mini-Circuits, Inc. to reduce feedback of the other tone into each synthesizer. The two tones were combined in a Butterworth isolating power divider and attenuated using two HP 33320 variable power dividers. These attenuators were then used to step the electrical input power to the laser to vary the signal power input to the photodiode under test. The optical signal was then split in a 5/95 coupler with the tap port going to the optical input of a HP 71209A microwave spectrum analyzer and the main port going to the photodiode using the previously characterized pigtailed focuser. The electrical output of the photodiode was then passed through a microwave switch system that could add a low noise amplifier to the loop and input to the electrical port of the microwave spectrum analyzer.

The linearity measurement was then performed by the following algorithm. For each input power to the laser, the optical input to the microwave spectrum analyzer is used to measure the DC optical power and the optical power of the two fundamental tones. The electrical input to the microwave spectrum analyzer is then used to measure the received electrical power of the two fundamental tones. The powers of the two mixing terms are then measured. The resulting measurements are fit to straight lines and averaged between the two tones. The data for the Ge-on-Si diodes at -1V and -3V bias are shown in (Figure 66).

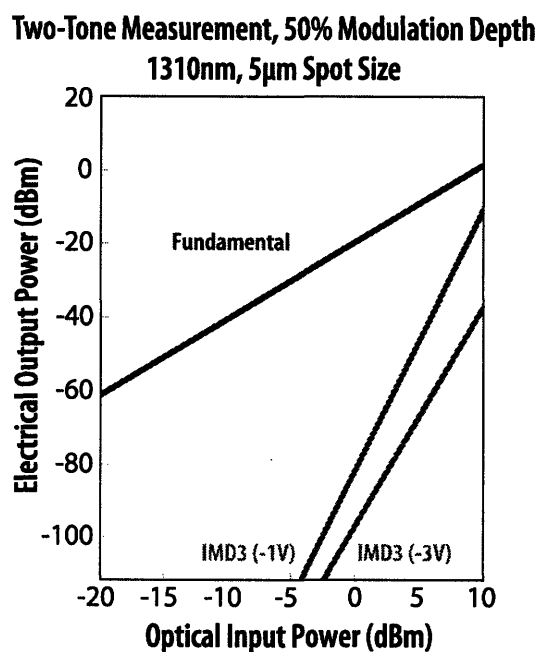


Figure 66. Fit experimental results from two-tone linearity measurements.

One interesting point of note is that the slopes of the mixing terms are different for the two bias points in this plot. It is expected that the slope of this line on a log-log plot would be six since the fact that this is a third order process and the conversion between optical and electrical power adds another factor of two. This factor of two results from the photodiode converting optical power to electrical current which must be squared to get electrical power. The measured slopes are 6.2 for the -3V line and 8 for the -1V line. This implies that higher order processes are important to the linearity of the photodiode, especially at low bias. Further study of these effects would be interesting, but are beyond the scope of this thesis.

The final point of note is the 5 μ m spot size used in these measurements. The photodiode under test is a 100x100 μ m square. Therefore for these measurements, a far larger spot size could be used for illumination. For the same incident power, the intensity incident on the photodiode would therefore be greatly reduced. Since in almost all cases the nonlinearity scales with intensity, the harmonic power could be reduced proportionally to the square of the spot size. This could lead to greatly improved linear performance over the data presented here.

Noise Floor

The noise floor is the next piece of required information to determine the linear dynamic range achievable with the photodiode. For this measurement, the MITEQ low noise amplifier is added to the electrical pathway and the laser modulation was shut off. Since the noise figure of the amplifier is only factory characterized between 1 and 8 GHz, the noise transfer function was characterized end to end using an Agilent 346C that has a stable characterized excess noise figure between 10 MHz and 26.5 GHz with a maximum uncertainty of 0.2 dB. This calibration was used to correct the measured noise powers from 10 MHz to 500 MHz. The noise power was not measured above 500 MHz to ensure that no noise filtering occurred as a result of limited device bandwidth. Instead, the 500 MHz data was extended to higher frequencies. The 1 Hz BW noise power was measured to be -153.5 dBm at 10MHz and -159.4 dBm at 500 MHz. For reference, the 1 Hz shot noise power for the DC photocurrent in these measurements was -162.3 dBm. This means that there is an excess noise in the photodiode of 8.8 dB. Integrating the measured noise for a 2 GHz system, a noise floor of -59.4 dBm for the sampling system is calculated.

Spurious Free Dynamic Range

Combining the noise floor with the linearity measurements, the dynamic range in which there is no interference from noise or harmonic tones is calculated for each optical input power. The optical input power level where the electrical output noise power is equal to the harmonic tone power maximizes this dynamic range and defines the spurious free dynamic range (SFDR) as shown in (Figure 67).

**Two-Tone Measurement, 50% Modulation Depth
1310nm, 5µm Spot Size**

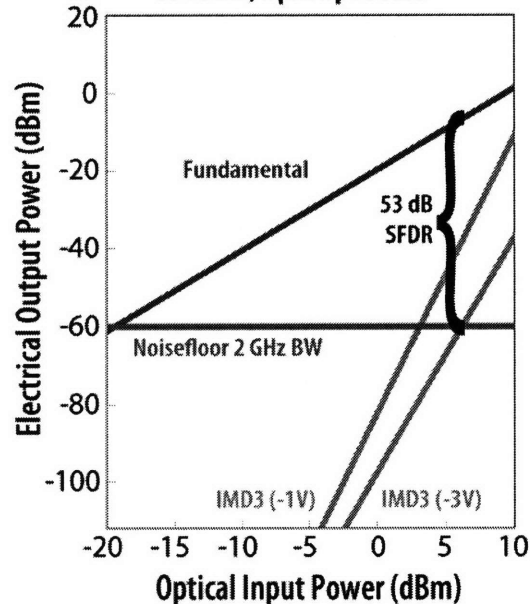


Figure 67. Fit experimental results from two-tone spurious free dynamic range measurements.

For the sampling system, the relevant quantity of interest is the effective number of bits enabled by this 52.9 dB SFDR. The translation between these two quantities is governed by the following formula [Analog Devices Ref.]:

$$ENOB = \frac{dB_{SFDR} - 1.76}{6.02} \quad (4.1)$$

Using this formula, the calculated ENOB for this measurement is 8.5 bits. Although this is smaller than desired for the 10 ENOB system goals, defocusing the optical spot to reduce the local intensity would increase linearity. No attempt to achieve this goal was attempted in measurement since the system goal at the time of measurement was only 8 ENOB.

Sampling System Bandwidth Requirements

Although the sample rate of 2 GHz seems to imply a natural 2 GHz bandwidth for the photodiode, it is interesting to consider this specification in more detail. Instead of having a sinusoidal modulation where a relevant performance metric is when the received power is half, the traditional bandwidth specification, the sampler photodiodes must respond to a

sequence of pulses. Additionally, the intersample interference (ISI), which is the charge from one pulse that extends into the timeslot of adjacent samples, must be less than the dynamic range of the sampling system. As a ceiling for ISI, we will choose half the value of the least significant bit (LSB) of the system.

Modeling the current pulse out of the photodiode as a Gaussian normalized to one, we can write the normalized current pulse, $i(t)$, occurring in the center of the sampling window between $t = 0$ and $t = T_{sample}$ in terms of a standard deviation σ_{pulse} :

$$i(t) = \frac{1}{\sigma_{pulse} \sqrt{2\pi}} \exp\left(\frac{-\left(t - \frac{T_{sample}}{2}\right)^2}{2\sigma_{pulse}^2}\right) \quad (4.2)$$

The ISI charge can be found by integrating the normalized current out side of the sample window. This is compared to the set limit of half an LSB to find the maximum pulse standard deviation:

$$2 \int_{T_{sample}}^{\infty} \frac{1}{\sigma_{pulse}^{\max} \sqrt{2\pi}} \exp\left(\frac{-\left(t - \frac{T_{sample}}{2}\right)^2}{2\sigma_{pulse}^{\max 2}}\right) dt = \frac{2^{-bitdepth}}{2} \quad (4.3)$$

This expression can be written in terms of the complementary error function to simplify numerical analysis:

$$erfc\left(\frac{T_{sample}}{2\sqrt{2}\sigma_{pulse}^{\max}}\right) = \frac{2^{-bitdepth}}{2} \quad (4.4)$$

Solving this expression numerically, the maximum pulse standard deviation to meet the ISI requirements can be found. The corresponding maximum pulse is shown in the time domain for a 1 Gs/s system is shown in (Figure 68).

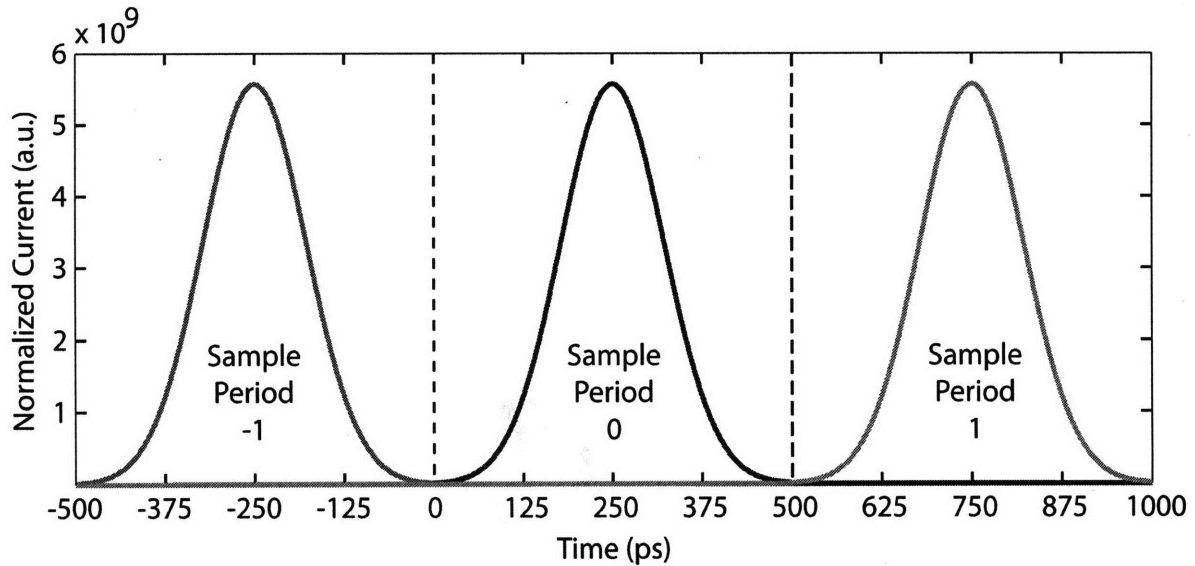


Figure 68.2 Gs/s Gaussian pulse train matching the maximum ISI specification for a 10 bit sampler system

The frequency response required to generate these pulses can be found by taking the Fourier transform of the normalized current response of Equation (4.2):

$$F \left\{ \frac{1}{\sigma_{pulse}^{max} \sqrt{2\pi}} \exp \left(-\frac{\left(t - \frac{T_{sample}}{2} \right)^2}{2\sigma_{pulse}^{max}} \right) \right\} = \exp \left(-2\pi^2 \sigma_{pulse}^{max 2} f^2 \right) \quad (4.5)$$

The traditional 3-dB bandwidth specification of this frequency response can be found by multiplying by 2 to convert from a current response to a power response and setting it equal to one half:

$$\frac{1}{2} = 2 \exp \left(-2\pi^2 \sigma_{pulse}^{max 2} f_{3dB}^2 \right) \quad (4.6)$$

Using the maximum pulse standard deviations calculated above, the minimum photodiode bandwidth can be plotted as a function of sample rate as shown in (Figure 69).

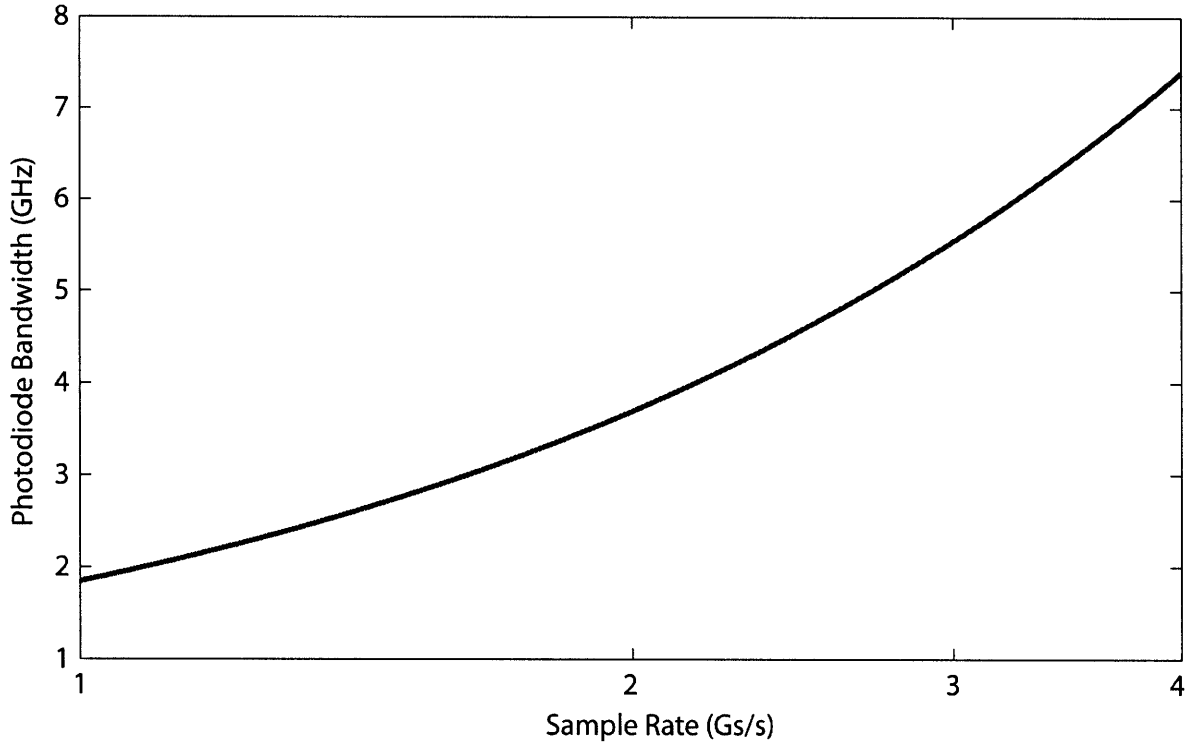


Figure 69. Minimum photodiode bandwidth as a function of sampler frequency to match 10 bit ISI specification

The resulting 2 Gs/s sampler photodiode bandwidth specification is 3.7 GHz. This is significantly larger than the approximate 2 GHz initial guess. The 3.7 GHz specification must be viewed as a rough guide as it is derived from a Gaussian pulse shape, but it can serve as a reasonable minimum since the Gaussian pulse is transform limited. The measured pulse response must be examined for potential photodiodes by similar out of sample window integration techniques to ensure the ISI specification will be met.

Impact of Trap States on Inter Sample Interference

In addition to the intrinsic diode response, the traps have a finite lifetime and results in current being generated after the main optical pulse as shown in the pulse response measurements of Chapter 3. The magnitude of this excess trap current can be calculated by more careful analysis of the impulse response tail at high bias. First, the diffusive tail is fit to an exponential while the photoresponse magnitude is still large as shown in (Figure 70) on a time axis where the zero point corresponds to the start of the photoresponse.

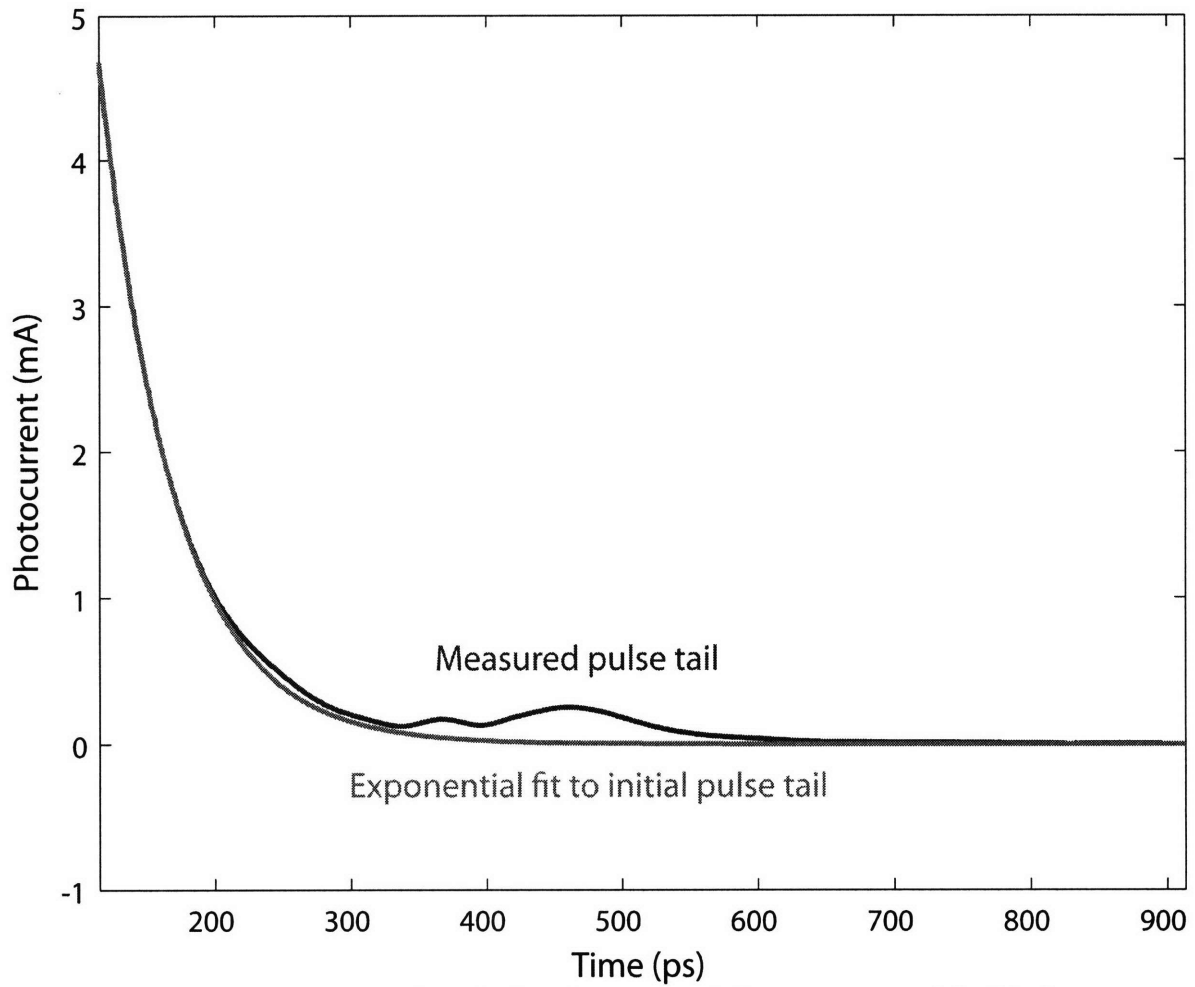


Figure 70. The tail of the measured photodiode pulse response is fit to an exponential tail in the upper decay region and compared to this fit in the excess current region.

The excess current can then be calculated by subtracting the exponential fit from the measured pulse as shown in (Figure 71).

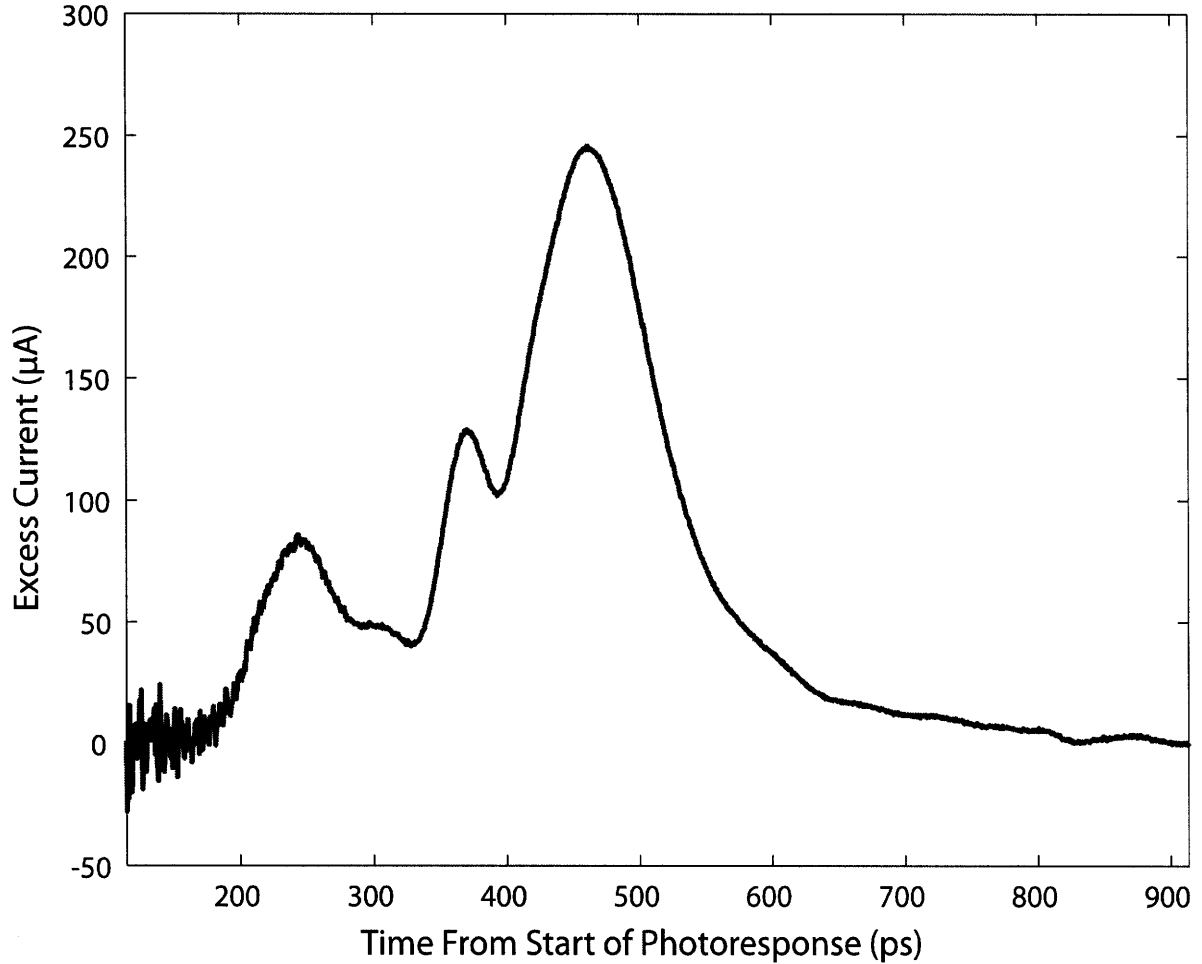


Figure 71. The difference between the exponential fit and the measured pulse response is plotted as a function of time.

The relevant metric for the sampling system is then intersample interference due to trap discharge which can be defined by the integration of current that occurs outside the sample window. This calculated charge is plotted as a function of the sample rate as shown in (Figure 72).

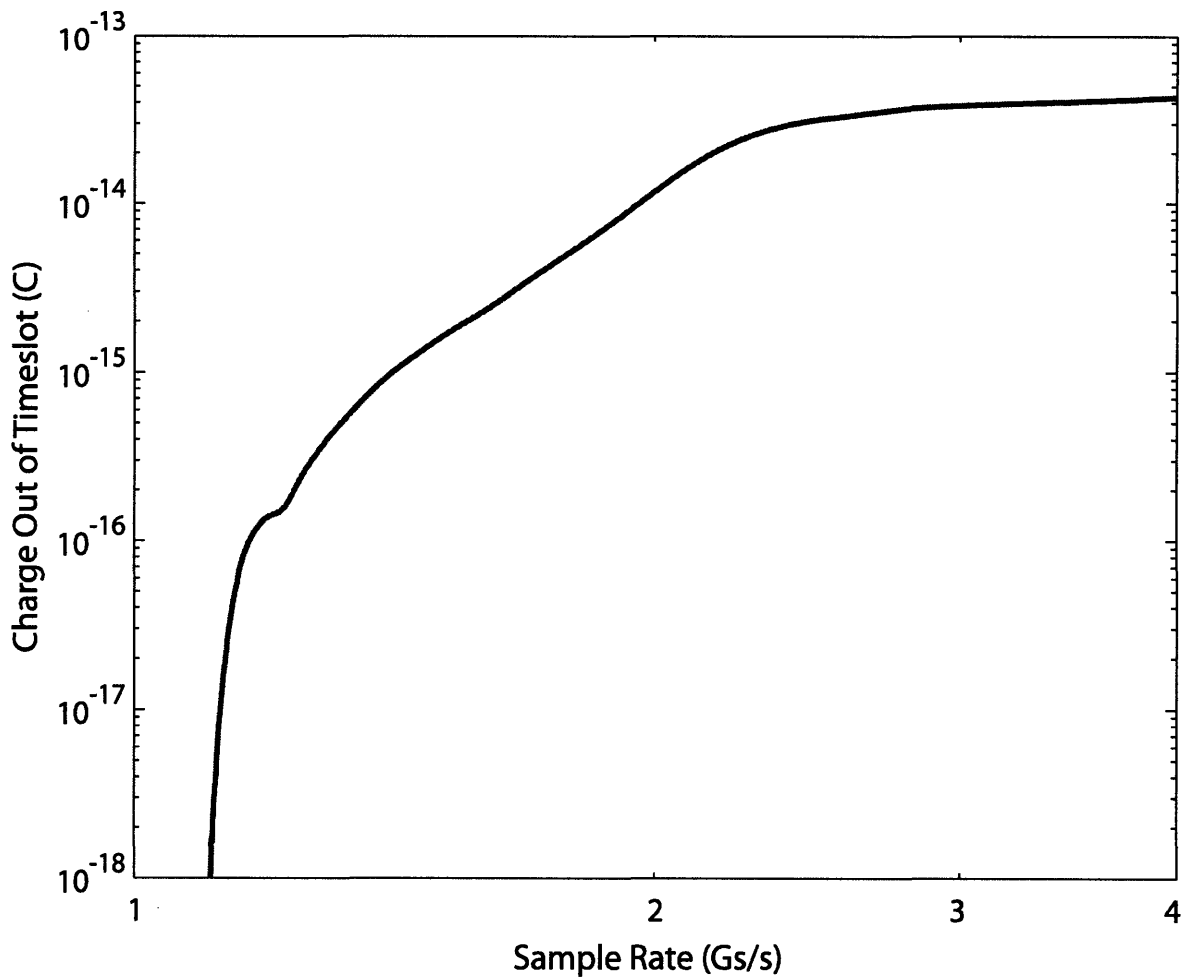


Figure 72. The excess current after the timeslot corresponding to sample rates between 1 and 4 Gs/s is integrated to calculate the corresponding quantity of charge out of timeslot.

This charge can then be further related to characteristics of the sampling system by comparing the trap charge with the charge expected from the sample pulse. The sample pulse energy is calculated by dividing the average incident optical power system specification, which is limited by waveguide nonlinearity, by the sample rate. Since in the saturation assumption the quantity of generated carriers is sufficient to fully occupy all available trap states, this excess trap charge out of timeslot will not change. Therefore, the ratio between the out of sample slot trap charge and the total pulse charge, the ISI dynamic range, can be quantified for various average optical powers. This calculation, expressed in terms of multiples of the LSB for a 10 bit sampler, is shown in (Figure 73).

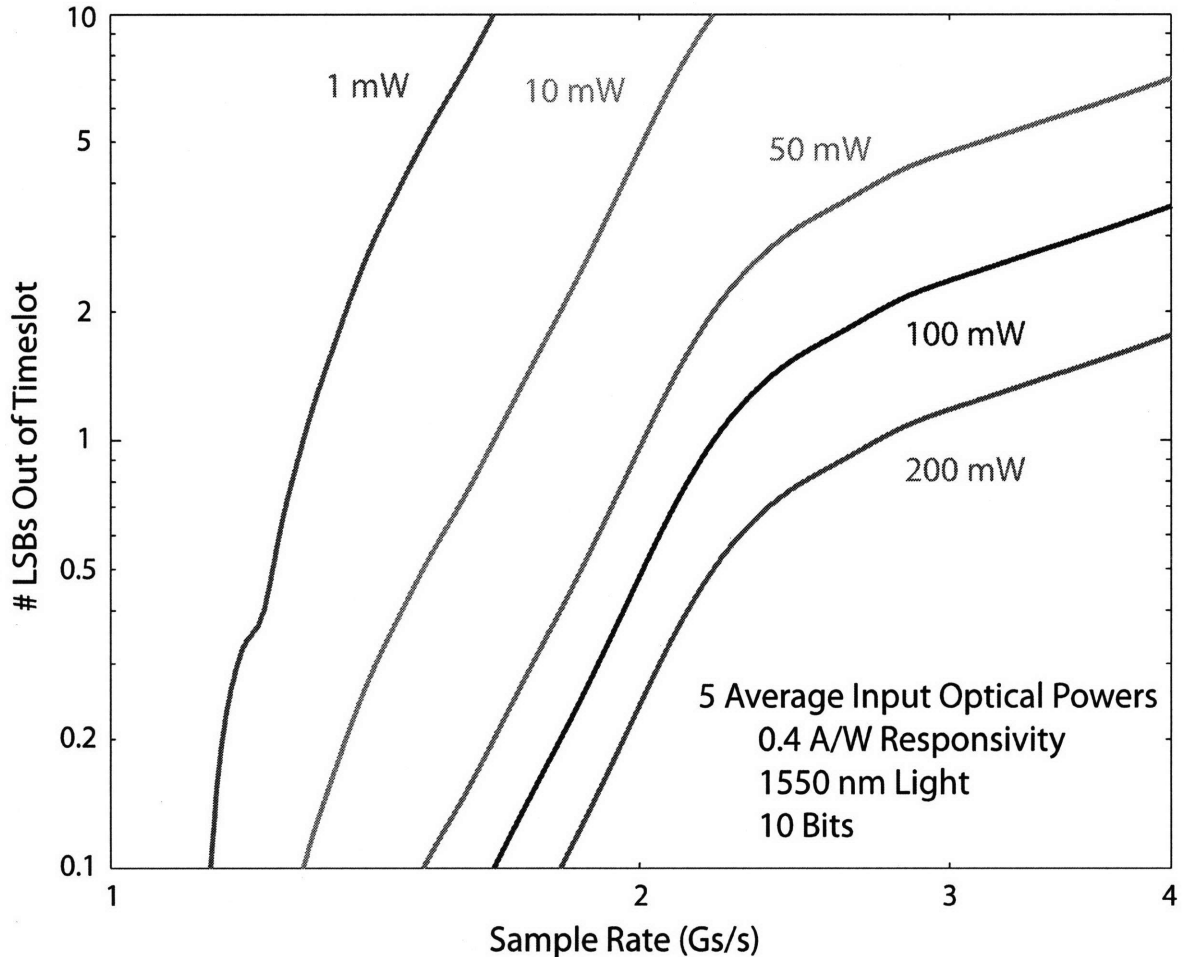


Figure 73. The pulse response trap excess charge is calculated in units of multiples of the LSB corresponding to various peak input powers.

For a 100 mW optical power, the approximate nonlinearity threshold for the modulator, the ISI magnitude due to excess trap current is approximately half a LSB at 2 Gs/s. This is the approximate limit at which ADC non-idealities become unacceptable. Therefore, although there is little margin for error, the existing photodiode trap densities could satisfy the sampler photodiode performance requirements.

Chapter 5 – Conclusion and Future Work

The work over the previous three chapters has focused on gaining a greater understanding of the current state of germanium-on-silicon photodiodes. It is now desired to briefly review this analysis in broader contexts and suggest pathways for future device improvement. This thesis will then conclude with propositions for future work in experiment, simulation, theory and fabrication.

Dark Current Reduction

The dark current was studied thoroughly in Chapter 2 to understand the R-G centers resulting from the threading dislocation flaw states. It has been previously noted that the dark current in the bulk is directly proportional to the threading dislocation density. This problem can only be addressed by a reduction of the threading dislocation density by modification of the germanium growth. However, the dark current for the diodes under study in this thesis are limited by perimeter states that are hypothesized to result from the interaction of the oxygen donors with the threading dislocations. These states will therefore be reduced by a reduction of the threading dislocation density as well.

Larger potential gains, however, could be achieved by improvements in the device processing. Most obvious and easiest to fix is the flawed region depletion at the diode perimeter. Depleting this high generation region causes the generation to contribute to current at the device contacts. Reducing the depleted volume of the flawed germanium would yield a proportional reduction in dark current. The depletion is due to the thin separating oxide between the germanium and the poly contact and is exacerbated by the large overhang area. Reducing the overlap area, which is currently far in excess of the mask alignment tolerance, and using a thicker oxide layer up to the limits of the polysilicon step coverage would serve to reduce the magnitude of this problem. If these measures are not

enough, the germanium at the device perimeter could be intentionally doped p+ to prohibit depletion of this region.

An ideal solution to the perimeter leakage would be to change the surface passivation to prevent the introduction of the oxygen atoms that form the A-centers. This is a hard technological problem but work with Hafnium based dielectrics have shown significant progress [86-90]. This will be especially important to enable small device geometries where the surface to volume ratio is far larger and surface effects are therefore far more important.

Bandwidth-Efficiency Product Analysis

As discussed in the general photodiode design introduction, vertically-illuminated device performance in responsivity and bandwidth are coupled in a trade off based on device thickness. If the photodiode absorbing layer is made thicker, the responsivity goes up as a result of more light being absorbed. If it is made thinner, the bandwidth will increase due to a reduction in the carrier transit time. By sweeping the absorbing layer thickness, the ideal device performance can be optimized from high bandwidth to high responsivity. Therefore, for any material system, the ideal device performance limit can be defined in the responsivity-bandwidth plane as the bandwidth-efficiency product based upon the absorption coefficient and the mobility. This limit is plotted in (Figure 74) along with the reported germanium-on-silicon device performance shown as red crosses and the current work shown as a blue circle.

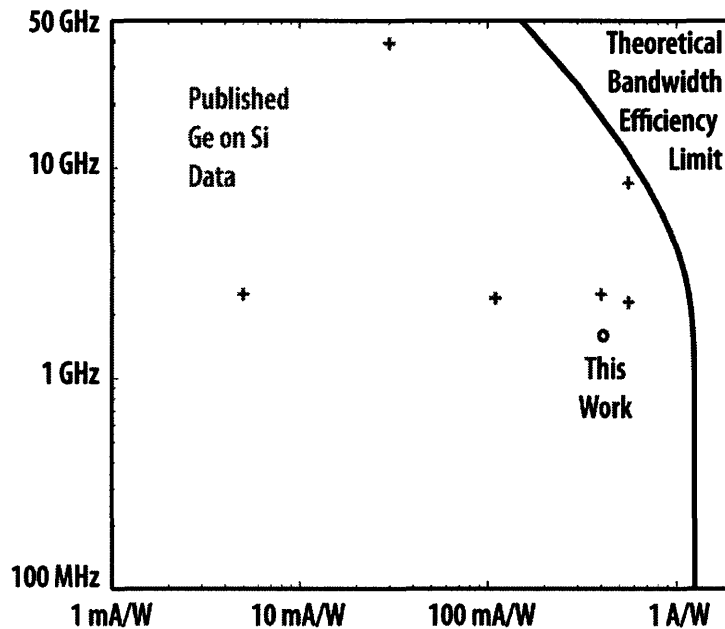


Figure 74. Data for germanium photodiode results plotted relative to bandwidth–efficiency limit.

The current work is clearly very far from the ideal performance limits. In fact, very few literature reported points are close to the limit, with the additional caveat that the top right data point responsivity value was measured using the setup that produced erroneous results for the diodes reported here. These discrepancies can be attributed to the many non-idealities reported in this thesis, most of which result from flaw states acting as both traps and R-G centers. Since greater understanding of these states and their impact on device performance has come from this work, it is now possible to comment on potential methods for device improvement.

Potential Responsivity Improvements

Although the measured responsivity is sufficient for the system specification of the sampler system, increased responsivity would lower input power requirements and is generally desirable for all applications. Two methods are proposed to increase this important figure of merit.

Addition of an Anti-Reflective Coating

One easy fix for responsivity improvement has nothing to do with the flaws in the germanium. As discussed in Chapter 3, one of the largest efficiency losses in the photodiodes under study is the reflection from the index step to the germanium layer. However, a single layer antireflective coating using SiON could be added to reduce the reflection to $< 0.2\%$ over an 80 nm bandwidth from 1506 nm to 1586 nm as shown in (Figure 75). This would lead to an increased responsivity.

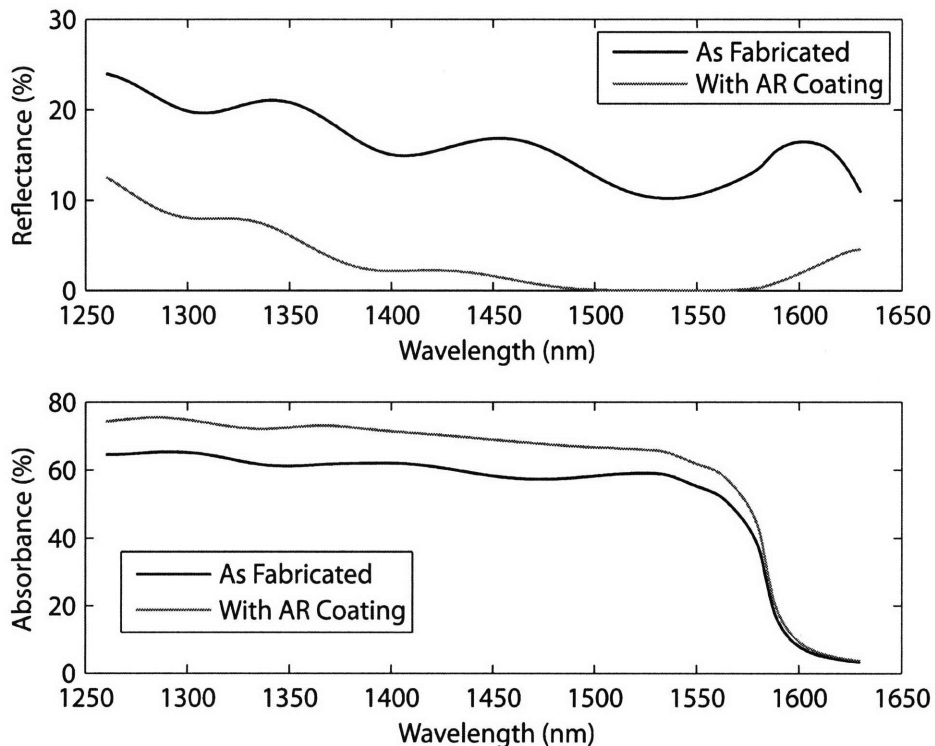


Figure 75. Reflectance and absorbance improvement with a single layer 197 nm SiN antireflection coating.

As can be seen from (Figure 76), the AR coating is robust to thickness variations. An improvement of this magnitude for this little effort would obviously be included in any final device, and its omission in this work is only due to the preliminary nature of these test devices as a technology analysis platform.

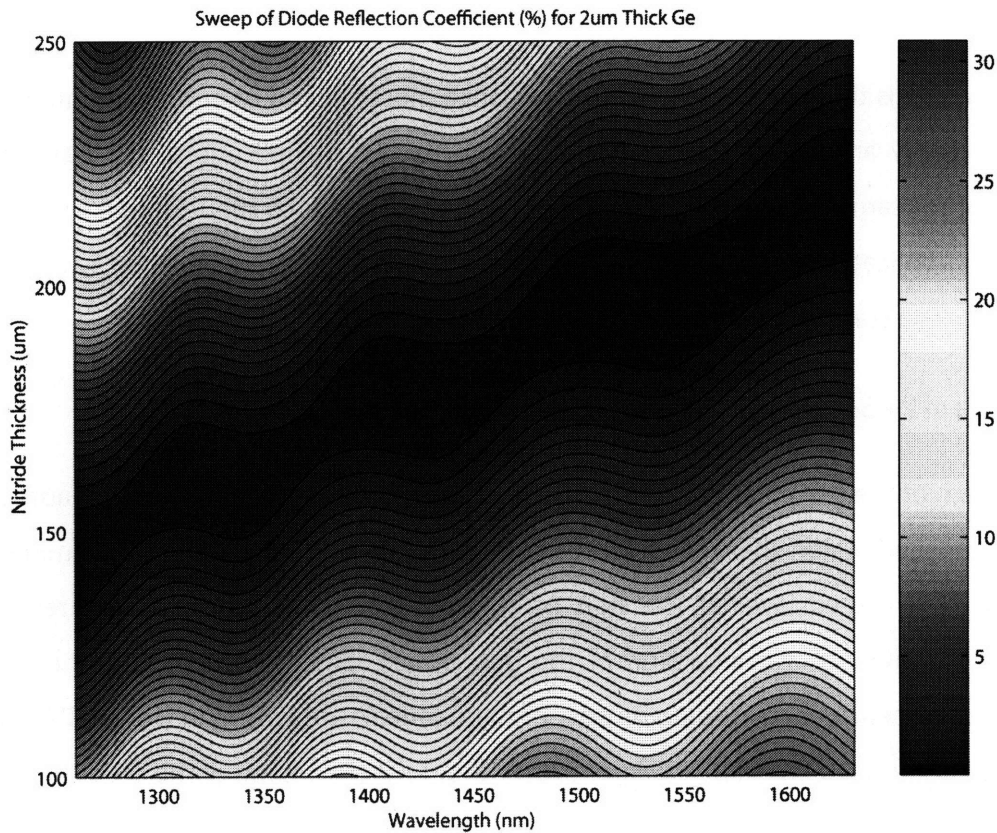


Figure 76. Reflection for calculated nitride AR coating thicknesses

Reduction of the Threading Dislocation Density

Since the internal quantum efficiency is limited by the threading dislocation dominated carrier lifetime, the IQE and therefore the responsivity can be improved by the reduction of threading dislocation density.

Improved Surface Passivation

Since the responsivity is seen to decrease within 5 μm of the device edge, the internal quantum efficiency in these areas is being reduced by the presence of passivation related R-G centers. The reduction of these states will be even more important to smaller sized devices where the entire active area is within 5 μm of the device edge.

Potential Bandwidth Improvements

The bandwidth is the aspect of device performance most in need of improvement. Although the responsivity and dark current are acceptable for most applications, the bandwidth is insufficient for sampler application. Additionally, 10 Gb/s data communication on chip is an important application area for silicon photonics that requires at least a 5 GHz device bandwidth. The current 1.8 GHz performance is very far from this goal.

Elimination of P+ Seed Layer

The problem of the germanium film not being intrinsic due to p-type autodoping and the implications on the frequency response were explored in Chapter 3. Eliminating or reducing the p+ seed layer at the start of epitaxial growth could potentially reduce this problem and allow a larger fraction of the germanium film to deplete at low bias. Initial growth studies without n+ doping or post-growth anneals are shown in (Figure 77) with the p+ doping of the seed layer and in (Figure 78) without the p+ doping of the seed layer.

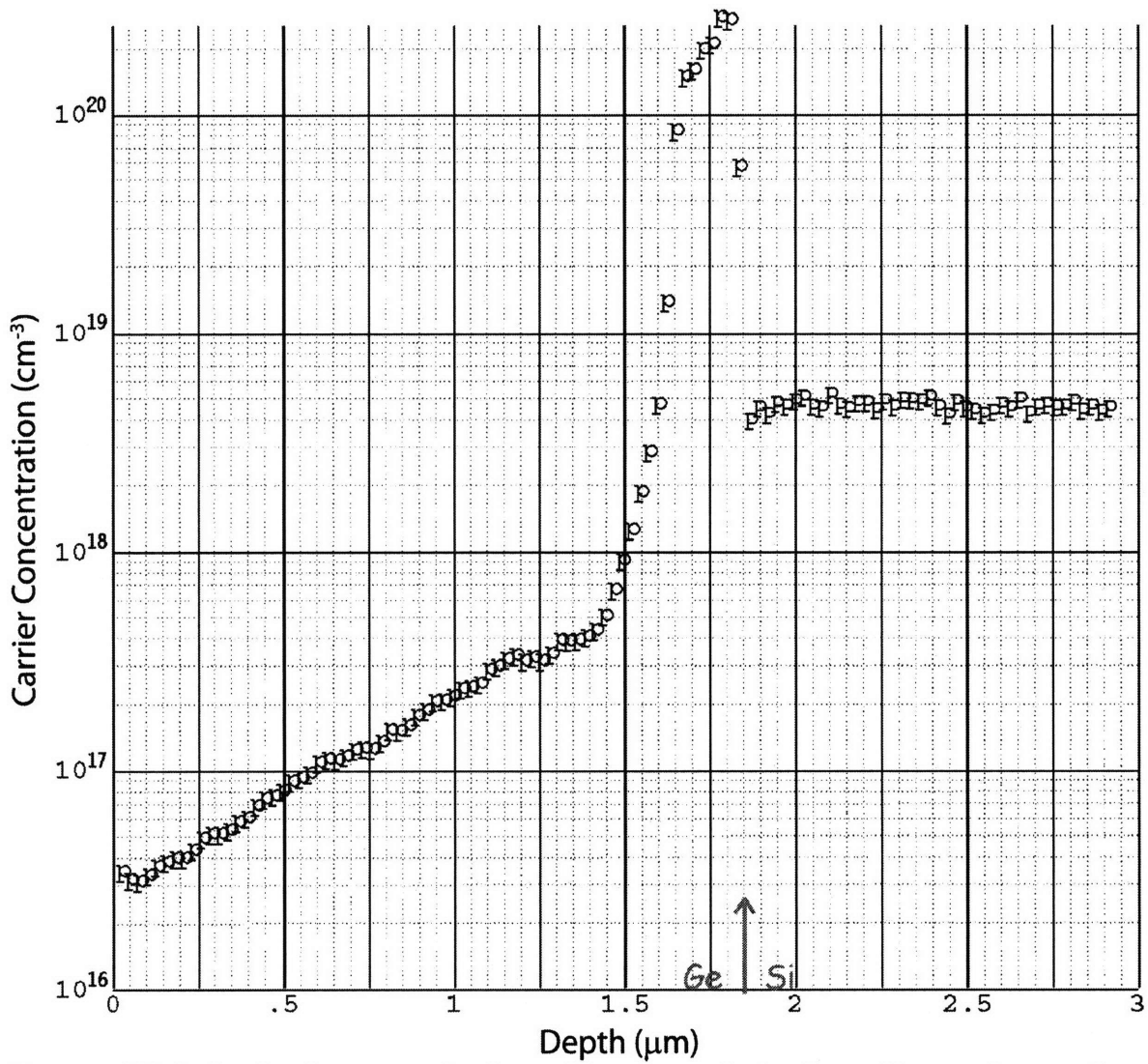


Figure 77. SRP doping data for a germanium layer without n-type doping. P+ seed layer at the start of growth results in autodoping of the germanium layer.

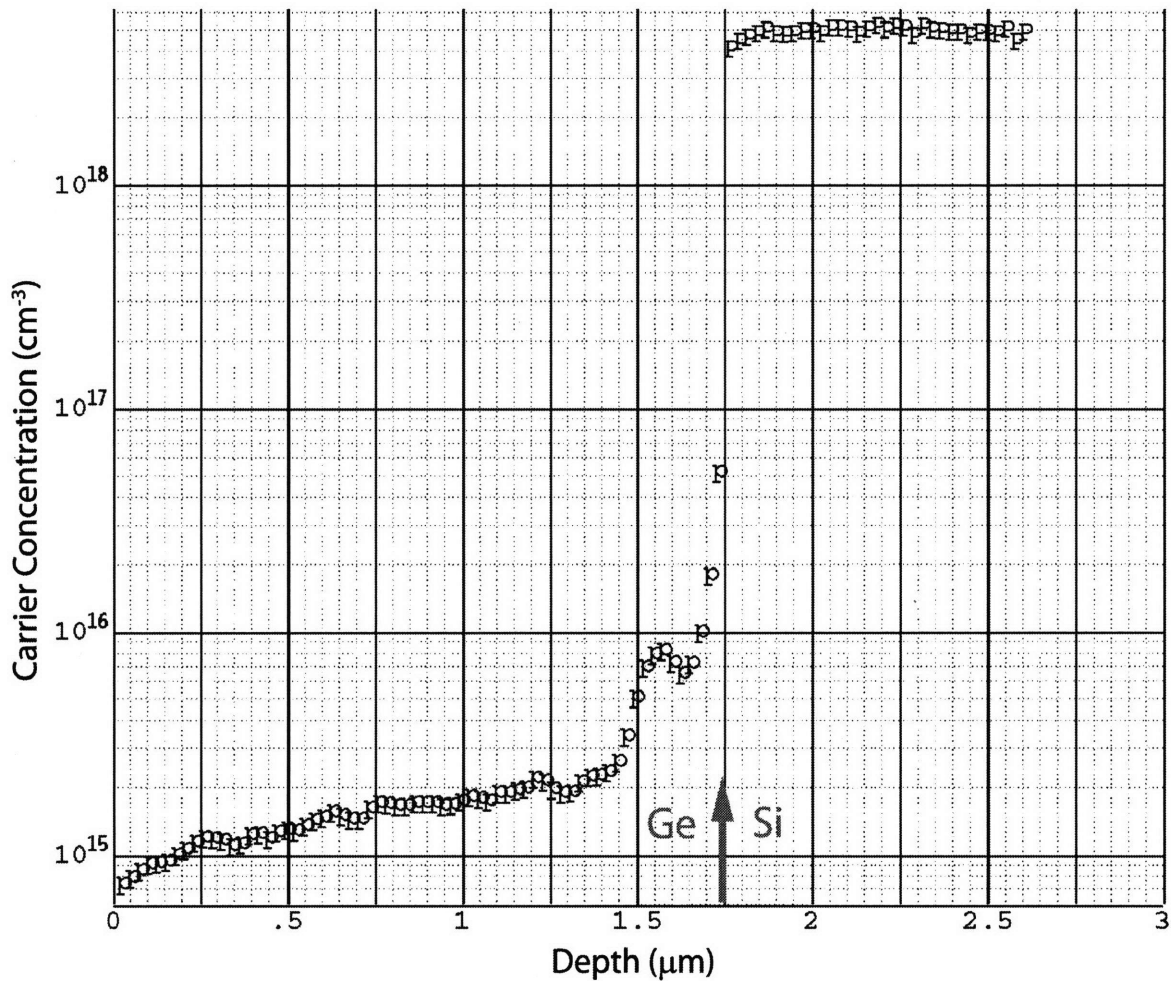


Figure 78. SRP doping data for a germanium layer without n-type doping. No seed layer doping results in a neutral germanium film.

From these figures it is clear that eliminating the p+ doping of the seed layer reduces the p-doping in the bulk of the germanium film by between one and two orders of magnitude. This will in theory allow a substantial increase in depletion region width and therefore frequency response. To quantify this improvement, the cylindrical coordinate finite element model used throughout this thesis is modified to replace the boron doping concentration of the current devices with the measured SRP data from this improved growth.

Reduction of the Threading Dislocation Density

The above discussion focuses on the improvements to the intrinsic diode frequency response. However, as previously noted, the high-bias frequency response is limited by trap states in

the current device design. Although this is a harder improvement to quantize, it is a necessary step to improve device performance.

For example the trap density was studied in Chapter 4 in terms of sampler ISI as a function of power level in the trap saturation region. If the threading dislocation is reduced to 10^4 cm^{-2} and the traps are assumed proportional dislocation density, the ISI can be recalculated as shown in (Figure 79). This demonstrates the applicability of these photodiodes for high resolution sampling systems at moderate optical powers.

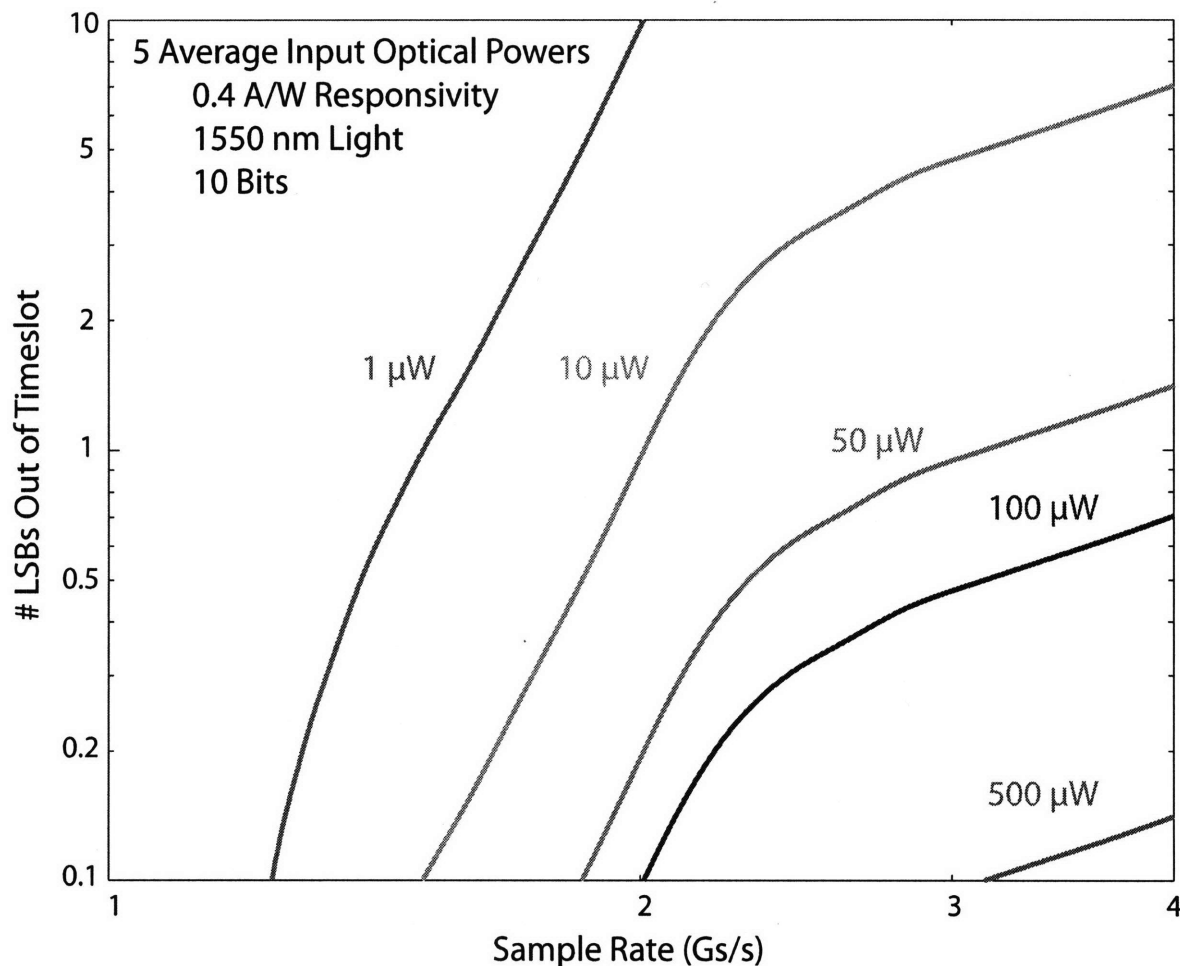


Figure 79. The pulse response trap excess charge with the reduced threading dislocation density is calculated in units of multiples of the LSB corresponding to various peak input powers.

Improved Surface Passivation

Although the frequency response in the center of large diodes does not appear to be affected by the surface passivation as shown in the spatial measurements of Chapter 3, small photodiode geometries will be dominated by surface behavior. The spatial frequency response measurements demonstrate that the high frequency response within 5 microns of the device perimeter can be suppressed by greater than 20 dB compared to device center. This must be fixed before high frequency devices can be made in small window openings.

Summary of Future Work

Since the scope of this thesis attempted to cover all aspects of photodiode performance in the germanium-on-silicon material system, much future work remains. This work will be broken down into four categories: experiment, simulation, theory and fabrication. Rather than go into detail, the future work will, for the most part, be outlined briefly in each category.

Experiment

For temperature dependant measurements, dark current and responsivity were shown in Chapter 2 and 3. An additional quantity of high interest would be the frequency response as a function of temperature. This characterization was not included in this thesis only because the microwave probes for the cryostation used were broken at the time of measurement. This data would be useful if any transitions in frequency response were observed as this would yield more information on the energies of related traps.

For the spatial measurements, automation in the x-y fiber translation would allow for 2-D plots and enable measurements that take a long time at each position that try human patience. One such quantity of interest would be the linearity as a function of position and excess noise as a function of position. Together they would yield information on the SFDR scaling with diode size and predict small device performance limits. Individually, the measurements would reveal the how each quantity scales with trap density and give more insight on the physics involved.

For the SFDR measurements in general, it is desirable to measure the linearity at 1550 nm instead of 1310 nm. Due to the lack of available highly linear sources in this region, external modulation is required. A suitable 1550 nm analog lithium niobate CATV modulator from JDSU Inc. has been located for this purpose. Additionally, since the modulator transfer function is sinusoidal and time varying, precise bias control must be used to stabilize the modulator at quadrature to eliminate even order harmonics. Since the acquired modulator has two outputs, a bias controller has been built to maintain a fixed ratio between the two outputs for stability. These measurements have not yet been performed, but are eminent.

The final area for further experimental work has not yet been explored in this thesis. In addition to characterizing the devices, it is desirable to directly characterize the material in separate test structures. This work includes: transmission measurements to accurately determine the absorption coefficient; n-i-n and p-i-p photoconductive detectors to measure optical decay transients; Raman strain characterization; Hall mobility measurements. Direct flaw characterization could also be attempted to validate results of the I-V fitting and to determine the nature of the traps influencing high-frequency performance.

Simulation

The simulation framework has several areas of possible improvement. First of all, a full simulation using the extracted recombination generation centers as discrete inputs would be desirable. This would verify the extraction procedure and demonstrate that the I-V characteristics can be regenerated with the fit R-G center density.

Second, and perhaps most interesting, would be to attempt to add trap states to simulate the excess current in the pulse response that degrades performance at frequencies greater than 2 GHz.

Additional efforts could be focused on simulating the SFDR results presented here. Noise analysis is available within Sentaurus, and when explicit trap models are added, pursuing such an analysis would be interesting. Linearity analysis is currently not explicitly available

using optical small signal simulation in Sentaurus, although multi-tone harmonic balance analysis is available for electrical simulations. Barring a software update to enable this functionality, analysis will have to be carried out in transient simulations, which is currently computationally burdensome to reach full steady state convergence.

In addition to material characterization experiments, material characterization simulations can be performed in two ways. First, analysis based upon adding strain to established germanium bandstructure models could provide improved estimates for the relevant effective masses. This analysis can be performed both by hand and by utilizing strained bandstructure tools such as those available in the Synopsys Sentaurus Tool Suite. Additionally, 1D Monte-Carlo analysis can be applied used with strain modified parameters to simulate the mobility in the grown films. This analysis can again be performed within the Synopsys Sentaurus framework using the SMOCA tool based upon the MOCA code from University of Illinois Urbana-Champaign.

An area of a different focus from this thesis, could be process based simulation to generate the finite element model. In Synopsys's Sentaurus TCAD suite, Sentaurus Process provides this functionality. Although the tool is primarily silicon focused, germanium is partially supported and suitability studies could be performed to determine the ability of the tool to reproduce known characteristics such as the final doping profile. The results of this study could determine the feasibility of fully process based device models. Goals of the final processed based simulations would be to study the possible diffusion length and profile of the oxygen from the surface passivation interface. This would yield more accurate spatial profiles for the suspected A-center flaws.

Theory

Several open questions remain after this thesis. First of all, the observed scaling of the flaw cross sections are observed to obey a cubic field dependence for both the center and the edge. This is unprecedented in the literature and speculated to result from the threading dislocations. Since this is the first detailed study of flaws in devices dominated by threading

dislocations, there is no comparable work to relate. However, knowledge of the electrostatic extended state of the threading dislocation could yield similar closed form analyses for barrier lowering as the Poole-Frenkel models based on the electrostatics of isolated states.

Additional unexplained behavior is seen in the band edge bias dependence of responsivity. As discussed in Chapter 3, the slope of the optical band edge shifts with increasing bias. The remaining question is whether this is explainable by the Franz-Keldysh effect or is a trap related phenomenon.

The physical explanation for the small electron R-G center cross sections would be interesting to explore further. These small cross sections are typically characteristic of repulsive traps and could yield further insight into the electrostatic nature of these flaws.

Fabrication

Although this thesis is not directly concerned with the fabrication of these diodes, the understanding gained for issues effecting device performance suggest certain changes for device improvement. In the previous sections the following changes have been outlined: reduction of series resistance, reduction of p+ doping of the seed layer, thinning of the germanium layer, new passivation schemes and reduction of the threading dislocation. All but two of these changes are straightforward and have been discussed sufficiently in the previous discussion.

Due to technological interest in germanium passivation for scaled CMOS transistors, significant improvements have been recently reported. Coupled with hafnium oxide based dielectrics, initial passivation processes using aqueous ammonium sulfide or ammonia gas treatment have demonstrated low fixed charge and low oxygen incorporation [91, 92]. The same techniques are transferable to the germanium photodiodes and can be seen as an enabling technology for small area detectors.

Reducing the threading dislocation density is the harder issue. As a result of its importance to the improvement of nearly all device characteristics, some further discussion is required. Although the defect density can be reduced by techniques such as growing on graded SiGe buffers, the growth is complicated and far slower. Since the goal growing photodiodes with LPCVD is to use high throughput simple techniques suitable for CMOS integration, these steps are not desirable

One technique that has demonstrated to be successful and has little impact on throughput is selective growth instead of the blanket films studied here. This is also more practical for CMOS integration as germanium is desired over only a small fraction of the chip area. Since epitaxial growth needs nucleation sites to begin crystal growth, selective growth of germanium is enabled by covering most of the silicon surface with oxide and opening the silicon surface only where germanium is desired. The reduction of the threading dislocation densities are enabled by the.

Conclusion

Over the course of this thesis, a complete set of experimental data has been gathered for a well characterized set of diodes. This bulk of data has sought to establish the current state of device performance. In conjunction to experimental measurement, a finite element model that matches trap-free device performance has been constructed.

Appendix A – Sentaurus Input Files

Structure Generation Scripts

Circular Diode 2-D Cylindrical Coordinates Structure

```
(sde:clear)

(define TGe      1.85)
(define TSub     10.00)
(define Opening  (/ @Window@ 2))
(define Space   15.00)
(define TOx     0.300)
(define TTopOx  0.050)
(define TFlaw   @FlawDepth@)
(define TPoly   0.200)
(define WCont   1.000)
(define WRing   5.000)
(define WRefine 8.00)

(define InRef   0.200)
(define OutRef  0.100)
(define RefXMin 0.075)
(define RefXMax 0.150)
(define CrsXMin 0.200)
(define CrsXMax 0.600)

(define Width (+ Opening Space))
(define Height (+ TSub (+ TGe (+ TOx (+ TPoly TTopOx)))))

(sdegeo:create-rectangle (position 0 0 0) (position Width TSub 0) "Silicon"
  "R.Sub")
(sdegeo:create-rectangle (position 0 TSub 0) (position Width (+ TSub TGe) 0)
  "Germanium" "R.Ge")
(sdegeo:create-rectangle (position 0 (+ TSub TGe) 0) (position Width Height
  0) "Oxide" "R.Ox")
(sdegeo:create-rectangle (position Opening (+ TSub TGe) 0) (position Width (+
  TSub (+ TGe TOx)) 0) "Oxynitride" "R.OxyNi")

(sdegeo:create-rectangle (position 0 (+ TSub TGe) 0) (position (- Width
  Space) (+ TSub (+ TGe TPoly)) 0) "PolySi" "R.Lid")
(sdegeo:create-rectangle (position (- Width (+ Space TPoly)) (+ TSub (+ TGe
  TPoly)) 0) (position Opening (- Height (+ TTopOx TPoly)) 0) "PolySi"
  "R.Join")
(sdegeo:create-rectangle (position (- Width (+ Space TPoly)) (- Height (+
  TPoly TTopOx)) 0) (position (+ Opening WRing) (- Height TTopOx) 0) "PolySi"
  "R.Ring")

(sdegeo:create-rectangle (position (- Width Space) (- (+ TSub TGe) TFlaw) 0)
  (position Width (+ TSub TGe) 0) "FlawedGermanium" "R.Flaws")
```

```

(define ContactRegion1 (sdegeo:create-rectangle (position (- (+ Opening
WRing) WCont) (- Height TTopOx) 0) (position (+ Opening WRing) Height 0)
"AnyMaterial" "R.Con1"))

(sdegeo:create-rectangle (position (- Width (+ WCont 0.5)) TSub 0) (position
Width Height 0) "Oxide" "R.Ox2")
(define ContactRegion2 (sdegeo:create-rectangle (position (- Width WCont)
TSub 0) (position Width Height 0) "AnyMaterial" "R.Con2"))

;----- Define Doping RefEval Windows

(sdedr:define-refeval-window "RefLine.Window" "Line" (position 0 (+ TSub TGe)
0) (position (- Width Space) (+ TSub TGe) 0))
(sdedr:define-refeval-window "RefLine.Surface" "Line" (position 0 (+ TSub
TGe) 0) (position (- Width (+ WCont 0.5)) (+ TSub TGe) 0))

;----- Define Doping

(sdedr:define-constant-profile "Const.Si" "BoronActiveConcentration" 2e19)
(sdedr:define-constant-profile "Const.PolySi" "PhosphorusActiveConcentration"
1e19)

(sdedr:define-constant-profile-material "PlaceCD.Si" "Const.Si" "Silicon")
(sdedr:define-constant-profile-material "PlaceCD.PolySi" "Const.PolySi"
"PolySi")

(sdedr:define-1d-external-profile "ProfSRP.N" "srp_ntype_with_fit.txt"
"Scale" 1.0 "Gauss" "Length" 0.1)
(sdedr:define-1d-external-profile "ProfSRP.P" "srp_ptype_with_fit.txt"
"Scale" 1.0 "Gauss" "Length" 0.0)
(sdedr:define-analytical-profile-placement "PlaceSRP.N" "ProfSRP.N"
"RefLine.Window" "Negative" "NoReplace" "Eval")
(sdedr:define-analytical-profile-placement "PlaceSRP.P" "ProfSRP.P"
"RefLine.Surface" "Negative" "NoReplace" "Eval")

;----- Define Meshing RefEval Windows

(sdedr:define-refeval-window "RefWin.Top" "Rectangle" (position InRef (- (+
TSub TGe) 0.05) 0) (position (- Width (+ Space OutRef)) (+ TSub TGe) 0))
(sdedr:define-refeval-window "RefWin.TopIn" "Rectangle" (position 0 (- (+
TSub TGe) 0.05) 0) (position InRef (+ TSub TGe) 0))
(sdedr:define-refeval-window "RefWin.TopOut" "Rectangle" (position (- Opening
OutRef) (- (+ TSub TGe) 0.05) 0) (position Opening (+ TSub TGe) 0))
(sdedr:define-refeval-window "RefWin.TopEdge" "Rectangle" (position (- Width
Space) (- (+ TSub TGe) 0.1) 0) (position (+ Opening 1.0) (+ TSub TGe) 0))
(sdedr:define-refeval-window "RefWin.TopPerim" "Rectangle" (position (+
Opening 1.0) (- (+ TSub TGe) 0.1) 0) (position Width (+ TSub TGe) 0))
(sdedr:define-refeval-window "RefWin.GeIn" "Rectangle" (position 0 (+ TSub
0.150) 0) (position InRef (- (+ TSub TGe) 1.2) 0))
(sdedr:define-refeval-window "RefWin.Depletion" "Rectangle" (position InRef
(- (+ TSub TGe) 1.2) 0) (position (- Width (+ Space OutRef)) (- (+ TSub TGe)
0.05) 0))
(sdedr:define-refeval-window "RefWin.DepletionIn" "Rectangle" (position 0 (-
+ TSub TGe) 1.2) 0) (position InRef (- (+ TSub TGe) 0.05) 0))
(sdedr:define-refeval-window "RefWin.DepletionOut" "Rectangle" (position (-
Opening OutRef) (- (+ TSub TGe) 1.2) 0) (position Opening (- (+ TSub TGe)
0.05) 0))

```

```

(sdedr:define-refeval-window "RefWin.DepletionEdge" "Rectangle" (position (-
Width Space) (- (+ TSub TGe) 1.2) 0) (position (+ Opening 0.5) (- (+ TSub
TGe) 0.1) 0))
(sdedr:define-refeval-window "RefWin.DepletionPerim" "Rectangle" (position (+
Opening 0.5) (- (+ TSub TGe) 1.0) 0) (position (+ Opening WRefine) (- (+ TSub
TGe) 0.1) 0))
(sdedr:define-refeval-window "RefWin.PolyInt" "Rectangle" (position InRef (+
TSub TGe) 0) (position (- Width (+ Space OutRef)) (+ TSub (+ TGe 0.05)) 0))
(sdedr:define-refeval-window "RefWin.PolyIntIn" "Rectangle" (position 0 (+
TSub TGe) 0) (position InRef (+ TSub (+ TGe 0.05)) 0))
(sdedr:define-refeval-window "RefWin.PolyIntOut" "Rectangle" (position (-
Opening OutRef) (+ TSub TGe) 0) (position Opening (+ TSub (+ TGe 0.05)) 0))
(sdedr:define-refeval-window "RefWin.PolyBend" "Rectangle" (position (-
Opening TPoly) (+ TSub (+ TGe 0.05)) 0) (position Opening (- Height TTopOx)
0))
(sdedr:define-refeval-window "RefWin.PolyContact" "Rectangle" (position (- (+
Opening WRing) WCont) (- Height (+ TTopOx TPoly)) 0) (position (+ Opening
WRing) (- Height TTopOx) 0))
(sdedr:define-refeval-window "RefWin.SiContact" "Rectangle" (position (-
Width WCont) (- TSub 0.200) 0) (position Width TSub 0))
(sdedr:define-refeval-window "RefWin.SiIn" "Rectangle" (position 0 0 0)
(position InRef (- TSub 0.020) 0))
(sdedr:define-refeval-window "RefWin.SiTop" "Rectangle" (position InRef (-
TSub 2.0) 0) (position Width (- TSub 0.020) 0))
(sdedr:define-refeval-window "RefWin.Bot1" "Rectangle" (position InRef (-
TSub 0.020) 0) (position Width (+ TSub 0.050) 0))
(sdedr:define-refeval-window "RefWin.Bot1In" "Rectangle" (position 0 (- TSub
0.020) 0) (position InRef (+ TSub 0.050) 0))
(sdedr:define-refeval-window "RefWin.Bot2" "Rectangle" (position InRef (+
TSub 0.050) 0) (position Width (+ TSub 0.150) 0))
(sdedr:define-refeval-window "RefWin.Bot2In" "Rectangle" (position 0 (+ TSub
0.050) 0) (position InRef (+ TSub 0.150) 0))
(sdedr:define-refeval-window "RefWin.SpacerOx1" "Rectangle" (position (-
Width Space) (+ TSub TGe) 0) (position (+ Opening WRing) (+ TSub (+ TGe TOx)
0))
(sdedr:define-refeval-window "RefWin.SpacerOx2" "Rectangle" (position (-
Width (+ Space TPoly)) (- Height TTopOx) 0) (position (+ Opening WRing)
Height 0))
(sdedr:define-refeval-window "RefWin.SpacerOx3" "Rectangle" (position 0 (+
TSub (+ TGe TPoly)) 0) (position (- Width (+ Space TPoly)) Height 0))
(sdedr:define-refeval-window "RefWin.SpacerOx4" "Rectangle" (position (+
Opening WRing) (+ TSub TGe) 0) (position Width Height 0))
(sdedr:define-refeval-window "RefWin.SpacerOx5" "Rectangle" (position (-
Width (+ WCont 0.5)) TSub 0) (position (- Width WCont) (+ TSub TGe) 0))

```

```

;----- Define Meshing Sizes

```

```

(sdedr:define-refinement-size "Size.GeStd" 1.000 0.600 0.000 0.500 0.200
0.000)
(sdedr:define-refinement-size "Size.FlawedGeStd" 1.000 0.020 0.000 0.500
0.010 0.000)
(sdedr:define-refinement-size "Size.GeIn" RefXMax 0.500 0.000 RefXMin 0.200
0.000)
(sdedr:define-refinement-size "Size.DepletionCrs" CrsXMax 0.150 0.000 CrsXMin
0.075 0.000)

```

```

(sdedr:define-refinement-size "Size.DepletionRef" RefXMax 0.150 0.000 RefXMin
0.075 0.000)
(sdedr:define-refinement-size "Size.DepletionEdge" 0.150 0.150 0.000 0.075
0.075 0.000)
(sdedr:define-refinement-size "Size.DepletionPerim" 0.250 0.250 0.000 0.150
0.150 0.000)
(sdedr:define-refinement-size "Size.SiStd" 5.00 5.000 0.000 1.500 1.500
0.000)
(sdedr:define-refinement-size "Size.SiTop" 1.500 1.500 0.000 0.500 0.500
0.000)
(sdedr:define-refinement-size "Size.SiIn" RefXMax 1.500 0.000 RefXMin 0.500
0.000)
(sdedr:define-refinement-size "Size.PolyStd" 1.500 0.500 0.000 0.500 0.100
0.000)
(sdedr:define-refinement-size "Size.PolyBend" 0.100 0.080 0.000 0.050 0.040
0.000)
(sdedr:define-refinement-size "Size.TopCrs" CrsXMax 0.020 0.000 CrsXMin 0.010
0.000)
(sdedr:define-refinement-size "Size.TopRef" RefXMax 0.020 0.000 RefXMin 0.010
0.000)
(sdedr:define-refinement-size "Size.TopEdge" 0.100 0.020 0.000 0.050 0.010
0.000)
(sdedr:define-refinement-size "Size.TopPerim" 0.500 0.050 0.000 0.200 0.010
0.000)
(sdedr:define-refinement-size "Size.PolyContact" 0.300 0.050 0.000 0.150
0.020 0.000)
(sdedr:define-refinement-size "Size.SiContact" 0.300 0.100 0.000 0.150 0.025
0.000)
(sdedr:define-refinement-size "Size.BotFine" 1.500 0.020 0.000 0.500 0.010
0.000)
(sdedr:define-refinement-size "Size.BotFineIn" RefXMax 0.020 0.000 RefXMin
0.010 0.000)
(sdedr:define-refinement-size "Size.BotCoarse" 1.500 0.050 0.000 0.500 0.020
0.000)
(sdedr:define-refinement-size "Size.BotCoarseIn" RefXMax 0.050 0.000 RefXMin
0.020 0.000)
(sdedr:define-refinement-size "Size.SpacerOx1" 1.500 0.125 0.000 0.500 0.075
0.000)
(sdedr:define-refinement-size "Size.SpacerOx2" 1.500 0.025 0.000 0.500 0.015
0.000)
(sdedr:define-refinement-size "Size.SpacerOx3" 5.000 0.200 0.000 1.000 0.100
0.000)
(sdedr:define-refinement-size "Size.SpacerOx4" 2.500 0.200 0.000 1.000 0.100
0.000)
(sdedr:define-refinement-size "Size.SpacerOx5" 0.200 0.500 0.000 0.100 0.250
0.000)

```

;----- Define Mesh Placements

```

(sdedr:define-refinement-material "Place.GeStd" "Size.GeStd" "Germanium")
(sdedr:define-refinement-material "Place.FlawedGeStd" "Size.FlawedGeStd"
"FlawedGermanium")
(sdedr:define-refinement-material "Place.SiStd" "Size.SiStd" "Silicon")
(sdedr:define-refinement-material "Place.PolyStd" "Size.PolyStd" "PolySi")
(sdedr:define-refinement-placement "Place.SiIn" "Size.SiIn" "RefWin.SiIn")
(sdedr:define-refinement-placement "Place.SiTop" "Size.SiTop" "RefWin.SiTop")
(sdedr:define-refinement-placement "Place.GeIn" "Size.GeIn" "RefWin.GeIn")

```

```

(sdedr:define-refinement-placement "Place.Top" "Size.TopCrs" "RefWin.Top")
(sdedr:define-refinement-placement "Place.TopIn" "Size.TopRef"
"RefWin.TopIn")
(sdedr:define-refinement-placement "Place.TopOut" "Size.TopRef"
"RefWin.TopOut")
(sdedr:define-refinement-placement "Place.TopEdge" "Size.TopEdge"
"RefWin.TopEdge")
(sdedr:define-refinement-placement "Place.TopPerim" "Size.TopPerim"
"RefWin.TopPerim")
(sdedr:define-refinement-placement "Place.Depletion" "Size.DepletionCrs"
"RefWin.Depletion")
(sdedr:define-refinement-placement "Place.DepletionIn" "Size.DepletionRef"
"RefWin.DepletionIn")
(sdedr:define-refinement-placement "Place.DepletionOut" "Size.DepletionRef"
"RefWin.DepletionOut")
(sdedr:define-refinement-placement "Place.DepletionEdge" "Size.DepletionEdge"
"RefWin.DepletionEdge")
(sdedr:define-refinement-placement "Place.DepletionPerim"
"Size.DepletionPerim" "RefWin.DepletionPerim")
(sdedr:define-refinement-placement "Place.PolyInt" "Size.TopCrs"
"RefWin.PolyInt")
(sdedr:define-refinement-placement "Place.PolyIntIn" "Size.TopRef"
"RefWin.PolyIntIn")
(sdedr:define-refinement-placement "Place.PolyIntOut" "Size.TopRef"
"RefWin.PolyIntOut")
(sdedr:define-refinement-placement "Place.PolyBend" "Size.PolyBend"
"RefWin.PolyBend")
(sdedr:define-refinement-placement "Place.PolyContact" "Size.PolyContact"
"RefWin.PolyContact")
(sdedr:define-refinement-placement "Place.SiContact" "Size.SiContact"
"RefWin.SiContact")
(sdedr:define-refinement-placement "Place.Bot1" "Size.BotFine" "RefWin.Bot1")
(sdedr:define-refinement-placement "Place.Bot1In" "Size.BotFineIn"
"RefWin.Bot1In")
(sdedr:define-refinement-placement "Place.Bot2" "Size.BotCoarse"
"RefWin.Bot2")
(sdedr:define-refinement-placement "Place.Bot2In" "Size.BotCoarseIn"
"RefWin.Bot2In")
(sdedr:define-refinement-placement "Place.SpacerOx1" "Size.SpacerOx1"
"RefWin.SpacerOx1")
(sdedr:define-refinement-placement "Place.SpacerOx2" "Size.SpacerOx2"
"RefWin.SpacerOx2")
(sdedr:define-refinement-placement "Place.SpacerOx3" "Size.SpacerOx3"
"RefWin.SpacerOx3")
(sdedr:define-refinement-placement "Place.SpacerOx4" "Size.SpacerOx4"
"RefWin.SpacerOx4")
(sdedr:define-refinement-placement "Place.SpacerOx5" "Size.SpacerOx5"
"RefWin.SpacerOx5")

```

```

;----- Define Contacts

```

```

(sdegeo:define-contact-set "TopContact" (color:rgb 1.0 1.0 1.0) "###")
(sdegeo:set-current-contact-set "TopContact")
(sdegeo:set-contact-boundary-edges ContactRegion1 "TopContact")
(sdegeo:delete-region ContactRegion1)

```

```

(sdegeo:define-contact-set "BotContact" (color:rgb 1.0 1.0 1.0) "###")

```

```

(sdegeo:set-current-contact-set "BotContact")
(sdegeo:set-contact-boundary-edges ContactRegion2 "BotContact")
(sdegeo:delete-region ContactRegion2)

*(sdegeo:define-contact-set "SubContact" (color:rgb 1.0 1.0 1.0) "##")
*(sdegeo:set-current-contact-set "SubContact")
*(sdegeo:define-2d-contact (find-edge-id (position 0.1 0 0)) "SubContact")

(sde:save-model "n@node@_bnd")
(sde:build-mesh "snmesh" "" "n@node@_msh")

```

Rectangular Diode 2-D Transverse Structure

```

(sde:clear)

(define TGe      1.849)
(define TSub     2.00)
(define Opening  20.00)
(define Space    30.00)
(define TOx      0.050)

(define Width (+ Opening (* Space 2)))
(define Height (+ TSub (+ TGe TOx)))
(define Junction (- (+ TSub TGe) 0.317))

(sdegeo:create-rectangle (position 0 0 0) (position Width TSub 0) "Silicon"
"R.Sub")
(sdegeo:create-rectangle (position 0 TSub 0) (position Width (+ TSub TGe) 0)
"Germanium" "R.Ge")
(sdegeo:create-rectangle (position 0 (+ TSub TGe) 0) (position Width Height
0) "Oxide" "R.Ox")

(define ContactRegion (sdegeo:create-rectangle (position Space (+ TSub TGe)
0) (position (- Width Space) Height 0) "AnyMaterial" "R.Con"))

(sdegeo:create-rectangle (position 0 (- (+ TSub TGe) 0.100) 0) (position
Space (+ TSub TGe) 0) "Germanium" "R.Traps1")
(sdegeo:create-rectangle (position (- Width Space) (- (+ TSub TGe) 0.100) 0)
(position Width (+ TSub TGe) 0) "Germanium" "R.Traps2")

;----- Define Doping RefEval Windows

(sdedr:define-refeval-window "RefLine.Window" "Line" (position Space (+ TSub
TGe) 0) (position (- Width Space) (+ TSub TGe) 0))
(sdedr:define-refeval-window "RefLine.Junction" "Line" (position 0 Junction
0) (position Width Junction 0))

;----- Define Doping

(sdedr:define-constant-profile "Const.Ge" "BoronActiveConcentration" 1e13)
(sdedr:define-constant-profile "Const.Si" "BoronActiveConcentration" 2e19)

(sdedr:define-constant-profile-region "PlaceCD.Ge" "Const.Ge" "R.Ge")
(sdedr:define-constant-profile-material "PlaceCD.Si" "Const.Si" "Silicon")

```

```

(sdedr:define-ld-external-profile "ProfSRP.N" "srp_n_type.txt" "Scale" 1.0
"Gauss" "Length" 0.2)
(sdedr:define-ld-external-profile "ProfSRP.P" "srp_p_type.txt" "Scale" 1.0
"Gauss" "Length" 0.1)
(sdedr:define-analytical-profile-placement "PlaceSRP.N" "ProfSRP.N"
"RefLine.Window" "Negative" "NoReplace" "Eval")
(sdedr:define-analytical-profile-placement "PlaceSRP.P" "ProfSRP.P"
"RefLine.Junction" "Negative" "NoReplace" "Eval")

;----- Define Meshing RefEval Windows

(sdedr:define-refeval-window "RefWin.TopCenter" "Rectangle" (position (-
Space 3.0) (- Height 0.200) 0) (position (- Width (- Space 3.0)) Height 0))
(sdedr:define-refeval-window "RefWin.Depletion" "Rectangle" (position (-
Space 2.5) (- Height 1.2) 0) (position (- Width (- Space 2.5)) (- Height
0.200) 0))
(sdedr:define-refeval-window "RefWin.TopLeft" "Rectangle" (position 0 (-
Height 0.200) 0) (position (- Space 3.0) Height 0))
(sdedr:define-refeval-window "RefWin.TopRight" "Rectangle" (position (- Width
(- Space 3.0)) (- Height 0.200) 0) (position Width Height 0))
(sdedr:define-refeval-window "RefWin.Bot1" "Rectangle" (position 0 (+ TSub
0.010) 0) (position Width (+ TSub 0.100) 0))
(sdedr:define-refeval-window "RefWin.Bot2" "Rectangle" (position 0 (- TSub
0.010) 0) (position Width (+ TSub 0.010) 0))

;----- Define Meshing Sizes

(sdedr:define-refinement-size "Size.GeStd" 0.500 0.100 0.000 0.100 0.020
0.000)
(sdedr:define-refinement-size "Size.SiStd" 0.500 0.500 0.000 0.200 0.200
0.000)
(sdedr:define-refinement-size "Size.TopCenter" 0.100 0.050 0.000 0.050 0.010
0.000)
(sdedr:define-refinement-size "Size.TopSide" 0.500 0.050 0.000 0.100 0.010
0.000)
(sdedr:define-refinement-size "Size.BotFine" 0.500 0.002 0.000 0.100 0.0002
0.000)
(sdedr:define-refinement-size "Size.BotCoarse" 0.500 0.010 0.000 0.100 0.002
0.000)

;----- Define Mesh Placements

(sdedr:define-refinement-material "Place.GeStd" "Size.GeStd" "Germanium")
(sdedr:define-refinement-material "Place.SiStd" "Size.SiStd" "Silicon")
(sdedr:define-refinement-placement "Place.TopCenter" "Size.TopCenter"
"RefWin.TopCenter")
(sdedr:define-refinement-placement "Place.Depletion" "Size.TopCenter"
"RefWin.Depletion")
(sdedr:define-refinement-placement "Place.TopLeft" "Size.TopSide"
"RefWin.TopLeft")
(sdedr:define-refinement-placement "Place.TopRight" "Size.TopSide"
"RefWin.TopRight")
(sdedr:define-refinement-placement "Place.Bot1" "Size.BotCoarse"
"RefWin.Bot1")
(sdedr:define-refinement-placement "Place.Bot2" "Size.BotFine" "RefWin.Bot2")

```

```

;----- Define Contacts

(sdegeo:define-contact-set "TopContact" (color:rgb 1.0 1.0 1.0) "###")
(sdegeo:define-contact-set "BotContact" (color:rgb 1.0 1.0 1.0) "###")

(sdegeo:set-current-contact-set "TopContact")
(sdegeo:set-contact-boundary-edges ContactRegion "TopContact")
(sdegeo:delete-region ContactRegion)

(sdegeo:set-current-contact-set "BotContact")
(sdegeo:define-2d-contact (find-edge-id (position (/ Width 2) 0 0))
"BotContact")

(sde:save-model "n@node@_bnd")
(sde:build-mesh "snmesh" "" "n@node@_msh")

```

Rectangular Diode 3-D Structure

```

(sde:clear)

(define TGe      1.849)
(define TSub     2.00)
(define Opening (/ @Window@ 2))
(define Space    5.00)
(define TOx     0.050)
(define TTraps  0.050)

(define Width (+ Opening Space))
(define Height (+ TSub (+ TGe TOx)))
(define Junction (- (+ TSub TGe) 0.317))

(sdegeo:create-rectangle (position 0 0 0) (position Width TSub 0) "Silicon"
"R.Sub")
(sdegeo:create-rectangle (position 0 TSub 0) (position Width (+ TSub TGe) 0)
"Germanium" "R.Ge")
(sdegeo:create-rectangle (position 0 (+ TSub TGe) 0) (position Width Height
0) "Oxide" "R.Ox")

(define ContactRegion (sdegeo:create-rectangle (position 0 (+ TSub TGe) 0)
(position (- Width Space) Height 0) "AnyMaterial" "R.Con"))

(sdegeo:create-rectangle (position (- Width Space) (- (+ TSub TGe) TTraps) 0)
(position Width (+ TSub TGe) 0) "Germanium" "R.Traps")

;----- Define Doping RefEval Windows

(sdedr:define-refeval-window "RefLine.Window" "Line" (position 0 (+ TSub TGe)
0) (position (- Width Space) (+ TSub TGe) 0))
(sdedr:define-refeval-window "RefLine.Junction" "Line" (position 0 Junction
0) (position Width Junction 0))

;----- Define Doping

(sdedr:define-constant-profile "Const.Ge" "BoronActiveConcentration" 1e13)

```

```

(sdedr:define-constant-profile "Const.Si" "BoronActiveConcentration" 2e19)

(sdedr:define-constant-profile-material "PlaceCD.Ge" "Const.Ge" "Germanium")
(sdedr:define-constant-profile-material "PlaceCD.Si" "Const.Si" "Silicon")

(sdedr:define-1d-external-profile "ProfSRP.N" "srp_n_type.txt" "Scale" 1.0
"Gauss" "Length" 0.5)
(sdedr:define-1d-external-profile "ProfSRP.P" "srp_p_type.txt" "Scale" 1.0
"Gauss" "Length" 0.1)
(sdedr:define-analytical-profile-placement "PlaceSRP.N" "ProfSRP.N"
"RefLine.Window" "Negative" "NoReplace" "Eval")
(sdedr:define-analytical-profile-placement "PlaceSRP.P" "ProfSRP.P"
"RefLine.Junction" "Negative" "NoReplace" "Eval")

;----- Define Meshing RefEval Windows

(sdedr:define-refeval-window "RefWin.TopCenter" "Rectangle" (position 0 (-
Height 0.200) 0) (position (- Width (- Space 3.0)) Height 0))
(sdedr:define-refeval-window "RefWin.Depletion" "Rectangle" (position 0 (-
Height 1.2) 0) (position (- Width (- Space 2.5)) (- Height 0.200) 0))
(sdedr:define-refeval-window "RefWin.TopRight" "Rectangle" (position (- Width
(- Space 3.0)) (- Height 0.200) 0) (position Width Height 0))
(sdedr:define-refeval-window "RefWin.Bot1" "Rectangle" (position 0 (+ TSub
0.010) 0) (position Width (+ TSub 0.100) 0))
(sdedr:define-refeval-window "RefWin.Bot2" "Rectangle" (position 0 (- TSub
0.010) 0) (position Width (+ TSub 0.010) 0))

;----- Define Meshing Sizes

(sdedr:define-refinement-size "Size.GeStd" 0.500 0.100 0.000 0.100 0.020
0.000)
(sdedr:define-refinement-size "Size.SiStd" 0.500 0.500 0.000 0.200 0.100
0.000)
(sdedr:define-refinement-size "Size.TopCenter" 0.100 0.050 0.000 0.050 0.010
0.000)
(sdedr:define-refinement-size "Size.TopSide" 0.500 0.050 0.000 0.100 0.010
0.000)
(sdedr:define-refinement-size "Size.BotFine" 0.500 0.002 0.000 0.100 0.0002
0.000)
(sdedr:define-refinement-size "Size.BotCoarse" 0.500 0.010 0.000 0.100 0.002
0.000)
(sdedr:define-refinement-size "Size.Traps" 0.100 0.010 0.000 0.050 0.005
0.000)

;----- Define Mesh Placements

(sdedr:define-refinement-material "Place.GeStd" "Size.GeStd" "Germanium")
(sdedr:define-refinement-material "Place.SiStd" "Size.SiStd" "Silicon")
(sdedr:define-refinement-region "Place.Traps" "Size.Traps" "R.Traps")
(sdedr:define-refinement-placement "Place.TopCenter" "Size.TopCenter"
"RefWin.TopCenter")
(sdedr:define-refinement-placement "Place.Depletion" "Size.TopCenter"
"RefWin.Depletion")
(sdedr:define-refinement-placement "Place.TopRight" "Size.TopSide"
"RefWin.TopRight")

```

```

(sdedr:define-refinement-placement "Place.Bot1" "Size.BotCoarse"
"RefWin.Bot1")
(sdedr:define-refinement-placement "Place.Bot2" "Size.BotFine" "RefWin.Bot2")

;----- Define Contacts

(sdegeo:define-contact-set "TopContact" (color:rgb 1.0 1.0 1.0) "##")
(sdegeo:define-contact-set "BotContact" (color:rgb 1.0 1.0 1.0) "##")

(sdegeo:set-current-contact-set "TopContact")
(sdegeo:set-contact-boundary-edges ContactRegion "TopContact")
(sdegeo:delete-region ContactRegion)

(sdegeo:set-current-contact-set "BotContact")
(sdegeo:define-2d-contact (find-edge-id (position (/ Width 2) 0 0))
"BotContact")

(sde:save-model "n@node@_bnd")
(sde:build-mesh "snmesh" "" "n@node@_msh")

```

Device Simulation Command Files

Parametric Lifetime Variation for I-V Fitting

```

Electrode {
  { Name="TopContact" voltage=0.0 Material="Titanium" }
  { Name="BotContact" voltage=0.0 Material="Titanium" }
}

*Thermode {
*   { Name="SubContact" Temperature=@Temperature@ }
*}

File {
  Grid = "@tdr@"
  Parameter = "@parameter@"
  Plot = "@tdrdat@"
  Output = "@log@"
  Current = "n@node@_des.plt"
}

Plot {
  eDensity hDensity
  eCurrent/Vector hCurrent/Vector
  Current/Vector ConductionCurrent/Vector DisplacementCurrent/Vector
  Potential SpaceCharge ElectricField/Vector
  eMobility/Element hMobility/Element
  eVelocity/Vector hVelocity/Vector
  eDriftVelocity/Vector hDriftVelocity/Vector
  eSaturationVelocity hSaturationVelocity

  OpticalGeneration
  SRHRecombination
  SurfaceRecombination

```

```

TotalRecombination
eLifetime hLifetime
eAugerRecombination hAugerRecombination
Band2Bandsdevice

ValenceBandEnergy
ConductionBandEnergy
ElectronAffinity
EquilibriumPotential
eQuasiFermi hQuasiFermi
eGradQuasiFermi/Vector hGradQuasiFermi/Vector
BuiltinPotential
BandGap
BandGapNarrowing EffectiveIntrinsicDensity
EffectiveBandGap

Doping
BoronConcentration bMinus
PhosphorusConcentration phPlus

TotalHeat
ThermalConductivity
eTemperature hTemperature
RecombinationHeat
eJouleHeat hJouleHeat
ThomsonHeat
PeltierHeat
Temperature
}

CurrentPlot {
    ElectricField/Vector (
        (!(puts [expr @Window@/4])! 11.3514)
        (!(puts [expr @Window@/2+2.5])! !(puts [expr 11.85-
@FlawDepth@/2])!))
    )
}

Physics {
    Temperature=@Temperature@
    Fermi
    EffectiveIntrinsicDensity(NoFermi)
    Mobility (
        PhuMob ( Phosphorus )
        eHighFieldSaturation
        hHighFieldSaturation
    )
    Recombination (
        SRH
    )
    HeteroInterfaces
}

Physics (Material="PolySi") {
    EffectiveIntrinsicDensity( TableBGN )
}

```

```

Physics (Material="Silicon") {
    EffectiveIntrinsicDensity( TableBGN )
}

Physics (Material="Germanium") {
    EffectiveIntrinsicDensity( TableBGN )
}

Physics (Material="FlawedGermanium") {
    EffectiveIntrinsicDensity( TableBGN )
}

Physics (MaterialInterface="Germanium/Silicon") {
    eThermionic
    hThermionic
}

Physics (MaterialInterface="Germanium/PolySi") {
    eThermionic
    hThermionic
}

Math {
    Cylindrical

    RecomputeQFP

    Digits=5
    ErrReff(electron)=1.e4
    ErrReff(hole)=1.e4
    RelErrControl

    Method=pardiso
    Number_of_Threads=1
    Number_of_Solver_Threads=1

    WallClock
}

Solve {
    Poisson
    Coupled(iterations=5000) { Poisson Electron Hole }

    Quasistationary ( InitialStep=1e-2 MaxStep=0.01 MinStep=1e-9
        Increment=1.5 Decrement=2.0
        Goal {Voltage=5.0 Name=TopContact}
        Plot {Range=(0 1) Intervals=5} ) {
        Coupled(iterations=15) { Poisson Electron Hole }
    }
}

```

Center Responsivity Simulation

```
Electrode {
```

```

    { Name="TopContact" voltage=0.0 Material="Titanium" }
    { Name="BotContact" voltage=0.0 Material="Titanium" }
}

*Thermode {
*   { Name="SubContact" Temperature=@Temperature@ }
*}

File {
    Grid = "@tdr@"
    Parameter = "@parameter@"
    Plot = "@tdrdat@"
    Output = "@log@"
    Current = "n@node@_des.plt"
}

Plot {
    eDensity hDensity
    eCurrent/Vector hCurrent/Vector
    Current/Vector ConductionCurrent/Vector DisplacementCurrent/Vector
    Potential SpaceCharge ElectricField/Vector
    eMobility/Element hMobility/Element
    eVelocity/Vector hVelocity/Vector
    eDriftVelocity/Vector hDriftVelocity/Vector
    eSaturationVelocity hSaturationVelocity

    OptBeam
    SRHRecombination
    SurfaceRecombination
    TotalRecombination
    eLifetime hLifetime
    eAugerRecombination hAugerRecombination
    Band2Bandsdevice

    ValenceBandEnergy
    ConductionBandEnergy
    ElectronAffinity
    EquilibriumPotential
    eQuasiFermi hQuasiFermi
    eGradQuasiFermi/Vector hGradQuasiFermi/Vector
    BuiltinPotential
    BandGap
    BandGapNarrowing EffectiveIntrinsicDensity
    EffectiveBandGap

    Doping
    BoronConcentration bMinus
    PhosphorusConcentration phPlus

    TotalHeat
    ThermalConductivity
    eTemperature hTemperature
    RecombinationHeat
    eJouleHeat hJouleHeat
    ThomsonHeat
    PeltierHeat
    Temperature

```

```

}

Physics {
    Temperature=@Temperature@
    Fermi
    EffectiveIntrinsicDensity(NoFermi)
    Mobility (
        PhuMob ( Phosphorus )
        eHighFieldSaturation
        hHighFieldSaturation
    )
    Recombination (
        SRH
    )
}

#if @<[string compare OptBeam "ON"] == 0>@

    OptBeam (
        ( WaveLength = 1.55e-4      # cm
          WavePower = !(puts [expr @IncidentPower@/7.85e-7])!      # W/cm^2
          SemAbs ( model=ODB )      # 1/cm
          SemSurf = 12.06e-4        # cm
          SemWind = (0.0,5.0e-4)    # cm
          WaveXYSigma = 0 )        # cm
        )
    )

#endif

    HeteroInterfaces
}

Physics (Material="PolySi") {
    EffectiveIntrinsicDensity( TableBGN )
}

Physics (Material="Silicon") {
    EffectiveIntrinsicDensity( TableBGN )
}

Physics (Material="Germanium") {
    EffectiveIntrinsicDensity( TableBGN )
}

Physics (Material="FlawedGermanium") {
    EffectiveIntrinsicDensity( TableBGN )
}

Physics (MaterialInterface="Germanium/Silicon") {
    eThermionic
    hThermionic
}

Physics (MaterialInterface="Germanium/PolySi") {
    eThermionic
    hThermionic
}

```

```

Math {
  Cylindrical

  RecomputeQFP
  RecBoxInteger (1e-3 10 1000)

  Digits=5
  ErrReff(electron)=1.e4
  ErrReff(hole)=1.e4
  RelErrControl

  Method=pardiso
  Number_of_Threads=1
  Number_of_Solver_Threads=1

  WallClock
}

Solve {
  Poisson
  Coupled(iterations=5000) { Poisson Electron Hole }

  Quasistationary ( InitialStep=1e-2 MaxStep=0.01 MinStep=1e-9
                    Increment=1.5 Decrement=2.0
                    Goal {Voltage=@BiasVoltage@ Name=TopContact}
                    Plot {Range=(0 1) Intervals=5} ) {
    Coupled(iterations=15) { Poisson Electron Hole }
  }
}

```

Overfill Responsivity Simulation

```

Electrode {
  { Name="TopContact" voltage=0.0 Material="PolySi"(N=5e19) }
  { Name="BotContact" voltage=0.0 Material="Aluminum" }
}

File {
  Grid = "@tdr@"
  Parameter = "@parameter@"
  Plot = "@tdrdat@"
  Output = "@log@"
  Current = "n@node@_des.plt"
}

Plot {
  eDensity hDensity
  eCurrent/Vector hCurrent/Vector
  Current/Vector ConductionCurrent/Vector DisplacementCurrent/Vector
  Potential SpaceCharge ElectricField/Vector
  eMobility hMobility
  eVelocity/Vector hVelocity/Vector
  eDriftVelocity/Vector hDriftVelocity/Vector
  Doping DonorConcentration AcceptorConcentration
}

```

```

eSaturationVelocity hSaturationVelocity

OptBeam
OpticalGeneration
SRHRecombination SurfaceRecombination
CDL CDL1 CDL2 CDL3
eCDL1Lifetime eCDL2Lifetime hCDL1Lifetime hCDL2Lifetime
TotalRecombination
eLifetime hLifetime
eAugerRecombination hAugerRecombination
eAvalanche hAvalanche
Band2Band

ValenceBandEnergy
ConductionBandEnergy
ElectronAffinity
EquilibriumPotential
eQuasiFermi hQuasiFermi
BandGap
BandGapNarrowing EffectiveIntrinsicDensity
EffectiveBandGap
}

Physics {
  Fermi
  *EffectiveIntrinsicDensity( BandGapNarrowing ( JainRoulston ))
  Mobility (
    PhuMob ( Phosphorus )
    eHighFieldSaturation
    hHighFieldSaturation
  )
  Recombination (
    SRH (
      DopingDependence
      ElectricField( Lifetime=Hurkx DensityCorrection=None )
    )
    Auger
    Band2Band(Hurkx)
    TrapAssistedAuger
    CDL
  )
  * OptBeam (
    *   ( WaveLength = 1.2e-4      # cm
    *     WavePower = 10.0        # W/cm^2
    *     SemAbs ( model=ODB )    # 1/cm
    *     SemSurf = 3.849e-4      # cm
    *     SemWind = (0.0,@HalfSpotSize@) # cm
    *     WaveXYSigma = 1.0e-5 ) # cm
    *   )
  HeteroInterfaces
}

Physics (MaterialInterface="Oxide/Germanium") {
  Recombination( surfaceSRH )
}

Physics (Material="Silicon") {

```

```

    EffectiveIntrinsicDensity( OldSlotboom )
}

Physics (Material="Germanium") {
    Traps (
        ( eNeutral Level EnergyMid=0.3 fromMidBandGap Tunneling(Hurkx)
          Conc=1e13 eXsection=2.1e-15 hXsection=2.1e-15 )
        ( hNeutral Level EnergyMid=0.0 fromMidBandGap Tunneling(Hurkx)
          Conc=1e13 eXsection=2.1e-15 hXsection=2.1e-15 )
    )
}

#if @[string compare Traps "ON"] == 0>@
Physics (Region="R.Traps") {
    Traps (
        ( hNeutral Level EnergyMid=0.21 fromCondBand Tunneling(Hurkx)
          Conc=1e17 eXsection=2.6e-15 hXsection=2.6e-15 )
        ( eNeutral Level EnergyMid=0.27 fromValBand Tunneling(Hurkx)
          Conc=1e17 eXsection=2.6e-15 hXsection=2.6e-15 )
    )
}
#endif

Math {
    Cylindrical

    Digits=5
    ErReff(electron)=1.e10
    ErReff(hole)=1.e10
    RelErrControl

    Number_of_Threads=1
    Method=ILS

    WallClock
}

Solve {
    Poisson
    Coupled(iterations=1000) { Poisson Electron Hole }

    Quasistationary ( InitialStep=0.001 MaxStep=0.50 MinStep=1e-12
                      Increment=1.5 Decrement=2.0
                      Goal { Voltage=@Bias@ Name="TopContact" } ) {
        Coupled(iterations=10) { Poisson Electron Hole }
    }
}

```

Spatial Responsivity Simulation

```

Electrode {
    { Name="TopContact" voltage=0.0 Material="PolySi"(N=5e19) }
    { Name="BotContact" voltage=0.0 Material="Aluminum" }
}

```

```

File {
  Grid = "@tdr@"
  Parameter = "@parameter@"
  Plot = "@tdrdat@"
  Output = "@log@"
  Current = "n@node@_des.plt"
}

Plot {
  eDensity hDensity
  eCurrent/Vector hCurrent/Vector
  Current/Vector ConductionCurrent/Vector DisplacementCurrent/Vector
  Potential SpaceCharge ElectricField/Vector
  eMobility hMobility
  eVelocity/Vector hVelocity/Vector
  eDriftVelocity/Vector hDriftVelocity/Vector
  Doping DonorConcentration AcceptorConcentration
  eSaturationVelocity hSaturationVelocity

  OptBeam
  OpticalGeneration
  SRHRecombination SurfaceRecombination
  CDL CDL1 CDL2 CDL3
  eCDL1Lifetime eCDL2Lifetime hCDL1Lifetime hCDL2Lifetime
  TotalRecombination
  eLifetime hLifetime
  eAugerRecombination hAugerRecombination
  eAvalanche hAvalanche
  Band2Band

  ValenceBandEnergy
  ConductionBandEnergy
  ElectronAffinity
  EquilibriumPotential
  eQuasiFermi hQuasiFermi
  BandGap
  BandGapNarrowing EffectiveIntrinsicDensity
  EffectiveBandGap
}

Physics {
  Fermi
  *EffectiveIntrinsicDensity( BandGapNarrowing ( JainRoulston ) )
  Mobility (
    PhuMob ( Phosphorus )
    eHighFieldSaturation
    hHighFieldSaturation
  )
  Recombination (
    SRH (
      DopingDependence
      ElectricField( Lifetime=Hurkx DensityCorrection=None )
    )
    Auger
    Band2Band(Hurkx)
  )
}

```

```

    OptBeam (
      ( WaveLength = 1.2e-4      # cm
        WavePower = 10.0        # W/cm^2
        SemAbs ( model=ODB )    # 1/cm
        SemSurf = 3.849e-4      # cm
        SemWind = (4.5e-4,5.5e-4) # cm
        SemVelocity = 70        # cm/s
        WaveXYSigma = 5.0e-5 ) # cm
    )
    HeteroInterfaces
  }

Physics (MaterialInterface="Oxide/Germanium") {
  Recombination( surfaceSRH )
}

Physics (Material="Silicon") {
  EffectiveIntrinsicDensity( OldSlotboom )
}

Math {
  Digits=5
  ErReff(electron)=1.e10
  ErReff(hole)=1.e10
  RelErrControl

  Number_of_Threads=2
  Method=ILS

  WallClock
}

Solve {
  Poisson
  Coupled(iterations=1000) { Poisson Electron Hole }

  Quasistationary ( InitialStep=0.010 MaxStep=0.10 MinStep=1e-6
                    Increment=1.35 Decrement=1.5
                    Goal { Voltage=1 Name=TopContact } ) {
    Coupled(iterations=10) { Poisson Electron Hole }
  }

  NewCurrentFile = "Spatial_"
  Transient ( Initialtime=0.0 Finaltime=1e-4
              Initialstep=1e-8 Increment=1.35 Decrement=1.35
              Minstep=1e-12 Maxstep=1e-6
              Plot { Range = (0 1e-7) Intervals= 5 } ) {
    Coupled(iterations=25) { Poisson Electron Hole }
  }
}

```

Optical AC Analysis

```

File{
  Output = "@log@"
}

```

```

    ACEExtract = "n@node@_acsweep"
}

Device sige_pd {
Electrode {
    { Name="TopContact" voltage=0.0 Material="PolySi"(N=5e19) }
    { Name="BotContact" voltage=0.0 Material="Aluminum" }
}

File {
    Grid = "@tdr@"
    Parameter = "@parameter@"
    Plot = "@tdrdat@"
    Current = "n@node@_des.plt"
}

Plot {
    eDensity hDensity
    eCurrent/Vector hCurrent/Vector
    Current/Vector ConductionCurrent/Vector DisplacementCurrent/Vector
    Potential SpaceCharge ElectricField/Vector
    eMobility hMobility
    eVelocity/Vector hVelocity/Vector
    eDriftVelocity/Vector hDriftVelocity/Vector
    Doping DonorConcentration AcceptorConcentration
    eSaturationVelocity hSaturationVelocity

    OptBeam
    OpticalGeneration
    SRHRecombination SurfaceRecombination
    CDL CDL1 CDL2 CDL3
    eCDL1Lifetime eCDL2Lifetime hCDL1Lifetime hCDL2Lifetime
    TotalRecombination
    eLifetime hLifetime
    eAugerRecombination hAugerRecombination
    eAvalanche hAvalanche
    Band2Band

    ValenceBandEnergy
    ConductionBandEnergy
    ElectronAffinity
    EquilibriumPotential
    eQuasiFermi hQuasiFermi
    BandGap
    BandGapNarrowing EffectiveIntrinsicDensity
    EffectiveBandGap
}

Physics {
    Fermi
    Mobility (
        PhuMob ( Phosphorus )
        eHighFieldSaturation
        hHighFieldSaturation
    )
    *Recombination (
    *    SRH (

```

```

*           DopingDependence
*           ElectricField( Lifetime=Schenk DensityCorrection=Local )
*       )
*       Auger
*)
OptBeam (
    ( WaveLength = 1.5e-4      # cm
      WavePower = 1571.9      # W/cm^2
      SemAbs ( model=ODB )    # 1/cm
      SemSurf = 11.35e-4      # cm
      SemWind = (0.0,3.0e-4) # cm
      WaveXYSigma = 3.0e-4 ) # cm
    )

    HeteroInterfaces
}

Physics (MaterialInterface="Oxide/Germanium") {
    Recombination( surfaceSRH )
}

Physics (Material="Germanium") {
    EffectiveIntrinsicDensity( TableBGN )
#if @<[string compare Traps "ON"] == 0>@
    Traps (
        ( eNeutral Level EnergyMid=0.42 fromCondBand
          Conc=8e13 eXsection=5.0e-12 hXsection=1.0e-30 )
        ( eNeutral Level EnergyMid=0.29 fromCondBand
          Conc=8e13 eXsection=1.8e-12 hXsection=1.0e-30 )
        ( hNeutral Level EnergyMid=0.19 fromValBand
          Conc=8e13 eXsection=1.0e-30 hXsection=1.0e-12 )
    )
#endif
}

Physics (Material="PolySi") {
    EffectiveIntrinsicDensity( TableBGN )
}

Physics (Material="Silicon") {
    EffectiveIntrinsicDensity( TableBGN )
}

Physics (Material="FlawedGermanium") {
    EffectiveIntrinsicDensity( TableBGN )
}

}

System {
    Vsource_pset vdc (input 0) {dc = 0}
    Resistor_pset rn (input nside) {resistance=50}
    sige_pd pd ("TopContact"=nside "BotContact"=pside)
    Resistor_pset rp (pside 0) {resistance=67}
}

```

```

Math {
  Cylindrical

  Digits=5
  ErReff(electron)=1.e8
  ErReff(hole)=1.e8
  RelErrControl

  TrapDLN = 25
  Traps(Damping=@TrapDamp@)

  Method=Blocked SubMethod=ILS
  ACMethod=Blocked ACSubMethod=ILS
  Number_of_Threads=2

  WallClock
}

Solve {

#if @<[string compare TrapFilling "None"] == 0>@
#else
  Set(TrapFilling=@TrapFilling@)
#endif

  Poisson

  Coupled(iterations=1000) { Poisson Electron Hole }

  Quasistationary ( InitialStep=0.001 MaxStep=1.0 MinStep=1e-6
                    Increment=2.0 Decrement=2.0
                    Goal { Parameter=vdc."dc" Value=@Bias@ } ) {
    Coupled(iterations=25) { Poisson Electron Hole }
  }

#if @<[string compare TrapFilling "None"] == 0>@
#else
  Unset(TrapFilling)
#endif

  ACCoupled ( StartFrequency=1e8 EndFrequency=2e10
              NumberOfPoints=21 Decade Node(inside pside) Optical ) {
    poisson electron hole
  }
}

```

Optical Transient Analysis

```

File{
  Output = "@log@"
  ACExtract = "n@node@_acsweep"
}

Device sige_pd {

```

```

Electrode {
  { Name="TopContact" voltage=0.0 Material="PolySi"(N=5e19) }
  { Name="BotContact" voltage=0.0 Material="Aluminum" }
}

File {
  Grid = "@tdr@"
  Parameter = "@parameter@"
  Plot = "@tdrdat@"
  Current = "n@node@_des.plt"
}

Plot {
  eDensity hDensity
  eCurrent/Vector hCurrent/Vector
  Current/Vector ConductionCurrent/Vector DisplacementCurrent/Vector
  Potential SpaceCharge ElectricField/Vector
  eMobility hMobility
  eVelocity/Vector hVelocity/Vector
  eDriftVelocity/Vector hDriftVelocity/Vector
  Doping DonorConcentration AcceptorConcentration
  eSaturationVelocity hSaturationVelocity

  eTrappedCharge hTrappedCharge
  eGapStatesRecombination hGapStatesRecombination

  OptBeam
  OpticalGeneration
  SRHRecombination SurfaceRecombination
  CDL CDL1 CDL2 CDL3
  eCDL1Lifetime eCDL2Lifetime hCDL1Lifetime hCDL2Lifetime
  TotalRecombination
  eLifetime hLifetime
  eAugerRecombination hAugerRecombination
  eAvalanche hAvalanche
  Band2Band

  ValenceBandEnergy
  ConductionBandEnergy
  ElectronAffinity
  EquilibriumPotential
  eQuasiFermi hQuasiFermi
  BandGap
  BandGapNarrowing EffectiveIntrinsicDensity
  EffectiveBandGap
}

Physics {
  Fermi
  Mobility (
    PhuMob ( Phosphorus )
    eHighFieldSaturation
    hHighFieldSaturation
  )
  *Recombination (
  *   SRH (
  *     DopingDependence

```

```

*      ElectricField( Lifetime=Schenk DensityCorrection=Local )
*      )
*      Auger
*)
OptBeam (
  (
    WaveLength = 1.5e-4      # cm
    WavePower = 1571.9      # W/cm^2
    SemAbs ( model=ODB )    # 1/cm
    SemSurf = 11.35e-4     # cm
    SemWind = (0.0,3.0e-4) # cm
    WaveXYSigma = 3.0e-4   # cm
    WaveTime = (@PulseStart@,!{puts [expr
@PulseStart@+@PulseWidth@]})!)
    WaveTSigma = 1e-12
  )
)

HeteroInterfaces
}

Physics (MaterialInterface="Oxide/Germanium") {
  Recombination( surfaceSRH )
}

Physics (Material="Germanium") {
  EffectiveIntrinsicDensity( TableBGN )
#if @<[string compare Traps "ON"] == 0>@
  Traps (
    ( eNeutral Level EnergyMid=0.28 fromCondBand
      Conc=8e13 eXsection=1.8e-12 hXsection=1.0e-18 )
    ( hNeutral Level EnergyMid=0.20 fromValBand
      Conc=8e13 eXsection=5.0e-12 hXsection=1.0e-12 )
  )
#endif
}

Physics (Material="PolySi") {
  EffectiveIntrinsicDensity( TableBGN )
}

Physics (Material="Silicon") {
  EffectiveIntrinsicDensity( TableBGN )
}

Physics (Material="FlawedGermanium") {
  EffectiveIntrinsicDensity( TableBGN )
}

}

System {
  Vsource_pset vdc (input 0) {dc = 0}
  Resistor_pset ranode (input anode) {resistance=67}
  sige_pd pd ("TopContact"=anode "BotContact"=cathode)
  Resistor_pset rcathode (cathode 0) {resistance=50}
}

```

```

Math {
  Cylindrical

  Digits=5
  ErReff(electron)=1.e8
  ErReff(hole)=1.e8
  RelErrControl

  CheckTransientError
  TransientDigits=3

  TrapDLN = 25
  Traps(Damping=@TrapDamp@)

  Method=Blocked SubMethod=ILS
  ACMethod=Blocked ACSubMethod=ILS
  Number_of_Threads=2

  WallClock
}

Solve {

#if @<[string compare Traps "ON"] == 0>@
  Set(TrapFilling=p)
#else
#endif

  Poisson

  Coupled(iterations=1000) { Poisson Electron Hole }

  Quasistationary ( InitialStep=0.001 MaxStep=1.0 MinStep=1e-6
                    Increment=2.0 Decrement=2.0
                    Goal { Parameter=vdc."dc" Value=@Bias@ } ) {
    Coupled(iterations=25) { Poisson Electron Hole }
  }

#if @<[string compare Traps "ON"] == 0>@
  Unset(TrapFilling)
#else
#endif

  NewCurrentPrefix = "Pulse_"

  Transient ( Initialtime=0.0 Finaltime=@SimTime@
             Plot { Range = (!(puts [expr 5e-12+@PulseStart@])! @SimTime@)
             Intervals = 4 } ) {
    Coupled(iterations=20) { Poisson Electron Hole }
  }

}

```

Material Parameter Definition

Germanium (Key Parameters Only)

```
eDOSMass
{
  * For effective mass specificatition Formula1 (me approximation):
  * or Formula2 (Nc300) can be used :
  Formula      = 1      # [1]
  * Formula1:
  * me/m0 = [ (6 * mt)^2 * ml ]^(1/3) + mm
  * mt = a[Eg(0)/Eg(T)]
  * Nc(T) = 2(2pi*kB/h_Planck^2*me*T)^3/2 = 2.540e19 ((me/m0)*(T/300))^3/2
  a           = 0.0000e+00      # [1]
  ml          = 0.0000e+00      # [1]
  mm          = 0.55           # [1]
}

hDOSMass
{
  * For effective mass specificatition Formula1 (mh approximation):
  * or Formula2 (Nv300) can be used :
  Formula      = 1      # [1]
  * Formula1:
  * mh = m0*[(a+bT+cT^2+dT^3+eT^4)/(1+fT+gT^2+hT^3+iT^4)]^(2/3) + mm}
  * Nv(T) = 2(2pi*kB/h_Planck^2*mh*T)^3/2 = 2.540e19 ((mh/m0)*(T/300))^3/2
  a           = 0      # [1]
  b           = 0      # [K^-1]
  c           = 0      # [K^-2]
  d           = 0      # [K^-3]
  e           = 0      # [K^-4]
  f           = 0      # [K^-1]
  g           = 0      # [K^-2]
  h           = 0      # [K^-3]
  i           = 0      # [K^-4]
  mm          = 0.382    # [1]
}

Bandgap
{ * Eg = Eg0 + alpha Tpar^2 / (beta + Tpar) - alpha T^2 / (beta + T)
  * Parameter 'Tpar' specifies the value of lattice
  * temperature, at which parameters below are defined
  * Chi0 is electron affinity.
  Chi0 = 3.95988      # [eV]
  Bgn2Chi = 0.45      # [1]
  Eg0 = 0.744         # [eV]
  alpha = 4.7700e-04  # [eV K^-1]
  beta = 2.3500e+02   # [K]
  Tpar = 0.0000e+00   # [K]
}

TableBGN
{
  Acceptor 1.000e13, 0.000713
  Acceptor 2.637e13, 0.000934
}
```

```

    Acceptor 6.952e13, 0.001226
    Acceptor 1.833e14, 0.001615
    Acceptor 4.833e14, 0.002135
    Acceptor 1.274e15, 0.002835
    Acceptor 3.360e15, 0.003779
    Acceptor 8.859e15, 0.005065
    Acceptor 2.336e16, 0.006826
    Acceptor 6.158e16, 0.009258
    Acceptor 1.624e17, 0.012645
    Acceptor 4.281e17, 0.017407
    Acceptor 1.129e18, 0.024164
    Acceptor 2.976e18, 0.033851
    Acceptor 7.848e18, 0.047881
    Acceptor 2.069e19, 0.068412
    Acceptor 5.456e19, 0.098766
    Acceptor 1.438e20, 0.144089
    Acceptor 3.793e20, 0.212408
    Acceptor 1.000e21, 0.316311
    Donor 1.000e13, 0.000628
    Donor 2.637e13, 0.000822
    Donor 6.952e13, 0.001078
    Donor 1.833e14, 0.001419
    Donor 4.833e14, 0.001873
    Donor 1.274e15, 0.002481
    Donor 3.360e15, 0.003300
    Donor 8.859e15, 0.004410
    Donor 2.336e16, 0.005924
    Donor 6.158e16, 0.008003
    Donor 1.624e17, 0.010882
    Donor 4.281e17, 0.014903
    Donor 1.129e18, 0.020568
    Donor 2.976e18, 0.028628
    Donor 7.848e18, 0.040211
    Donor 2.069e19, 0.057025
    Donor 5.456e19, 0.081682
    Donor 1.438e20, 0.118207
    Donor 3.793e20, 0.172837
    Donor 1.000e21, 0.255312
}

Scharfetter * relation and trap level for SRH recombination:
{ * tau = taumin + ( taumax - taumin ) / ( 1 + ( N/Nref )^gamma)
  * tau(T) = tau * ( (T/300)^Talpha ) (TempDep)
  * tau(T) = tau * exp( Tcoeff * ((T/300)-1) ) (ExpTempDep)
    taumin = 0.0000e+00 , 0.0000e+00 # [s]
    taumax = @BulkLifetime@ , @BulkLifetime@ # [s]
    Nref = 1.0000e+16 , 1.0000e+16 # [cm^(-3)]
    gamma = 1 , 1 # [1]
    Talpha = -1.5000e+00 , -1.5000e+00 # [1]
    Tcoeff = 2.55 , 2.55 # [1]
    Etrap = 0.0000e+00 # [eV]
}

Band2BandTunneling
{ * See Sentaurus Device manual `Band-To-Band Tunneling'
  A = 8.9770e+20 # [cm / (s V^2)]
  B = 2.1466e+07 # [eV^(-3/2) V/cm]
}

```

```

hbarOmega = 0.0186 # [eV]

* Traditional models for the following keywords in input file:
* Band2Band(E1) : A1*E*exp(-B1/E)
* Band2Band(E1_5): A1_5*E^1.5*exp(-B1_5/E)
* Band2Band(E2) : A2*E^2*exp(-B2/E)
  A1 = 1.1000e+27 # [1/cm/sec/V]
  B1 = 2.1300e+07 # [V/cm]
  A1_5 = 1.9000e+24 # [1/cm/sec/V^1.5]
  B1_5 = 2.1900e+07 # [V/cm]
  A2 = 3.5000e+21 # [1/cm/sec/V^2]
  B2 = 2.2500e+07 # [V/cm]

* Hurkx model for the following keywords in input file:
* Band2Band(Hurkx) : -Agen*D*(E/E0)^Pgen*exp(-Bgen*(Eg/Eg300)^1.5/E) if D
< 0
* -Arec*D*(E/E0)^Prec*exp(-Brec*(Eg/Eg300)^1.5/E) if D
> 0
* D = (n*p-ni^2)/(n+ni)/(p+ni)*(1-|alpha|)+alpha, E0 =
1 V/cm
* So, if alpha = 0, it's original Hurkx model,
* if alpha = -1, it's only generation,
* if alpha = +1, it's only recombination.
  Agen = 3.5000e+21 # [1/cm^3/sec]
  Bgen = 2.2500e+07 # [V/cm]
  Pgen = 2 # [1]
  Arec = 3.5000e+21 # [1/cm^3/sec]
  Brec = 2.2500e+07 # [V/cm]
  Prec = 2 # [1]
  alpha = 0.0000e+00 # [1]

* min length to interfaces (for traditional & Hurkx models):
  dDist = 0.0000e+00 # [cm]
* min potential difference on length dPot/E (for traditional & Hurkx
models):
  dPot = 0.0000e+00 # [V]
}

PhuMob:
{
  mumax_As = 397.7 # [cm2/(Vs)]
  mumin_As = 61.2 # [cm2/Vs]
  theta_As = 2.285 # [1]
  n_ref_As = 9.6800e+16 # [cm^(-3)]
  alpha_As = 0.68 # [1]
  mumax_P = 397.7 # [cm2/(Vs)]
  mumin_P = 61.2 # [cm2/Vs]
  theta_P = 2.285 # [1]
  n_ref_P = 9.6800e+16 # [cm^(-3)]
  alpha_P = 0.68 # [1]
  mumax_B = 792.048 # [cm2/(Vs)]
  mumin_B = 69.0 # [cm2/Vs]
  theta_B = 2.247 # [1]
  n_ref_B = 2.2300e+17 # [cm^(-3)]
  alpha_B = 0.719 # [1]
  nref_D = 4.0000e+20 # [cm^(-3)]
  nref_A = 7.2000e+20 # [cm^(-3)]
}

```

```

    cref_D = 0.21 # [1]
    cref_A = 0.5 # [1]
    me_over_m0 = 1 # [1]
    mh_over_m0 = 1.258 # [1]
    f_CW = 2.459 # [1]
    f_BH = 3.828 # [1]
}

HighFieldDependence:
{ * Caughey-Thomas model:
* mu_highfield = ( (alpha+1)*mu_lowfield ) /
* ( alpha + ( 1 + ( (alpha+1)*mu_lowfield*E/vsat)^beta )^(1/beta) )
* beta = beta0 (T/T0)^betaexp.
  beta0 = 1.109 , 1.213 # [1]
  betaexp = 0.66 , 0.17 # [1]
  alpha = 0.0000e+00 , 0.0000e+00 # [1]

* Smoothing parameter for HydroHighField Caughey-Thomas model:
* if T1 < Tc < (1+K_dT)*T1, then smoothing between low field mobility
* and HydroHighField mobility is used.
  K_dT = 0.2 , 0.2 # [1]
* Transferred-Electron Effect:
* mu_highfield = (mu_lowfield+(vsat/E)*(E/E0_TrEf)^4)/(1+(E/E0_TrEf)^4)
  E0_TrEf = 4.0000e+03 , 4.0000e+03 # [1]
  Ksmooth_TrEf = 1 , 1 # [1]

* For vsat either Formula1 or Formula2 can be used.
  Vsat_Formula = 1 , 1 # [1]
* Formula1 for saturation velocity:
* vsat = vsat0 (T/T0)^(-Vsatexp)
* (Parameter Vsat_Formula has to be not equal to 2)
  vsat0 = 7.4300e+06 , 7.4300e+06 # [1]
  vsatexp = 0.87 , 0.52 # [1]
}

```

FlawedGermanium (Differences From Germanium Only)

```

Scharfetter * relation and trap level for SRH recombination:
{ * tau = taumin + ( taumax - taumin ) / ( 1 + ( N/Nref )^gamma)
* tau(T) = tau * ( (T/300)^Talpha ) (TempDep)
* tau(T) = tau * exp( Tcoeff * ((T/300)-1) ) (ExpTempDep)
  taumin = 0.0000e+00 , 0.0000e+00 # [s]
  taumax = @FlawedLifetime@ , @FlawedLifetime@ # [s]
  Nref = 1.0000e+16 , 1.0000e+16 # [cm^(-3)]
  gamma = 1 , 1 # [1]
  Talpha = -1.5000e+00 , -1.5000e+00 # [1]
  Tcoeff = 2.55 , 2.55 # [1]
  Etrap = 0.0000e+00 # [eV]
}

```

Silicon (Key Parameters Only)

eDOSMass

```

{
* For effective mass specificatition Formula1 (me approximation):
* or Formula2 (Nc300) can be used :
  Formula      = 1      # [1]
* Formula1:
* me/m0 = [ (6 * mt)^2 * ml ]^(1/3) + mm
* mt = a[Eg(0)/Eg(T)]
* Nc(T) = 2(2pi*kB/h_Planck^2*me*T)^3/2 = 2.540e19 ((me/m0)*(T/300))^3/2
  a           = 0.1905      # [1]
  ml          = 0.9163      # [1]
  mm          = 0.0000e+00   # [1]
}

hDOSMass
{
* For effective mass specificatition Formula1 (mh approximation):
* or Formula2 (Nv300) can be used :
  Formula      = 1      # [1]
* Formula1:
* mh = m0*{[(a+bT+cT^2+dT^3+eT^4)/(1+fT+gT^2+hT^3+iT^4)]^(2/3) + mm}
* Nv(T) = 2(2pi*kB/h_Planck^2*mh*T)^3/2 = 2.540e19 ((mh/m0)*(T/300))^3/2
  a           = 0.443587    # [1]
  b           = 0.003609528  # [K^-1]
  c           = 0.0001173515 # [K^-2]
  d           = 1.263218e-06 # [K^-3]
  e           = 3.025581e-09 # [K^-4]
  f           = 0.004683382  # [K^-1]
  g           = 0.0002286895 # [K^-2]
  h           = 7.469271e-07 # [K^-3]
  i           = 1.727481e-09 # [K^-4]
  mm          = 0           # [1]
}

Bandgap
{ * Eg = Eg0 + dEg0 + alpha Tpar^2 / (beta + Tpar) - alpha T^2 / (beta + T)
  * dEg0(<bgn_model_name>) is a band gap correction term. It is used
  together with
  * an appropriate BGN model, if this BGN model is chosen in Physics section
  * Parameter 'Tpar' specifies the value of lattice
  * temperature, at which parameters below are defined
  * Chi0 is electron affinity.
  Chi0 = 4.05      # [eV]
  Bgn2Chi = 0.48   # [1]
  Eg0 = 1.16964   # [eV]
  dEg0(Bennett) = 0.0000e+00      # [eV]
  dEg0(Slotboom) = -4.7950e-03    # [eV]
  dEg0(OldSlotboom) = -1.5950e-02 # [eV]
  dEg0(delAlamo) = -1.4070e-02    # [eV]
  alpha = 4.7300e-04      # [eV K^-1]
  beta = 6.3600e+02      # [K]
  Tpar = 0.0000e+00      # [K]
}

TableBGN
{
  Acceptor 1.000e18, 0.031287
  Acceptor 1.668e18, 0.036888
}

```

```

    Acceptor 2.783e18, 0.043583
    Acceptor 4.642e18, 0.051607
    Acceptor 7.743e18, 0.061251
    Acceptor 1.292e19, 0.072871
    Acceptor 2.154e19, 0.086914
    Acceptor 3.594e19, 0.103932
    Acceptor 5.995e19, 0.124614
    Acceptor 1.000e20, 0.149822
    Donor 1.000e18, 0.026253
    Donor 1.668e18, 0.030795
    Donor 2.783e18, 0.036184
    Donor 4.642e18, 0.042590
    Donor 7.743e18, 0.050223
    Donor 1.292e19, 0.059340
    Donor 2.154e19, 0.070256
    Donor 3.594e19, 0.083357
    Donor 5.995e19, 0.099123
    Donor 1.000e20, 0.118144
}

Scharfetter * relation and trap level for SRH recombination:
{ * tau = taumin + ( taumax - taumin ) / ( 1 + ( N/Nref )^gamma)
  * tau(T) = tau * ( (T/300)^Talpha ) (TempDep)
  * tau(T) = tau * exp( Tcoeff * ((T/300)-1) ) (ExpTempDep)
    taumin = 0.0000e+00 , 0.0000e+00 # [s]
    taumax = 1.0000e-05 , 3.0000e-06 # [s]
    Nref = 1.0000e+16 , 1.0000e+16 # [cm^(-3)]
    gamma = 1 , 1 # [1]
    Talpha = -1.5000e+00 , -1.5000e+00 # [1]
    Tcoeff = 2.55 , 2.55 # [1]
    Etrap = 0.0000e+00 # [eV]
}

Band2BandTunneling
{ * See Sentaurus Device manual `Band-To-Band Tunneling'
  A = 8.9770e+20 # [cm / (s V^2)]
  B = 2.1466e+07 # [eV^(-3/2) V/cm]
  hbarOmega = 0.0186 # [eV]

  * Traditional models for the following keywords in input file:
  * Band2Band(E1) : A1*E*exp(-B1/E)
  * Band2Band(E1_5) : A1_5*E^1.5*exp(-B1_5/E)
  * Band2Band(E2) : A2*E^2*exp(-B2/E)
    A1 = 1.1000e+27 # [1/cm/sec/V]
    B1 = 2.1300e+07 # [V/cm]
    A1_5 = 1.9000e+24 # [1/cm/sec/V^1.5]
    B1_5 = 2.1900e+07 # [V/cm]
    A2 = 3.5000e+21 # [1/cm/sec/V^2]
    B2 = 2.2500e+07 # [V/cm]

  * Hurkx model for the following keywords in input file:
  * Band2Band(Hurkx) : -Agen*D*(E/E0)^Pgen*exp(-Bgen*(Eg/Eg300)^1.5/E) if D
< 0
  * -Arec*D*(E/E0)^Prec*exp(-Brec*(Eg/Eg300)^1.5/E) if D
> 0
  * D = (n*p-ni^2)/(n+ni)/(p+ni)*(1-|alpha|)+alpha, E0 =
1 V/cm

```

```

*           So, if alpha = 0, it's original Hurkx model,
*           if alpha = -1, it's only generation,
*           if alpha = +1, it's only recombination.
Agen = 3.5000e+21 # [1/cm^3/sec]
Bgen = 2.2500e+07 # [V/cm]
Pgen = 2 # [1]
Arec = 3.5000e+21 # [1/cm^3/sec]
Brec = 2.2500e+07 # [V/cm]
Prec = 2 # [1]
alpha = 0.0000e+00 # [1]

* min length to interfaces (for traditional & Hurkx models):
dDist = 0.0000e+00 # [cm]
* min potential difference on length dPot/E (for traditional & Hurkx
models):
dPot = 0.0000e+00 # [V]
}

PhuMob:
{ * Philips Unified Mobility Model:
mumax_As = 1.4170e+03 # [cm^2/Vs]
mumin_As = 52.2 # [cm^2/Vs]
theta_As = 2.285 # [1]
n_ref_As = 9.6800e+16 # [cm^(-3)]
alpha_As = 0.68 # [1]
mumax_P = 1.4140e+03 # [cm^2/Vs]
mumin_P = 68.5 # [cm^2/Vs]
theta_P = 2.285 # [1]
n_ref_P = 9.2000e+16 # [cm^(-3)]
alpha_P = 0.711 # [1]
mumax_B = 4.7050e+02 # [cm^2/Vs]
mumin_B = 44.9 # [cm^2/Vs]
theta_B = 2.247 # [1]
n_ref_B = 2.2300e+17 # [cm^(-3)]
alpha_B = 0.719 # [1]
nref_D = 4.0000e+20 # [cm^(-3)]
nref_A = 7.2000e+20 # [cm^(-3)]
cref_D = 0.21 # [1]
cref_A = 0.5 # [1]
me_over_m0 = 1 # [1]
mh_over_m0 = 1.258 # [1]
f_CW = 2.459 # [1]
f_BH = 3.828 # [1]
f_e = 1 # [1]
f_h = 1 # [1]
}

HighFieldDependence:
{ * Caughey-Thomas model:
* mu_highfield = ( (alpha+1)*mu_lowfield ) /
* ( alpha + ( 1 + ( (alpha+1)*mu_lowfield*E/vsat)^beta )^(1/beta) )
* beta = beta0 (T/T0)^betaexp.
beta0 = 1.109 , 1.213 # [1]
betaexp = 0.66 , 0.17 # [1]
alpha = 0.0000e+00 , 0.0000e+00 # [1]

* Smoothing parameter for HydroHighField Caughey-Thomas model:

```

```

* if T1 < Tc < (1+K_dT)*T1, then smoothing between low field mobility
* and HydroHighField mobility is used.
  K_dT = 0.2 ,      0.2 # [1]
* Transferred-Electron Effect:
* mu_highfield = (mu_lowfield+(vsat/E)*(E/E0_TrEf)^4)/(1+(E/E0_TrEf)^4)
  E0_TrEf = 4.0000e+03 ,      4.0000e+03 # [1]
  Ksmooth_TrEf = 1 , 1 # [1]

* For vsat either Formula1 or Formula2 can be used.
  Vsat_Formula = 1 , 1 # [1]
* Formula1 for saturation velocity:
* vsat = vsat0 (T/T0)^(-Vsatexp)
* (Parameter Vsat_Formula has to be not equal to 2)
  vsat0 = 1.0700e+07 ,      8.3700e+06 # [1]
  vsatexp = 0.87 ,      0.52 # [1]
}

```

Syntax Required for Explicit Trap Definition

Material Parameter File Syntax

```

Traps
{
* G is degeneracy factor
  G = 1 , 1 # [1]

* XsecFormula=1: Xsec(F) = Xsec
* XsecFormula=2: Xsec(F) = Xsec*(1+a1*(F/F0)^p1+a2*(F/F0)^p2)^p0, F0 =
1 V/cm
* XsecFormula=3: Xsec(F) = Xsec*(1+Gt), Gt is Hurkx TATunneling factor
* XsecFormula=4: Xsec(F) = Xsec*(1+Gpf), Gpf is Poole-Frenkel factor
  XsecFormula = 1 , 2 # [1]
  Xsec = 5.0000e-12 ,      2.5000e-22 # [cm^2]
  a1 = 0.0000e+00 ,      5.0000e-8 # [1]
  p1 = 1 , 3 # [1]
  a2 = 0.0000e+00 ,      0.0000e+00 # [1]
  p2 = 1 , 1 # [1]
  p0 = 1 , 1 # [1]

* VthFormula=1: Vth(T) = Vth*(T/300)^1/2
* VthFormula=2: Vth(T) = (3*k*T/m_300)^1/2,
* m_300 is DOS mass calculated at T=300
  VthFormula = 1 , 1 # [1]
  Vth = 2.0420e+07 ,      1.5626e+07 # [cm/s]
  Jcoef = 1.0000e+00 ,      1.0000e+00 # [1]

* Tunneling to traps is determined by the interaction volume
* TrapVolume, the Huang-Rhys factor, and the Phonon energy.
  TrapVolume = 0.0000e+00 # [um^3]
  HuangRhys = 0.0000e+00 # [1]
  PhononEnergy = 0.0000e+00 # [eV]

* Constant emission rate term
  ConstEmissionRate = 0.0000e+00 ,      0.0000e+00 # [1/s]
}

```

```
}
```

Command File Syntax

```
Physics (Material="Germanium") {  
  Traps (  
    ( Acceptor Level EnergyMid=0.42 fromCondBand Conc=1.32e15 )  
  )  
}
```

```
Physics (Material="FlawedGermanium") {  
  Traps (  
    ( Acceptor Level EnergyMid=0.21 fromCondBand Conc=1.92e18 )  
  )  
}
```


Appendix B – Matlab Scripts

Dark Current Fitting

fit_single_temp_version2.m

```
clear all

temp = 300;
meas_date = '2007-08-16';
sim_dir = ['~/sim_results/ge-si_dark_iv/', num2str(temp), 'K/'];
meas_dir = '~/data/cryostation/';

load([sim_dir, 'sim_summary.mat'])

voltages = 0.1:0.1:5.0;

num_volt = length(voltages);
num_wind = length(windows);
num_bulk = length(bulk_lifetimes);
num_flaw = length(flaw_lifetimes);

min_flaw_log = floor(log10(flaw_lifetimes(1)));
max_flaw_log = ceil(log10(flaw_lifetimes(num_flaw)));
ave_flaw = 10^((min_flaw_log+max_flaw_log)/2);

min_bulk_log = floor(log10(bulk_lifetimes(1)));
max_bulk_log = ceil(log10(bulk_lifetimes(num_bulk)));
ave_bulk = 10^((min_bulk_log+max_bulk_log)/2);

meas_current = zeros(num_volt,num_wind);

for circ_index=1:num_wind
    load([meas_dir, 'iv_11-8_sample-1_die-3_circle-', int2str(circ_index),
    '_' ,meas_date, '_', num2str(temp), 'K_iv.mat'])

    start_index = 1;
    while iv_data(start_index,1) < 0.001
        start_index = start_index + 1;
    end

    fitcurrent_vs_voltage =
    fit(squeeze(iv_data(start_index:end,1)),squeeze(iv_data(start_index:end,2)), '
    pchipinterp');

    for volt_index = 1:num_volt
```

```

        meas_current(volt_index,circ_index) =
fitcurrent_vs_voltage(voltages(volt_index));
    end
end

sim_flow_time = zeros(num_volt,num_wind,num_bulk);

logged_flow_lifetimes = log10(fl原因_lifetimes);

for wind_index=1:num_wind
    for volt_index=1:num_volt
        for bulk_index=1:num_bulk
            sim_current = zeros(num_flow,1);

            voltage = voltages(volt_index);
            target_current = meas_current(volt_index,wind_index);

            for flow_index=1:num_flow
                sim_current(flow_index) =
getSimCurrent(sim_dir,voltage,wind_index,bulk_index,flow_index);
            end

            if target_current < min(sim_current) || target_current >
max(sim_current)
                warning('Target current out of range for following case')
                wind_index
                volt_index
                bulk_index
                target_current
                min_sim_current = min(sim_current)
                max_sim_current = max(sim_current)
            else
                fitcurrent_vs_logflaw =
fit(logged_flow_lifetimes,sim_current,'pchipinterp');
                fzero_time_result = fzero(@(x) fitcurrent_vs_logflaw(x)-
target_current, log10(ave_flow));
                sim_flow_time(volt_index,wind_index,bulk_index) =
10^fzero_time_result;
            end
        end
    end
end

end

%
% Plot individual fit curves
%

for fig_index=1:5
    figure(fig_index)
    for row = 1:3
        for column = 1:4
            if (fig_index-1)*12+(row-1)*4+column <= num_volt
                subplot(3,4,(row-1)*4+column)
                for wind_index=1:num_wind

```

```

        switch wind_index
            case 1
                line_string = 'rd-';
            case 2
                line_string = 'bd-';
            case 3
                line_string = 'gd-';
            case 4
                line_string = 'cd-';
            case 5
                line_string = 'md-';
            case 6
                line_string = 'yd-';
            otherwise
                line_string = 'bd-';
        end
        loglog(bulk_lifetimes,squeeze(sim_flaw_time((fig_index-
1)*12+(row-1)*4+column,wind_index,:)),line_string)
        hold on
    end
    title(['Simulated Lifetimes Matching Measured Currents - '
num2str(voltages((fig_index-1)*12+(row-1)*4+column)), 'V Bias'])
    xlabel('Germanium Film Lifetime (s)')
    ylabel('Flawed Germanium Lifetime (s)')
    hold off
end
end
end
end

%
% Calculate and plot the average and variance of flaw lifetime as a
% function of bulk lifetime
%

% Generate fitlines with data endpoints for all simulations
for volt_index=1:num_volt
    for wind_index=1:num_wind
        clear flaw_times
        clear bulk_times

        max_bulk_time = 0;
        min_bulk_time = 0;
        index = 1;

        for bulk_index=1:num_bulk
            if bulk_lifetimes(bulk_index) ~= 0
                if min_bulk_time == 0
                    min_bulk_time = bulk_lifetimes(bulk_index);
                end

                flaw_times(index) =
sim_flaw_time(volt_index,wind_index,bulk_index);
                bulk_times(index) = bulk_lifetimes(bulk_index);
            end
        end
    end
end
end
end

```

```

        max_bulk_time = bulk_lifetimes(bulk_index);
        index = index + 1;
    end
end

if index < 3
    error('only one data point for fitting')
else
    fit_data(volt_index,wind_index).min_bulk_time = min_bulk_time;
    fit_data(volt_index,wind_index).max_bulk_time = max_bulk_time;
    fit_data(volt_index,wind_index).fit_func =
fit(bulk_times',flaw_times','pchipinterp');
    end
end
end

% Calculate the best guess bulk and flaw lifetimes
lifetime_averages = zeros(num_volt,2); % column 1, bulk; column 2, flaw
lifetime_variances = zeros(num_volt,2); % column 1, bulk; column 2, flaw

for volt_index=1:num_volt
    clear fit_intersections
    index = 1;

    for n=1:num_wind
        for m=1:num_wind
            if n ~= m
                min_bulk_n = fit_data(volt_index,n).min_bulk_time;
                max_bulk_n = fit_data(volt_index,n).max_bulk_time;
                min_bulk_m = fit_data(volt_index,m).min_bulk_time;
                max_bulk_m = fit_data(volt_index,m).max_bulk_time;
                min_bulk = max(min_bulk_n,min_bulk_m);
                max_bulk = min(max_bulk_n,max_bulk_m);

                if max_bulk > min_bulk
                    mid_bulk = 10^((log10(min_bulk) + log10(max_bulk))/2);
                    start_flaw_time_n =
fit_data(volt_index,n).fit_func(min_bulk);
                    start_flaw_time_m =
fit_data(volt_index,m).fit_func(min_bulk);
                    end_flaw_time_n =
fit_data(volt_index,n).fit_func(max_bulk);
                    end_flaw_time_m =
fit_data(volt_index,m).fit_func(max_bulk);
                    %if sign(log10(start_flaw_time_n)-
log10(start_flaw_time_m)) ~= sign(log10(end_flaw_time_n)-
log10(end_flaw_time_m))
                        fit_intersections(index,1) = 10.^(fzero(@(x)
fit_data(volt_index,n).fit_func(10.^(x))-
fit_data(volt_index,m).fit_func(10.^(x)), log10(mid_bulk)));
                        fit_intersections(index,2) =
fit_data(volt_index,n).fit_func(fit_intersections(index,1));
                        index = index + 1;
                    %else
                    %    warning('Non-intersecting fit lines')
                end
            end
        end
    end
end

```

```

        %     volt_index
        %     n
        %     m
        %end
    else
        warning('Non-overlapping fit windows')
        volt_index
        n
        m
    end
end
end
end
means = mean(fit_intersections,1);
vars = var(fit_intersections,0,1);
lifetime_averages(volt_index,1) = means(1);
lifetime_averages(volt_index,2) = means(2);
lifetime_variances(volt_index,1) = vars(1);
lifetime_variances(volt_index,2) = vars(2);
end

lifetime_voltages = voltages

% Save the extracted lifetimes to the simulation directory
data_file = [sim_dir, 'extracted_lifetimes.mat'];
save(data_file, 'lifetime_voltages', 'lifetime_averages', 'lifetime_variances');

% Plot fit results
figure(10)
subplot(2,1,1)
semilogy(voltages, squeeze(lifetime_averages(:,1)), 'b.')
title('Fit Bulk Lifetime v.s. Voltage')
xlabel('Voltage (V)')
ylabel('Bulk Carrier Lifetime (s)')
subplot(2,1,2)
semilogy(voltages, squeeze(lifetime_averages(:,2)), 'b.')
title('Fit Flaw Lifetime v.s. Voltage')
xlabel('Voltage (V)')
ylabel('Flawed Carrier Lifetime (s)')

% Plot fit results with errorbars
%figure(3)
%subplot(2,1,1)
%errorbar(voltages, squeeze(lifetime_averages(:,1)), squeeze(lifetime_variances
(:,1)), 'b.')
%set(gca, 'YScale', 'log')
%title('Fit Bulk Lifetime v.s. Voltage')
%xlabel('Voltage (V)')
%ylabel('Bulk Carrier Lifetime (s)')
%subplot(2,1,2)
%errorbar(voltages, squeeze(lifetime_averages(:,2)), squeeze(lifetime_variances
(:,2)), 'b.')
%set(gca, 'YScale', 'log')
%title('Fit Flaw Lifetime v.s. Voltage')
%xlabel('Voltage (V)')
%ylabel('Flawed Carrier Lifetime (s)')

```

getSimCurrent.m

```
function sim_current =
getSimCurrent(sim_dir,voltage,wind_index,life_index,flaw_index)

load([sim_dir 'sim_data_' int2str(wind_index) '_' int2str(life_index) '_'
int2str(flaw_index) '.mat']);

start_index = 1;
while sim_data(start_index,1) < 0.001
    start_index = start_index + 1;
end

fitcurrent_vs_voltage =
fit(squeeze(sim_data(start_index:end,1)),squeeze(sim_data(start_index:end,2))
,'pchipinterp');
sim_current = fitcurrent_vs_voltage(voltage);
```

fit_lifetimes_vs_field.m

```
clear all

temp = 300; % K

h = 6.62620e-34; % J s
q = 1.602e-19; % C
e_0 = 8.854e-14; % F cm-1
kB = 1.38e-23; % J K-1
m_0 = 9.11e-31; % kg

e_Ge = e_0 * 16.2; % F cm-1
e_Ge_pf = e_0 * 15.8; % F cm-1
ni_Ge = 8.5163e11; % cm-3
m_eff_cond = 0.12*m_0; % kg
v_th_Ge_mks = sqrt(2*kB*temp./m_eff_cond); % m/s
v_th_Ge = v_th_Ge_mks*100; % cm/s

flaw_depth = 100e-7; % cm
N_t_midgap = 1e8*1.6e6; % cm-3

Nc_Ge = 1.98e15*temp^(3/2);
Nv_Ge = 9.6e14*temp^(3/2);
Ec_Ge = 0.63; % eV
Eg_Ge = 0.63; % eV
Ei_Ge = Ec_Ge./2 + kB./2.*temp.*log(Nc_Ge./Nv_Ge); % [eV]

Et_bulk = Ec_Ge - 0.29; % eV (Dislocation assumpt)
Et_edge = Ec_Ge - 0.21; % eV (A-center assumpt)
Nt_bulk = 1e15; % cm-3
Nt_edge = 1e18; % cm-3
```

```

cross_bulk_elec_baumann = 1.8e-12./v_th_Ge;          % cm2

sim_dir = ['~/sim_results/ge-si_dark_iv/', num2str(temp),'K/'];
%sim_dir = ['C:\Userdata\Jason\Hoyt Diode Data\sim_', num2str(temp),'K\'];

load([sim_dir, 'fields_300K.mat'])
load([sim_dir, 'extracted_lifetimes.mat'])

numpoints = length(lifetime_voltages);

center_field_vs_voltage = fit(sim_voltages,sim_center_fields,'pchipinterp');
edge_field_vs_voltage = fit(sim_voltages,sim_edge_fields,'pchipinterp');

voltages = lifetime_voltages;

center_fields = center_field_vs_voltage(voltages);
edge_fields = edge_field_vs_voltage(voltages);

% Depletion Region Generation Rate extrapolation

bulk_lifetimes = lifetime_averages(:,1);
flawed_lifetimes = lifetime_averages(:,2);
U_bulk = ni_Ge./(2*bulk_lifetimes);
U_flawed_volume = ni_Ge./(2*flawed_lifetimes);
U_flawed_area = flaw_depth*U_flawed_volume;

% Calculate Cross Sections Term

cross_bulk = 2./(v_th_Ge.*Nt_bulk.*bulk_lifetimes);
cross_flaw = 2./(v_th_Ge.*Nt_edge.*flawed_lifetimes);

% Plot Cross Section Terms

figure(1)
subplot(2,2,1)
semilogy(center_fields,cross_bulk,'b.')
xlabel('Electric Field (V/cm)')
ylabel('Combined Bulk Cross Sections (cm^2)')
subplot(2,2,2)
semilogy(edge_fields,cross_flaw,'b.')
xlabel('Electric Field (V/cm)')
ylabel('Combined Surface Cross Sections (cm^2)')
subplot(2,2,3)
plot(center_fields,cross_bulk,'b.')
xlabel('Electric Field (V/cm)')
ylabel('Combined Bulk Cross Sections (cm^2)')
subplot(2,2,4)
plot(edge_fields,cross_flaw,'b.')
xlabel('Electric Field (V/cm)')
ylabel('Combined Surface Cross Sections (cm^2)')

%% Cross Section Enhancement Models

```

```

% % Basic Poole-Frenkel
%
% cross_hole_center = [ 1e-12 ];
% cross_elec_center = [ 1e-17];
%
% cross_hole_edge = [ 1e-12 ];
% cross_elec_edge = [ 1e-16 ];
%
% num_hole_cross = length(cross_hole_center);
% num_elec_cross = length(cross_elec_center);
%
% delta_em_center = sqrt(q.^3.*100.*center_fields./pi./e_Ge_pf);
% delta_em_edge = sqrt(q.^3.*100.*edge_fields./pi./e_Ge_pf);
%
% enhance_factor_cond_center = 1+exp(delta_em_center./(kB*temp));
% enhance_factor_cond_edge = 1+exp(delta_em_edge./(kB*temp));
% enhance_factor_val_center = ones(numpoints,1);
% enhance_factor_val_edge = ones(numpoints,1);

% % Sentaurus PooleFrenkel
%
% cross_hole_center = [ 6.75e-13 6.5e-13 6.25e-13];
% cross_elec_center = [ 2e-18 1.5e-18 1e-18];
%
% cross_hole_edge = [ 6e-13 4e-13 2e-13];
% cross_elec_edge = [ 5e-16 2.5e-16 1e-16];
%
% num_hole_cross = length(cross_hole_center);
% num_elec_cross = length(cross_elec_center);
%
% fp_sent_alpha_center =
1./(kB*temp).*sqrt(q^3*100*center_fields./pi./e_Ge_pf);
% fp_sent_alpha_edge = 1./(kB*temp).*sqrt(q^3*100*edge_fields./pi./e_Ge_pf);
%
% fp_sent_gamma_center = (fp_sent_alpha_center.^-
2).*(1+(fp_sent_alpha_center-1).*exp(fp_sent_alpha_center))-0.5;
% fp_sent_gamma_edge = (fp_sent_alpha_edge.^-2).*(1+(fp_sent_alpha_edge-
1).*exp(fp_sent_alpha_edge))-0.5;
%
% enhance_factor_cond_center = 1+fp_sent_gamma_center;
% enhance_factor_cond_edge = 1+fp_sent_gamma_edge;
% enhance_factor_val_center = ones(numpoints,1);
% enhance_factor_val_edge = ones(numpoints,1);

% % Sentaurus J-Model
%
% cross_hole_center = [ 5e-13 2.5e-13 1e-13];
% cross_elec_center = [ 5e-17 2.5e-17 1e-17];
%
% cross_hole_edge = [ 5e-13 2.5e-13 1e-13];
% cross_elec_edge = [ 5e-16 2.5e-16 1e-13];
%
% num_hole_cross = length(cross_hole_center);
% num_elec_cross = length(cross_elec_center);
%
% a1 = 1e2;

```

```

% a2 = 0.0;
% p0 = 0.5;
% p1 = 1;
% p2 = 1;
% F0 = 1; % V/cm
%
% enhance_factor_cond_center =
(1+a1*(center_fields./F0).^p1+a2*(center_fields./F0).^p2).^p0;
% enhance_factor_cond_edge =
(1+a1*(edge_fields./100).^p1+a2*(edge_fields./100).^p2).^p0;
% enhance_factor_val_center = ones(numpoints,1);
% enhance_factor_val_edge = ones(numpoints,1);

% Sentaurus Hurkx TAT Model

m_tunnel_cond = m_0 * 0.33;
m_tunnel_val = m_0 * 0.20;

En_cond_center = Ec_Ge - Et_bulk;
En_cond_edge = Ec_Ge - Et_edge;
En_val_center = Eg_Ge - En_cond_center;
En_val_edge = Eg_Ge - En_cond_edge;

F_rel_cond_center = center_fields.*q.*h./sqrt(8*m_tunnel_cond*kB^3*temp^3);
F_rel_val_center = center_fields.*q.*h./sqrt(8*m_tunnel_cond*kB^3*temp^3);
F_rel_cond_edge = edge_fields.*q.*h./sqrt(8*m_tunnel_cond*kB^3*temp^3);
F_rel_val_edge = edge_fields.*q.*h./sqrt(8*m_tunnel_cond*kB^3*temp^3);

gamma_tat_cond_center = quadv(@(u) exp(u-
2./3.*sqrt(u.^3)./F_rel_cond_center),0,En_cond_center./kB./temp);
gamma_tat_val_center = quadv(@(u) exp(u-
2./3.*sqrt(u.^3)./F_rel_val_center),0,En_val_center./kB./temp);
gamma_tat_cond_edge = quadv(@(u) exp(u-
2./3.*sqrt(u.^3)./F_rel_cond_edge),0,En_cond_edge./kB./temp);
gamma_tat_val_edge = quadv(@(u) exp(u-
2./3.*sqrt(u.^3)./F_rel_val_edge),0,En_val_edge./kB./temp);

enhance_factor_cond_center = 1+gamma_tat_cond_center;
enhance_factor_val_center = 1+gamma_tat_val_center;
enhance_factor_cond_edge = 1+gamma_tat_cond_edge;
enhance_factor_val_edge = 1+gamma_tat_val_edge;

% Plot the Enhancement Factors

figure(2)
subplot(2,1,1)
plot(center_fields,enhance_factor_cond_center, 'bo', edge_fields,
enhance_factor_cond_edge, 'b+', center_fields,enhance_factor_val_center, 'ro',
edge_fields, enhance_factor_val_edge, 'r+')
xlabel('Electric Field (V/cm)')
ylabel('Cross Section Enhancement Factor')
subplot(2,1,2)
semilogy(center_fields,enhance_factor_cond_center, 'bo', edge_fields,
enhance_factor_cond_edge, 'b+', center_fields,enhance_factor_val_center, 'ro',
edge_fields, enhance_factor_val_edge, 'r+')

```

```

xlabel('Electric Field (V/cm)')
ylabel('Cross Section Enhancement Factor')

% Generate Combined Cross Section Term With Enhancement Factor

combined_cross_center = zeros(numpoints,num_elec_cross,num_hole_cross);
for i=1:numpoints
    for j=1:num_elec_cross
        for k=1:num_hole_cross
            combined_cross_center(i,j,k) =
cross_hole_center(k).*cross_elec_center(j).*enhance_factor_cond_center(i).*en
hance_factor_val_center(i)./(cross_elec_center(j).*enhance_factor_cond_center
(i).*exp((Et_bulk-
Ei_Ge)/(kB*temp/q))+cross_hole_center(k).*enhance_factor_val_center(i).*exp((
Ei_Ge-Et_bulk)./(kB*temp/q)));
            combined_cross_edge(i,j,k) =
cross_hole_edge(k).*cross_elec_edge(j).*enhance_factor_cond_edge(i).*enhance_
factor_val_edge(i)./(cross_elec_edge(j).*enhance_factor_cond_edge(i).*exp((Et
_bulk-
Ei_Ge)/(kB*temp/q))+cross_hole_edge(k).*enhance_factor_val_edge(i).*exp((Ei_G
e-Et_bulk)./(kB*temp/q)));
        end
    end
end

% Plot the models

figure(3)

for j=1:num_elec_cross
    for k=1:num_hole_cross
        switch mod((j-1)*num_hole_cross+k,6)
            case 0
                line_string = 'r.';
            case 1
                line_string = 'b.';
            case 2
                line_string = 'g.';
            case 3
                line_string = 'c.';
            case 4
                line_string = 'm.';
            case 5
                line_string = 'y.';
        end
        subplot(2,2,1)
        semilogy(center_fields,combined_cross_center(:,j,k),line_string)
        hold on
        subplot(2,2,2)
        semilogy(edge_fields,combined_cross_edge(:,j,k),line_string)
        hold on
        subplot(2,2,3)
        plot(center_fields,combined_cross_center(:,j,k),line_string)
        hold on
        subplot(2,2,4)
        plot(edge_fields,combined_cross_edge(:,j,k),line_string)
    end
end

```

```

        hold on
    end
end

subplot(2,2,1)
semilogy(center_fields,cross_bulk,'k.')
xlabel('Electric Field (V/cm)')
ylabel('Combined Bulk Cross Sections (cm^2)')
hold off
subplot(2,2,2)
semilogy(edge_fields,cross_flow,'k.')
xlabel('Electric Field (V/cm)')
ylabel('Combined Surface Cross Sections (cm^2)')
hold off
subplot(2,2,3)
plot(center_fields,cross_bulk,'k.')
xlabel('Electric Field (V/cm)')
ylabel('Combined Bulk Cross Sections (cm^2)')
hold off
subplot(2,2,4)
plot(edge_fields,cross_flow,'k.')
xlabel('Electric Field (V/cm)')
ylabel('Combined Surface Cross Sections (cm^2)')
hold off

%% Attempt to estimate the correct electron capture cross section for an
% assumed donor like defect

cross_bulk_elec_guess = 1e-10;
cross_bulk_hole = [ 1e-10 1e-11 1e-12 5e-12];
num_cross = length(cross_bulk_hole);

cross_bulk_fp_sent_elec = zeros(numpoints,num_cross);
cross_flow_fp_sent_elec = zeros(numpoints,1);
for i=1:numpoints
    for j=1:num_cross
        cross_bulk_elec_guess(i,j) = fzero(@(x) cross_bulk(i) -
cross_bulk_hole(j).*x.*enhance_factor_center(i)./(x.*enhance_factor_center(i)
.*exp((Et_bulk-Ei_Ge)/(kB*temp/q))+cross_bulk_hole(j).*exp((Ei_Ge-
Et_bulk)./(kB*temp/q))),cross_bulk_elec_guess);
    end
    cross_flow_elec_guess(i) = cross_flow(i)/enhance_factor_edge(i);
end

% Plot the guessed cross sections

figure(3)
subplot(2,1,1)
for cross_index=1:num_cross
    switch cross_index
        case 1
            line_string = 'r.';
        case 2
            line_string = 'b.';
        case 3
            line_string = 'g.';

```

```

        case 4
            line_string = 'c.';
        case 5
            line_string = 'm.';
        case 6
            line_string = 'y.';
        otherwise
            line_string = 'k.';
    end
    plot(center_fields,cross_bulk_elec_guess(:,cross_index),line_string)
    hold on
end
title('Sentaurus PooleFrenkel Corrected Bulk Hole Cross Sections')
xlabel('Electric Field (V/cm)')
ylabel('Effective Cross Section (cm-2)')
hold off

subplot(2,1,2)
plot(edge_fields,cross_flaw_elec_guess,'b.')
title('Sentaurus PooleFrenkel Corrected Surface Hole Cross Sections')
xlabel('Electric Field (V/cm)')
ylabel('Effective Cross Section (cm-2)')

```

Transmission Matrix Optical Analysis

Tmatrix_geslab_oxide_sweep_lambda.m

```

% based on a program written by Peter Mayer

clear;
j=sqrt(-1);

% center wavelength of interest
lambda=1550e-9;

% relevant indices
nair=1;

nSiO2=1.53;
len_SiO2_min=1e-9; % lengths are in units of m
len_SiO2_max=500e-9; % lengths are in units of m
apSi=300e2;
npSi=3.48-j*lambda/4/pi*apSi;
len_pSi=200e-9;
aGe=3000.0e2;
nGe=4.3-j*lambda/4/pi*aGe;
len_Ge=2e-6;
asub=300e2; % 300cm-1
nsub=3.48-j*lambda/2/pi*asub;
len_sub=500e-6;

```

```

len_air=1/2*lambda; % just some air to plot fields in

% other useful constants
num_thick_swept=500;
thick_spacing=(len_SiO2_max-len_SiO2_min)/num_thick_swept;
len_SiO2_vec = (len_SiO2_min:thick_spacing:len_SiO2_max);

num_lambdas_swept=100;
lambda_sweep_range=2.0; % pcnt difference from lambda (designed) over which
the search is made
lambda_ref=lambda; % keep track of the center wavelength

r_struct = zeros(num_thick_swept,num_lambdas_swept);

for lambda_index=1:num_lambdas_swept
for index=1:(num_thick_swept+1)

lambda_vec(lambda_index)=(100-
lambda_sweep_range)/100*lambda_ref+2*lambda_sweep_range/100*lambda_index*lambda_ref/num_lambdas_swept;
lambda=lambda_vec(lambda_index);

len_SiO2 = len_SiO2_min+thick_spacing*(index-1);

% specify basic layer structure w/ lengths and complex indices
%detector_struct=[len_air nair len_SiO2 nSiO2 len_pSi npSi len_Ge nGe len_air
nair];
detector_struct=[len_sub nsub len_Ge nGe len_pSi npSi len_SiO2 nSiO2 len_air
nair];
struct=detector_struct;

% calculate T matrix from arbitrary layer structure
T_tot=[1, 0 ; 0, 1]; % initial T-matrix
for ind=1:(length(struct)-2)/2
na=struct(2*ind);
nb=struct(2*(ind+1));
L=struct(2*ind-1);
r=(nb-na)/(nb+na);
t=sqrt(1-r^2);
beta=2*pi*na/lambda;
% this is the Tmat for propagating a length L of a material w/ index na
T_bulk=[exp(j*beta*L),0;0,exp(-j*beta*L)];
% and this Tmat associated with the interface right after the propagation
T_int=[1/t,-r/t;-r/t,1/t];
% Tmatrices can be cascaded like this...
T_tot=T_tot*T_bulk*T_int;
end
r_struct(index,lambda_index)=-T_tot(1,2)/T_tot(1,1); % this is the
reflection coeff for the structure
end

end

%[c,h] = contour(len_Ge_vec/1e-6,len_SiO2_vec/1e-9,(abs(r_struct).^2).*100);
clabel(c,h), colorbar

```

```

[c,h] = contourf(lambda_vec/1e-9,len_SiO2_vec/1e-
9,(abs(r_struct).^2).*100,50); colorbar
title('Sweep of Diode Reflection Coefficient (%) for 2um Thick Ge');
xlabel('Wavelength (nm)');
ylabel('Oxide Thickness (um)');

```

Tmatrix_geslab_oxide_sweep.m

```

% based on a program written by Peter Mayer

clear;
j=sqrt(-1);

% center wavelength of interest
lambda=1550e-9;

% relevant indices
nair=1;

nSiO2=1.53;
len_SiO2_min=300e-9; % lengths are in units of m
len_SiO2_max=1000e-9; % lengths are in units of m
apSi=300e2;
npSi=3.48-j*lambda/4/pi*apSi;
len_pSi=200e-9;
aGe=4300.0e2;
nGe=4.3-j*lambda/4/pi*aGe;
len_Ge_min=1.5e-6;
len_Ge_max=2.5e-6;
asub=300e2; % 300cm-1
nsub=3.48-j*lambda/2/pi*asub;
len_sub=500e-6;

len_air=1/2*lambda; % just some air to plot fields in

% other useful constants
num_thick_swept=500;
thick_spacing=(len_SiO2_max-len_SiO2_min)/num_thick_swept;
len_SiO2_vec = (len_SiO2_min:thick_spacing:len_SiO2_max);

num_ge_thick_swept=101;
ge_thick_spacing=(len_Ge_max-len_Ge_min)/num_ge_thick_swept;
len_Ge_vec = (len_Ge_min:ge_thick_spacing:len_Ge_max);

r_struct = zeros(num_thick_swept,num_ge_thick_swept);

for ge_index=1:(num_ge_thick_swept+1)
for index=1:(num_thick_swept+1)

len_SiO2 = len_SiO2_min+thick_spacing*(index-1);
len_Ge = len_Ge_min + ge_thick_spacing*(ge_index-1);

```

```

% specify basic layer structure w/ lengths and complex indices
%detector_struct=[len_air nair len_SiO2 nSiO2 len_pSi npSi len_Ge nGe len_air
nair];
detector_struct=[len_sub nsub len_Ge nGe len_pSi npSi len_SiO2 nSiO2 len_air
nair];
struct=detector_struct;

% calculate T matrix from arbitrary layer structure
T_tot=[1, 0 ; 0, 1]; % initial T-matrix
for ind=1:(length(struct)-2)/2
    na=struct(2*ind);
    nb=struct(2*(ind+1));
    L=struct(2*ind-1);
    r=(nb-na)/(nb+na);
    t=sqrt(1-r^2);
    beta=2*pi*na/lambda;
% this is the Tmat for propagating a length L of a material w/ index na
    T_bulk=[exp(j*beta*L),0;0,exp(-j*beta*L)];
% and this Tmat associated with the interface right after the propagation
    T_int=[1/t,-r/t;-r/t,1/t];
% Tmatrices can be cascaded like this...
    T_tot=T_tot*T_bulk*T_int;
end
r_struct(index,ge_index)=-T_tot(1,2)/T_tot(1,1); % this is the reflection
coeff for the structure
end

end

%[c,h] = contour(len_Ge_vec/1e-6,len_SiO2_vec/1e-9,(abs(r_struct).^2).*100);
clabel(c,h), colorbar
[c,h] = contourf(len_Ge_vec/1e-6,len_SiO2_vec/1e-9-
300,(abs(r_struct).^2).*100,20); colorbar
title('Sweep of Diode Reflection Coefficient (%) at 1550nm');
ylabel('Additional Oxide Layer Thickness (nm)');
xlabel('Ge Thickness (um)');

```

Measurement Postprocessing

freqresponse_nofit.m

```

load('~\from_peltier/freq_resp_40x100_center_11-29-06.mat');
frequencies = frequency_data(:,1);
optical_input = frequency_data(:,2:2:12);
electrical_output_raw = frequency_data(:,3:2:13);
electrical_output = electrical_output_raw;

% Add in loss bias-T and cable loss
for i=1:length(frequencies)
    if (frequencies(i) <= 5.0e7)
        electrical_output(i,:) = electrical_output(i,:) +
log10(frequencies(i))/log10(5.0e7)*0.322;
    end
end

```

```

elseif ((frequencies(i) > 5.0e7) && (frequencies(i) <= 3.66e8))
    electrical_output(i,:) = electrical_output(i,:) + (0.322 +
(log10(frequencies(i))-log10(5.0e7))/(log10(3.66e8)-log10(5.0e7))*(0.943-
0.322));
elseif ((frequencies(i) > 3.66e8) && (frequencies(i) <= 4.12e8))
    electrical_output(i,:) = electrical_output(i,:) + (0.943 +
(log10(frequencies(i))-log10(3.66e8))/(log10(4.12e8)-log10(3.66e8))*(0.684-
0.943));
elseif ((frequencies(i) > 4.12e8) && (frequencies(i) <= 4.98e8))
    electrical_output(i,:) = electrical_output(i,:) + (0.684 +
(log10(frequencies(i))-log10(4.12e8))/(log10(4.98e8)-log10(4.12e8))*(0.808-
0.684));
elseif ((frequencies(i) > 4.98e8) && (frequencies(i) <= 1.489e9))
    electrical_output(i,:) = electrical_output(i,:) + (0.808 +
(log10(frequencies(i))-log10(4.98e8))/(log10(1.489e9)-log10(4.98e8))*(1.536-
0.808));
elseif ((frequencies(i) > 1.489e9) && (frequencies(i) <= 4.0e9))
    electrical_output(i,:) = electrical_output(i,:) + (1.536 +
(log10(frequencies(i))-log10(1.489e9))/(log10(4.0e9)-log10(1.489e9))*(2.500-
1.536));
end
end

% Add in loss probe
for i=1:length(frequencies)
    if (frequencies(i) <= 0.396e9)
        electrical_output(i,:) = electrical_output(i,:) +
log10(frequencies(i))/log10(0.396e9)*0.049;
    elseif ((frequencies(i) > 0.369e9) && (frequencies(i) <= 0.792e9))
        electrical_output(i,:) = electrical_output(i,:) + (0.049 +
(log10(frequencies(i))-log10(0.369e9))/(log10(0.792e9)-
log10(0.369e9))*(0.074-0.049));
    elseif ((frequencies(i) > 0.792e9) && (frequencies(i) <= 1.188e9))
        electrical_output(i,:) = electrical_output(i,:) + (0.074 +
(log10(frequencies(i))-log10(0.792e9))/(log10(1.188e9)-
log10(0.792e9))*(0.093-0.074));
    elseif ((frequencies(i) > 1.188e9) && (frequencies(i) <= 1.584e9))
        electrical_output(i,:) = electrical_output(i,:) + (0.093 +
(log10(frequencies(i))-log10(1.188e9))/(log10(1.584e9)-
log10(1.188e9))*(0.108-0.093));
    elseif ((frequencies(i) > 1.584e9) && (frequencies(i) <= 1.98e9))
        electrical_output(i,:) = electrical_output(i,:) + (0.108 +
(log10(frequencies(i))-log10(1.584e9))/(log10(1.98e9)-log10(1.584e9))*(0.121-
0.108));
    elseif ((frequencies(i) > 1.98e9) && (frequencies(i) <= 3.96e9))
        electrical_output(i,:) = electrical_output(i,:) + (0.121 +
(log10(frequencies(i))-log10(1.98e9))/(log10(3.96e9)-log10(1.98e9))*(0.157-
0.121));
    elseif ((frequencies(i) > 3.96e9) && (frequencies(i) <= 4.356e9))
        electrical_output(i,:) = electrical_output(i,:) + (0.157 +
(log10(frequencies(i))-log10(3.96e9))/(log10(4.356e9)-log10(3.96e9))*(0.164-
0.157));
    end
end

oes21 = electrical_output-optical_input;

```

```

semilogx(frequencies,oeS21(:,1),frequencies,oeS21(:,2),frequencies,oeS21(:,3)
,frequencies,oeS21(:,4),frequencies,oeS21(:,5),frequencies,-
35.6*ones(length(frequencies),1))
%semilogx(frequencies,electrical_output(:,2),frequencies,electrical_output_ra
w(:,2))
title('Center and Perimeter Frequency Response of a 40x100 micron 11-8
Photodiode')
xlabel('Frequency (Hz)')
ylabel('Optical to Electrical S21 (dB)')

```

hold on

```

load('~\from_peltier/freq_resp_20x100_edge_11-29-06.mat');
frequencies = frequency_data(:,1);
optical_input = frequency_data(:,2:2:12);
electrical_output_raw = frequency_data(:,3:2:13);
electrical_output = electrical_output_raw;

% Add in loss bias-T and cable loss
for i=1:length(frequencies)
    if (frequencies(i) <= 5.0e7)
        electrical_output(i,:) = electrical_output(i,:) +
log10(frequencies(i))/log10(5.0e7)*0.322;
    elseif ((frequencies(i) > 5.0e7) && (frequencies(i) <= 3.66e8))
        electrical_output(i,:) = electrical_output(i,:) + (0.322 +
(log10(frequencies(i))-log10(5.0e7))/(log10(3.66e8)-log10(5.0e7))*(0.943-
0.322));
    elseif ((frequencies(i) > 3.66e8) && (frequencies(i) <= 4.12e8))
        electrical_output(i,:) = electrical_output(i,:) + (0.943 +
(log10(frequencies(i))-log10(3.66e8))/(log10(4.12e8)-log10(3.66e8))*(0.684-
0.943));
    elseif ((frequencies(i) > 4.12e8) && (frequencies(i) <= 4.98e8))
        electrical_output(i,:) = electrical_output(i,:) + (0.684 +
(log10(frequencies(i))-log10(4.12e8))/(log10(4.98e8)-log10(4.12e8))*(0.808-
0.684));
    elseif ((frequencies(i) > 4.98e8) && (frequencies(i) <= 1.489e9))
        electrical_output(i,:) = electrical_output(i,:) + (0.808 +
(log10(frequencies(i))-log10(4.98e8))/(log10(1.489e9)-log10(4.98e8))*(1.536-
0.808));
    elseif ((frequencies(i) > 1.489e9) && (frequencies(i) <= 4.0e9))
        electrical_output(i,:) = electrical_output(i,:) + (1.536 +
(log10(frequencies(i))-log10(1.489e9))/(log10(4.0e9)-log10(1.489e9))*(2.500-
1.536));
    end
end

% Add in loss probe
for i=1:length(frequencies)
    if (frequencies(i) <= 0.396e9)
        electrical_output(i,:) = electrical_output(i,:) +
log10(frequencies(i))/log10(0.396e9)*0.049;
    elseif ((frequencies(i) > 0.369e9) && (frequencies(i) <= 0.792e9))
        electrical_output(i,:) = electrical_output(i,:) + (0.049 +
(log10(frequencies(i))-log10(0.369e9))/(log10(0.792e9)-
log10(0.369e9))*(0.074-0.049));
    elseif ((frequencies(i) > 0.792e9) && (frequencies(i) <= 1.188e9))

```

```

        electrical_output(i,:) = electrical_output(i,:) + (0.074 +
(log10(frequencies(i))-log10(0.792e9))/(log10(1.188e9)-
log10(0.792e9))*(0.093-0.074));
        elseif ((frequencies(i) > 1.188e9) && (frequencies(i) <= 1.584e9))
            electrical_output(i,:) = electrical_output(i,:) + (0.093 +
(log10(frequencies(i))-log10(1.188e9))/(log10(1.584e9)-
log10(1.188e9))*(0.108-0.093));
        elseif ((frequencies(i) > 1.584e9) && (frequencies(i) <= 1.98e9))
            electrical_output(i,:) = electrical_output(i,:) + (0.108 +
(log10(frequencies(i))-log10(1.584e9))/(log10(1.98e9)-log10(1.584e9))*(0.121-
0.108));
        elseif ((frequencies(i) > 1.98e9) && (frequencies(i) <= 3.96e9))
            electrical_output(i,:) = electrical_output(i,:) + (0.121 +
(log10(frequencies(i))-log10(1.98e9))/(log10(3.96e9)-log10(1.98e9))*(0.157-
0.121));
        elseif ((frequencies(i) > 3.96e9) && (frequencies(i) <= 4.356e9))
            electrical_output(i,:) = electrical_output(i,:) + (0.157 +
(log10(frequencies(i))-log10(3.96e9))/(log10(4.356e9)-log10(3.96e9))*(0.164-
0.157));
        end
    end
end

```

```

oeS21 = electrical_output-optical_input;
semilogx(frequencies,oeS21(:,1),frequencies,oeS21(:,2),frequencies,oeS21(:,3)
,frequencies,oeS21(:,4),frequencies,oeS21(:,5),frequencies,-
43.6*ones(length(frequencies),1))
%semilogx(frequencies,electrical_output(:,2),frequencies,electrical_output_ra
w(:,2))
title('Center and Perimeter Frequency Response of a 20x100 micron 11-8
Photodiode')
xlabel('Frequency (Hz)')
ylabel('Optical to Electrical S21 (dB)')

print -dpng freqresponse_nofit.png

```

pulse_response.m

```

%directory = '~/data/probestation/pulse_response/final_11-8/';
directory = 'C:\Userdata\Jason\Hoyt Diode Data\pulse_response\final_11-8\';
%filename = '15v_2n.txt';
filename = '15v_250p.txt';
%filename = 'opt20p_3.txt';
num_header_lines = 24;
color = 'm';

optical_power_correction_factor = 40.00;

% open the file
file_id = fopen([directory, filename], 'r');

% get the number of points
result = textscan(file_id, '%s%f', 1, 'Headerlines', 1, 'Delimiter', ':');
num_points = squeeze(result{2})

```

```

% Get the x axis step size
result = textscan(file_id,'%s%f',1,'Headerlines',3,'Delimiter',':');
x_step = squeeze(result{2})

% Get the x axis origin
result = textscan(file_id,'%s%f',1,'Delimiter',':');
x_start = squeeze(result{2})

% Get the x range
result = textscan(file_id,'%s%f',1,'Headerlines',10,'Delimiter',':');
x_range = squeeze(result{2})

% Get the y range
result = textscan(file_id,'%s%f',1,'Headerlines',3,'Delimiter',':');
y_range = squeeze(result{2})

% Get the y offset
result = textscan(file_id,'%s%f',1,'Headerlines',1,'Delimiter',':');
y_start = squeeze(result{2})

% Get the x_unit
x_unit = 'second';

% Get the y_unit
y_unit = 'Volt';

% Get the real data
result = textscan(file_id,'%f',num_points,'Headerlines',24);
amplitudes = squeeze(result{1});

% Close the file
fclose(file_id);

time = (x_start:x_step:x_start+x_range-x_step);
if length(time) == num_points
    x_axis = time ./ 1e-9; % plot in nanoseconds
else
    time = (x_start:x_step:x_start+x_range);
    x_axis = time ./ 1e-9; % plot in nanoseconds
end

if strcmp('Watt',y_unit)
    y_axis = amplitudes .* optical_power_correction_factor; % correct for
attenuation
else
    y_axis = -amplitudes ./ 50; % convert to current
end

% Plot the time domain response

figure(1)

```

```

plot(x_axis, y_axis./1e-3, color)
xlim([x_start, (x_start+x_range)]./1e-9)
%xlim([36.2, 40])
ylim([-0.2, 8])
xlabel('Time (Nanoseconds)');

if strcmp('Watt',y_unit)
    title(['20 GHz Optical Front-End Pulse Response: ', filename])
    ylabel('Optical Power (Watts)')
else
    title(['Photodiode Pulse Response: ', filename])
    ylabel('Photocurrent (Miliamps)')
end

figure(2)

tail_start_index = 242;
tail_stop_index = 1550;

a = 1.123013453290948e+291;
b = -18.449572250629959;
exponential_tail = a*exp(b*x_axis);

plot(1000*(x_axis(tail_start_index:tail_stop_index)-
36.5),y_axis(tail_start_index:tail_stop_index)./1e-
3,'b',1000*(x_axis(tail_start_index:tail_stop_index)-
36.5),exponential_tail(tail_start_index:tail_stop_index)./1e-3,'r')
xlabel('Time (ps)');
ylabel('Photocurrent (mA)')
xlim([x_axis(tail_start_index)-36.5 x_axis(tail_stop_index)-36.5]*1000)

x_tail = 1000*(x_axis(tail_start_index:tail_stop_index)-36.5);
excess_current = squeeze(y_axis(tail_start_index:tail_stop_index)) -
squeeze(exponential_tail(tail_start_index:tail_stop_index));

figure(3)
plot(x_tail,excess_current)
xlabel('Time (ps)');
ylabel('Excess Current (mA)')
xlim([x_axis(tail_start_index)-36.5 x_axis(tail_stop_index)-36.5]*1000)

numpoints = length(x_tail);
sample_rate = zeros(numpoints,1);
remaining_charge = zeros(numpoints,1);

for i=1:numpoints
    sample_rate(i) = 1./(x_tail(i)*1e-12);
    remaining_charge(i) = sum(excess_current(i:end))*x_step;
end

figure(4)
loglog(sample_rate./1e9,remaining_charge)
xlabel('Sample Rate (Gs/s)');
ylabel('Charge Out of Timeslot (C)');

```

```

xlim([1 4])
ylim([1e-18 1e-13])

% Compute LSB analysis

average_power = [200e-3 100e-3 50e-3 10e-3 1e-3];
numpowers = length(average_power);
pulse_energy = (1./sample_rate)*average_power; % J

photon_energy = 0.8; % eV
responsivity = 0.4; % A/W
pulse_charge = responsivity*pulse_energy./photon_energy; % C

bit_depth = 10;
lsb_size = pulse_charge*2^-bit_depth;

figure(5)
for i=1:numpowers
    switch i
        case 1
            line_string = 'r';
        case 2
            line_string = 'b';
        case 3
            line_string = 'g';
        case 4
            line_string = 'c';
        case 5
            line_string = 'm';
        case 6
            line_string = 'y';
        otherwise
            line_string = 'b';
    end
    loglog(sample_rate./1e9,remaining_charge./lsb_size(:,i),line_string)
    hold on
    xlabel('Sample Rate (Gs/s)');
    ylabel('# LSBs Out of Timeslot');
    xlim([1 4])
    ylim([1e-1 1e1])
end
hold off

% % Compute and plot the FFT
%
% sample_time = x_step;
% sample_frequency = 1/sample_time;
%
% fft_result = fft(y_axis, num_points)./num_points;
% frequencies = sample_frequency/2*linspace(0,1,num_points/2);
%
% figure(2)
%
% single_sided_response = 2*abs(fft_result(1:num_points/2));
% response_db = 10*log10(single_sided_response);
%

```

```

% semilogx(frequencies,response_db,color);
% xl = xlim
% xlim([1e8,2e10]);
% ylim([-60,-40]);
% xlabel('Frequency (Hz)');
% ylabel('fft result');

```

Sampler Performance Specifications

required_pulse_bw.m

```

numpoints = 100;
sample_rate = linspace(1e9,4e9,numpoints);
t_sample = 1./sample_rate;
bit_depth = 10;

sigma = ones(1,numpoints);
for i=1:numpoints
    sigma(i) = fzero(@(x) erfc(t_sample(i)/(2*sqrt(2)*x)) - 2^-
bit_depth/2,t_sample(i)/2);
end

figure(1)
time = linspace(-0.5e-9,1e-9,1000);
index = 34;
pulse = 1/(sqrt(2*pi)*sigma(index))*exp(-(time-
t_sample(index)/2).^2/(2*sigma(index)^2));
prepulse = 1/(sqrt(2*pi)*sigma(index))*exp(-
(time+t_sample(index)/2).^2/(2*sigma(index)^2));
postpulse = 1/(sqrt(2*pi)*sigma(index))*exp(-(time-
3*t_sample(index)/2).^2/(2*sigma(index)^2));
semilogy(time./1e-12,prepulse,'r',time./1e-12,pulse,'b',time./1e-
12,postpulse,'g')
xlim([-500 1000])

figure(2)
f_3dB = sqrt(log(4))./(sqrt(2)*pi*sigma);
semilogx(sample_rate,f_3dB)

```


Appendix C – Python Scripts

Sentaurus Output File Postprocessing

extract_datafiles.py

```
# Find all plot files, extract data and corresponding simulation parameters,
and save these as matlab files with a summary file.
```

```
from glob import glob
from scipy import *
from os import path
import re
import sys

#data_folders = ['/data/sprojects/pd_ge_on_si_3D_cyl_flawed_300K_3']
#output_folder = '~/sim_results/ge-si_dark_iv/300K'
data_folders = 'C:\\Userdata\\Jason\\Hoyt Diode
Data\\pd_ge_on_si_3D_cyl_flawed_300K_[3-4]'
output_folder = 'C:\\Userdata\\Jason\\Hoyt Diode Data\\sim_300K'

plotfiles = glob(path.join(data_folders,"*.plt"))

node_re = re.compile(r'(n)(\\d+)')
struct_node_re = re.compile(r'Grid\\s*=\\s*"n(\\d+)_msh.tdr"')
window_re = re.compile(r'define\\s+Opening\\D+(\\d+\\.?.?\\d*)')
bulk_lifetime_re =
re.compile(r'Material\\s*=\\s*"Germanium".*?Scharfetter.*?taumax\\s*=\\s*(\\d+\\.?.?
d*e+?-?\\d+)', re.DOTALL)
flaw_lifetime_re =
re.compile(r'Material\\s*=\\s*"FlawedGermanium".*?Scharfetter.*?taumax\\s*=\\s*(\\
d+\\.?.?\\d*e+?-?\\d+)', re.DOTALL)

raw_data = list()
for plotfile in plotfiles:
    node_number = node_re.search(path.basename(plotfile)).group(2)
    data_folder = path.dirname(plotfile)

    # Find and read the command file
    cmd_filename = path.join(data_folder,'pp'+node_number+'_des.cmd')
    if path.isfile(cmd_filename):
        cmd_obj = open(cmd_filename, 'r')
        cmd_file = cmd_obj.read()
    else:
        print "Filename ", cmd_filename, " does not exist"
        sys.exit()

    # Find the structure nodenumber and read the structure file
    struct_node_number = struct_node_re.search(cmd_file).group(1)
```

```

    struct_filename =
path.join(data_folder, 'pp'+struct_node_number+'_dvs.cmd')
    if path.isfile(struct_filename):
        struct_obj = open(struct_filename, 'r')
        struct_file = struct_obj.read()
    else:
        print "Filename ", struct_filename, " does not exist"
        sys.exit()
# Extract the window size
window_diameter = float(window_re.search(struct_file).group(1))

# Find and read the parameter file
param_filename = path.join(data_folder, 'pp'+node_number+'_des.par')
if path.isfile(param_filename):
    param_obj = open(param_filename, 'r')
    param_file = param_obj.read()
else:
    print "Filename ", param_filename, " does not exist"
    sys.exit()

bulk_lifetime = float(bulk_lifetime_re.search(param_file).group(1))
flaw_lifetime = float(flaw_lifetime_re.search(param_file).group(1))

param_obj.close()

data_obj = open(plotfile, 'r')

data_array = io.read_array(data_obj, columns=(0,5), lines=(16,-4))

data_obj.close()

raw_data.append((data_array, window_diameter, bulk_lifetime, flaw_lifetime))

windows = list()
bulk_lifetimes = list()
flaw_lifetimes = list()
for data, window, bulk_time, flaw_time in raw_data:
    if windows.count(window) == 0:
        windows.append(window)
    if bulk_lifetimes.count(bulk_time) == 0:
        bulk_lifetimes.append(bulk_time)
    if flaw_lifetimes.count(flaw_time) == 0:
        flaw_lifetimes.append(flaw_time)

windows.sort()
bulk_lifetimes.sort()
flaw_lifetimes.sort()

summary_dict = {'windows':array(windows),
                'bulk_lifetimes':array(bulk_lifetimes),
                'flaw_lifetimes':array(flaw_lifetimes)}

for data, window, bulk_time, flaw_time in raw_data:
    wind_index = windows.index(window)+1

```

```

    bulk_index = bulk_lifetimes.index(bulk_time)+1
    flaw_index = flaw_lifetimes.index(flaw_time)+1

    outfilename = path.join(output_folder, 'sim_data_%d_%d_%d.mat' %
(wind_index,bulk_index,flaw_index))
    data_dict = {'sim_data':data}
    io.savemat(outfilename,dict=data_dict)

outfilename = path.join(output_folder,"sim_summary.mat")
io.savemat(outfilename,dict=summary_dict)

```

extract_fields.py

Find all plot files, extract data and corresponding simulation parameters, and save these as matlab files with a summary file.

```

from glob import glob
from scipy import *
from os import path
import re
import sys
import math
import string

data_file = 'C:\\\\Userdata\\\\Jason\\\\Hoyt Diode
Data\\\\pd_ge_on_si_3D_cyl_flawed_300K_fields\\\\current_plot_20um.plt'
output_file = 'C:\\\\Userdata\\\\Jason\\\\Hoyt Diode
Data\\\\sim_fields\\\\fields_300K.mat'

data_obj = open(data_file,'r')
for time in range(0,20,1):
    line = data_obj.readline()

voltages = list()
center_fields = list()
edge_fields = list()
while line:
    line = data_obj.readline()
    voltage_data = line.split()

    voltages.append(float(voltage_data[0]))

    line = data_obj.readline()
    data = line.split()

    center_fields.append(abs(float(data[1])))
    edge_fields.append(abs(float(data[3])))

    for time in range(0,2,1):
        line = data_obj.readline()

data_obj.close()

```

```
summary_dict = {'sim_voltages':array(voltages),  
'sim_center_fields':array(center_fields),  
'sim_edge_fields':array(edge_fields)}  
  
io.savemat(output_file,dict=summary_dict)
```


References

- [1] R. People, "Physics and applications of Ge x Si 1-x/Si strained-layer heterostructures," *Quantum Electronics, IEEE Journal of*, vol. 22, pp. 1696-1710, 1986.
- [2] D. D. Cannon, "Strain-engineered CMOS-compatible Ge Photodetectors," MIT, 2003.
- [3] D. D. Cannon, J. Liu, Y. Ishikawa, K. Wada, D. T. Danielson, S. Jongthammanurak, J. Michel, and L. C. Kimerling, "Tensile strained epitaxial Ge films on Si(100) substrates with potential application in L-band telecommunications," *Applied Physics Letters*, vol. 84, pp. 906-908, 2004.
- [4] L. Colace, M. Balbi, G. Masini, G. Assanto, H.-C. Luan, and L. C. Kimerling, "Ge on Si p-i-n photodiodes operating at 10 Gbit/s," *Applied Physics Letters*, vol. 88, p. 101111, 2006.
- [5] L. Colace, G. Masini, and G. Assanto, "Ge-on-Si approaches to the detection of near-infrared light," *Quantum Electronics, IEEE Journal of*, vol. 35, pp. 1843--1852, 1999.
- [6] L. Colace, G. Masini, and G. Assanto, "Guided-wave near-infrared detector in polycrystalline germanium on silicon," *Applied Physics Letters*, vol. 87, p. 203507, 2005.
- [7] L. Colace, G. Masini, S. Cozza, G. Assanto, F. DeNotaristefani, and V. Cencelli, "Near-infrared camera in polycrystalline germanium integrated on complementary-metal-oxide semiconductor electronics," *Applied Physics Letters*, vol. 90, p. 011103, 2007.
- [8] L. Colace, G. Masini, F. Galluzzi, G. Assanto, G. Capellini, L. D. Gaspare, E. Palange, and F. Evangelisti, "Metal-Ge-Si heterostructures for near-infrared light detection," *Journal of Vacuum Science & Technology B: Microelectronics and Nanometer Structures*, vol. 17, pp. 465-467, 1999.
- [9] J. Liu, D. D. Cannon, K. Wada, Y. Ishikawa, S. Jongthammanurak, D. T. Danielson, J. Michel, and L. C. Kimerling, "Tensile strained Ge p-i-n photodetectors on Si platform for C and L band telecommunications," *Applied Physics Letters*, vol. 87, pp. 011110-3, 2005.
- [10] J. Liu, J. Michel, W. Giziewicz, D. Pan, K. Wada, D. D. Cannon, S. Jongthammanurak, D. T. Danielson, L. C. Kimerling, J. Chen, F. O. Ilday, F. X. Kartner, and J. Yasaitis, "High-performance, tensile-strained Ge p-i-n photodetectors on a Si platform," *Applied Physics Letters*, vol. 87, pp. 103501-3, 2005.
- [11] J. F. Liu, D. D. Cannon, K. Wada, Y. Ishikawa, S. Jongthammanurak, D. T. Danielson, J. Michel, and L. C. Kimerling, "Tensile strained Ge p-i-n photodetectors on Si platform for C and L band telecommunications," *Applied Physics Letters*, vol. 87, p. 011110, July 2005.
- [12] J. F. Liu, J. Michel, W. Giziewicz, D. Pan, K. Wada, D. D. Cannon, S. Jongthammanurak, D. T. Danielson, L. C. Kimerling, J. Chen, F. O. Ilday, F. X. Kartner, and J. Yasaitis, "High-performance, tensile-strained Ge p-i-n photodetectors on a Si platform," *Applied Physics Letters*, vol. 87, p. 103501, September 2005.
- [13] H.-C. Luan, "Ge Photodetectors for Si Microphotonics," MIT, 2000.
- [14] H. C. Luan, K. Wada, L. C. Kimerling, G. Masini, L. Colace, and G. Assanto, "High efficiency photodetectors based on high quality epitaxial germanium grown on silicon substrates," *Optical Materials*, vol. 17, pp. 71--73, 2001.

- [15] C. Masini, L. Calace, G. Assanto, H.-C. Luan, and L. C. Kimerling, "High-performance p-i-n Ge on Si photodetectors for the near infrared: from model to demonstration," *Electron Devices, IEEE Transactions on*, vol. 48, pp. 1092--1096, 2001.
- [16] G. Masini, L. Colace, and G. Assanto, "Near-infrared waveguide photodetectors based on polycrystalline Ge on silicon-on-insulator substrates," *Optical Materials*, vol. 17, pp. 243--246, 2001.
- [17] G. Masini, L. Colace, and G. Assanto, "2.5 Gbit/s polycrystalline germanium-on-silicon photodetector operating from 1.3 to 1.55 μm ," *Applied Physics Letters*, vol. 82, pp. 2524-2526, 2003.
- [18] G. Masini, L. Colace, G. Assanto, H. C. Luan, and L. C. Kimerling, "Germanium on silicon pin photodiodes for the near infrared," *Electronics Letters*, vol. 36, pp. 2095--2096, 2000.
- [19] G. Masini, L. Colace, G. Assanto, H. C. Luan, K. Wada, and L. C. Kimerling, "High responsivity near infrared Ge photodetectors integrated on," *Electronics Letters*, vol. 35, pp. 1467--1468, 1999.
- [20] G. Masini, L. Colace, F. Petulla, G. Assanto, V. Cencelli, and F. DeNotaristefani, "Monolithic and hybrid near infrared detection and imaging based on poly-Ge photodiode arrays," *Optical Materials*, vol. 27, pp. 1079--1083, February 2005.
- [21] J. Oh, S. K. Banerjee, and J. C. Campbell, "Metal-germanium-metal photodetectors on heteroepitaxial Ge-on-Si with amorphous Ge Schottky barrier enhancement layers," *Photonics Technology Letters, IEEE*, vol. 16, pp. 581--583, 2004.
- [22] R. People, "Physics and applications of $\text{Ge}_{1-x}\text{Si}_x$ /Si strained-layer heterostructures," *Quantum Electronics, IEEE Journal of*, vol. 22, pp. 1696--1710, 1986.
- [23] S. B. Samavedam, M. T. Currie, T. A. Langdo, and E. A. Fitzgerald, "High-quality germanium photodiodes integrated on silicon substrates using optimized relaxed graded buffers," *Applied Physics Letters*, vol. 73, pp. 2125--2127, October 1998.
- [24] O. O. Olubuyide, "Low Pressure Epitaxial Growth, Fabrication and Characterization of Ge-on-Si Photodiodes," MIT, 2007.
- [25] Y. Taur and T. K. Ning, *Fundamentals of Modern VLSI Devices*. New York: Cambridge University Press, 1998.
- [26] R. S. Muller and T. I. Kamins, *Device Electronics for Integrated Circuits*, 3rd ed. New York: John Wiley & Sons, 2002.
- [27] SOITEC, "Fully Depleted UNIBOND Wafers." vol. 2008.
- [28] F. Xia, L. Sekaric, and Y. Vlasov, "Ultracompact optical buffers on a silicon chip," *Nat Photon*, vol. 1, pp. 65-71, 2007.
- [29] R. Soref and B. Bennet, "Electrooptical effects in silicon," *Quantum Electronics, IEEE Journal of*, vol. 23, pp. 123- 129, Jan 1987.
- [30] Q. Xu, S. Manipatruni, B. Schmidt, J. Shakya, and M. Lipson, "12.5 Gbit/s carrier-injection-based silicon micro-ring silicon modulators," *Opt. Express*, vol. 15, pp. 430-436, 2007.
- [31] Q. Xu, B. Schmidt, S. Pradhan, and M. Lipson, "Micrometre-scale silicon electro-optic modulator," *Nature*, vol. 435, pp. 325-327, 2005.
- [32] M. W. Geis, S. J. Spector, M. E. Grein, R. T. Schulein, J. U. Yoon, D. M. Lennon, S. Deneault, F. Gan, F. X. Kaertner, and T. M. Lyszczarz, "CMOS-Compatible All-Si High-Speed

- Waveguide Photodiodes with High Responsivity in Near-Infrared Communication Band," *Photonics Technology Letters, IEEE*, vol. 19, pp. 152-154, 2007.
- [33] C. Gunn, "CMOS Photonics for High-Speed Interconnects," *IEEE Micro*, vol. 26, pp. 58-66, 2006.
- [34] K. Katsura, T. Hayashi, F. Ohira, S. Hata, and K. Iwashita, "A novel flip-chip interconnection technique using solder bumps for high-speed photoreceivers," *Journal of Lightwave Technology*, vol. 8, pp. 1323-1327, 1990.
- [35] P. Grillot, S. Ringel, and E. Fitzgerald, "Effect of composition on deep levels in heteroepitaxial GeSi_{1-x} layers and evidence for dominant intrinsic recombination-generation in relaxed Ge layers on Si," *Journal of Electronic Materials*, vol. 25, pp. 1028--1036, July 1996.
- [36] L. C. Kimerling, D. Ahn, A. B. Apsel, M. Beals, D. Carothers, Y. K. Chen, T. Conway, D. M. Gill, M. Grove, C. Y. Hong, M. Lipson, J. Liu, J. Michel, D. Pan, S. S. Patel, A. T. Pomerene, M. Rasras, D. K. Sparacin, K. Y. Tu, A. E. White, and C. W. Wong, "Electronic-photonic integrated circuits on the CMOS platform," in *Silicon Photonics. Edited by Kubby, Joel A.; Reed, Graham T. Proceedings of the SPIE, Volume 6125, pp. 6-15 (2006)*. 2006, pp. 6-15.
- [37] D. Ahn, C.-y. Hong, J. Liu, W. Giziewicz, M. Beals, L. C. Kimerling, J. Michel, J. Chen, and F. X. Kärtner, "High performance, waveguide integrated Ge photodetectors," *Opt. Express*, vol. 15, pp. 3916-3921, 2007.
- [38] A. Schenk, *Advanced Physical Models for Silicon Device Simulation* New York: Springer Wien, 1998.
- [39] A. G. Milnes, *Deep Impurities in Semiconductors*. New York: John Wiley & Sons, 1973.
- [40] L. M. Giovane, H.-C. Luan, A. M. Agarwal, and L. C. Kimerling, "Correlation between leakage current density and threading dislocation density in SiGe p-i-n diodes grown on relaxed graded buffer layers," *Applied Physics Letters*, vol. 78, pp. 541--543, 2001.
- [41] Blakemore, *Semiconductor Statistics*.
- [42] O. O. Olubuyide, D. T. Danielson, L. C. Kimerling, and J. L. Hoyt, "Impact of seed layer on material quality of epitaxial germanium on silicon deposited by low pressure chemical vapor deposition," *Thin Solid Films*, vol. 508, pp. 14-19, 2006.
- [43] J. G. Sandland, "Defect characterization and electrical analysis of UHV-CVD deposited germanium on silicon " in *Material Science*. vol. S.B. Cambridge: Massachusetts Institute of Technology, 1999.
- [44] L. C. Kimerling and J. R. Patel, "Defect states associated with dislocations in silicon," *Applied Physics Letters*, vol. 34, p. 73, 1979.
- [45] G. K. Wertheim and G. L. Pearson, "Recombination in plastically deformed germanium," *Physical Review*, vol. 107, pp. 694-698, 1957.
- [46] Y. S. Ju and K. E. Goodson, "Short-Time-Scale Thermal Mapping of Microdevices Using a Scanning Thermoreflectance Technique," *Journal of Heat Transfer*, vol. 120, p. 306, 1998.
- [47] J. Christofferson, "Thermoreflectance based thermal microscope," *Review of Scientific Instruments*, vol. 76, p. 20, 2005.
- [48] J. V. Christofferson, D. Shakouri, A. Melese, P. Labounty, C. Bowers, and J. E. Croke, "Thermoreflectance imaging of superlattice micro refrigerators," *Semiconductor*

- Thermal Measurement and Management, 2001. Seventeenth Annual IEEE Symposium*, pp. 58-62, 2001.
- [49] Z. Bian, J. Christofferson, A. Shakouri, and P. Kozodoy, "High-power operation of electroabsorption modulators," *Applied Physics Letters*, vol. 83, p. 3605, 2003.
- [50] G. Tessier, C. Filloy, M. L. Polignano, I. Mica, G. Jerosolimski, S. Holé, and D. Fournier, "High resolution thermoreflectance imaging on transistor arrays with defect-induced leakage," *J. Phys. IV France*, vol. 125, pp. 423-425, 2005.
- [51] D. Luerksen, J. A. Hudgings, P. M. Mayer, and R. J. Ram, "Nanoscale thermoreflectance with 10mK temperature resolution using stochastic resonance," *Semiconductor Thermal Measurement and Management Symposium, 2005 IEEE Twenty First Annual IEEE*, pp. 253-258, 2005.
- [52] P. M. Mayer, D. Lüerßen, R. J. Ram, and J. A. Hudgings, "Theoretical and experimental investigation of the thermal resolution and dynamic range of CCD-based thermoreflectance imaging," *Journal of the Optical Society of America A*, vol. 24, pp. 1156-1163, 2007.
- [53] S. C. Jain and D. J. Roulston, "A simple expression for band gap narrowing (BGN) in heavily doped Si, Ge, GaAs and GexSi1-x strained layers," *Solid-State Electronics*, vol. 34, pp. 453--465, May 1991.
- [54] S. D. Lester, F. A. Ponce, M. G. Craford, and D. A. Steigerwald, "High dislocation densities in high efficiency GaN-based light-emitting diodes," *Applied Physics Letters*, vol. 66, pp. 1249-1251, 1995.
- [55] D. B. Holt and B. G. Yacobi, *Extended defects in semiconductors*. Cambridge, UK: Cambridge University Press, 2007.
- [56] J. W. Cook and J. F. Schetzina, "Blue-green light-emitting diodes promise full-color displays," *Laser Focus World*, pp. 101-104, March 1995.
- [57] M. Kittler and W. Seifert, "On the sensitivity of the EBIC technique as applied to defect investigations in silicon," *Physica Status Solidi*, vol. A66, pp. 1588-1589, 1981.
- [58] S. Ringel and P. Grillot, "Electronic Properties and Deep Levels in Germanium-Silicon," in *Germanium Silicon*, 1999, pp. 304-246.
- [59] F. H. Baumann and W. Schroter, "Deformation-induced point defects in germanium," *Philosophical Magazine B*, vol. 48, pp. 55-61, 1983.
- [60] F. H. Baumann and W. Schroter, *Physica Status Solidi (A)*, vol. 79, p. K123, 1983.
- [61] A. Broniatowski, "Measurement of the grain-boundary states in semiconductors by deep-level transient spectroscopy," *Phys. Rev. B*, vol. 36, pp. 5895--, October 1987.
- [62] A. Broniatowski and J. C. Bourgoin, "Transient-Capacitance Measurement of the Grain Boundary Levels in Semiconductors," *Phys. Rev. Lett.*, vol. 48, pp. 424--, February 1982.
- [63] E. Simoen, P. Clauws, and J. Vennik, "DLTS of grown-in dislocations in p- and n- type high-purity germanium," *Solid State Communications*, vol. 54, pp. 1025--1029, June 1985.
- [64] J. C. Bourgoin, P. M. Mooney, and F. Poulin, in *Defects and Radiation Effects in Semiconductors*, R. R. Hasiguti, Ed. London: Institute of Physics, 1980, pp. 33-43.
- [65] P. M. Mooney, F. Poulin, and J. C. Bourgoin, *Phys. Rev. B*, vol. 28, p. 3372, 1983.
- [66] F. Poulin and J. C. Bourgoin, *Phys. Rev. B*, vol. 26, p. 6788, 1982.

- [67] J. Fage-Pedersen, A. N. Larsen, and A. Mesli, "Irradiation-induced defects in Ge studied by transient spectroscopies," *Physical Review B*, vol. 62, p. 10116, 2000.
- [68] A. Carvalho, R. Jones, J. Coutinho, V. J. B. Torres, S. Oberg, J. M. Campanera Alsina, M. Shaw, and P. R. Briddon, "Local-density-functional calculations of the vacancy-oxygen center in Ge," *Physical Review B*, vol. 75, p. 115206, 2007.
- [69] N. I. Bochkareva, "Capacitance spectroscopy of germanium containing growth dislocations," *Soviet Physics of Semiconductors*, vol. 25, pp. 323-328, 1991.
- [70] A. Carvalho, R. Jones, V. J. B. Torres, J. Coutinho, V. P. Markevich, S. Oberg, and P. R. Briddon, "Oxygen defects in irradiated germanium," *Journal of Material Science: Electronic Materials*, vol. 18, pp. 781-186, 2007.
- [71] V. P. Markevich, I. D. Hawkins, A. R. Peaker, V. V. Litvinov, L. I. Murin, L. Dobaczewski, and J. L. Lindstrom, "Electronic properties of vacancy--oxygen complex in Ge crystals," *Applied Physics Letters*, vol. 81, pp. 1821-1823, 2002.
- [72] V. Nagesh and J. W. Farmer, "Study of irradiation-induced defects in germanium," *Journal of Applied Physics*, vol. 63, pp. 1549-1553, 1988.
- [73] L. Colalongo, M. Valdinoci, G. Baccarani, P. Migliorato, G. Tallarida, and C. Reita, "Numerical Analysis of Poly-TFTs Under Off Conditions," *Solid State Electronics*, vol. 41, pp. 627-633, 1997.
- [74] P. T. Landsberg, *Recombination in Semiconductors*. New York: Cambridge University Press, 1991.
- [75] J. L. Hartke, "The three-dimensional Poole-Frenkel Effect," *Applied Physics Letters*, pp. 4871-4873, 1967.
- [76] G. A. M. Hurkx, D. B. M. Klaassen, and M. P. G. Knuvers, "A new recombination model for device simulation including tunneling," *Electron Devices, IEEE Transactions on*, vol. 39, pp. 331--338, 1992.
- [77] O. K. B. Lui and P. Migliorato, "A new generation-recombination model for device simulation including the Poole-Frenkel effect and phonon-assisted tunnelling," *Solid-State Electronics*, vol. 41, pp. 575--583, April 1997.
- [78] R. J. Krantz, L. W. Aukerman, and T. C. Zietlow, "Applied field and total dose dependence of trapped charge buildup in MOS devices," United States, 1987, pp. Pages: 1196-1201.
- [79] M. Lax, "Cascade Capture of Electrons in Solids," *Physical Review*, vol. 119, pp. 1502-1523, 1960.
- [80] J. L. Leray, P. Paillet, O. Flament, and A. Torres, "Oxide charge modeling with CEA-TRAPPOX code version 4. Comparison of trapping models on desktop computer," *Radiation and Its Effects on Components and Systems, 1999. RADECS 99. 1999 Fifth European Conference on*, pp. 53-58, 1999.
- [81] Synopsys, *Sentaurus Device User Guide, Z-2007.03 ed.*, 2007.
- [82] J. M. Hartmann, A. M. Papon, P. Holliger, G. Rolland, T. Billon, M. Rouviere, L. Vivien, and S. Laval, "Reduced Pressure Chemical Vapor Deposition of Ge thick layers on Si(001) for microelectronics and optoelectronics purposes," in *High-Mobility Group-IV Materials and Devices*, San Francisco, 2004, pp. 147-151.
- [83] G. C. Valley, "Photonic analog-to-digital converters," *Optics Express*, vol. 15, pp. 1955-1982, 2007.

- [84] S. J. Spector, T. M. Lyszczarz, M. W. Geis, D. M. Lennon, J. U. Yoon, M. E. Grein, R. T. Schulein, R. Amatya, J. Birge, and J. Chen, "Integrated optical components in silicon for high speed analog-to-digital conversion," *Proceedings of SPIE*, vol. 6477, p. 64770O, 2007.
- [85] F. X. Kärtner, R. Amatya, M. Araghchini, J. Birge, H. Byun, J. Chen, M. Dahlem, N. A. DiLello, F. Gan, and C. W. Holzwarth, "Photonic analog-to-digital conversion with electronic-photonic integrated circuits," *Proceedings of SPIE*, vol. 6898, p. 689806, 2008.
- [86] M. M. Frank, S. J. Koester, M. Copel, J. A. Ott, V. K. Paruchuri, H. Shang, and R. Loesing, "Hafnium oxide gate dielectrics on sulfur-passivated germanium," *Applied Physics Letters*, vol. 89, p. 112905, 2006.
- [87] F. Gao, S. J. Lee, J. S. Pan, L. J. Tang, and D. L. Kwong, "Surface passivation using ultrathin AlN film for Ge-metal-oxide-semiconductor devices with hafnium oxide gate dielectric," *Applied Physics Letters*, vol. 86, p. 113501, 2005.
- [88] W. P. Bai, N. Lu, and D. L. Kwong, "Si interlayer passivation on germanium MOS capacitors with high- κ /dielectric and metal gate," *Electron Device Letters, IEEE*, vol. 26, pp. 378-380, 2005.
- [89] S. Van Elshocht, M. Caymax, T. Conard, S. De Gendt, I. Hoflijck, M. Houssa, B. De Jaeger, J. Van Steenberghe, M. Heyns, and M. Meuris, "Effect of hafnium germanate formation on the interface of HfO₂/germanium metal oxide semiconductor devices," *Applied Physics Letters*, vol. 88, p. 141904, 2006.
- [90] A. Delabie, F. Bellenger, M. Houssa, T. Conard, S. Van Elshocht, M. Caymax, M. Heyns, and M. Meuris, "Effective electrical passivation of Ge (100) for high-k gate dielectric layers using germanium oxide," *Applied Physics Letters*, vol. 91, p. 082904, 2007.
- [91] M. F. Martin, J. K. Steven, C. Matthew, A. O. John, K. P. Vamsi, S. Huiling, and L. Rainer, "Hafnium oxide gate dielectrics on sulfur-passivated germanium," *Applied Physics Letters*, vol. 89, p. 112905, 2006.
- [92] D. Annelies, B. Florence, H. Michel, C. Thierry, E. Sven Van, C. Matty, H. Marc, and M. Marc, "Effective electrical passivation of Ge(100) for high-k gate dielectric layers using germanium oxide," *Applied Physics Letters*, vol. 91, p. 082904, 2007.